UNIVERSITY OF SOUTHAMPTON

FACULTY OF ENGINEERING AND THE ENVIRONMENT

Ship Science

Volume 1 of 1

Modelling, Characterization and Development of New Magnetorheological Elastomers with Enhanced Vibration Control Performance

by

Kyriaki Sapouna

Thesis for the degree of Doctor of Philosophy

May 2018

UNIVERSITY OF SOUTHAMPTON

ABSTRACT

FACULTY OF ENGINEERING AND THE ENVIRONMENT)

Ship Science

Thesis for the degree of Doctor of Philosophy

MODELLING, CHARACTERIZATION AND DEVELOPMENT OF NEW MAGNETORHEOLOGICAL ELASTOMERS WITH ENHANCED VIBRATION CONTROL PERFORMANCE

Kyriaki Sapouna

Magnetorheological elastomers (MRE) are a category of smart materials that can adjust their mechanical properties according to the intensity of an external magnetic field. The aim of this project is to develop new magnetorheological elastomers with improved isolation efficiency for applications in the marine industry. For this reason, novel silicon isotropic/anisotropic and anisotropic/anisotropic, with particles aligned at different directions, composite MR elastomers were manufactured. The samples were tested under pure compression and combined shear/compression loading mode, using an inclined prototype isolator device, to examine the principal elastic axis stiffness $\frac{k_p}{k_q}$ and damping ratio $\frac{c_p}{c_q}$. MR effect of dynamic stiffness is higher in pure compression isolator than the inclined isolator while MR effect of tangent of loss angle tanδ is higher in inclined isolator than pure compression. For the inclined test, the highest MR effect of 48% for K' and 68% for K'', is observed for the pure anisotropic sample and the lowest of 26% and 30% respectively for the isotropic MRE. Anisotropic/anisotropic parallel configuration has the same zero field static stiffness, lower dynamic stiffness, higher tanδ and same MR effect with anisotropic MRE. For all samples, the principal elastic axis stiffness $\frac{k_p}{k_q}$ and damping ratio $\frac{c_p}{c_q}$ changes with the magnetic field. A nonlinear viscoelastic model was also developed using receptance and mobility instead of stiffness and dashpot, to express the moduli of elasticity in respect to the applied force. Finally, a single degree of freedom mass-isolator with composite samples was simulated to show the enhanced vibration isolation properties of the composite samples.

Table of Contents

List of Tables

List of Figures

DECLARATION OF AUTHORSHIP

I, Kyriaki Sapouna declare that this thesis and the work presented in it are my own and has been generated by me as the result of my own original research.

Modelling, Characterization and Development of New Magnetorheological Elastomers with Enhanced Vibration Control Performance

I confirm that:

1. This work was done wholly or mainly while in candidature for a research degree at this University;

2. Where any part of this thesis has previously been submitted for a degree or any other qualification at this University or any other institution, this has been clearly stated;

3. Where I have consulted the published work of others, this is always clearly attributed;

4. Where I have quoted from the work of others, the source is always given. Except for such quotations, this thesis is entirely my own work;

5. I have acknowledged all main sources of help;

6. Where the thesis is based on work done by myself jointly with others, I have made clear exactly what was done by others and what I have contributed myself;

7. Parts of this work have been published as:

    - K. Sapouna, Y. Xiong and A. Shenoi. Smart vibration isolator using magnetorhelogical elastomers. *International workshop on Ship Vibration & Noise IWSVN, Wuxi, China, Oct 2015*
    - K. Sapouna, Y P Xiong and R A Shenoi. ‘’Dynamic mechanical properties of isotropic/anisotropic silicon magnetorheological elastomer composites.’’ 2017 *Smart Mater. Struct.* **26** 115010

Signed: .....

Date: .....

Acknowledgements

I would like to thank my supervisors, the management of the university of Southampton and all the administration staff for their support and consideration so that I could finish my PhD while raising a family. In addition, many thanks to my main supervisor Assistant professor Yeping Xiong for not letting me quit.

Loads of thanks to Dr Adam Sobey and Dr Nick Townsend for the advice and guidance they have provided during all these years and my husband for accepting Mr Effect as part of our family.

Finally, I would like to thank Lloyds Register Foundation (LRF) for funding part of this project and my parents for funding my previous studies that allowed me to apply for the LRF funding in the first place.

Definitions and Abbreviations

MRE	magnetorheological elastomers
MR effect	Magnetorheological effect
DMA	Dynamic mechanical analyser
M*	Complex modulus
$\|M^*\|$	Absolute modulus
M'	Storage modulus
M''	Loss modulus
E*	Complex compression modulus
$\|E^*\|$	Absolute compression modulus
E'	Storage compression modulus
E''	Loss compression modulus
G*	Complex shear modulus
$\|G^*\|$	Absolute shear modulus
G'	Shear storage modulus
G''	Shear loss modulus
δ	Loss angle
tanδ	Tangent of the loss angle
K*	Dynamic stiffness
$\|K^*\|$	Absolute dynamic stiffness
K'	Real component of dynamic stiffness
K''	Imaginary component of dynamic stiffness
S	Shape function
SC	Shape function parameter
SDOF	Single degree of freedom
P,Q,R	Principal elastic axis
k_p	Stiffness in the P principal axis
k_q	Stiffness in the Q principal axis
k_r	Stiffness in the R principal axis
c_p	Damping in the P principal axis
c_q	Damping in the Q principal axis
c_r	Damping in the R principal axis
I	Electric current
B	Magnetic flux density

Chapter 1: Introduction

1.1 The need of smart vibration isolators in marine vessels

Progress in engineering can only be achieved through constantly increasing speed, efficiency and precision of machines. This practically means lighter and more powerful engines that, unfortunately, tend to vibrate more or are more sensitive to external vibrations. The solution to this problem is the use of complicated isolation systems that reduce the unwanted vibrations transferred by the machine to the environment or the other way around. The appropriate materials and design of such isolation systems are selected according to the range of frequencies where efficient isolation is needed, the natural frequencies of system, the static stiffness to support the weight of the machine, general environmental conditions and finally cost. An ideal isolation system, should have a resonance frequency lower than the natural frequencies of the system and low transmissibility at resonance that in addition decreases rapidly with frequency. Therefore, isolators with low dynamic stiffness and high damping are required.

Efficient vibration isolation systems for marine applications are complicated mostly due to the different loading conditions and flexible foundations found on a ship or sailing boat and the large weight of marine engines. The engine room of a marine vessel is full of rotating, reciprocating and forging machines that generate huge amounts of noise and vibration. Except the main engine, a typical engine room will contain several generators, compressors, pumps, separators, refrigerators and auxiliary engines that vibrate constantly especially when containing unbalanced parts. These vibrations are then transmitted through the mounts of the machines to the hull of the ship resulting to the degradation of the shell and the surrounding machinery as well as passenger discomfort.

In addition, the ship hull is considered as a flexible structure that is subjected to random harmonic loading conditions while travelling at sea. The movement of the ship will subject the hull to multidirectional loads that are finally transmitted to the machines through their mounts. The hull, in most cases, vibrates in relatively low frequencies compared to engine generated vibrations that are mainly caused by the rotating parts. It is crucial, therefore, to mount all machines to efficient isolators to reduce the vibration levels transmitted to the hull and the surrounding equipment and in the same time protect the machines from shock and vibration generated by the surrounding environment. In addition, any isolation system used must survive the rough marine environment.

The simplest isolation system is the modest passive rubber resilient mount or metal spring mounts present in most machines today. Passive isolators do not have the ability to vary their stiffness or damping and therefore their natural frequency. They are simply designed to have a low natural

frequency that does not lie within the operating frequency range of the machine and can support its weight. However, most machines do not start running immediately to their full speed but are driven slowly passing through their critical speeds, while most of the time they have more than one natural frequency. Passive isolation systems cannot provide efficient isolation in a wide frequency range and are designed having in mind only the dominant natural frequency. Thus, they can provide efficient isolation only at high frequencies. In applications where isolation is required in a wide frequency range, especially at low frequencies, active vibration isolation systems are used. Most of these systems work by shifting their natural frequency according to an input signal to avoid resonance.

1.2 Aim and Objectives

The aim of this project is to:

Examine practical ways of improving the isolation efficiency of MRE isolators so that they can be used in the marine industry.

The project can be divided in an experimental and a theoretical part with the following objectives:

a) Experimental part

- Setting up a reliable measuring system that includes an appropriate magnetic circuit and fixtures for pure compression loading tests.
- Perform dynamic mechanical characterization tests of isotropic and anisotropic MREs with small (4-6μm) and large particles (<220μm) under varying pure compression load amplitude, frequency, static load and magnetic field.
- Manufacture and test composite isotropic/anisotropic and anisotropic/anisotropic MREs.
- Setting up a reliable measuring system that includes an appropriate magnetic circuit and fixtures for shear/compression loading tests.
- Test the simple and composite MREs under shear/compression loading conditions.
- Build and test a vibration isolator prototype device.

b) Theoretical part

- Produce a nonlinear model of MRE.
- Validate the model with the experimental data using MATLAB.
- Simulate a single degree of freedom mass-MRE isolator system in MATLAB and Simulink.
- Propose the control system.

Available resources:

- Dynamic mechanical tester (DMA) INSTRON Electropuls E1000 machine in TSRL laboratory.
- Silicon rubber and iron particles.
- Very limited budget.

1.3 Novelty

To the authors knowledge, the novel pieces of this work are:

a) Experimental part:

✓ Examine the mechanical properties of silicon MREs made with very large particles (diameter <220μm) compared to the most traditional silicon MREs with small particles (4-6 μm).

✓ Examine the effect of size and shape of isotropic MRE samples on zero field dynamic mechanical properties (scaling effect) and magnetorheological effect.

✓ Manufacture and test composite isotropic/anisotropic MREs with iron particles of different sizes in parallel and series configurations.

✓ Examine the dynamic mechanical properties of composite isotropic/anisotropic and anisotropic/anisotropic (with particles aligned in different directions) MREs in axial, lateral and longitudinal directions.

✓ Test the pure isotropic, pure anisotropic and the above mentioned composite MREs under shear/compression loading mode in a 45^0 inclined isolator device and under pure compression mode in a compression isolator device. Define how principal stiffness and damping ratios changes with magnetic field.

a) Theoretical part:

✓ Make a force dependent viscoelastic model of MREs to simulate the force transmissibility of a single degree of freedom mass- MRE isolator system working in pure compression and shear/compression mode.

✓ Examine the principal stiffness ratio of combined isotropic/anisotropic and anisotropic/anisotropic MREs

Chapter 2: Literature review

2.1 Smart materials

Smart materials are a new type of material that responds to the environment changes by adjusting their physical or chemical properties. Material properties can be controlled by many external factors, including stress, temperature, pH level, moisture content, electric fields or magnetic fields. They are mostly used as actuators and sensors in civil engineering, industrial and household appliances, medical appliances and automotive industry. Common examples of smart materials are presented in Table 1.

Table 1: Summary of smart materials

Stimulus	***Change in***			
	Shape/Deformation	**Colour**	**Electric charge**	**Rheological Properties**
Stress	-	Piezocromic	Piezoelectric	-
Temperature	Shape memory materials (SMA)	Thermochromic	*Thermoelectric* (TE)	-
Electric field	*Electrostrictive* (ES)	Electrochromic	-	Electrorheological fluids (ERF) elastomers (ERE)
Magnetic field	*Magnetostrictive* (MS)	-	-	Magnetorheological fluids (MRF) gels (MRG) elastomers (MRE)
Light level	-	Photocromic	-	-
pH level	pH sensitive	pH sensitive	-	-

MRE and MRF belong in the same category of smart materials with Electrorheological elastomers (ERM) and fluids (ERF). Unlike Electrorheological materials that require a strong electrical voltage in order to adjust their mechanical properties, magnetorheological materials are controlled by an external magnetic field that is supplied by an electromagnet fed by a moderate electrical current that require low voltage. Thus, they are less power consuming and much safer to use in real

vibration control systems. MR fluids were developed first and have been used in many commercial applications. Although MR fluids require a smaller magnetic field to operate than MR elastomers, the metal particles in the fluid tend to settle down with time and the appropriate seals are necessary . Designing therefore, practical isolation devices with MR fluids become complicated and MR elastomers seem a more attractive solution for long term applications in tough environments like the ones found in the marine industry.

2.2 Working principle of magnetorheological elastomers

Magnetorheological elastomers (MREs) consist of ferromagnetic particles suspended in a low permeability elastomer matrix with medium values of hardness and viscosity before curing, to allow for the particles to dispense in the matrix. When an external field is applied to the MR elastomer during curing, the filler particles tend to align parallel to the direction of the magnetic field forming 3D chains and the material is called *anisotropic or aligned MRE*. On the other hand, when the elastomer is cured without the presence of the field, the particles are randomly dispensed inside the matrix and the elastomer is called *isotropic MRE*.

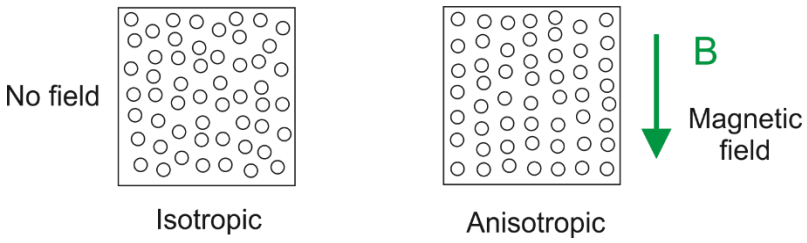

Figure 1: Illustration of isotropic and anisotropic MREs

The original mechanical properties of MREs, under zero magnetic field, are determined mostly by the properties of the matrix elastomer as well as the concentration and size of magnetic filler particles. The performance of MREs is usually evaluated by the MR effect which is the relative change of the modulus of elasticity when the field increases from 0T to a certain value. MR effect decrease or remain constant for field strengths greater than a value due to the magnetic saturation of the iron particles. This value depends mostly on the type of the particles while for iron particles it is around 0.6T. The strength of the magnetic field where the filler particles saturate is a limiting factor for all MR materials. However, generating magnetic fields greater than 0.6T is very difficult and thus any device using MREs should be designed to work below that value.

$$\text{MR effect} = \frac{M_0 - M_B}{M_0} \text{ x } 100 \ \ (\%) \qquad (2.2.1)$$

Where:M_0= absolute modulus at zero field and M_B = absolute modulus at a certain field value.

The working principle of MR elastomers is simple (Figure 2), although the exact mechanism is not fully understood. When an external magnetic field is applied to a MRE the ferromagnetic filler particles get magnetized and interact with surrounding particles. Forced by the magnetic moments, the particles start to move inside the matrix elastomer to align parallel to the direction of the applied field, pushing or destroying the polymer molecule chains on the process. As the magnetic field increases, so are the magnetic moments that forces the particles to overcome any obstacles placed by the matrix elastomer. The result is a change of shape and an elongation in the direction of the applied magnetic field occurs. When the external magnetic field is removed, the particles are pushed back to their original positions as the elastomer molecule chains return to their original form. Therefore, the process is fully reversible. Since the exact particle distribution is not known it is expected that there are areas inside the material where the local magnetic forces are higher than the rest and thus, even isotropic MRE are anisotropic materials.

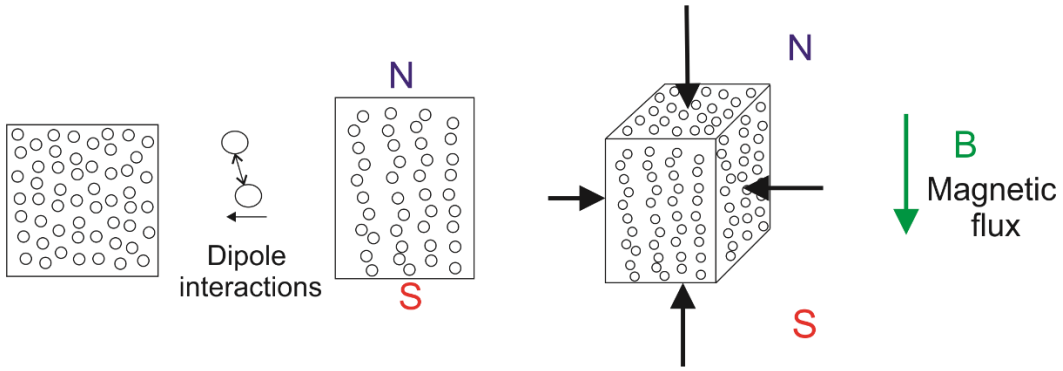

Figure 2: Working principle of MRE

The alignment of filler particles parallel to the magnetic field increases significantly the static and dynamic modulus of the material in that direction. The increase (or MR effect) is therefore proportional to the magnetic field. However, the modulus in the direction perpendicular to the applied magnetic field is not influenced greatly, as illustrated in Figure 2. The same principle applies for the zero-field modulus of anisotropic MREs, that it is higher at the direction of the aligned particle chains.

The actual structural composition of MR elastomers is not even fully understood and cannot be controlled easily. In most MREs, the filler particles are not chemically bonded with the elastomer but are trapped between the long crosslinked molecule chain structures during the polymerization process and their exact position cannot be determined. For isotropic samples the particles are considered to be randomly dispensed inside the matrix, while for anisotropic samples the classical theory considers that the particles form identical columns separated by the same distance between each other, depending on the applied magnetic field and particle distribution.

However, recent studies showed that this is not true. Gunther et al (Gunther D 2012), used electron microscopy methods to study the microstructure of the anisotropic samples and found that the column diameter was larger in the lower part of the samples due to gravity forces, while the number of columns increased at the bottom of the sample. In addition, Bombarth et al (Borbath T 2012), used X-ray micro-computer tomography to study the size and distance between the columns of anisotropic MREs at different magnetic fields during curing process. They found that strong magnetic fields result in higher repulsing forces between particles and thus to closely packed columns at greater distances between them. At lower magnetic fields, the number of columns increases while they become thinner. However, significant gravitational sedimentation and the formation of agglomerates at the bottom of the sample was also observed. Thus, it is not necessary to apply a very high magnetic field up to the saturation value during the curing process to achieve the best result regarding column structure.

2.3 Magnetorheological effect

When an external magnetic field is applied to MREs, static and dynamic stiffness of all MREs increase by an amount that depends on matrix material, particle concentration, particle size and for anisotropic MREs particle alignment and magnetic field while curing. Danas et all (Danas K 2012), proposed a theory of how particles interact inside the matrix when the external field is applied, in order to explain the different deformation mechanism when the field is in parallel or perpendicular to the chains of anisotropic MREs. They claimed that a larger magnetostriction is obtained for MREs with particle columns perpendicular to the external magnetic field and not for the ones with particles aligned in parallel. This leads to a greater extension in the perpendicular sample and thus to a smaller change in stiffness measured in the same direction of the applied magnetic field which is the parallel one. This is in agreement with other older studies (Abramchuck S 2007) and the general accepted fact that the strongest magnetic reinforcement effect is when the applied field is parallel to the particle aligned columns and the applied load.

The strong dependence of MR effect on loading conditions as well as sample size and different magnetic field intensity during testing and curing, makes it impossible to compare the data published in literature. Therefore, the MR effect numbers mentioned later are just an indication and more emphasis is given on general trends. Blom et al (Blom P 2011), performed dynamic shear tests at high frequencies to natural rubber MREs to find that dynamic stiffness increases while damping factor decreases with increasing magnetic field. Zhu et al (Zhu J T 2012), however, reported also an increase of dynamic stiffness but a small increase of damping factor in natural rubber MREs. Wei et al (Wei B 2010), reported a huge increase of the dynamic stiffness by 120% when the field was increased from zero to 0.8T but a small decrease of damping factor in

polyurethane anisotropic MREs. Xu et al (Xu Y 2011), reported a much higher MR effect for the shear modulus of polyurethane MREs of 532% for the anisotropic samples and 1225% for the isotropic ones, although it has to be noted that the samples were only 1 mm thick. Damping factor of both samples decreased significantly with increasing magnetic field. Lokander et al (Lokander M 2003), reported a 25% maximum MR effect for nitrile rubber MREs.

Kallio et al (Kallio M 2007), reported that stiffness and damping factor of anisotropic silicone rubber MREs increased by 11% and 18.5% respectively with increasing magnetic field (0.35T). When silicon oil was used, Gong et al (Gong X L 2005), reported a 60% increase in stiffness for isotropic silicon MREs while Schubert and Harrison (Schubert G 2015), a 284% increase on static stiffness of anisotropic silicon MREs. Ju et al (Ju B X 2012), experimented with porous silicone MREs to achieve an increase of 170% of the stiffness with an increasing magnetic field up to 0.6T while damping factor stayed almost unaffected. The latter was also reported by Behrooz et al (S. J. Behrooz M 2015), while the maximum stiffness increase was 16%. Hu et al (Hu Y 2005), reported a higher MR effect for silicon MREs (33%) than polyurethane although, their blend MRE gave a slightly higher MR effect (35%). From the available published data, it can be concluded that both static and dynamic stiffness increase significantly with the application of the magnetic field but the case for damping is different. Damping appears to increase or decrease slightly depending on matrix material and the type of dynamic test performed. It can be assumed therefore that damping is not affected significantly by the magnetic field.

In addition, the type of applied load influences greatly MR effect. Schubert and Harrison (Schubert G 2015), reported that MR effect of isotropic and anisotropic silicon MREs is higher under static compression that static shear, while for anisotropic MREs with particles aligned perpendicular to the applied load MR effect was higher under static shear. Their experiments also presented that MR effect decreases with increasing static strain. A similar finding was also reported by Li and Sun (Li R 2013), where MR effect of dynamic stiffness and tangent of the loss angle decreased with increasing load amplitude and frequency for both shear and compression tests. They also reported that MR effect was slightly higher under compression than shear dynamic load which also agrees with the findings of Gordaninejab et al (Gordaninejad F 2012).

2.4 Materials and manufacturing methods

Type of matrix elastomer

The type of matrix material defines the mechanical and physical properties of magnetorheological elastomers. In general, natural rubber (NR) is considered the best choice for isolation applications due to its superior mechanical properties. It is reported that natural rubber MREs, have higher moduli of elasticity and MR effect than butadiene rubber MREs (G. X. Zhang W 2010) and better physical properties, similar MR effect but much lower damping capability that bromobutyl rubber (BIIR) MREs (Zhu J T 2013). MREs made of a soft matrix elastomer like polyurethane (PU) rubber, have higher MR effect than natural rubber MREs (Wei B 2010) (Mitsumata T 2011) (Xu Y 2011), mostly due to the lower friction between matrix and particles that allows the particles to move easier inside the matrix molecules under the influence of the magnetic field.

Another soft polymer that is widely used in MREs is silicon (Si) rubber. Silicon MREs have excellent insulating properties, excellent chemical resistance and excellent stability over large temperature range but have low room temperature strength and are sensitive to oil. In general, they do not have the mechanical stability of polyurethanes or the advanced mechanical properties of natural rubber but are very simple and safe to manufacture and do not require a specific temperature or pressure to be applied to the samples while curing. Li and Sun (Li W 2013) used Polydimethylsiloxane (PDMS) MREs as another type of silicon rubber with better mechanical properties, but a low MR effect was observed. In order to improve the properties of MREs, some researchers experimented with blends of two different matrix rubbers like polyurethane (PU)/silicone (Hu Y 2005) and polystyrene/silicone (Wang Y 2007) blend MREs, which had an increased MR effect when compared to pure silicon MREs but a much more complicated manufacturing process.

Type of particles

In recent years, much attention has been given on investigating possible combinations of particle and matrix materials that can enhance the zero field mechanical properties of MREs and MR effect. Padalka et al (Padalka O 2010), reported that the MR effect (dynamic stiffness) is higher for MREs with carbonyl iron particles than for those with Nickel and Cobalt. Yang et al (G. X. Yang J 2013) and Anderspn et al (Anderson K 2015), used MREs with nano strontium ferrite and hard M-type barium Hexaferrite (BaM) particles respectively to conclude that carbonyl iron is a better choice for MREs. Khimi et al (P. K. Khimi S R 2015), used the much cheaper iron sand in natural rubber MREs and the Taguchi method to optimize the concentration, size and magnetic field during curing in order to achieve the highest possible damping in different loading conditions. They also concluded that the

particle size itself is not of great importance but the optimal conditions mostly depend on the loading frequency, amplitude and temperature.

Yu et al (J. B. Yu M 2012), reported that the carbon content of carbonyl iron particles does not influence the stiffness of MREs but both damping and MR effect are higher for samples with low carbon content particles. Yang et al (G. X. Yang J 2013), used a small amount of Silicon Carbide (SiC) particles, with the common carbonyl iron particles, to increase stiffness and damping of the MRE and improve the MR effect. The improved performance however, is observed only for an optimum concentration of 3.2 wt % and 6mm size particles which is the same size with the carbonyl iron particles.

Size and density of particles

Other important parameters that influence the mechanical properties and MR effect of MREs are the size and density of magnetic particles. It has been well established that the maximum MR effect in silicon MREs is achieved when the particle/matrix material ratio is about 30% per volume or 70% per weight (Kallio M 2007), (Popp KM 2010), (Schubert G 2015). Bose and Roder (Bose H 2009), performed dynamic tests on silicon rubber MRE with large diameter (40 μm) and small diameter (5 μm) particles at different particle densities, to report that both stiffness and damping increase with increasing density while the MR effect is higher for samples with large particles. Li and Zhang (Li W H 2010), experimented with silicon MREs containing large (50 μm) and small diameter (5μm) iron particles to conclude that the samples that combined the two kinds of particles had a low zero field modulus but a much higher MR effect than the samples with one type. However, Chertovich et al (Chertovich A V 2010), performed similar tests to conclude to the opposite result.

In addition, Aloui and Kluppel (Aloui S 2015), used nanosized Magsilica and microsized CIP particles, alone and together at a total fixed concentration. They reported an increase of the tensile strength with increasing nanoscale particle concentration due to formation of a physically bonded filler network and to strong polymer-filling coupling. However, the MR effect also decreased significantly because the magnetic moment for the nanosized particles is too small for delivering sufficient attraction when an external field is applied. Kashima et al (Kashima S 2012), also experimented with silicon MREs made out of large (30 μm) or small diameter (6μm) iron particles at different concentrations, to find that increasing particle density improves the saturation magnetization while increasing particle size improves the relative permeability bus does not influence the saturation magnetization. Yang et al (G. X. Yang J 2012), investigated in detail the damping mechanism of MREs to found that the damping capability increases significantly with increasing particle density.

Additives

Another aspect to be considered is the effect of other additive materials found in most of conventional rubbers used in isolators. Carbon black is the most common filler material which gives a black colour to the original translucent elastomers. Its main purpose is to increase the mechanical strength and stiffness of the material, while it also absorbs UV radiation protecting the material from degradation when exposed to sunlight. Adding carbon black to MREs, along with the iron particles, increases stiffness, damping and thermal stability (Nayak B 2004). However, carbon black constrain the iron particles from moving freely inside the matrix when the external field is applied. In the case of anisotropic MREs, this leads to shorter and less aligned chain-like columnar structures (a. P. Khimi S R 2015).

Other types of additives used are plasticizers that help the dispersion of fillers in the chains while improving flow in moulding and antioxidants that improve the aging properties of the elastomer. Fan et al (Fan Y C 2010), used maleic anhydrite to improve the bonding between particles and matrix and thus, decrease damping. Chung et al (Chung K 2015), reported that MR effect on Natural rubber MREs could be increased with the addition of peptisizer to control viscosity of matrix natural rubber. Other researchers used silicon oil to silicon rubber MREs in order to improve particle-matrix interaction and increase the MR effect (Gong X L 2005).

Patterned elastomers

In another approach, some researches tried to increase the MR effect by patterning the particles inside the matrix in order to create more complicated structures than simple anisotropic or isotropic MREs. Zhang et al, (Zhang X 2008) fabricated patterned MREs with PDMS as matrix material and positioned the iron particles using micro technology techniques to form two different types of MRE, one with a lattice structure and one with a body cantered tetragonal (BCT) structure. The BCT structure was found to decrease its field-induced modulus while none of the samples showed significant results. The same research group, also manufactured hybrid natural rubber MR elastomers with MR gel filled columns through the matrix material (G. X. Zhang W 2010). They claimed that the new samples offered significantly improved mechanical properties than conventional MREs especially regarding the damping capability of the material. However, this combined material is difficult to manufacture with relative small stiffness that limits its uses in real practical applications.

Ju et al (Ju B X 2012), manufactured porous MREs by immersing ammonium bicarbonate (NH_4HCO_3) to silicon rubber and then mix it with the iron particles, following the findings of Choi(Choi 2009) that reported that MRE with holes in them have higher MR effect. By this way, they were able to

control the amount of pores created inside the material. The experimental shear tests, showed a decrease of the stiffness of the samples with increasing NH4HCO3 but an increase of the damping factor and the MR effect. Yu et al, (X. Z. Yu M 2015) showed that a simple method of punching circular honeycomb holes in anisotropic MREs, at an optimum porosity of 13%, increases significantly the MR effect and zero field damping while decreases zero field stiffness.

Forster and al (Forster E 2012), used a new wax cast moulding pattering method, similar to lithography technique, to create columns of MREs on top of a substrate. The samples produced were extremely soft, when PDMS was used as a matrix, and agglutinative in the case of silicone rubber. However, no full mechanical characterization was performed and no definite results could be drawn regarding the advantages of this method. Lian et al (Lian C 2015), suggested a new structured MRE where a silicon MRE is wraped with a polyurethane MRE in order to improve wear resisting properties while maintaining high MR effect. The new elastomer was shown to have the best durability when compared to pure silicone and polyurethane MREs. Finally, Boczkowska et al (Boczkowska A 2012), manufactured anisotropic polyurethane MREs where the iron particles were not aligned parallel to the applied external magnetic field and load but in an angle. The highest yield stress was observed for samples with particles at an angle of 30 degrees to the direction of the magnetic field, but this could be also attributed to the coupling effects between the applied load, direction of the applied load and particle orientation.

2.5 Factors influencing the dynamic mechanical properties of MREs

Load amplitude and frequency

Magnetorheological elastomers show a similar dependence on frequency with all filled rubbers. When load frequency increases, dynamic stiffness increases slightly while damping factor passes through a maximum at a frequency depending on the matrix material to decrease for higher values (Kallio M 2007), (Opie S 2011), (Gong X 2012). Similar to all filled rubbers, dynamic stiffness of all types of MREs decreases with increasing load amplitude while this trend is more pronounced for anisotropic MREs under both compression and shear loading tests (Kallio M 2007) (Opie S 2011). This is the well-known Payne effect defined as:

Payne Effect: *Payne effect is the decrease of modulus with increasing strain amplitude that occurs only in filled rubbers. It is believed to be caused by the breaking and rearranging of the molecule chains with the increasing load. The material usually needs 30 min to recover to its original state.*

Again like all filled rubbers, stiffness of MR elastomers decreases during the first loading cycles until it reaches a stable point. This is the well-known Mullins effect defined as:

Mullins effect: *Mullins effect is the phenomenon where stiffness decreases with loading cycles until the material comes to a stable point after some cycles (usually 3-5). This means a lower resulting stress for the same applied strain during the first loading cycles. There are a lot of theories trying to explain the origins of Mullins effect but none has been proven or is valid for all rubbers. It is believed in general that it is due to the breakdown of the original firm binding structure between the filler particles and the rubber molecules when a load is applied. If the material is left unloaded for a long period of time this firm binding will start forming again and the material will recover partly its original stiffness. The recovery procedure can be speeded up if the material is heated for a certain time. The recovery time is usually more than 24 hours and some materials never recover totally to their original state depending on the strain they are loaded to.*

The situation is not so straight forward for damping. Opie and Yim (Opie S 2011), performed dynamic tests on silicon rubber MRE to report that damping factor increases slightly with increasing amplitude that came in agreement with the data published (Gong X 2012) regarding polybutadiene (BR) rubber MREs. On the other hand, Zhu et al (Zhu J T 2012), reported that damping factor decreases with increasing amplitude for natural rubber MREs while Kallio et al (Kallio M 2007), showed that it remains practically constant for silicone rubber MREs.

Temperature

The effects of temperature to the material have has very little been studied. Lejon jonas (Lejon Jonas 2012) showed that MRE was still in the rubbery region at 0^0 C =, but both shear modulus and tangent of the loss angle increased with further temperature decrease indicating that the transition region is reached. However, shear modulus and tangent of the loss angle did not seem to increase greatly for temperatures up to 45^0 C. Nayak et al (Nayak B 2004), reported that storage modulus increases slightly with temperature while tangent of the loss angle drops for silicone rubber MREs while the addition of carbon black improves thermal stability. Zhang et al (G. X. Zhang W 2011), investigated the effect of temperature on natural rubber and polybutadiene (BR) rubber MR elastomers. The results showed that tangent of the loss angle decreases with temperature for both types of MREs while storage modulus behave differently for each type. Dynamic modulus of elasticity decreased with temperature for Natural rubber MREs, while for BR MREs it decreased up to 50^0 C to slightly increase for higher values.

Static preload

An important factor determining the dynamic mechanical properties of all filled elastomers is the prestrain (or prestress) applied to the elastomer, usually due to the weight of the machine it supports. It is well established that both storage and loss moduli increase with increasing prestrain especially for high filler content (Thorin A 2012) . The same results are expected for MREs, although not many researchers dealt with this matter. Lejon Jonas (Lejon Jonas 2012) studied the influence of the prestrain to the dynamic mechanical properties of isotropic elastomers to conclude that as the prestrain increases the material becomes softer before it starts to get stiffer after a certain value, while damping factor also increases slightly. Feng et al (Feng J 2015), studied the effect of the applied prestress on dynamic stiffness and MR effect of anisotropic MREs, to report that both increase at small prestress valued while they present a decreasing trend at large prestress values. They attributed this behaviour to the altering of spacing between the particles when they are overstressed that after some point start to touch each other. The particle concentration affects the point when this starts to happen. However, they did not report the effects of prestress on damping.

Fatigue, wear and ageing

Another aspect of MRE behaviour that only recently has been studied is their ageing, wear and fatigue properties under constant dynamic load. It is expected than these properties will be similar to the properties of the pure matrix rubber used, for example natural rubber MREs, have better ageing but worst fatigue properties than butadiene rubber MREs (G. X. Zhang W 2010). However, it was reported that polyurethane MREs showed lower wear resistance and thermal conductivity than pure polyurethane rubber due to the presence of magnetic fillers (Lian C 2015). The same study also suggested that both silicon and polyurethane MREs improve their wear resistance when the field is applied, due to higher hardness values.

Absolute modulus $E^*$of silicon MREs decreases with increasing number of loading cycles, until a limiting value independent of the applied strain amplitude (Zhou Y 2015). However, while moduli of elasticity decreased MR effect increased with increasing number of loading cycles (G. X. Zhang W 2010). The latter was attributed to the lower value of moduli at zero field since the magnetic field caused absolute moduli increase remained the same. In addition, anisotropic silicon MREs showed higher fatigue resistance than isotropic silicon MREs at zero field (Zhou Y 2015). The effect of oxidation on the mechanical properties of silicon MREs was studied by Brhrooz et al (S. J. Behrooz M 2015). It was found that oxidation reduces significantly the shear modulus of MREs while MR effect is higher, due again to the lower zero field modulus. The same study reported that polymer coating particles preserves stiffness in oxidative environments.

Size and shape of MRE

One of the great challenges when designing isolators with rubber is the prediction of static and dynamic properties when scaling up the rubber component. In theory, the dynamic stiffness for any elastomer can be estimated using equation (2.5.1). For relatively small sized elastomers this can provide a good estimation when the elastomer is subjected to shear loads ($|M^*| = |G^*|$). In case of compression load however, the size and shape of elastomer becomes of importance and equation (2.5.2) should be used instead. An experimentally defined shape correction parameter SC is introduced to minimize the error between the predicted stiffness form equation (2.5.1) and the actual one. The shape correction parameter SC is a different parameter than the shape factor S defined by equation (2.5.3).

$$K^* = \frac{Area}{L} M^* \tag{2.5.1}$$

$$K^* = SC \ \frac{Area}{L} E^* \tag{2.5.2}$$

$$S = \frac{Area\ to\ which\ the\ force\ is\ applied}{force - free\ area} \tag{2.5.3}$$

Where Area=effective area of the elastomer the force is applied to, L=length of the elastomer, SC is the shape correction parameter and S= shape factor. The parameters of the shape function depend on the shape, type and hardness of elastomer of interest and are available on the published literature (Davey A B 1965).

In the case of MREs, the effect of size and shape has barely been studied. Gordaninejab et al (Gordaninejad F 2012), used anisotropic silicon MREs of different heights under quasi-static shear and compression loads, to report that the MR effect of both moduli is independent of size. Oguro et al (Oguro T 2017), performed static compression tests on disk isotropic MREs of different diameters at no field and when placed on a single permanent magnet. They showed that the zero field static stress measured at the same strain and the magnetically induced stress increment gradually increases with the sample size but the magnetic field produced from a single magnet is non uniform. However, neither investigated the effect of MRE sample size and shape on the dynamic mechanical properties.

2.6 Models of magnetorheological elastomers

MR elastomers at zero field, like all filled elastomers, are governed by a nonlinear stress-strain relationship with a complex modulus of elasticity that depends weakly on load frequency and strongly on load amplitude and static prestrain. Thus, it is common practice to use the models developed for filled elastomers modified to consider magnetorheological effect. In general. there are two ways to model the behaviour of an elastomer. The first is to use linear and nonlinear rheological elements connected in different configurations, like the modest Kelvin, Maxell and Zener models. This modelling approach is practical because model parameters can be extracted from curve fitting to experimental values of moduli of elasticity, but often have no physical meaning. The second modelling approach is to establish constitutive equations using continuum solid mechanics principles, taking under consideration the coupled mechanical and magnetic behaviour. This method can produce strain energy functions that are physically meaningful and can be used in finite element software. However, these models require equibiaxial tests to determine the stiffness coupling coefficients. Such a test is the bubble inflation test that make sense in zero field conditions. When the magnetic field is applied, it becomes very difficult to construct a test setup that can provide a stable magnetic field around the inflated MRE sample without restricting the free movement of the elastomer.

Viscoelastic models

A short description of the viscoelastic models developed for MREs is presented next while an extended description can be found to a recently published review by Cantera et al (Cantera M A 2017). Blom and Kari (Blom P 2011) proposed a model where the total stress was decomposed into three-time dependent component. An elastic one where stress in linear with strain, a viscoelastic part where stress is related to the strain rate history and a friction component where the stress is related nonlinearly with strain. The nonlinear friction component is further linearized to work in the frequency domain, although its value still depends on the applied strain. The model ignores the magnetic field - viscoelastic properties coupling effects as well as the prestrain dependence. Xin et al (Xin F L 2016) proposed a linear viscoelastic model of two kelvin chains in parallel, one represented the frequency and amplitude dependent mechanical viscoelasticity and the second the frequency, amplitude and magneto-dependent magnetic viscoelasticity. This model too ignores the effect of static prestrain on viscoelastic properties.

Eem et al (Eem S H, Modeling of Magneto-Rheological Elastomers for Harmonic shear Deformation 2012), used a Ramberg-Osgood model in parallel with a Maxwell chain to describe the nonlinearity and viscoelastic behaviour of the MRE respectively. The parameters were extracted using the force-displacement hysteresis curves for frequencies only up to 3Hz, which does not indicate accurate

results. The main disadvantage of this approach is that a wide range of dynamic loading experiments are required to define the parameters. Norouzi et al, (Norouzi M 2015) proposed a nonlinear model based on Kelvin model where the frequency dependency on MRE stiffness and damping as well as the strain dependency on stiffness is represented by power functions, while damping does not vary with strain. The magnetic field dependency is represented by a polynomial function. The model could predict accurately the variation of stiffness and tangent of the loss angle with magnetic field and strain amplitude but was only validated for a short frequency range (up to 8Hz).

Yang et al, (D. H. Yang J 2013) proposed a model for a seismic isolator that incorporates a Bouc-Wen component, which reproduces hysteresis loops, in parallel with a Voigt element, which describes solid-material behaviours. They studied in detail, the influence of each magnetic field dependent parameter on the shape of hysteresis loop but a different parameter values were used for each strain amplitude and frequency. Behrouz et al, (W. X. Behrooz M 2014) used electric current dependent Booc-Wen, spring and dashpot elements in parallel to a three-element standard solid model to model the magnetorheological effect and zero field viscoelastic behaviour respectively. The model could predict the behaviour of a MRE isolator for different magnetic field values but a new set of parameters were used for each strain amplitude and did not consider the loading frequency. Li Y and Li J (J 2017) used a power law strain stiffening element in parallel to the standard three parameter linear viscoelastic model to model the response of a laminated MRE seismic isolator. This rate dependent model can describe better the behaviour of the device under large strains.

Chen and Jerrams (a. J. Chen L 2011) used the standard linear solid model parallel to a nonlinear spring and a spring-Coulomb friction slider to model the viscoelasticity of the polymer composite, the magnetic field induced mechanical properties and the interfacial slippage between the matrix and the particles respectively. Although, the model can theoretically describe the general trends of the material it was not validated using experimental while it is mentioned that the parameters of the friction slider and stiffness can be obtained from macroscopic slippage experiments that cannot be performed with standard mechanical testing machines. On another point of view, Yu et al (Yu Y 2015) used artificial neural network modelling method that did not require the knowledge of any physical parameters of the system but is based on the input and output variables. The proposed model could forecast the hysteric responses of MRE base isolator under various loading conditions, while it was faster than other MRE device models like the Bouc-Wen and strain stiffening model.

Zhu et al (Zhu J T 2012) proposed a viscoelastic model that combined a spring and a fractional dashpot element to represent the frequency response of the matrix parallel to a nonlinear spring

and dashpot to represent the magnetic field induced effect. The model could predict the general trends of the moduli of elasticity in a restricted frequency range (up to 10Hz) and magnetic field but does not deal with the amplitude nonlinearity or the coupling effects between amplitude, frequency and magnetic field. Agirre-Olabide et al, (Agirre-Olabide I 2017) developed a four-parameter fractional derivative viscoelastic model to describe the dynamic shear behaviour of isotropic magnetorheological elastomers (MREs) as a function of the matrix, particle content and magnetic field. However, they too did not consider the magnetic field-amplitude coupling effects.

Constitutive equation models

Hyperelastic constitutive models are basically mathematical equations of a strain energy density function W. The strain energy W is expressed as a function of strain invariants (I_1, I_2, I_3) or principal stretch ratios ($\lambda_1, \lambda_2, \lambda_3$). These models are widely used in commercial finite element analysis (FEA) software application (like ANSYS and ABAQUS) which also provide the option of user defined strain energy equations that are scalar functions of one of the strain or deformation tensors. Hyperelastic models can predict the strain dependence of elastomers for most cases in the quasi-static case but the situation is more complicated when it comes to the response under dynamic loads. Ansys FEA software has a curve fitting option that can find the parameters of the equations when experimental data from pure shear and equibiaxial extension/compression tests or creep/relaxation tests for the dynamic case are provided. However, passing from the time domain to the frequency response and vice versa means a loss of accuracy. Moreover, these data are not easily available due to the complexity of the tests and in most cases approximate values are used.

A key point in modelling MR elastomers is defining the filler particle distribution pattern and thus understanding of how the magnetic flux density distributes itself inside the material. In a simplified approach, only the effect of magnetic field is considered and a constitutive equation model that can predict only the MR effect is of interest. These models are based on dipole magnetic particle interactions and require the particle distribution to be known. One of the most popular models concerning the prediction of the stress induced by the magnetic field was presented by Jolly et al (Jolly M R 1996). The proposed quasi-static model was based on the assumption that the particle sizes are uniform, homogenous spheres that could be magnetically modelled as identical induced dipole moments and that the particles are aligned in perfect chains. The model did not take under consideration of the particle size but the distance between each other. Some years later, Davis (D. L. C 1999) used the Ogden Hyper elastic model of elastomers and the magnetic dipole moment of each particle to model the material in FEA software by fitting the parameters to experimental data. The same assumptions were made again were the particles were considered as perfect spheres

spaced at equal distances between each other. The main disadvantage of the above-mentioned models is that they assume the particles to be perfect spheres aligned in perfect chains inside the matrix. However, this is not the case for most MREs.

Zhang et al (G. X. Zhang W 2010), proposed a Gaussian distribution model where the filler particles form body centred tetragonal BCT structures in the matrix of the same direction and width but different length that obeys the Gaussian distribution law. The simulated results were compared with shear static loading while the dynamic loading conditions were not examined. The same authors improved the previous model to account for the temperature influence on the magnetorheological effect but they were unable to produce a model that could describe the effect of temperature to the dynamic properties of the MR elastomers under study. Castaneda and Calipeau (E 2011) proposed a homogenization-based constitutive model for MRE with elliptical particles, under the assumption that the material behaves linear for small strains, capable of predicting the nonlinear ferromagnetic particle response of the MR elastomers. The same researches expanded their theory to account for the torques generated by nonaligned loadings in MREs composed of aligned fibres with elliptical cross section instead of spherical particles (P 2012). However, the above work was purely theoretical and no validation with experimental data was conducted.

Danas et al (Danas K 2012) suggested an anisotropic energy density function containing seven invariants, two purely mechanical and five magneto-mechanical that are adding up based on the experimental results that showed that stress does not affect the magnetization response. The energy function depends nonlinearly on the two mechanical invariants to explain the nonlinear tension-compression asymmetry. The model parameters where extracted from the experimentally measured magnetization slopes and magnetostriction curvatures in uniaxial static compression-tension and simple shear tests. The model could theoretically be implemented in FEA modelling software but there is still the issue of validating the model under dynamic loads and examine the magnetic field-dynamic mechanical response coupling effects.

2.7 Vibration absorbers and isolators with MRE

MRE absorbers

MR elastomers, find broad applications on vibration absorbers and isolators mostly as frequency shifting semi active devices. Deng and Gong, developed an adaptive tuned vibration absorber in shear mode and tested the device using silicone rubber MRE (Deng H X 2008) and natural rubber MRE (Deng H X, Adaptive Tuned Vibration Absorber based on Magnetorheological Elastomer 2007). The results showed a resonance frequency shift from 27.5 Hz to 40Hz for silicon rubber and from 40 Hz to 60Hz for the natural rubber MRE. Xu et al (Xu Z 2010), used the same shear mode absorber device to develop an active damping compensated absorber that behaved like a conventional ATVA with smaller damping. In their results the average damping ratio reduced from 0.16 to 0.06 by the active force. Hoang et all, (Hoang N 2011) proposed a shear mode MRE active tuned vibrations absorber for powertrain vibration suppression. The proposed device could shift the frequency to deal with the resonant phenomena during starting up and accelerating of a vehicle. Kim et all (Kim Y K 2011), developed a shear mode active tuned vibrations absorber based on MRE for a cryogenic cooler compressor used in space applications, capable of tuning the notch frequencies from 32 to 60 Hz in maximum magnetic flux density of 240 mT.

In a theoretical study, Collette et all (Collette C 2010), showed that a MRE vibration absorber can reduce the stress in a n-story mass varying structure 50% better than a classical absorber. In order to increase the maximum load capacity of the device Sun et al, (D. H. Sun S 2015) developed a laminated absorber composed of 16 layers of MRE and 16 layers of steel that was used to suppress lateral vibration. The laminated structure was bonded to two permanent magnets before placed into the magnetic circuit, which provided a stable magnetic field which further increased of decreases according to the direction of the electric current fed in the electromagnet. As a consequence, the MRE absorber could shift its natural frequency down to 3.2Hz and deal with vibrations of much larger amplitude.

Adaptive vibration absorbers working in shear mode have well been studied, but the situation is not the same for their compression mode equivalent. Lerner and Cunefare (Lerner A A 2008), studied the frequency shift capability of an anisotropic MRE absorber working in shear and compression mode. They concluded that the absorber in compression mode had a larger zero field natural frequency but a much higher tuneable frequency ranges due to a higher MR effect, than the shear mode absorber. The same conclusion was validated by Sun et al (D. H. Sun S 2015) where the compression mode absorber could shift its natural frequency two times more that the shear mode device. The same group also examined the application of a compression working model

absorber on beam vibration absorption (Sun S S 2014). The tests showed that the device could shift its natural frequency from 37Hz to 67Hz.

MRE isolators

One of the first practical MRE isolators was a suspension bushing developed by Ginder at Ford Technologies (Steward, Ginder et al. 1998). Opie and Yim (Opie S 2011), tested a shear mode MRE isolator and the possible semi active or active control methods. The experimental results showed that the on-off controlled device can offer improved resonance control and velocity isolation when compared to the considered passive systems. Alberdi-Muniain et al (Alberdi-Muniain A 2012), examined the isolation efficiency of a shear mode natural rubber MRE isolator-mass system using energy flow as an indication. Their experiments showed that the energy flow into the foundation was reduced by 50% at the zero field resonance frequency by adaptively controlling the magnetic field.

Gu et al (Gu X 2015), developed an adaptive laminated base isolator system, suitable for seismic isolation, capable of increasing its stiffness and damping by six times. Eem at al (Eem S H 2011), examined the seismic performance of a smart MRE base isolation system that could reduce the structural responses by 60% compared to a passive isolation system. Yang et al (S. S. Yang J 2014), used a 16 layers MRE-steel thin plate device like the one examined before in a mass-absorber system. The laminated structure was bonded to two permanent magnets, before placed into the magnetic circuit that provided a stable magnetic field which further increased of decreases according to the direction of the electric current fed in the electromagnet. The mass-MRE isolator system could increase stiffness and damping by 180% under shear loading conditions.

MRE devices working in both compression-shear mode

Very few researchers have examined designs where the MRE isolator works in both shear and compression loading modes. Yang et al (Yang CY 2015) examined an isolator with a closed magnetic circuit where two MREs were embedded in the device, one operating in shear mode and the second in compression. They claimed that this mixed mode type of design increases its stiffness 18 times and damping 8 times more than a similar isolator working only in shear mode, while the device could shift its natural frequency by 100%. In another approach, Du et al (Du H 2011), studied a vehicle seat suspension that followed the design principle of an inclined isolator, although the inclination angle was small. When the magnetic field was applied, the dynamic stiffness of the isolator increased by three times while damping by two.

2.8 Challenges and opportunities

The static and dynamic properties of MREs have been extensively studied in the past, but the wide variation of sample size, materials used, manufacturing method and experimental methods often result to contradicting outcomes especially regarding particle size. Therefore, the effect of particle size on dynamic properties and MR effect and the use of particles larger than 60μm, which are much cheaper, should also be considered. In addition, the following topics have not yet been addressed and offer opportunities for further research:

- Variation of dynamic mechanical properties in respect to MRE size and shape (scaling effect) since the studies published in the literature deal with static mechanical properties.
- Some researchers used MRE-metal laminated structures (Li Y 2013) to increase the static stiffness of MRE isolators while Allajyarov et al (Allahyarov E 2015) considered the theoretical magnetomechanical coupling of two magnetic elastomers into a bilayered composite material. However, none examined the possibility of combining isotropic and anisotropic MREs in one elastomer to adjust the mechanical properties.
- Several isolators have been presented in the literature that work in either shear or compression mode but very few working in mixed shear/compression modes. More research is therefore needed in such devices, like an inclined isolator.
- Many researchers have produced linear and nonlinear models of MREs that can predict the material properties under varying strain amplitude while displacement transmissibility is examined. However, in many practical applications force transmissibility is of interest and a force depended model would be useful.

2.9 Thesis organization

The thesis is organized in eight chapters three of which (chapter 4, 5 and 6) present the experimental results while chapter 7 the theoretical work. In more details:

Chapter 1: The aim of this chapter is to explain why the author spend six years of her life doing this work.

Chapter 2: This chapter presents the main characteristics of magnetorheological elastomers and their working principle. In addition, the current state of research regarding materials and manufacturing methods, viscoelastic and constitutive equation models and practical applications (vibration absorbers and isolators) with MREs is presented. Finally, the areas not yet studied are identified and discussed under the challenges and opportunities section.

Chapter 3: The first section of this chapter presents the methodology approach of this work and the reasons why this approach was followed. The rest of the chapter explains in detail the manufacturing method of MRE samples, the general experimental system setup, how the magnetic field produced and the method the experimental data were analysed. In addition, the advantages and limits of the experimental system are presented. In this chapter only the general experimental system is presented while additional information on MRE samples and test sequence are given in each chapter.

Results of experimental tests

Chapter 4: This chapter presents the experimental results of the dynamic compression tests performed in isotropic and anisotropic MREs with large (diameter <220 μm) and small (diameter=4-6 μm) particles under varying load amplitude, frequency, static prestrain and magnetic field. The coupling effects between load amplitude, frequency, static prestrain and magnetic field are examined in detail for all samples. In addition, the influence of size and shape of MRE sample on zero field dynamic mechanical properties and magnetorheological effect is examined for isotropic MRE with small particles.

Chapter 5: This chapter is broken in two parts. The first examines the principle of combining isotropic and anisotropic MR elastomers with small and large particles in one composite, to adjust the zero-field dynamic properties of silicon MREs without compromising MR effect. The second examines the dynamic mechanical properties of isotropic/anisotropic and anisotropic/anisotropic (with particles aligned in different directions) composite MREs in three directions.

Chapter 6: In this chapter, the composite isotropic/anisotropic and anisotropic/anisotropic MREs are tested in practice by examining the mechanical properties of a MRE prototype isolator working in pure compression and compression/shear (inclined) mode. The experimental data are then used to determine the principal elastic axis stiffness ratio $\frac{k_p}{k_q}$ and how this is influenced by the magnetic field.

Theoretical part

Chapter 7: In this chapter, the experimental results presented in the previous chapters are used to make a parametric phenomenological viscoelastic model of MREs. The model is then used to simulate the force transmissibility of a single degree of freedom mass MRE isolator system under different harmonic loading conditions.

Chapter 8: The general conclusions and the major breakthroughs of this work are presented.

Chapter 3: Methodology and experimental system setup

3.1 Methodology approach

The project was broken down to an experimental and a theoretical part. The experimental part involved the mechanical characterization of pure and composite MREs under dynamic pure compression and compression/shear loading conditions. The results of these tests were then used to make a nonlinear model of MREs and finally simulate a single degree of freedom mass-MRE isolator system.

Experimental part

The experimental part itself involved three steps. The first step was to determine how loading conditions, magnetic field, iron particle size and size/shape of samples influence stiffness and damping capability of pure isotropic and anisotropic MREs. Thus, dynamic compression tests of varying load amplitude, frequency and static prestrain were performed in isotropic and anisotropic MREs with large (diameter <220 μm) and small (diameter=4-6 μm) particles. The effect of size and shape on zero field dynamic mechanical properties was examined only for isotropic MREs with small particles because it was impossible to ensure that anisotropic MREs with different heights would be cured under the same magnetic field.

The second step was to examine the possibility of combining isotropic and anisotropic MREs in one composite elastomer to adjust the zero field mechanical properties without compromising MR effect. To improve the isolation characteristics of high tangent of the loss angle rubbers at high frequencies, a second rubber with lower damping factor and stiffness can be placed in parallel. The dynamic modulus of the combined isolator can be tailored by selecting the dimensions of each rubber. Since the combined elastomer will have lower stiffness but similar damping capability than the high damping rubber itself, the transmissibility of the combined isolator will increase slower with frequency than the transmissibility of the high tangent of the loss angle rubber alone before the natural frequency and decrease faster than the high tangent of the loss angle rubber at frequencies higher than the natural frequency (S. J. C 1968).

Under the same logic, the isolation efficiency of anisotropic MREs at high frequencies can be improved by placing an isotropic MRE in parallel. The new composite elastomer should have a lower dynamic stiffness than anisotropic MRE and higher tangent of the loss angle than isotropic MRE without a great compromise of the MR effect. However, the mechanical properties of anisotropic MREs depend on the alignment of particle chains and therefore, have different axial (y axis), transverse (x axis) and longitudinal (z axis) stiffness. For this reason, the possibility of combining

two types of anisotropic MREs with different particle directions is also examined to create a composite elastomer that will have a similar axial, transverse or longitudinal dynamic stiffness.

The third step was to test the behaviour of the pure isotropic, pure anisotropic and composite isotropic/anisotropic and anisotropic/anisotropic MREs in a real application scenario by examining the mechanical properties of a small MRE prototype isolator working in pure compression and compression/shear (inclined by 45^0 degrees) mode. The experimental data are then used to determine the principal elastic axis stiffness ratio $\frac{k_p}{k_q}$ and how this is influenced by the magnetic field.

Theoretical part

The aim of the theoretical part of this project was to simulate a MRE isolator under loading conditions that can be found on the engine room of a ship and examine its isolation efficiency. For this reason, the case of a single degree of mass-isolator system excited by an harmonic disturbing force resulting from rotating unbalance is considered. The purpose of the isolator is to decrease the vibrations generated by the unbalanced mass to the hull of the ship, therefore the force transmissibility is of interest and a nonlinear model that depends on force rather than displacement is preferred.

The phenomenological parametric viscoelastic modelling approach is selected because accurate constitutive equations models require tests (to extract the parameters) that could not be performed in our laboratory like equibiaxial loading test. Since the magnetorheological effect of MRE devices is usually higher than the one reported under material characterization, the parameters of the viscoelastic model of the MRE material are extracted from both the material and isolator device characterization steps to get more realistic results. The force transmissibility of a general single degree of freedom mass-isolator is then simulated under varying magnetic fields. Finally, the possible control strategies are briefly discussed, and the isolation efficiency of a semi active system is examined.

3.2 Manufacturing process of MRE samples

Selection of rubber matrix material

For this work, a two-component room-temperature vulcanization silicon rubber was selected mostly because it is easy to get and make. The typical rubbers used in large scale isolators like natural rubber or Neoprene have much better mechanical properties but require special mixers and controlled pressure and temperature curing devices that were too expensive for the budget of this project. Therefore, the (RTV) 4644 Elastosil mould making silicon rubber from Wacker Silicones was chosen due to its viscosity that could allow the particles to be mixed inside.

Selection of filler particles

For the filler particles, we selected two types of iron particles, one with an average diameter lower than 220 μm (Sigma-Aldrich) and the other with average diameter of 6 μm (Sigma-Aldrich), from now on referred as large and small particles respectively. Although most researches prefer particles of smaller diameter to avoid agglomeration, we examined the use of particles with much larger diameter mostly because they are much cheaper and therefore a more attractive solution for commercial applications. The 70% to 30% per volume matrix-particle ratio was used for all samples, since it is proven to give the highest magnetorheological effect (Li W H 2010) (Kallio M 2007) for this type of MREs.

Manufacturing process-isotropic MREs

The samples were composed of 30% per volume iron particles and 70% per volume two component silicon rubber (4644 Elastosil). The silicon rubber components were first mixed together on a 10:1 component A to component B ratio and then the iron particles were added. Two types of iron particles were used, one with an average diameter lower than 220 μm (large particles) and the other with average diameter of 6 μm (small particles). The mixture was placed in a vacuum chamber for about 10 min to remove the air bubbles trapped inside the material during mixing and was finally placed in aluminium moulds and left to cure for 24 hours at room temperature. The manufacturing procedure is illustrated in Figure 3. All isotropic samples manufactured are presented in Table 2 and Table 3.

MR elastomers, like all elastomers, show a relative high variability of their mechanical properties even on items of the same batch. Thus, the directions of the ISO 7743:2011 standard were followed and three different samples of each MRE type were tested while the values reported on chapters 4, 5 and 6 are the average of these values. The three different samples were manufactured from three different batches made on different days.

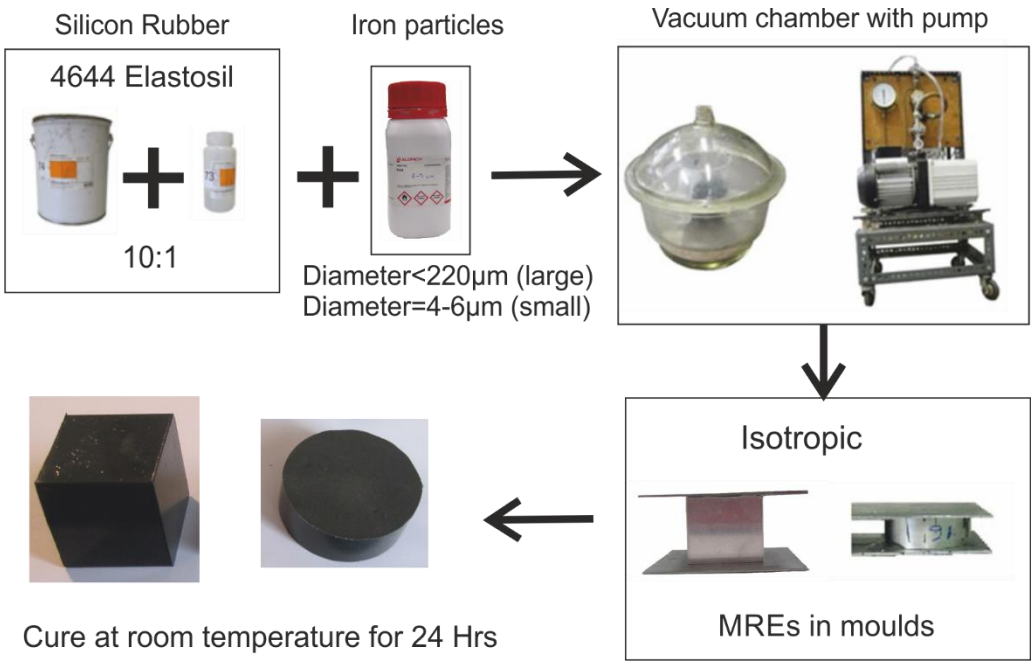

Figure 3: Isotropic MRE manufacture diagram

Table 2: Summary of isotropic MRE samples

Particles	Name	Dimensions	Number of samples	Sample was used for
Large	Isotropic a-l	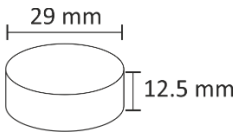	5*	Examine the effect of iron particle size Examine the properties of isotropic/anisotropic combined samples
Small	Isotropic a-s		5*	
Small	Isotropic b	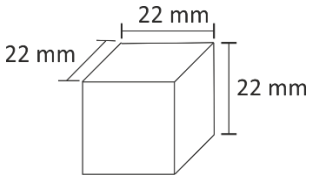	3	Examine properties in axial, transverse and longitudinal direction
Small	Isotropic c	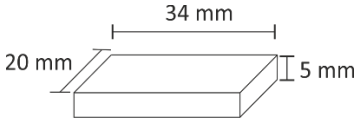	3	MRE isolator

* Five samples from different batches were manufactured and the average values of three set of samples are reported disregarding the samples with the highest and lowest MR effect.

Table 3: Summary of isotropic MRE samples used to examine the effect of size and shape on dynamic properties

Particles	**Name**	**Dimensions**			**Number of samples**	
	Disk	*d (mm)*		*h (mm)*		
Small	a_1	28.5		6.25	3	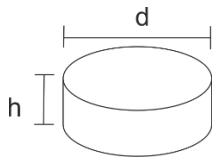
Small	a_2	28.5		12.5	3	
Small	a_3	28.5		21	3	
Small	a_4	56.5		12.5	3	
Small	a_5	15.5		10.5	3	
Small	a_6	41.5		14.5	3	
	rectangular	*h1 (mm)*	*h2 (mm)*	*h (mm)*		
Small	c_1	20	34	5.25	3	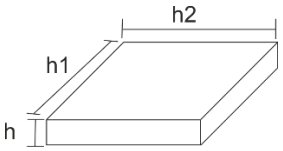
Small	c_2	30	60.5	6.25	3	
Small	c_3	41	59.5	10.5	3	
	Square	*h1 (mm)*	*h1 (mm)*	*h (mm)*		
Small	b_1	22	22	6.25	3	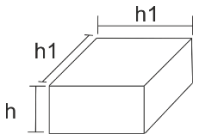
Small	b_2	22	22	10.5	3	
Small	b_3	22	22	22	3	
Small	b_4	34	34	5.5	3	
	Ring	*Din (mm)*	*Dout(mm)*	*h (mm)*		
Small	r_1	19.5	32.5	10.5	3	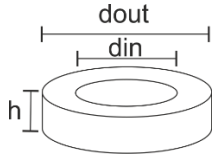
Small	r_2	54.5	23.5	16.5	3	

Important note:

A set of all isotropic samples mentioned in Table 3 were manufactured simultaneously from the same batch. In total, three different sets of samples were manufactured from three different batches on different days. The values reported are the average of these.

Manufacturing process-anisotropic MREs

For the anisotropic material, the moulds were placed between two strong cylindrical grade N42 neodymium permanent magnets of diameter 40mm and thickness 5mm that produced a stable magnetic field. Two magnets were stacked together to increase the magnetic field thus, the final length of each magnet pole is 10mm.

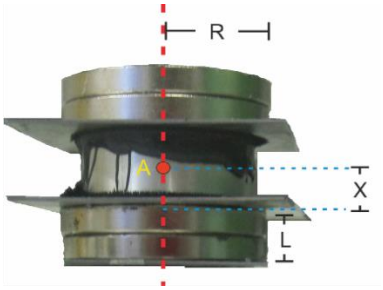

$$B_x = B_r\left(\frac{L+X}{\sqrt{R^2+(L+X)^2}} - \frac{X}{\sqrt{R^2+X^2}}\right) \qquad (3.2.1)$$

Figure 4: Magnetic field while curing

Table 4 provides the calculated and measured values of the magnetic flux density B_A at point A in the middle of the distance between permanent magnets (X=6.25 mm and X=11 mm for disk and square samples respectively), as illustrated in Figure 4. These values where calculated using formulae (3.2.1) that gives the magnetic flux at a distance X of a disk magnet where, L=length of the magnet, X= distance from the surface of the magnet, R=radius of the disk magnet (20mm), B_r= material constant ($B_r = 12800$ for the N42 grade neodymium magnets). The total magnetic flux B_A will be double the calculated value. Flux density was measured by placing a magnetic probe in the middle of the 12.5mm and 22mm gap using aluminium blocks on the sides to hold the permanent magnets apart. These values are measured and calculated assuming air as the intermediate medium between magnets. All anisotropic samples manufactured are presented in

Table 5. Three set of samples of all sizes and shapes were manufactured from three different batches. The experimental values presented in later chapters are the average values of these for each sample.

Table 4: Values of magnetic flux produced from permanent magnets during curing process.

	Gap height			
	12.5 mm		**22 mm**	
	Calculated	*Measured*	*Calculated*	*Measured*
$\boldsymbol{B_A}$	0.43 T	0.48 T	0.31 T	0.33T

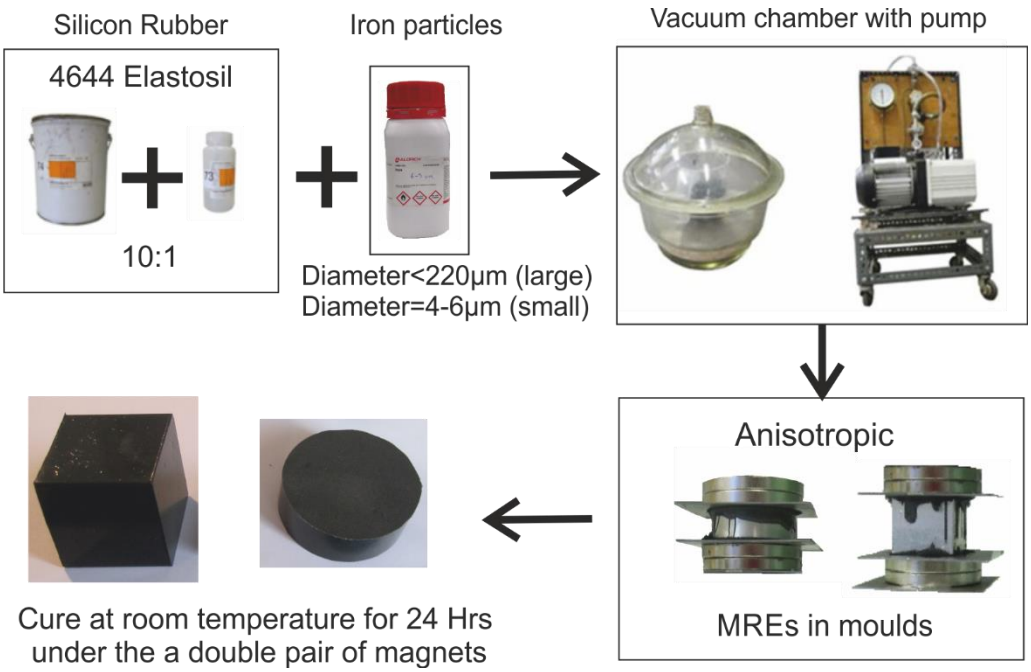

Figure 5: Manufacturing process of anisotropic MREs

Table 5: Summary of anisotropic MRE samples

Particles	Name	Dimensions	Number of samples	Sample was used for
Large	Anisotropic a-l	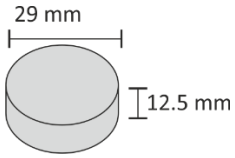	5*	Examine the effect of particle size Examine the properties of isotropic/anisotropic combined samples
Small	Anisotropic a-s		5*	
Small	Anisotropic b	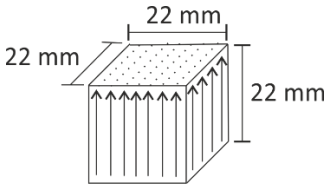	3	Examine the properties in axial, transverse and longitudinal direction
Small	Anisotropic c	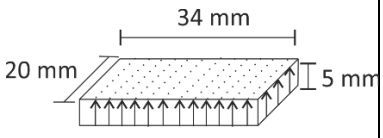	3	MRE isolator

* Five samples were manufactured and the average values of three set of samples are reported disregarding the samples with the highest and lowest MR effect.

Manufacturing process-isotropic/anisotropic series combination MREs

The manufacturing process of the isotropic/anisotropic series combination composite MR elastomers involves two stages. Sample 2a was manufactured by cutting a pure anisotropic a sample in the middle, place one half in the bottom of another aluminium mould and pure the isotropic MRE on top of it. All anisotropic parts of these disk samples are of the same height and thus, they were all cured under 0.5T magnetic flux density. The magnetic flux was produced using a set of cylindrical grades N42 neodymium permanent magnets of diameter 40mm and thickness 10mm. For sample 2c, the isotropic half was first made and after it had cured it was placed back to the mould and the anisotropic part was poured on top. The sample was then left to cure under a double set of magnets.

Table 6: Summary of isotropic/anisotropic series combination MRE samples

Particles	**Name**	**Dimensions**	**Number of samples**	**Sample was used for**
Small	Sample 2a	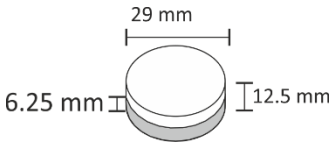	3	Examine the properties of isotropic/anisotropic combined samples
Small	Sample 2b	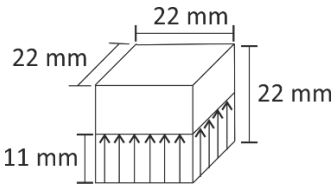	3	Examine the properties in axial, transverse and longitudinal direction
Small	Sample 2c	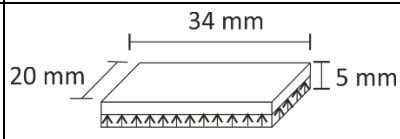	3	MRE isolator

Manufacturing process-isotropic/anisotropic parallel combination MREs

The manufacturing process of the composite MR elastomers involves two stages. For sample 1a, anisotropic discs were first made in the appropriate aluminium moulds and were left to cure under a double pair of permanent magnets for 24 Hours. After they had cured they were placed inside another aluminium mould and the isotropic MRE was poured to fill the gaps and left to cure again at room temperature, to achieve perfect adhesion. For sample 1c, a cured anisotropic c sample was cut in 4 pieces of 8.5 mm x20mm each. Two of these parts when then placed back to the aluminium mould and the isotropic MRE was poured to fill the gaps.

Table 7: Summary of isotropic/anisotropic parallel combination MRE samples

Particles	Name	Dimensions	Number of samples	Sample was used for
large	Sample 1a-1	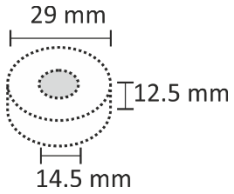	3	Examine the properties of isotropic/anisotropic combined samples of different particle sizes
Large small	Sample 1a-2	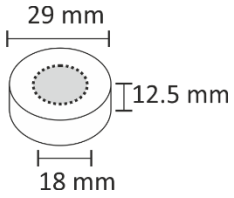	3	
large	Sample 1a-3	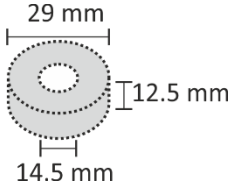	3	
small	Sample 1a-4	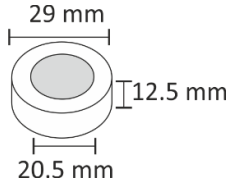	3	
Small	Sample 1b	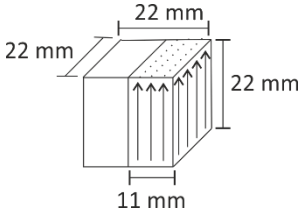	3	Examine the properties in axial, transverse and longitudinal direction
Small	Sample 1c	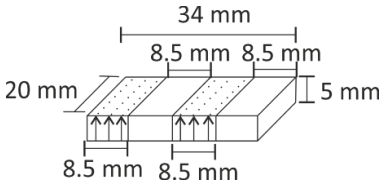	3	MRE isolator

Manufacturing process- anisotropic/anisotropic parallel combination MREs

Anisotropic/anisotropic parallel combination samples were manufactured in two steps. Samples 3b and 4 were manufactured by again cutting an anisotropic b sample in the middle, place one half in one side of the mould, pure MRE to fill the gap of the other side and then place the mould between the permanent magnets to cure the other anisotropic part. In this way, all anisotropic parts were

cured under the same magnetic flux of 0.35T. For sample 3c, a cured anisotropic c sample was cut in 4 pieces of 5mm x 34mm each. Two of these pieces were then rotated by 90^0 (so that the particles were aligned in the longitudinal direction) and placed back to the mould. New anisotropic MRE was poured to fill in the gaps and the mould was left to cure again under a double set of permanent magnets. Three set of samples of all sizes and shapes were manufactured from three different batches. The experimental values presented in later chapters are the average values of these for each sample.

Table 8: Summary of anisotropic/anisotropic parallel combination MRE samples

Particles	**Name**	**Dimensions**	**Number of samples**	**Sample was used for**
Small	Sample 3b	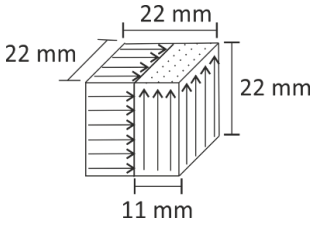	3	Examine the properties in axial, transverse and longitudinal direction
Small	Sample 4	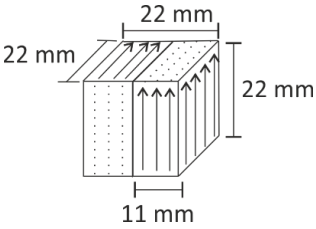	3	
Small	Sample 3c	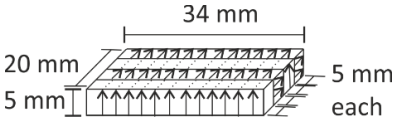	3	MRE isolator

Important note

A set of square anisotropic b, isotropic c, samples 1b, 2b, 3b and 4 were manufactured together from the same MRE batches. The vertically aligned (as shown in the figure) anisotropic part of sample 3b and sample 4 came from the same anisotropic b sample cut in the middle while the anisotropic parts of sample 1b and 2b were also from the same batch. The other isotropic and anisotropic parts in the second manufacturing stage also came from the same batch of MRE. The same procedure was also followed for samples 1c, 2c, 3c and disk samples 1a-1, 1a-2, 1a-3 and 1a-4. In total three different sets of samples were manufactured and the values reported in later chapters are the average of these.

3.3 Test system for material characterisation

General test setup with INSTRON PULS E1000

The static and dynamic compression tests were performed according to BS ISO 7743-1:2011 standard (Rubber, vulcanized of thermoplastic-Determination of compression stress-strain properties) and BS ISO 4664-1:2011 standard (Rubber, vulcanized of thermoplastic-Determination of dynamic properties) respectively, using INSTRON PULS E1000 electromechanical dynamic tester and custom made aluminium compression plates. The compression plates were thick enough (15mm height) to have a much higher stiffness than the MRE samples under test and isolate the load cell of the magnetic field generated by the permanent magnets. They were fixed to the bottom frame and load cell using aluminium screws.

The samples where first preloaded under static load for four cycles in order to avoid the Mullins effect and then the strain amplitude (0.25% to 2%) and load frequency (0.5Hz to 70Hz) dynamic loading cycles where performed under a static prestrain. Figure 6 presents the test setup used for the compression tests. The machine had to be tuned each time that the stiffness changed, which was for every time the amplitude, magnetic field and prestrain values changed. However, it was found in practice that increasing the strain amplitude (at the range of interest) did not change the tuned string stiffness value significantly, so tuning was performed only at the amplitude of 0.5% strain at each value of magnetic field.

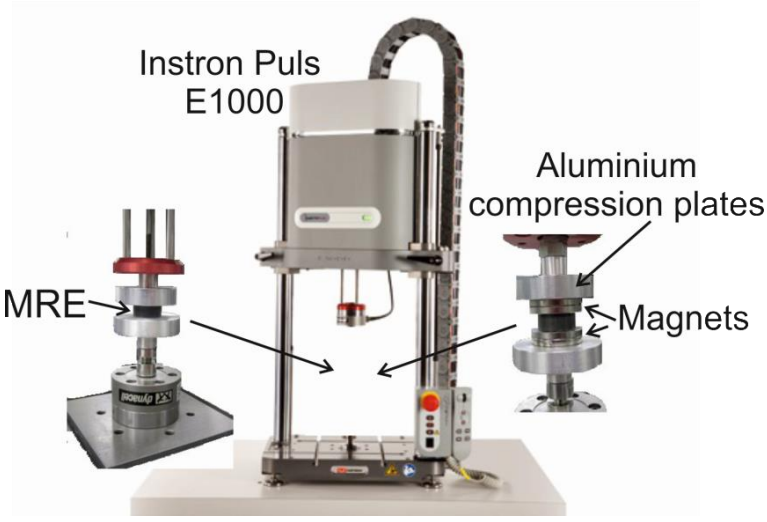

Figure 6: Test setup for pure compression tests

Generation of magnetic field while testing

The magnetic field during testing was produced using the same set of disk grade N42 neodymium permanent magnets of diameter 40mm and thickness 5mm, in a pair of single (L=5mm) and double (L=10mm) disk magnets configuration where two magnets are stacked together (Figure 7). The

magnetic flux B_x between the magnets in respect to distance h is shown in Figure 8. The flux values were calculated using equation (3.1.1) assuming air at the intermediate gap and X=h/2, $B_r = 12800$, R=20mm and L=5mm for single pair while L=10mm for double pair. Thus, the magnetic flux values reduces significantly with increasing height of the MRE sample

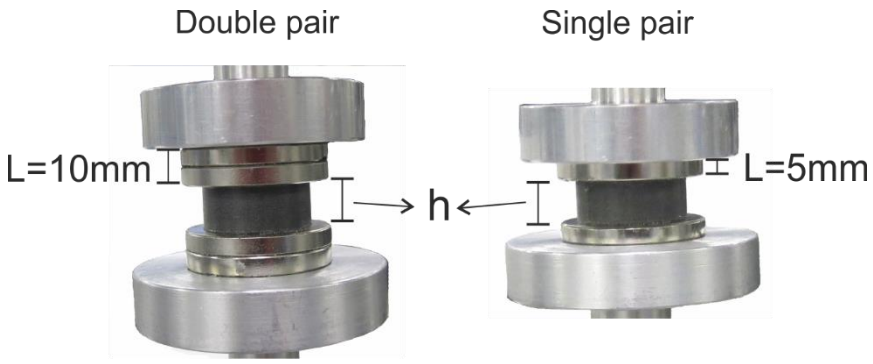

Figure 7: Configuration of magnets while testing.

The magnetic flux values at the middle of the 12.5mm (for disk samples) and 22mm (for cube samples) air gap are presented in Table 11. However, MREs have a higher relative permeability μ_r than air of μ_r=3.7 for isotropic and μ_r=4.45 for anisotropic MREs with particles aligned parallel to the direction of the magnetic field (Harrison, Equi-biaxial tension tests on magnetorheological elastomers 2016). Therefore, the actual magnetic field inside the MREs should be higher than the one calculated assuming air as medium and will have slightly higher values for anisotropic MREs. For simplicity reasons and since the aim of this work is to compare the performance of different types of MREs, one value of magnetic field is chosen for all MRE samples that is approximated to be slightly higher than the measured value.

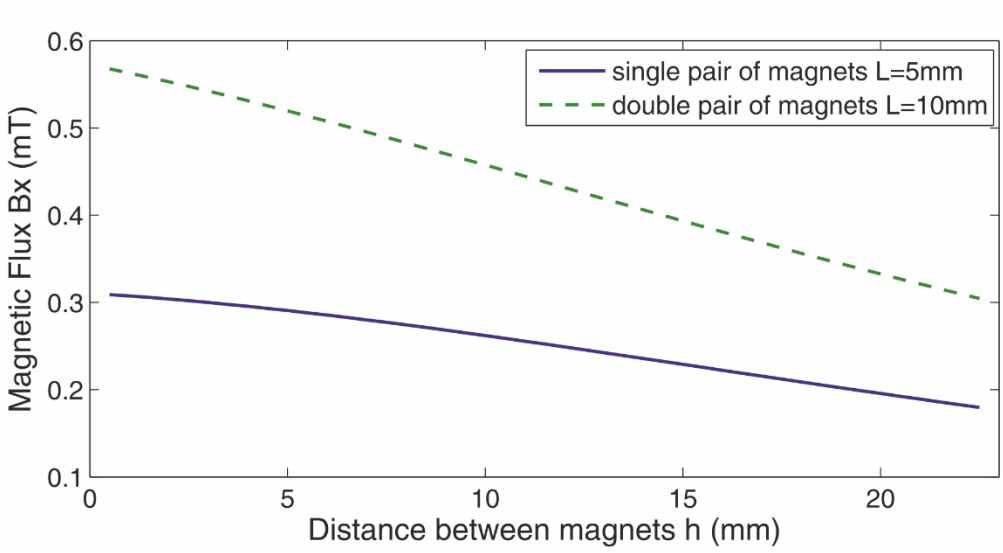

Figure 8: Magnetic flux between permanent magnets in respect the distance between them.

In this testing configuration, the magnets come in direct contact with the MRE under test in contrast to the curing process where the magnets were held apart from the aluminium mould. The attraction

force between the permanent magnets themselves causes an original prestress to the MRE under test and a resulting axial compressive extension that limits the axial positive elongation caused by the magnetic field due to the rearrangement of iron particles. The attraction force between two identical disk shaped permanent magnets at a distance x between each other can be estimated using equation (3.3.1) (Vokoun D 2009, Jolly M R 1996), where R=radius and L=height of disk magnets, μ_0=permeability of vacuum ($4\pi\ 10^{-7}$) and M= saturation magnetization and are presented in Table 11. Saturation magnetization M is related to the maximum value of magnetic flux at the surface of each magnet B_0 by equation (3.3.2) where B_0 can be estimated by substituting X=0 to equation (3.3.1).

$$F = -\frac{1}{4}\pi\mu_0 M^2 R^4 \left(\frac{1}{x^2} + \frac{1}{(x+2L)^2} - \frac{2}{(x+L)^2}\right) \quad (3.3.1)$$

$$B_0 = M\,\mu_0 \quad (3.3.2)$$

The attraction forces between the two magnets when the gap is 22mm (cube samples) are not strong enough to create a significant precompression to the MREs under test. The situation is different for disk samples with 12.5mm height (gap) when a pair of double disk magnets are used. The result is a 30N static load applied to all MREs under test causing a static deformation according to each sample's stiffness by also influencing its dynamic stiffness. Since this static force will be the same for all samples and there is not much that can be done about it, it was considered as a characteristic of the measurement setup system.

Table 9: Magnetic flux and attraction forces produced by permanent magnets while testing.

Gap height	**12.5 mm**		**22 mm**			
	Magnetic Flux B_A	*Attraction Force F*	*Magnetic Flux B_A*	*Attraction Force F*	B_0	
Pair of single disk magnets (L=5mm)	0.246 T	4.72 N	T	0.76 N	0.1552 T	*Calculated*
	0.28 T	-	0.19 T	-	*0.16 T*	*Measured*
	0.3 T	5 N	**0.2 T**	1 N	-	*Approximated*
Pair of double disk magnets (L=10mm)	0.426 T	28.56 N	T	5.71 N	0.2862 T	*Calculated*
	0.48 T	-	0.33 T	-	*0.29 T*	*Measured*
	0.5 T	30 N	**0.35 T**	6 N	-	*Approximated*

Lubrication of compression plates

According to BS ISO 7743-1:2011 standard (Rubber, vulcanized of thermoplastic-Determination of compression stress-strain properties) and BS ISO 4664-1:2011 standard (Rubber, vulcanized of thermoplastic-Determination of dynamic properties), the compression plates should be lubricated during testing to allow perfect slip and ensure uniform distribution of shear strain. In the case of MREs, this can be achievable only for the zero field tests. When the magnetic field is applied the MRE sample is stuck to the magnets similar to the bonded test condition where non-uniform distribution of shear strain arises from the constraints at the end surfaces, while the compression behaviour becomes dependent on the shape and hardness of the MRE. In order to be precise a shape factor correction equation for compression modulus should be used. However, this has not been dealt with or reported in any other previous published work on compression tests on MREs and the parameters of the shape factor equation are unknown. For this reason, no lubrication was used for all tests since the aim of this work is to compare the different types of MREs and study the influence of loading conditions and magnetic field on the dynamic mechanical properties. In addition, a phenomenological viscoelastic model is used to predict the behaviour of the material for practical applications where pure compression or pure shear are not of interest unlike hyper elastic constitutive equation models.

Dealing with inertia forces

One of the challenges to overcome regarding the measuring setup system was dealing with the inertia forces imposed by the measuring system especially in frequencies above 30 Hz. In the standard INSTRON machine setup the load cell is placed directly on the moving actuator of the machine, and since it has a mass it introduces inertia moments that result to harmonics in the recorded signal as the frequency and amplitude increases. To solve this problem, I used compression plates made from aluminium that are much lighter and in addition do not let the magnetic field pass to the load cell and affect its readings. The thickness of the plates is 15mm to ensure that the stiffness of the plates is much higher than the stiffness of the elastomer under test.

Figure 9 shows the load-displacement curves of the actuator mounted with the load cell moving on its own at displacement amplitude of 0.06mm. At 10 Hz, the load cell does not record any signal and the curve is flat corresponding only to the movement of the actuator that records the displacement. With increasing frequency, the recorded signal of the load cell increases resulting to the observed hysteresis curve. This feature must be taken under consideration when analysing the

data because it can lead to the wrong estimation of damping of the material under testing. After discussing with other more experienced users of the INSTRON machines it was suggested to place the load cell on the bottom frame of the machine and perform the test again to check the differences. It becomes obvious that inertia does not influence the signals when the load cell is positioned on the base of the machine and therefore, this configuration was selected for frequencies above 10 Hz.

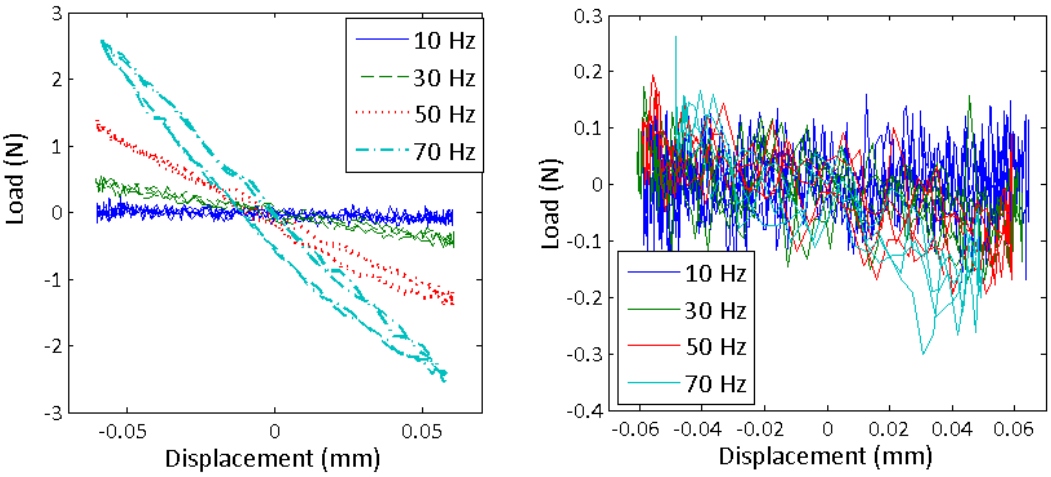

Figure 9: Load-displacement curves of the actuator and the load cell alone at different frequencies for the same displacement amplitude of 0.06 mm with the load cell positioned on top (left) and with the load cell positioned on the bottom (right).

3.4 Test system for compression and inclined isolator

Magnetic circuit

To examine the behaviour of the material under combined shear and compression loading conditions, a small-scale test device was manufactured using an old EI shaped laminated core transformer. The original E shaped core consisted of 100 laminations of 0.4mm thickness each giving a total 40mm thickness of the complete assembly. After being stripped out of its coil and coil former the old core was modified to create a C shaped electromagnet core by hand cutting the middle left of each lamination separately as shown in Figure 11. The top I shaped part of the transformer had then to be hand cut to create the desired 45 degrees of inclination angle. Then two new coils were hand wounded around new coil formers and placed in each leg of the new core. The two separate top parts were fixed to the main C core using the existing holes of the old core and a thin aluminium sheet of 0.5mm thickness. For the middle top part, a new hole had to be punched for each lamination separately.

Each of the two coils had 500 turns of enamelled 0.71mm diameter copper wire (SWG22). Both coils were connected to a power source providing a stable electric current up to 3Amps. The magnetic circuit was simulated using MagNet 2D software and the path the magnetic flux follows is illustrated in : , assuming air gap in the place of MREs. Table 10 presents the values of the produced magnetic field at 1, 2 and 3 Amps electric current. The magnetic field values were measured using a magnetic probe in the middle of the 5mm gap without the MRE samples. The measured magnetic flux values are in agreement with the simulated values.

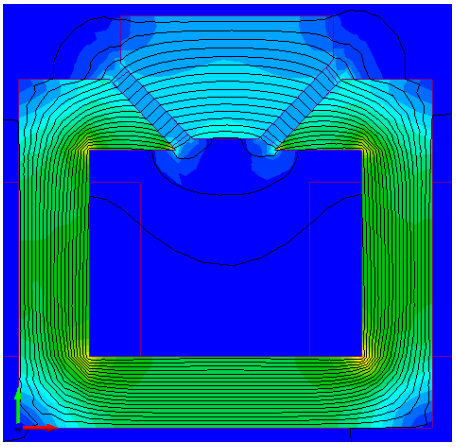

Figure 10: Simulated magnetic circuit

Table 10: Characteristics of magnetic circuit

Electric current I (Amp)	**1**	**2**	**3**
Voltage V (V)	4.46	8.93	13.4
Magnetic field B (mT)	60	120	190
Power (Watt)	4.46	17.86	40.2

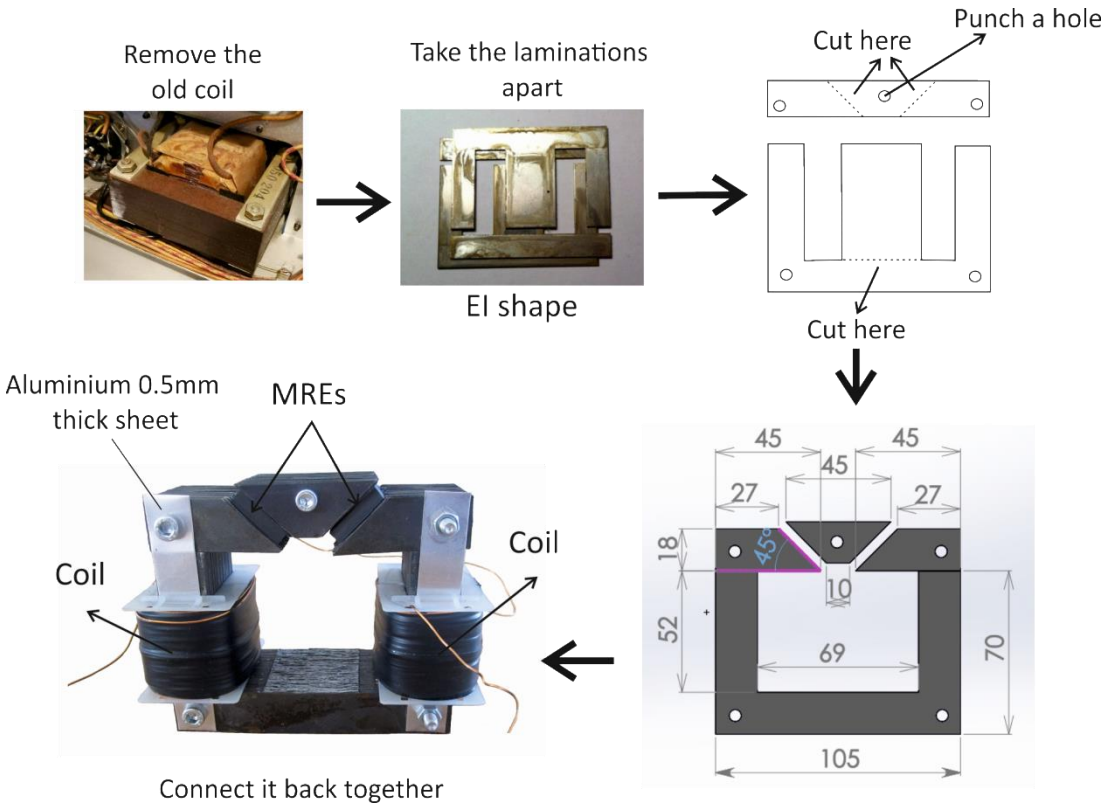

Figure 11: Electromagnet test device manufacturing procedure (dimensions are in mm).

However, the field is expected to be slightly higher since MREs have higher permeability than air. The magnetic circuit does not require high voltages and therefore is a low power consumption device. The dimensions of the electromagnet were based on the original dimensions of the old transformer that was big enough to create an adequate magnetic field but at the same time small enough to fit in INSTRON PULS tester. The values of the magnetic flux mentioned consider air in the gap between the magnetic circuit but MREs have a higher magnetic relative permeability μ_r than air. It has been reported that isotropic and anisotropic with particles aligned perpendicular to the magnetic field have a similar relative permeability, while for anisotropic MREs with particles aligned parallel to the direction of the magnetic field it becomes higher (Harrison, Equi-biaxial tension tests on magnetorheological elastomers 2016). Thus, the actual magnetic flux will be higher than the one mentioned and even different for each type of MRE under test. However, this will be the case for every MRE isolator device working in compression or compression/shear (inclined) loading mode.

System setup

The test setup diagram for the combined shear and compression tests is shown in Figure 12. The electromagnet was placed between two aluminium compression plates that were fixed on the frame of Instron Puls mechanical tester. Electric current up to 3 Amps was provided to each coil of the electromagnet by a constant current power source. It was observed however, that the

electromagnet was getting really hot when it was fed with 3 Amps although the 0.71mm copper wire could cope with this current value. For this reason, some of the experiments were restricted to maximum 2 Amps electric current to make sure that the measurement system remained stable.

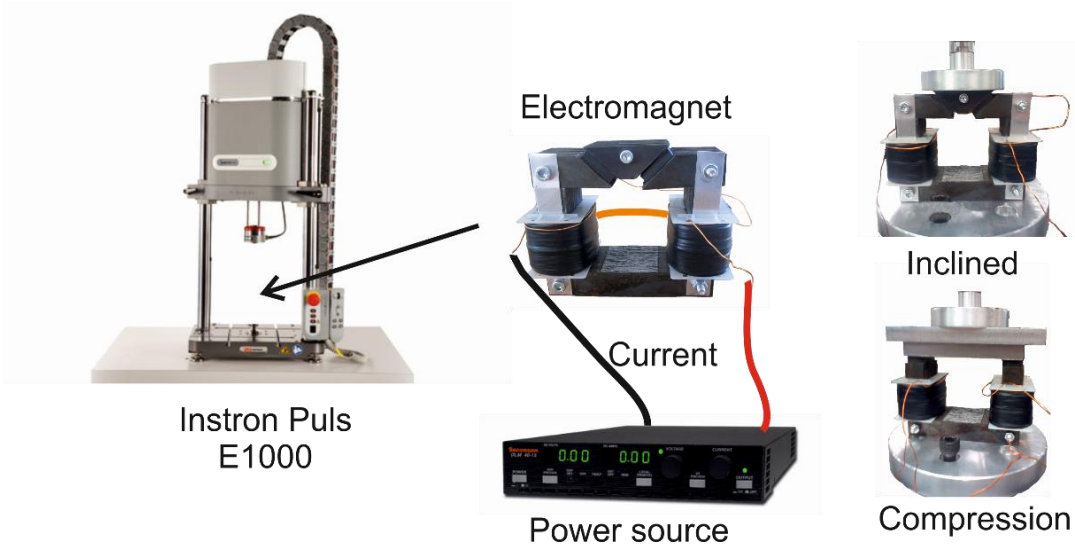

Figure 12:Test setup for inclined tests

For comparison reasons, pure compression tests were also performed using the same test setup. The same rectangular MRE samples were placed on top of each leg of the electromagnet and the top part was replaced by a solid low carbon iron rectangular bar thus, providing similar magnetic flux values. An extra aluminium rectangular bar was also placed on top of the iron bar before the compression plate, to provide extra isolation of the produced magnetic field and assure homogeneous load distribution. Instron Wavematrix control software offers the ability to measure transmissibility using the force and displacement readings of the sensors on the load cell and actuator. This works by defining a required displacement amplitude and frequency range and the machine runs several loading cycles until the amplitude value is reached for each frequency. The software then finds the dynamic stiffness and tangent of the loss angle of the system under test to finally calculate natural frequency ω_n and transmissibility using these values and equations (3.3.1) and (3.3.2).

3.5 Analysis of experimental data

Methods of extracting the dynamic moduli of elasticity

INSTRON Puls mechanical tester only records the applied force $\tilde{F} = F_0 \sin(\omega t)$ and position $\tilde{x} = x_0 \sin(\omega t + \varphi)$ signals from the load cell and actuator position sensor. Thus, the moduli of elasticity are calculated using the INSTRON Wavematrix software and its DMA calculations toolbox, following the directions of the ISO 4664-1:2011 standard. According to the Wavematrix DMA manual the dynamic stiffness (or else the value of absolute modulus$|\mathrm{M}^*|$) can be easily calculated by dividing the stress range $|\tilde{\sigma}|$ (peak to peak amplitude) to the strain range $|\tilde{\varepsilon}|$. In order to determine the moduli of elasticity the phase difference (loss angle) δ between the input and output signal is also needed. For linear specimens where the output signal is a pure sine wave this can be fairly simple, but the situation is much more complicated for distorted nonlinear signals. According to the Wavematrix DMA manual there are three ways to calculate the phase difference δ.

$$|\mathrm{M}^*| = \frac{|stress\ range|}{|strain\ range|} = \frac{|\tilde{\sigma}|}{|\tilde{\varepsilon}|} = \frac{\left|\frac{F}{A}\right|}{\left|\frac{x}{L}\right|} \tag{3.5.1}$$

Where A=area of the sample the force is applied too and L=length of the sample.

- **Loop width method**

This method uses the formula (3.4.2) to calculate the loss angle. It is susceptible to measurement noise and requires sinusoidal waveforms.

$$\text{Loss angle} = \text{Arcsine}\left(\frac{\text{width of loop at mean force}}{\text{displacement range}}\right) \tag{3.5.2}$$

- **Energy method**

This method uses the formulae (3.4.3) to calculate the loss angle. This method can deal with distorted signals since it calculates the area of the loop and it is more suitable for nonlinear specimens.

$$\text{Loss angle} = \text{Arcsine}\left(\frac{\text{area enclosed by the hysteresis loop (energy)}}{\pi \frac{\text{displacement range}}{2} \frac{\text{force range}}{2}}\right) \tag{3.5.3}$$

- **Correlation method**

This method is based on finding the best fit sinusoidal waveform of the measured input and output signals. Once the individual phase angles are found the loss angle is the difference between them.

The correlation method is ideal for linear specimens but it cannot give relatively good results for slightly distorted waveforms.

$$\text{Loss angle} = \textit{Force phase angle-displacement phase angle} \quad (3.5.4)$$

The calculated moduli of elasticity using the three different methods in Matlab are shown in Table 11. The three methods give similar results for storage modulus but different ones for loss modulus and tangent of the loss angle depending on the applied strain amplitude and thus, the nonlinearity of the signals. In the case of MREs, the energy method was selected because it can cope with the nonlinearity of the hysteresis curves although it should be noted that the moduli of elasticity make sense only if the first harmonic of the output signal is considered and the harmonic balance method is followed.

Table 11: Calculated values of moduli of elasticity using the different methods.

Method:	**Loop width**	**Energy**	**Correlation**	
Loss angle δ	4.057 ^{0}	4.5532 ^{0}	2.23 ^{0}	0.5 %
Storage modulus E’	8.972 MPa	8.966 MPa	8.9878 MPa	5 Hz
Loss modulus E’’	0.6363 MPa	0.714 MPa	0.35 MPa	
Tangent of the loss angle tanδ	0.071	0.079	0.039	0T
Loss angle δ	5.075 ^{0}	4.7035 ^{0}	5.92 ^{0}	2 %
Storage modulus E’	7.9585 MPa	7.9628 MPa	7.9471 MPa	5 Hz
Loss modulus E’’	0.7067 MPa	0.655167 MPa	0.824 MPa	
Tangent of the loss angle tanδ	0.089	0.082	0.103	0T

Variability of measured values

MR elastomers, like all elastomers, show a relative high variability of their mechanical properties even on items of the same batch. Unfortunately, the silicon MRE samples produced were left to cure at room temperature in a laboratory with no temperature and humidity control. Due to this, the zero field values of the mechanical properties, especially stiffness, were found to vary between samples of the same type manufactured at different days using the same procedure. However, all samples of the same type behaved the same way showing the same general trends, except the MR effect that showed great variation depending on the batch. For example, MR effect of isotropic samples, manufactured at different days, varied from 15% to 70%. It should be noted here that great effort was put on finding a way to achieve constant high MR effect but could not succeed. It is believed though, that if a different rubber elastomer was used under a controlled manufacturing

process the variability of MR effect could be less. In order to make safe conclusions when comparing the different types of MRE samples between each other, again the instructions of the ISO 4664-1:2011 standard was followed, since this is common to all filled rubbers. Therefore, when comparing the different types of MREs between each other, three different set of MRE samples manufactured at different days and for each type of material of interest were selected. The average values of three set of samples are then reported disregarding the samples with the highest and lowest MR effect.

Considering higher harmonics

As mentioned earlier, for high values of strain amplitude the recorded waveforms are not perfect sinusoidal signals with one frequency but include higher harmonics. Figure 13 illustrates the Fast Fourier Transform (FFT) spectrum of the magnitude of displacement channel for 0.5% and 2% strain amplitude for both isotropic and anisotropic samples with small particles. It can be noticed that the second harmonic is present for both samples at the high amplitude value while the anisotropic sample shows a third harmonic as well. For the low amplitude value, only the first harmonic is of importance. This can be explained by the fact that anisotropic samples are stiffer than isotropic and therefore generate more harmonics although, their magnitude are less than 5% of the first harmonic for all samples.

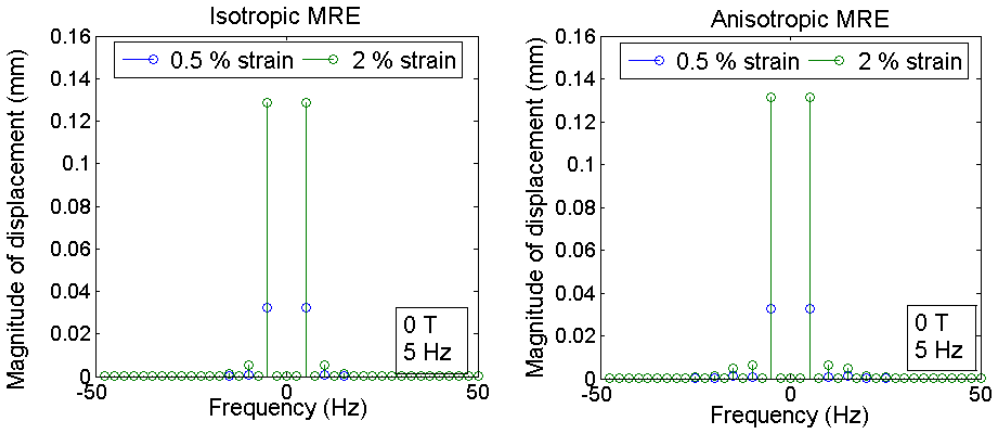

Figure 13: FFT spectrum of displacement signal for isotropic and anisotropic MRE with small particles at 0.5% and 2% strain amplitudes.

However, before arriving to any results regarding the harmonics it is essential to investigate which of these harmonics are due to measurement error and which are generated by the material itself. The improved measurement setup reduced significantly the harmonics caused by inertial forces at high frequencies but as the load or strain amplitude increases it becomes impossible for INSTRON machine to keep the input signal a pure sine wave. The observed harmonics to the output signal can therefore be the result of the harmonics of the input signal rather than the response of the material itself. This is mostly due to the fact that INSTRON prefers to be controlled in displacement

mode since the movement of the actuator can be controlled more accurately than the load cell. This practically means that the force signal cannot be the input as assumed in theory, which is not a problem for linear materials where only the phase difference between the two signals is of interest. In the case of nonlinear elastomers considering a displacement signal as an input to find the corresponding force signal with higher harmonics is not a straight forward procedure.

Figure 14 present the absolute values of the three first harmonics of the magnitude of displacement and force signals for anisotropic MRE at different strain amplitudes calculated using the FFT transform. Both signals contain higher harmonics that grow with increasing strain amplitude. At low strain amplitudes, the magnitude of the second and third harmonic are almost equal but as the strain amplitude increases the second harmonic grows to become bigger. Figure 15 presents the hysteresis curves of the recorded signals and the curves when the first, second and third harmonics are taken under consideration for both displacement and force channels. It becomes obvious that in order to get a good fit all three harmonics for both channels have to be taken under consideration. However, neither stiffness nor the area of the hysteresis curve, and thus the resulting damping capability of the material, are affected significantly by the increasing number of harmonics, as

Table 12 indicates.

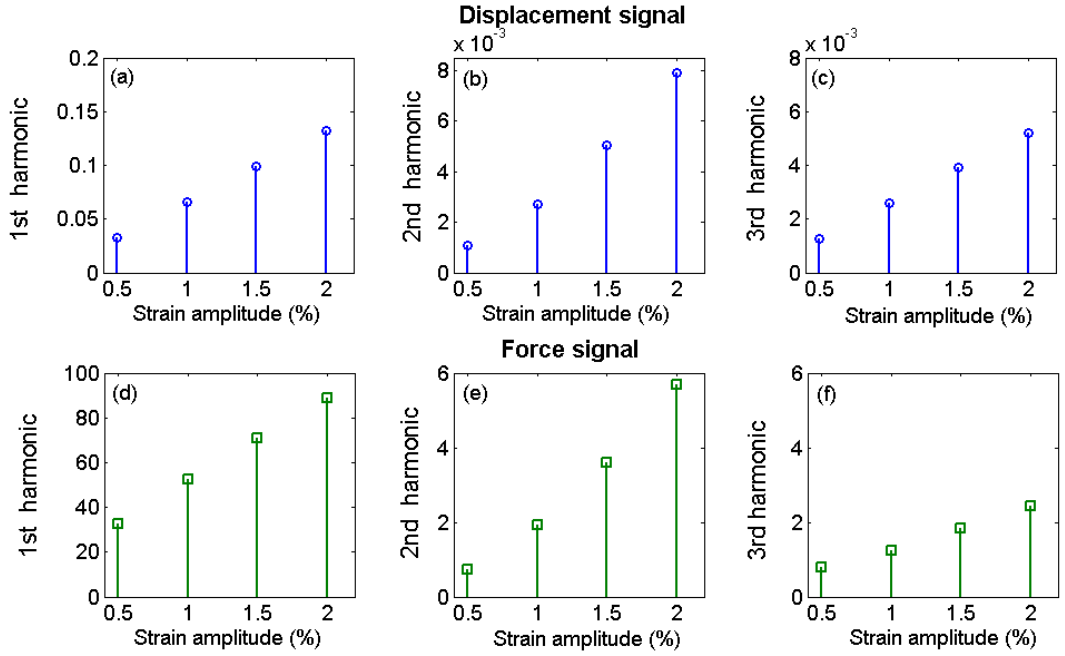

Figure 14: Absolute values of the three first harmonics of the magnitude of displacement and force signals for anisotropic MRE at different strain amplitudes.

Table 12: Calculated area of the hysteresis loop considering higher harmonics

	Recorded data	**1 harmonic**	**2 harmonics**	**3 harmonics**
Area	25.1418	23.5772	24.6825	25.1147
Dynamic stiffness	648.6038	670.9848	632.2282	642.4307

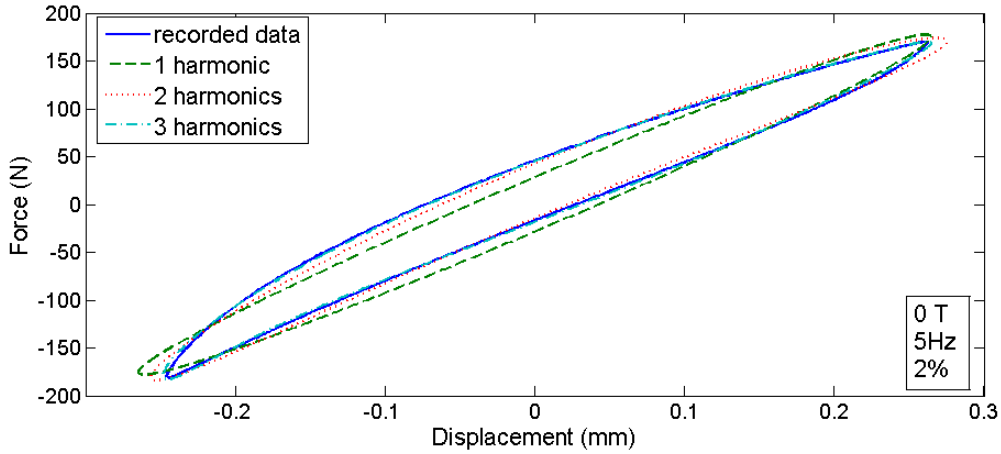

Figure 15: Force-displacement hysteresis curves when taking under consideration the 1, 2 and 3 harmonics for both channels.

Figure 16 illustrates the hysteresis curves when taking under consideration all three harmonics of the force channel and one, two and three harmonics of the displacement channel under the logic that the displacement channel is the input. Again, it can be seen that at least the second harmonic for the displacement channel should be taken under consideration to be able to simulate accurately the recorded data. This means that not even the displacement channel is a pure sine signal and therefore the higher harmonics cannot be experimentally defined.

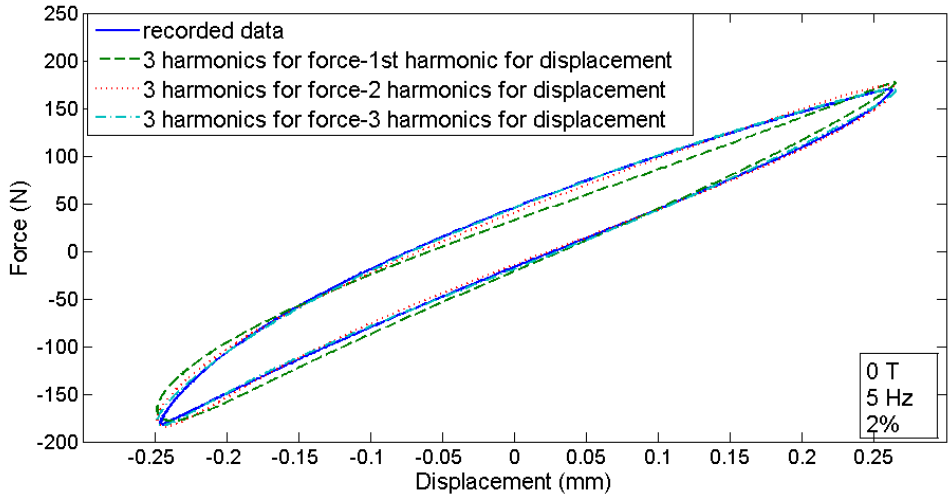

Figure 16: Force-displacement hysteresis curves when taking under consideration 1, 2 and 3 harmonics for displacement channel and the all 3 harmonics for the force channel.

3.6 Chapter summary

The basic characteristics of the experimental system used in this work can be summarized as:

- A two-component room-temperature vulcanization silicon rubber was used as the rubber matrix. For the filler particles, I selected two types of iron particles, one with an average diameter lower than 220 μm (Sigma-Aldrich) and the other with average diameter of 4-6 μm (Sigma-Aldrich), referred as large and small particles respectively.
- Anisotropic MRE samples were cured under a stable magnetic field of 0.5T for samples with 12.5mm height and 0.35T for samples with 22 mm height. The magnetic field was produced using permanent magnets.
- The static and dynamic compression tests were performed according to BS ISO 7743-1:2011 and BS ISO 4664-1:2011 standards, using INSTRON PULS E1000 electromechanical dynamic tester and custom made aluminium compression plates.
- The magnetic field for material characterization tests was produced using permanent magnets. The tests were performed for two values of magnetic flux densities. Those are 0.3T and 0.5T for samples with 12.5mm height and 0.2T and 0.35T for samples with 22 mm height.
- The magnetic circuit used for both pure compression and 45^0 inclined tests was manufactured using an old EI shaped laminated core transformer and two coils of 500 turns each resulting a maximum magnetic flux of 0.2T with a 5mm air gap.
- Five different batches of each type of MRE samples were made and the average values of three set of samples are reported, disregarding the samples with the highest and lowest MR effect.
- The energy method was used to calculate the loss angle and thus the complex stiffness and moduli of elasticity.

Chapter 4: Dynamic mechanical properties of isotropic and anisotropic MREs under pure compression

4.1 Introduction

The static and dynamic properties of MREs have been widely studied in the past, but the wide variation of sample size, materials used and measuring methods often results to contradicting results. Thus, the first step was to understand how the material behaves under varying loading conditions following the directions of the relevant ISO standards. The results of these tests will be used in later to compare their behaviour with the composite isotropic/anisotropic MREs and make a phenomenological parametric viscoelastic model of anisotropic and isotropic MREs. This chapter presents the experimental results of the dynamic compression tests performed in isotropic and anisotropic MREs with large (diameter <220 μm) and small (diameter=4-6 μm) particles under varying load amplitude, frequency, static prestrain and magnetic field. In more detail the purpose of this chapter is to:

- Examine the performance of MREs with very large particles compared to conventional MREs with small particles.
- Examine the effect of strain amplitude and frequency on zero field dynamic mechanical properties and their coupling effects.
- Examine the effect of static load on zero field dynamic mechanical properties at different strain amplitudes and frequencies.
- Examine the effect of the external magnetic field (MR effect) on dynamic mechanical properties and how this varies with strain amplitude, frequency and static prestrain.
- Examine the effect of size and shape of MRE samples on mechanical properties (scaling effect) and MR effect.

4.2 Details of experiment

MRE samples

The first test performed was the mechanical characterization of the traditional isotropic and anisotropic MR elastomers. For this type of tests, disk samples of 29 ± 0.5 mm diameter and 12.5 ± 0.5 mm height (standard test piece A) were used, following the directions of the BS ISO 4664-1:2011 standard for compression loads on rubber. In total four types of silicon MRE samples are examined as presented in Table 13. Two isotropic MREs made with small (diameter=4-6 μm) and large (diameter<220 μm) iron particles and two equivalent anisotropic MREs. All samples were manufactured using the procedure explained in details in section 3.1, while all anisotropic MREs were cured under 0.5T magnetic field.

Table 13: Names and characteristics of MRE samples used for material characterization

Type	Particles	Name
Isotropic	Large (<220 μm)	Isotropic a-l
Isotropic	Small (4-6 μm)	Isotropic a-s
Anisotropic	Large (<220 μm)	Anisotropic a-l
Anisotropic	Small (4-6 μm)	Anisotropic a-s

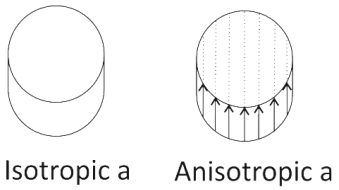

Diameter: 29 ± 0.5 mm

Height: 12.5 ± 0.5 mm

In order to examine the scaling effect, sixteen additional isotropic disc, square, rectangular and ring shaped MRE samples with small particles of different sizes were manufactured, as illustrated in Figure 17, Figure 18, Figure 19 and Figure 20 respectively. All samples were manufactured using the procedure explained in detail in section 3.1.

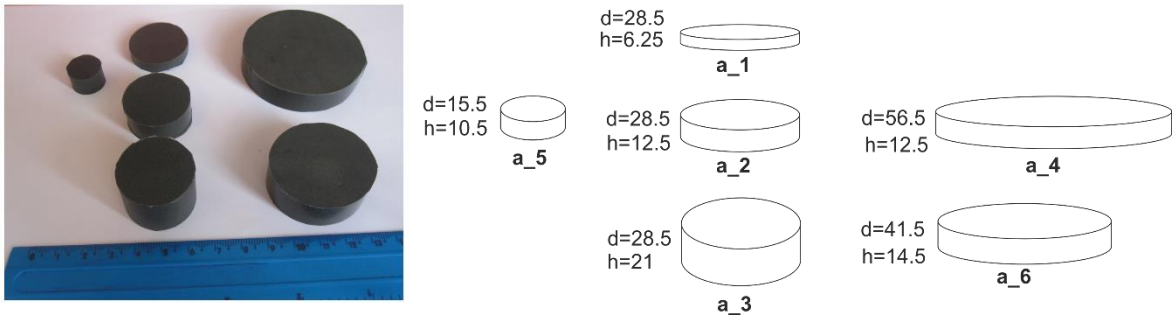

Figure 17: Names and dimensions of disk shaped isotropic MRE samples

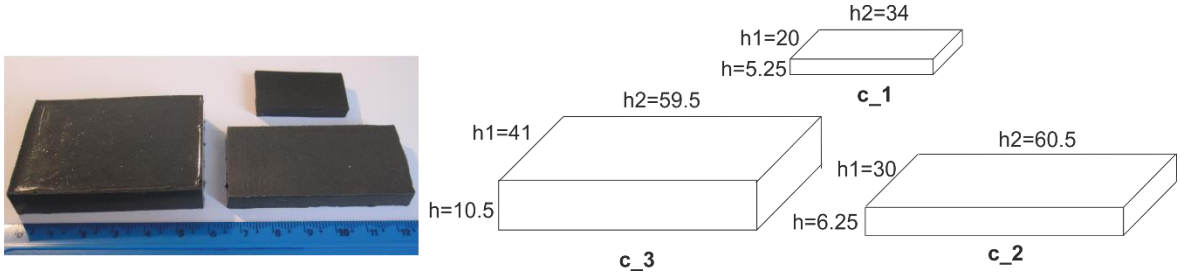

Figure 18: Names and dimensions of rectangular shaped isotropic MRE samples.

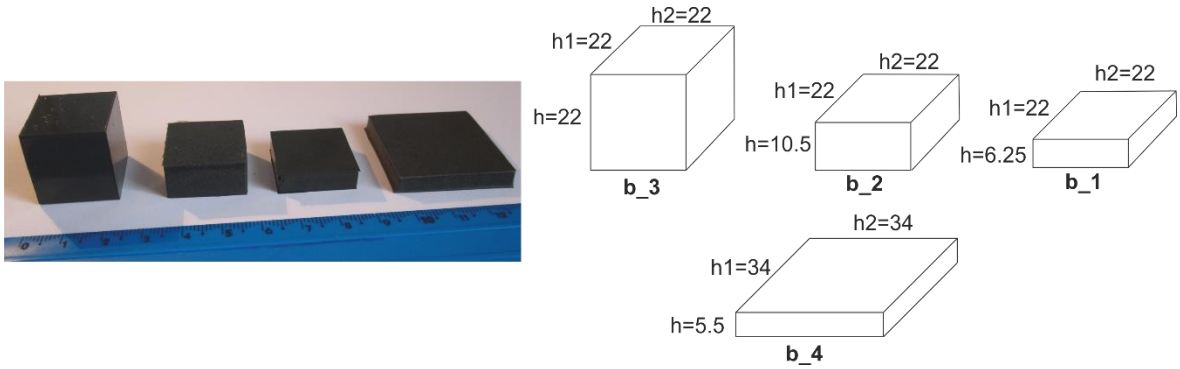

Figure 19: Names and dimensions of square shaped isotropic MRE samples.

Figure 20: Names and dimensions of ring shaped isotropic MRE samples

Test details

The dynamic tests were performed according to BS ISO 7743-1:2011 and BS ISO 4664-1:2011 standards respectively, using INSTRON PULS E1000 electromechanical dynamic tester and the experimental setup described in detail in section 4.2. For most samples only two types of dynamic loading cycles were performed at 0, 0.3T and 0.5T magnetic field values. One amplitude sweep cycle, where the strain amplitude was increased from 0.25% to 2% at a constant frequency of 5 Hz, and a second frequency sweep cycle where the frequency was increased from 0.5Hz to 70 Hz at constant strain amplitude of 0.5%. For three samples of each MRE category the amplitude sweep cycle was repeated at each frequency and magnetic field, to examine the coupling effects. This type of test is referred as compete test on the following table. The values reported are the average of the values of three different samples manufactured at different time.

Table 14: Summary of test loading cycles for dynamic compression tests

Amplitude sweep test	Strain Amplitude (%)	0.25,0.5,0.75,1,1.25,1.5,1.75,2 (50 loading cycles for each amplitude)	**Magnetic field** 0 0.3T 0.5 T For standard disk samples
	Loading frequency	5 Hz (at 5KHz sampling rate)	
	Prestrain	10 %	
Frequency sweep test	Strain Amplitude	0.5 %	
	Loading frequency (Hz)	0.5,1,5,10,20,30,40,50,60,70 (20,30,50,100,150,250,300,350,400,450 loading cycles for each corresponding frequency at 5KHz sampling rate) *	
	Prestrain	10 (%)	
Prestrain effect test	Strain Amplitude (%)	0.25,0.5,0.75,1,1.25,1.5,1.75,2 (50 loading cycles for each amplitude)	
	Loading frequency	5 Hz (at 5KHz sampling rate)	
	Prestrain (%)	2,3,4,6,8,10	
Complete test	Strain Amplitude (%)	0.25,0.5,0.75,1,1.25,1.5,1.75,2 (50 loading cycles for each amplitude)	
	Loading frequency (Hz)	0.5,1,5,10,20,30,40,50,60,70 (20,30,50,100,150,250,300,350,400,450 loading cycles for each corresponding frequency at 5KHz sampling rate) *	
	Prestrain	10%	

*The number of cycles was increased for each frequency to allow for the amplitude control feature of the wavematrix software to reach the desired amplitude with increasing frequency.

4.3 Influence of load amplitude and frequency

Figure 21 illustrates the zero field absolute modulus$|E^*|$, tangent of the loss angle tanδ and storage modulus E' and loss modulus E'' of isotropic and anisotropic samples with large (<220µm) and small (6µm) particles. The samples with large particles have higher values of absolute $|E^*|$ and storage modulus E', which means they are slightly stiffer than the samples with small particles for both isotropic and anisotropic cases. As load amplitude increases, absolute modulus $|E^*|$, storage modulus E' and loss modulus E'' decrease for all samples, which is nothing more than the Payne effect observed for all filled rubbers. This trend is more pronounced in anisotropic samples due to the destruction-deformation mechanism of the filler chain structure inside the matrix when the material is overstressed, that makes it softer (Sorokin V V 2014).

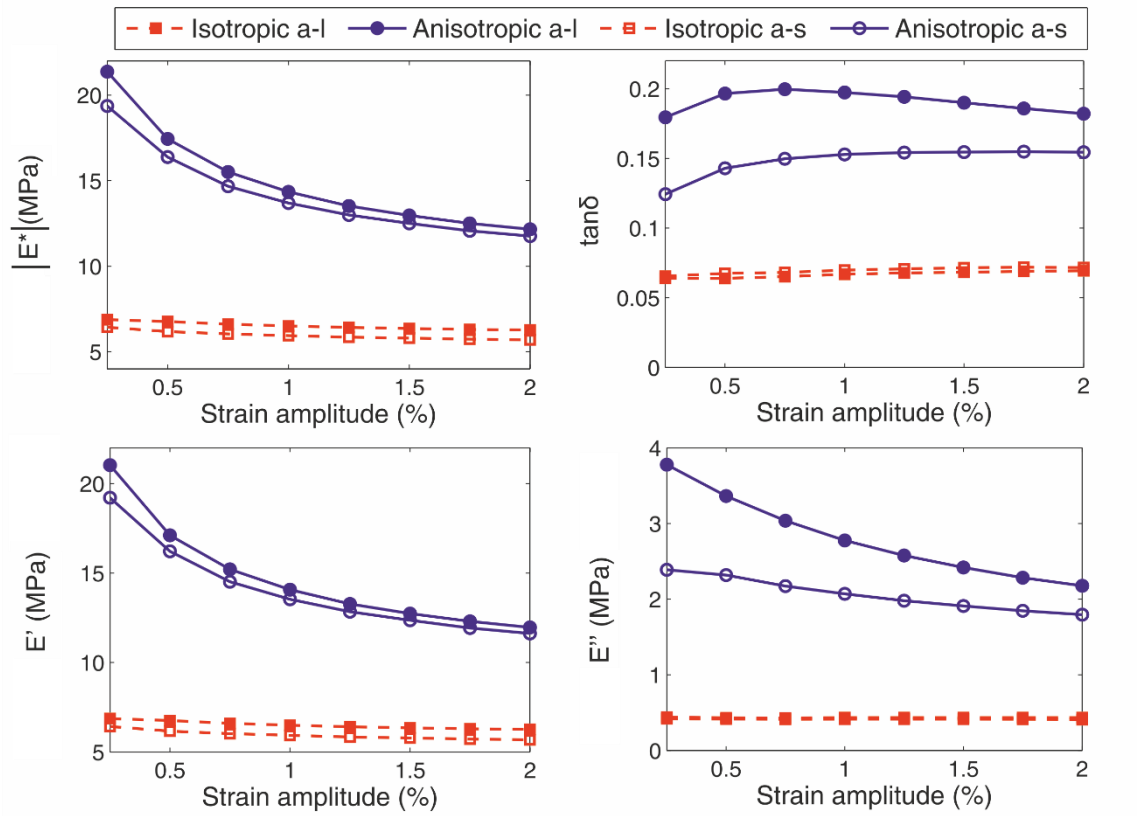

Figure 21: Variation of absolute modulus $|E^*|$, tangent of the loss angle tanδ, storage modulus E' and loss modulus E'' in respect to strain amplitude (at 0T, 10% prestrain and 5Hz frequency). Force applied in the axial direction parallel to particle alignment for anisotropic MREs.

Both isotropic MREs have similar loss modulus E'' and tangent of the loss angle tanδ and therefore, have similar damping capability that increases slightly with increasing strain amplitude. This agrees with the data published in the literature (G. X. Yang J 2012). On the other hand, anisotropic samples with large particles have much higher loss modulus E'' and tangent of the loss angle than anisotropic samples with small particles. Both anisotropic samples decrease their loss modulus E'' with

increasing strain amplitude but this drop is higher for anisotropic MREs with large particles causing tanδ to increase until 0.75% strain amplitude and to decrease later. This behaviour can be attributed to the larger size of filler particles that tend to cause more destruction to the matrix-filler structure with increasing load, making the material softer and allowing the large particles to move easier inside the matrix. As a result, less energy is dissipated and damping capability is decreased.

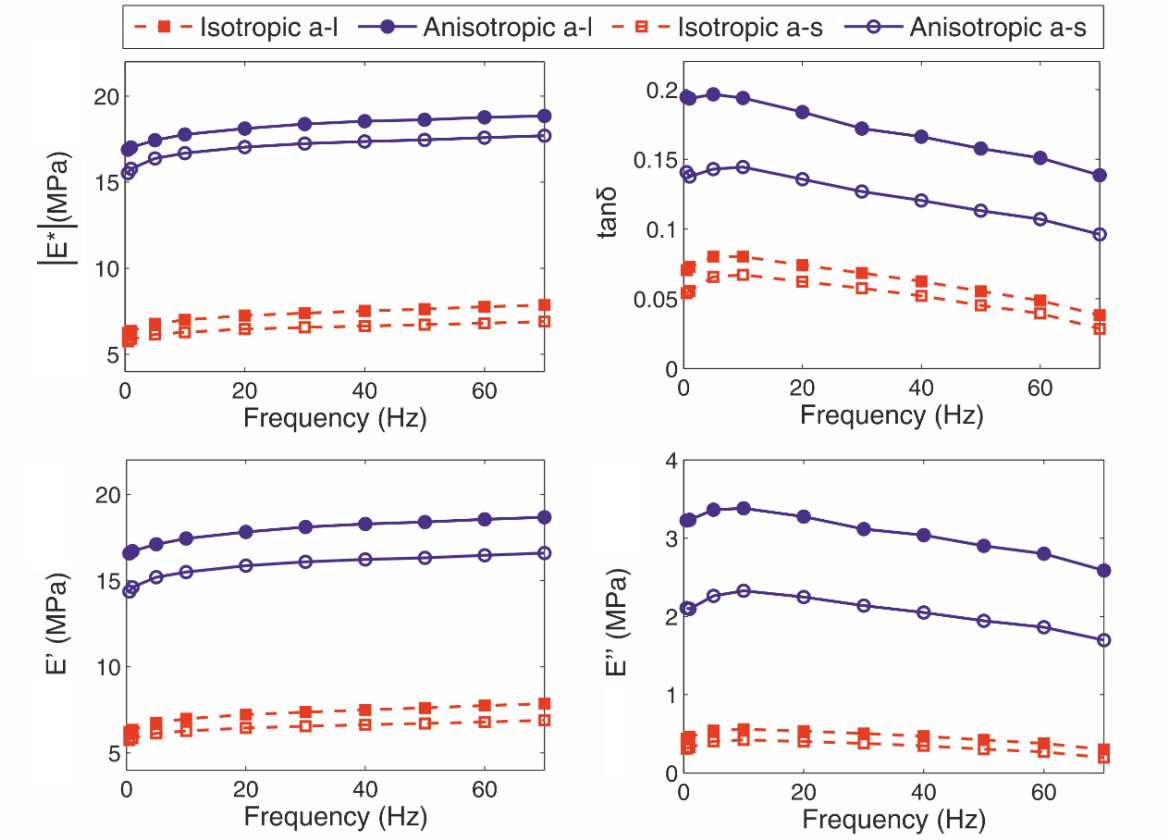

Figure 22: Absolute modulus $|E^*|$, tanδ, storage E' and loss modulus E'' in respect to load frequency (at 0T,10% prestrain and 0.5% strain amplitude). Force applied in the axial direction parallel to particle alignment for anisotropic MREs.

Figure 22 illustrates the influence of load frequency on the absolute modulus $|E^*|$, tangent of the loss angle tanδ, storage modulus E' and loss modulus E'' of anisotropic and isotropic MREs with large and small particles. All samples become stiffer with increasing frequency while loss factor E'' and tanδ increases until about 10 Hz after which they decrease rapidly. These results differ from previous published work on compressive loading tests on silicone MREs (Li R 2013), where tangent of the loss angle tanδ is shown to increase slightly with frequency. We assume that the deviation is due to the smaller samples used in those experiments as well as the method used to calculate the area of the hysteresis loop during DMA calculations. In each case the variation of tangent of the loss angle is not significant enough when it comes to designing isolators for real applications.

Load amplitude-frequency interaction

Figure 23 and Figure 24 illustrate the three-dimensional curves of absolute modulus $|E^*|$ and tangent of the loss angle tanδ of isotropic and anisotropic MRE with small particles respectively, in respect to loading amplitude and frequency at zero field and 10% prestrain value. The general trends observed before also apply in this case, while no strong amplitude-frequency coupling effects are observed for either sample.

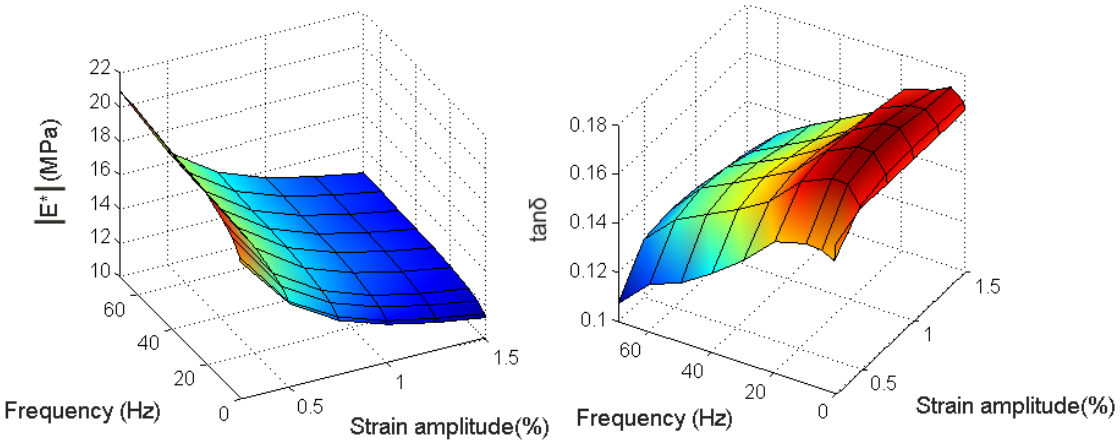

Figure 23: 3D representation of absolute modulus $|E^*|$ and tangent of the loss angle tanδ of isotropic MRE with small particles (at 0 Tand 10% static prestrain). Force applied in the axial direction.

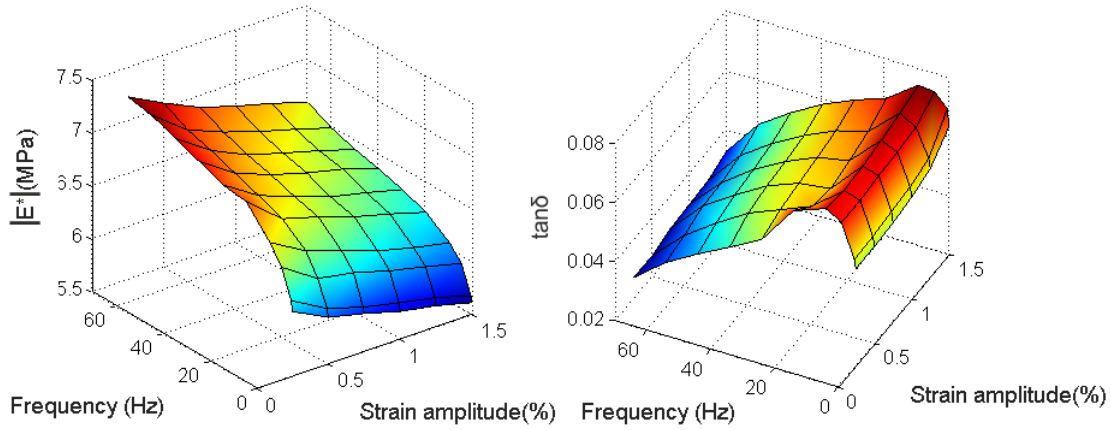

Figure 24: 3D representation of absolute modulus $|E^*|$ and tangent of the loss angle tanδ of anisotropic MRE with small particles (at 0 T and 10% static prestrain). Force applied in the axial direction parallel to particle alignment for anisotropic MREs.

Figure 25 and Figure 26 provide a better insight to the possible amplitude-frequency coupling effects for isotropic and anisotropic samples with small particles. It becomes obvious that the shape of the curves does not vary with increasing amplitude but only the absolute values are different. If the curves were brought to the same starting point they would be very close to each other. Tangent of the loss angle is considered to behave similarly since the small variation between the curves lies in the range of measurement errors. The same principle applies for MREs with large particles as it can be seen in Figure 27 and Figure 28. Again, if the curves of moduli of elasticity E' and E'' were

brought to the same starting point they would be very close to each other and therefore, no great strain amplitude-frequency coupling effect is observed.

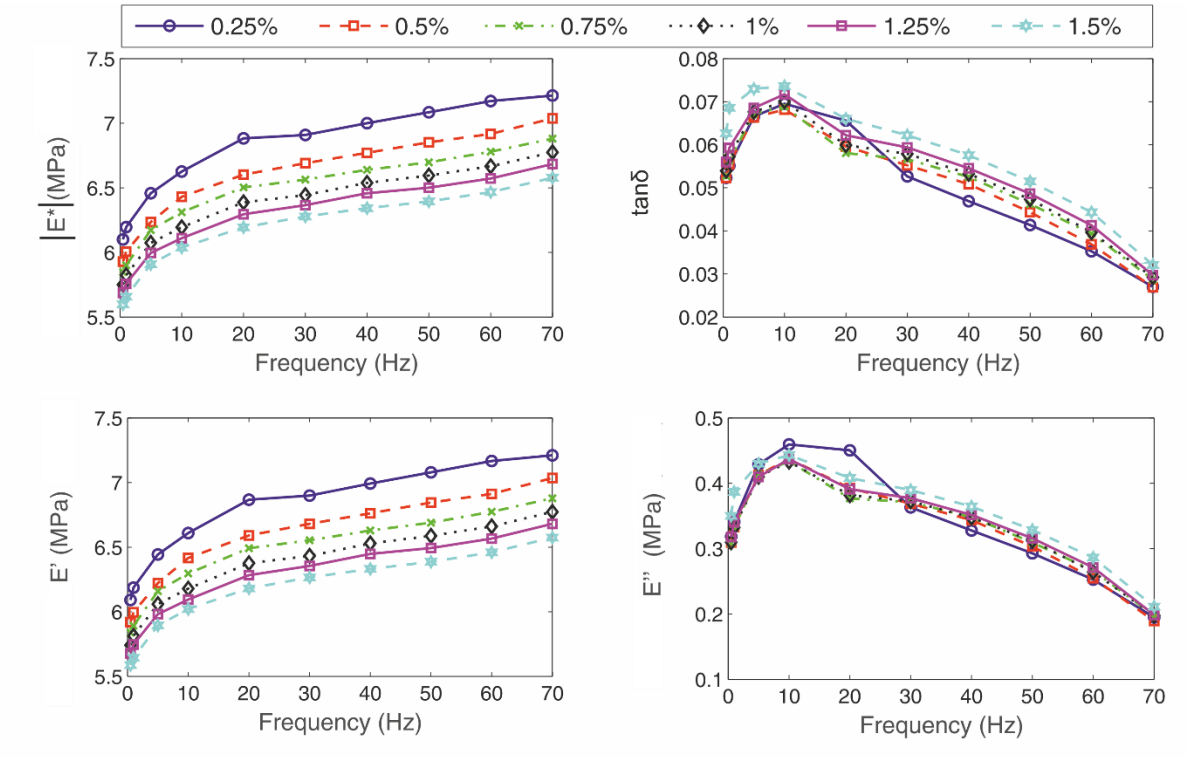

Figure 25: Dynamic mechanical characteristics of isotropic MRE with small particles in respect to frequency at different strain amplitudes (at 0T and 10% static prestrain)

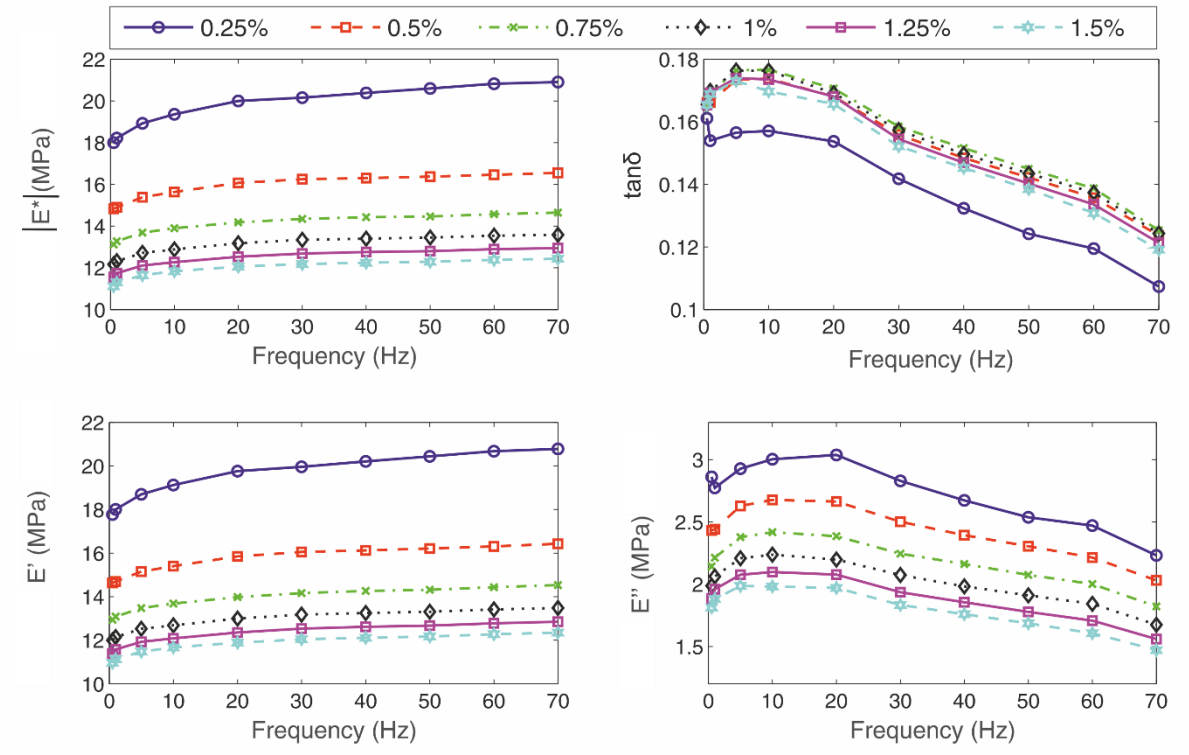

Figure 26: Dynamic mechanical characteristics of anisotropic MRE with small particles in respect to frequency at different strain amplitudes (at 0T and 10% static prestrain).

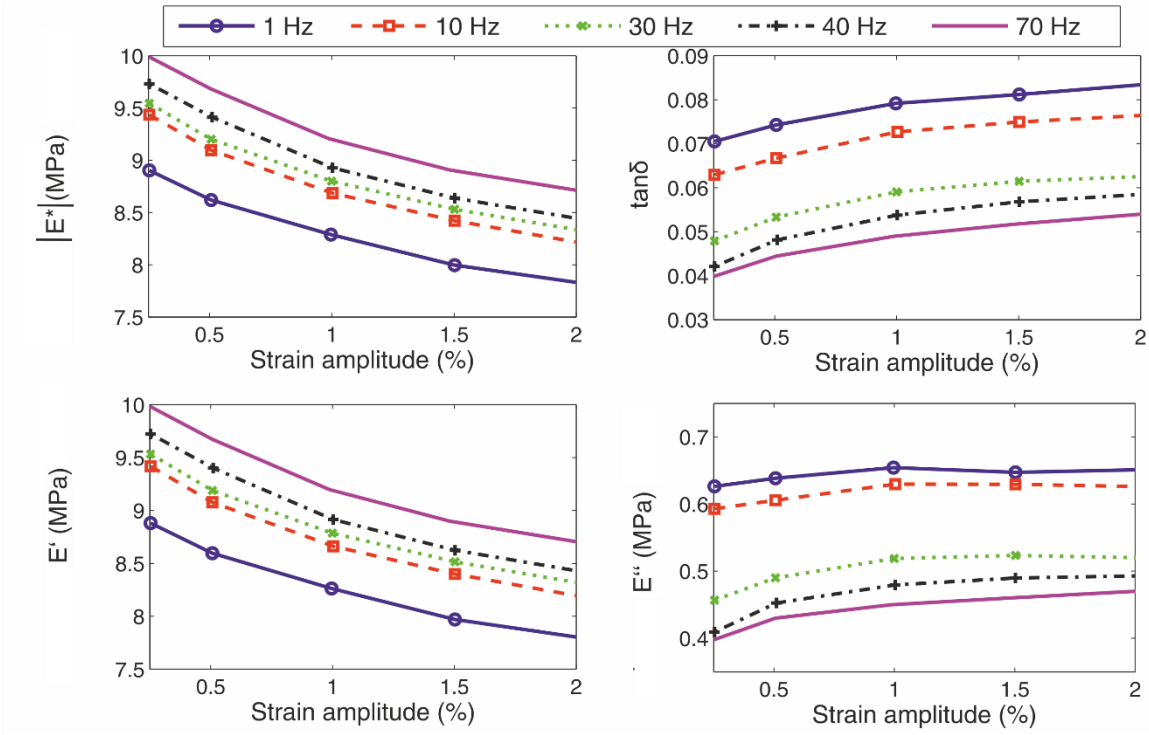

Figure 27: Dynamic mechanical properties of isotropic MRE with large particles in respect to strain amplitude at different load frequencies (at 0T and 10% static prestrain).

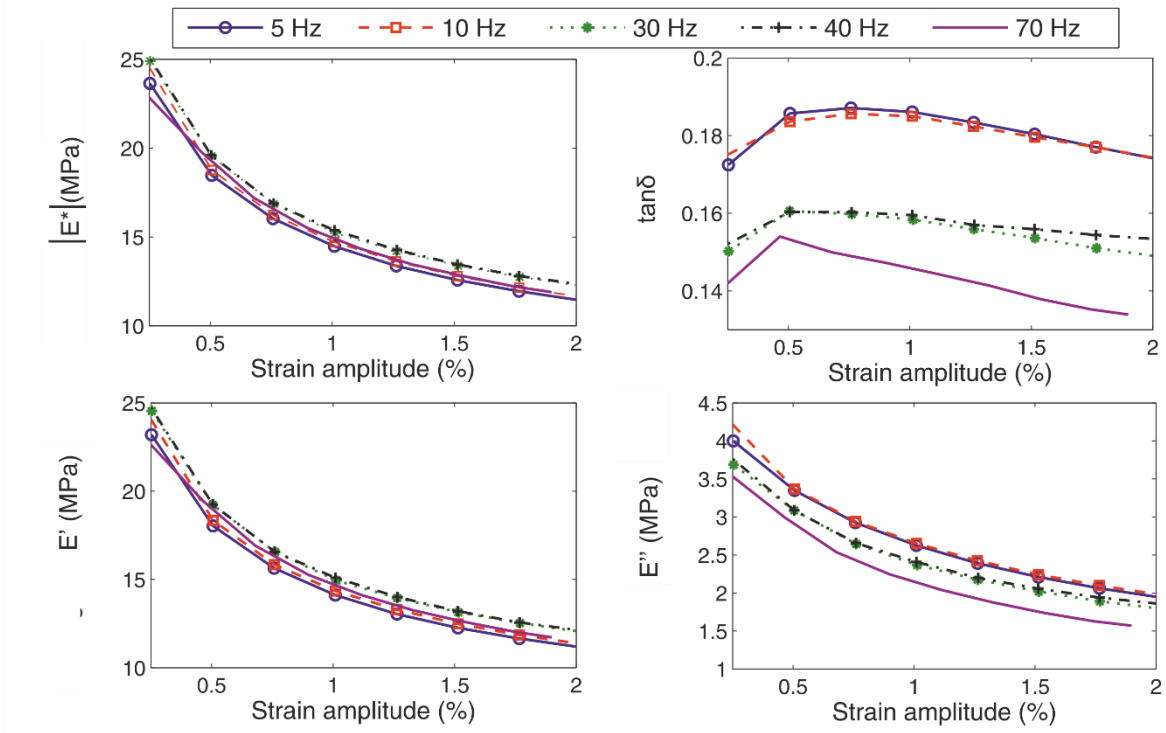

Figure 28: Dynamic mechanical characteristics of anisotropic MRE with large particles in respect to strain amplitude at different load frequencies (at 0T and 10% static prestrain).

4.4 Influence of static prestrain

All MREs used in practical vibration isolators, will be subjected to an amount of prestrain due to the weight of the machine they support. The dynamic load is then superimposed on the static prestrain and cannot have a higher amplitude than the prestrain value itself. In this section, the influence of the prestrain on the zero-field dynamic mechanical properties of MREs is examined. Figure 29 presents the variation of zero field absolute modulus $|E^*|$, tanδ and moduli of elasticity for all four types of MRE samples, in respect to static prestrain value (measured at 0.5% dynamic strain amplitude and 5Hz load frequency). All MRE samples increase steadily their storage E' and absolute $|E^*|$ modulus with increasing prestrain values, common characteristic of all filled rubbers. However, loss modulus E'' of anisotropic samples increases fast for small prestrain values up to 4% to remain constant for greater values of prestrain. As a result, tanδ also increases for prestrain values up to 3% to later decrease with increasing static prestrain values.

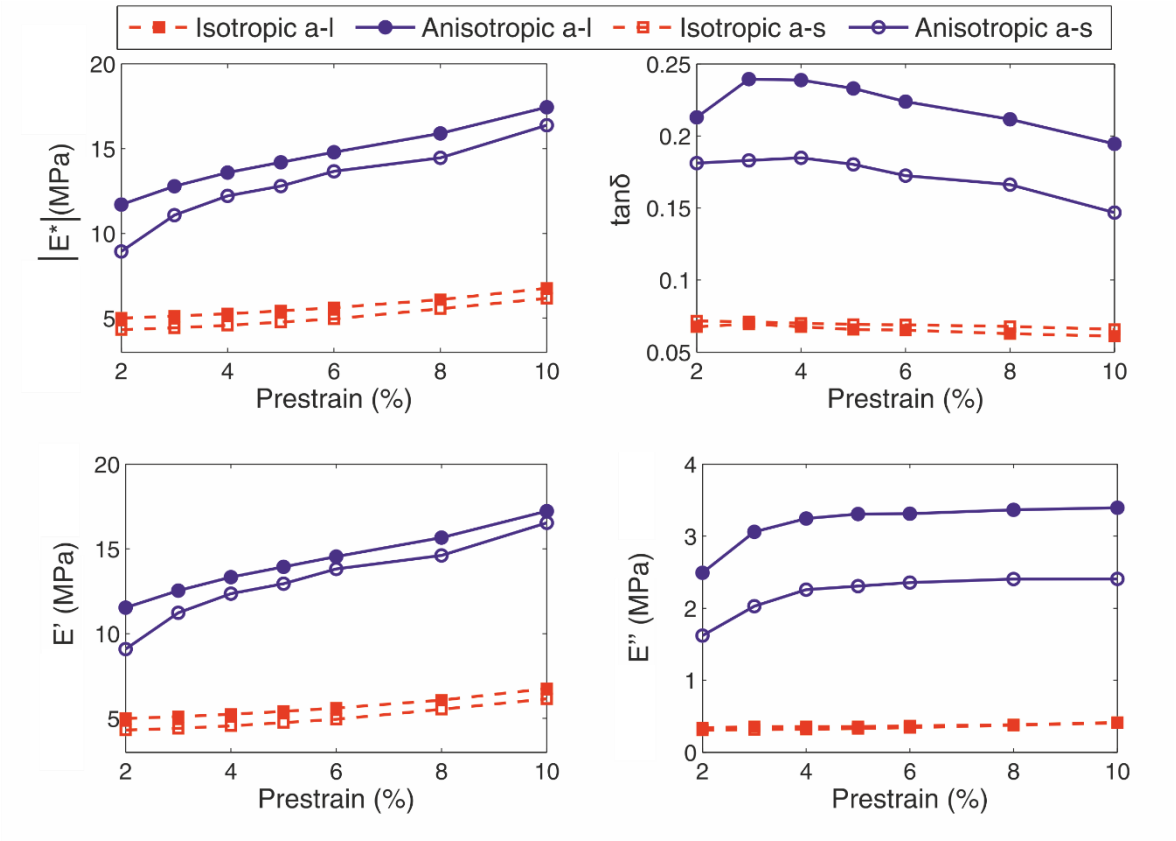

Figure 29: Variations of absolute modulus $|E^*|$, tanδ, storage modulus E' and loss modulus E'' in respect to static prestrain (at 0 T, 0.5% amplitude and 5 Hz loading frequency).

The effect of prestrain on dynamic mechanical properties of anisotropic MREs is much stronger than the one observed for isotopic elastomers. Anisotropic MREs increase their absolute modulus by 50% while isotropic MREs by 25% when the applied prestrain varies from 2% to 10%. This behaviour is attributed to the matrix-particles structure and the gaps between the particles themselves that vary with increasing prestrain. In anisotropic MREs the particles are already aligned

inside the elastomer and the application of a static force in the same direction with the aligned particles will bring them even closer together. Therefore, the movement of particles inside the elastomer matrix under a dynamic load is limited causing a higher increase of stiffness in anisotropic MREs than it would do in the case of isotropic MREs.

Under the same logic, the energy dissipated (indicated by loss modulus E'') in anisotropic MREs is lower at low prestrain values where the particles can still move freely inside the matrix. These results come in agreement with previous work published in the literature about the influence of prestrain on mechanical properties of highly filled elastomers (Thorin A 2012). The fact that Storage modulus E' increases faster that loss modulus E'' for prestrain values above 4%, causes tanδ to decrease at higher prestrain values especially for anisotropic MREs. In practical applications, this would suggest that the material loses energy less efficient at high prestrain values. Therefore, the general rule all elastomer isolators should be designed not to operate above 5% static prestrain should be followed for MREs as well to avoid poor isolation efficiency.

Prestrain-dynamic load amplitude interaction

The dynamic strain amplitude-static prestrain coupling effect for isotropic and anisotropic MREs with small and large particles is illustrated in Figure 30, Figure 31, Figure 32 and Figure 33 respectively. As strain amplitude increases and becomes comparable to the prestrain value (e.g. the 1.5% strain amplitude values correspond to 3% peak to peak amplitude that is very close to the 4% prestrain value), measurement errors occur. This is the reason why the high strain amplitude values at small restrains are omitted. It is shown again that absolute modulus $|E^*|$ and storage modulus E' (that indicate stiffness) both increase with increasing applied static load for all strain amplitudes at the same manner. Thus, regarding stiffness there are no great prestrain-dynamic load amplitude coupling effects for MREs.

Loss modulus E'' follows the same pattern and increases slightly with increasing static prestrain for isotropic MREs. In the case of anisotropic MREs loss modulus E'' again increases for low values of prestrain while it remains content or even decreases slightly for higher values of prestrain. As the static load applied to the elastomer increases, the movement of the particles inside the matrix becomes limited. Therefore, with increasing applied static load the particles need more energy to move inside the matrix under the same dynamic load, leading to an increase of loss modulus E''. This trend is again more pronounced for anisotropic MREs due to the pre-structure of particles inside the matrix. Thus, there are no great prestrain-dynamic load amplitude coupling effects regarding damping either.

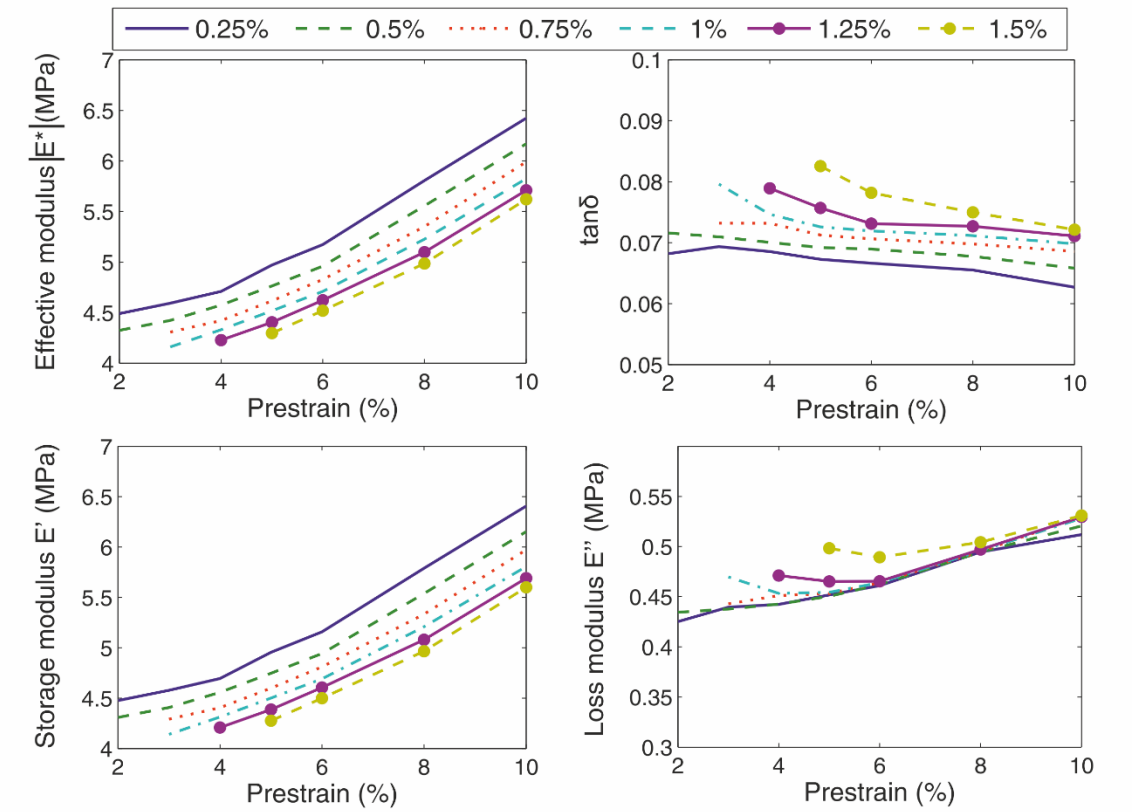

Figure 30: Absolute modulus $|E^*|$, tanδ, storage E' and loss E'' modulus in respect to prestrain at different load amplitudes for isotropic MRE with small particles (at 0 T and 5 Hz).

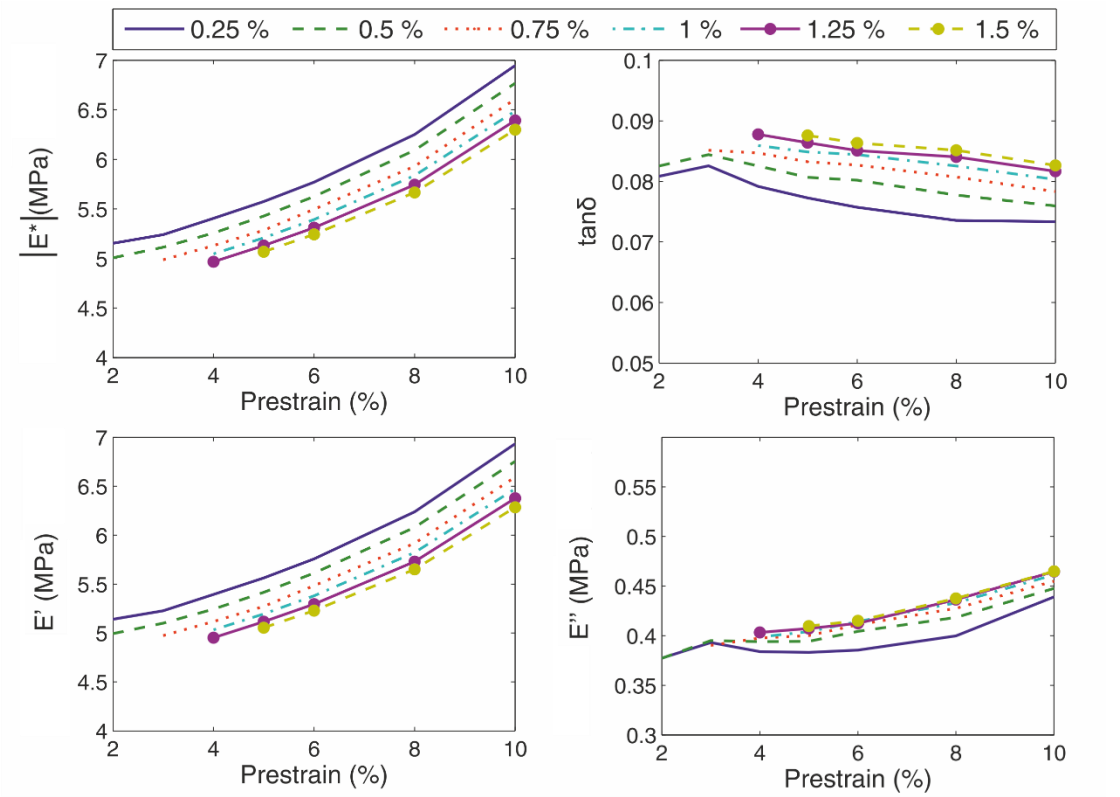

Figure 31: Absolute modulus $|E^*|$, tanδ, storage E' and loss E'' modulus in respect to prestrain at different load amplitudes for isotropic MRE with large particles (at 0 T and 5 Hz).

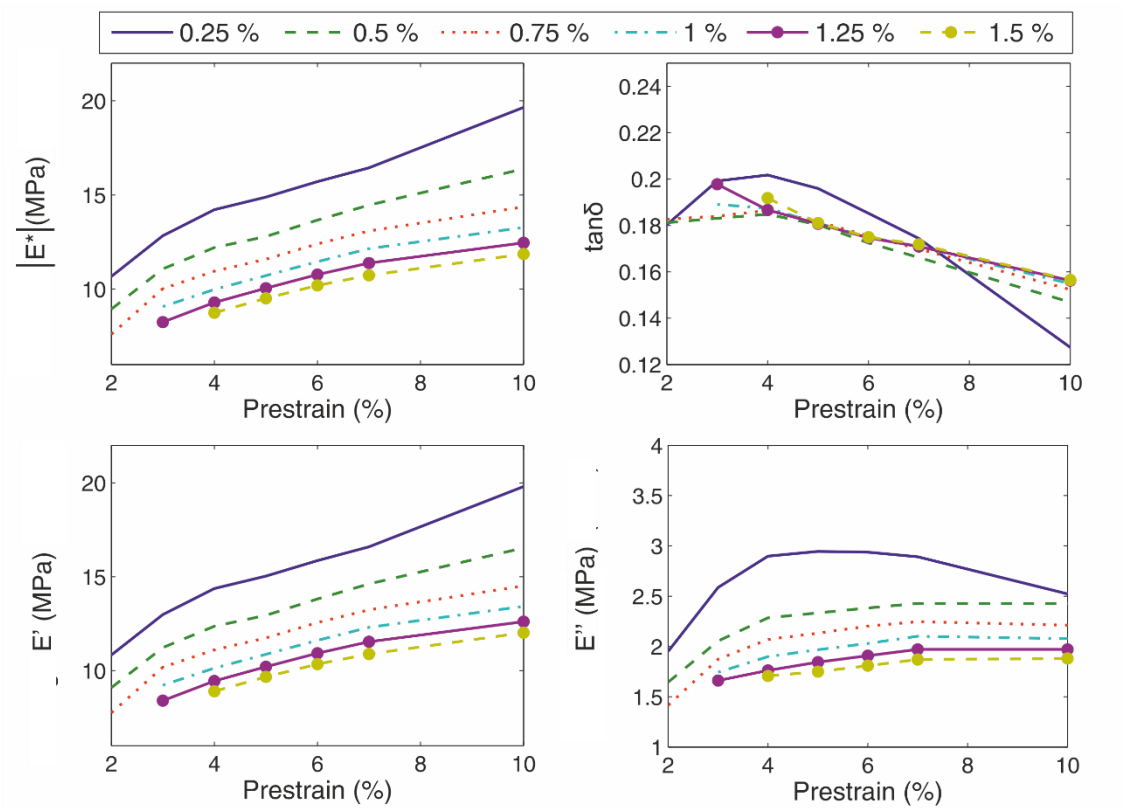

Figure 32: Absolute modulus $|E^*|$, tanδ, storage E' and loss E'' modulus in respect to prestrain at different load amplitudes for anisotropic MRE with small particles (at 0 T and 5 Hz).

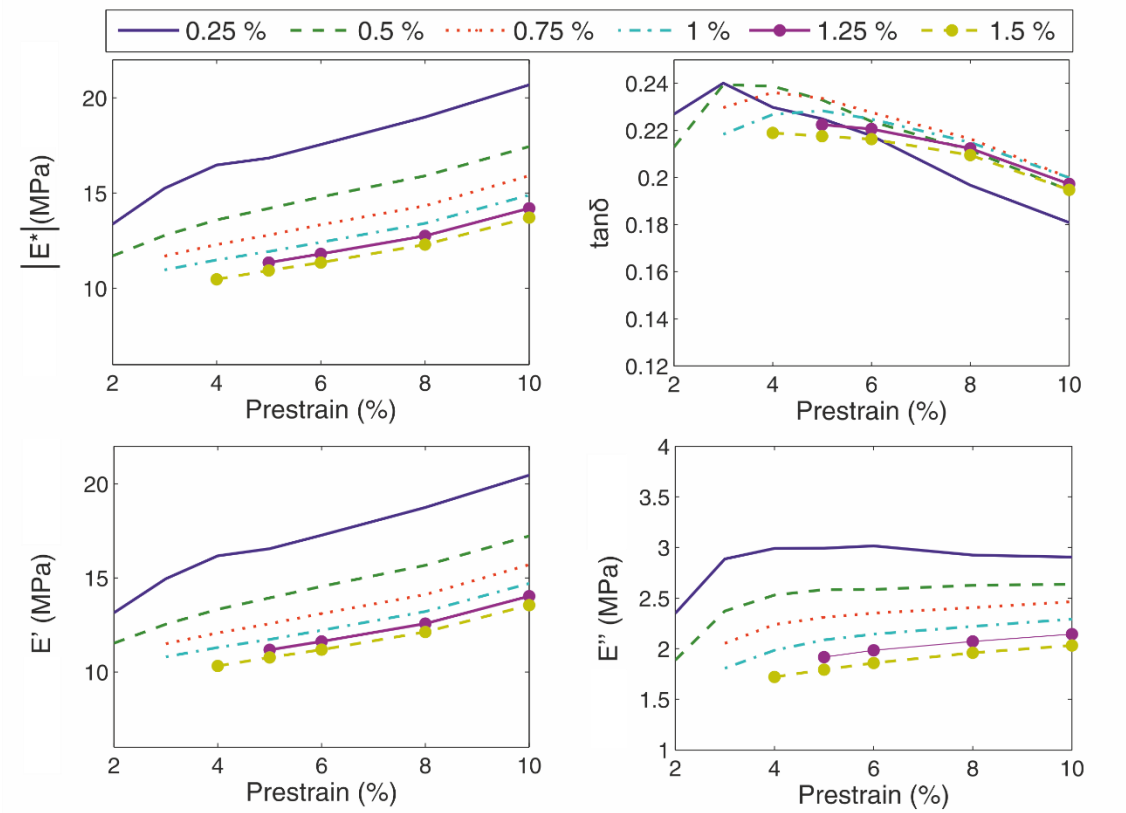

Figure 33: Absolute modulus $|E^*|$, tanδ, storage E' and loss E'' modulus in respect to prestrain at different load amplitudes for anisotropic MRE with large particles (at 0 T and 5 Hz).

4.5 Influence of magnetic field

Relative MR effect

When an external magnetic field is applied to the MREs, the particles get magnetised and start to interact with each other. The developed magnetic forces cause the particles to move inside the matrix in order to align parallel to the direction of the magnetic field. This phenomenon leads to a significant increase of dynamic stiffness (expressed by storage E' and absolute modulus $|E^*|$) of all samples, as it can be seen in Table 15. The highest MR effect of 32% is observed for the anisotropic MRE with small particles (sample anisotropic a-s), while the lowest of 17% for the isotropic MRE with large particles (sample isotropic a-l), when the field is increased from 0 to 0.5T. Isotropic MRE with small particles and anisotropic MRE with large particles have similar MR effects of about 22%. Anisotropic MREs have higher MR effect than their equivalent isotropic samples, due to the original particle chain structure that allows for the formation of greater particle to particle magnetic coupling forces when an external magnetic field is applied (Sorokin V V 2014). In another perspective, anisotropic MREs have higher relative permeability μ than isotropic MRE (Harrison, Equi-biaxial tension tests on magnetorheological elastomers 2016) and thus, a stronger magnetic field is created inside the material when the same external field is applied.

Table 15: Absolute increase/decrease and relative MR effect of isotropic and anisotropic MREs with small and large particles.

Sample	**Absolute difference**				**MR effect**				Increase in magnetic field
	$\|E^*\|$ (MPa)	tanδ	E' (MPa)	E'' (MPa)	$\|E^*\|$ (%)	Tanδ (%)	E' (%)	E'' (%)	
Isotropic a-l	0.42	0.03	0.42	0.307	6.2	5.1	6.2	7.3	*0.3 T*
	1.18	-0.03	1.18	0.47	17.4	-5.0	17.4	11.2	*0.5 T*
Anisotropic a-l	*2.30*	*0.002*	*2.22*	*0.63*	*13.2*	*1.0*	*13.0*	*18.8*	*0.3 T*
	3.83	*-0.01*	*3.76*	*0.54*	*22.0*	*-5.3*	*22.1*	*16.0*	*0.5 T*
Isotropic a-s	0.35	0	0.35	0.02	5.7	0	5.7	5.0	*0.3 T*
	1.31	-0.003	1.31	0.06	21.2	-5.0	21.3	15.0	*0.5 T*
Anisotropic a-s	*1.6*	*0.003*	*1.57*	*0.185*	*9.7*	*1.6*	*9.7*	*8.0*	*0.3 T*
	5.19	*-0.026*	*5.19*	*0.267*	*31.6*	*-17.2*	*32.0*	*11.5*	*0.5 T*

The magnetic field-dynamic stiffness relationship is not linear for all four samples thus, both isotropic and anisotropic samples with large particles have higher MR effect than the equivalent samples with small particles when measured from 0T to 0.3T magnetic field. large particles develop greater magnetic forces between each other and therefore have more energy to move inside the matrix elastomer to align themselves parallel to the external field, which also explains the higher values of loss modulus E'' (indicates how much energy is consumed). As the external magnetic field increases, the magnetic forces between particles increase but large particles cannot overcome the resistance of the elastomer matrix structure as they cannot push over the long molecules of the polymer. However, small particles do not face such problems and can pass through the molecules much easier. As they approach each other, their magnetic coupling moments grow resulting to a greater increase in dynamic stiffness (storage modulus E') when the field is increased from 0.3T to 0.5T than from 0T to 0.3T.

Storage E' and loss E'' moduli both increase with the application of the magnetic field but in different rates, causing tangent of loss angle tanδ to slightly increase for low values of magnetic fields while it decreases for higher values. The latter indicates that as the magnetic field increases the energy is stored than lost and thus, damping efficiency decreases. For anisotropic MRE sample with small particles storage modulus E' increases almost 3 times more than loss modulus E'', when the field goes from 0T to 0.5T, causing tangent of loss angle tanδ to decrease by 18%. However, when it comes to absolute increase/decrease values this variation is not important and it can be generally assumed that the damping capability of MREs is not greatly influenced by the magnetic field.

Magnetic field-load amplitude and frequency interaction

To provide a better understanding on how the dynamic properties of MREs are influenced by the magnetic field, the magnetic field-strain amplitude interaction is examined. Figure 34 illustrates the MR effect of absolute $|E^*|$, storage E' and loss E'' moduli of elasticity with the tangent of loss angle tanδ in respect to strain amplitude. Regarding storage modulus E' and absolute modulus $|E^*|$, a weak field-amplitude coupling effect is observed for both isotropic samples and the anisotropic sample with large particles. For these samples, MR effect of storage modulus E' decreases by 4% when strain amplitude increases from 0.25% to 2% for both values of the magnetic field. However, a strong strain amplitude – MR effect of storage modulus E' is observed for the anisotropic a-l MRE with large particles.

This is attributed to the destruction of matrix structure mechanism occurring with increasing amplitude (Payne effect) that also affects the position of the iron particles. The result of Payne effect on matrix-particles structure could explain the increase of loss modulus E'' MR effect with increasing amplitude, since more energy must get dissipated for the particles to overcome the matrix elastomer resistance and align themselves parallel to the magnetic field. However, MR effect of loss E'' and storage E' modulus of anisotropic MRE with large particles is not influenced by increasing strain amplitude in contrast to the anisotropic MRE with small particles. In this case, as amplitude increases the realigned large iron particles could start getting even closer to each other that leads to stronger magnetic forces between larger iron particles that keep them in place. For the anisotropic sample with small particles, Payne effect could destroy the original chain like structure of the particles inside the matrix making the MRE more isotropic like and thus decreasing the MR effect.

Figure 35 present the MR effect of absolute $|E^*|$, storage E' and loss E'' moduli of elasticity with the tangent of loss angle tanδ in respect to load frequency for isotropic and anisotropic MRE with small and large particles. MR effect of both storage E' and loss E'' moduli does not appear to vary greatly with increasing load frequency for all MRE samples. The slight variation of loss modulus E'' observed at low frequencies is neglected since the absolute value of E'' corresponding to 5% MR effect is very small and lie between the limits of measurement error. Therefore, it is considered that magnetorheological effect is not influenced by loading frequency for all MREs that agrees with the results already published at the literature (Xin F L 2016), (Sorokin V V 2014).

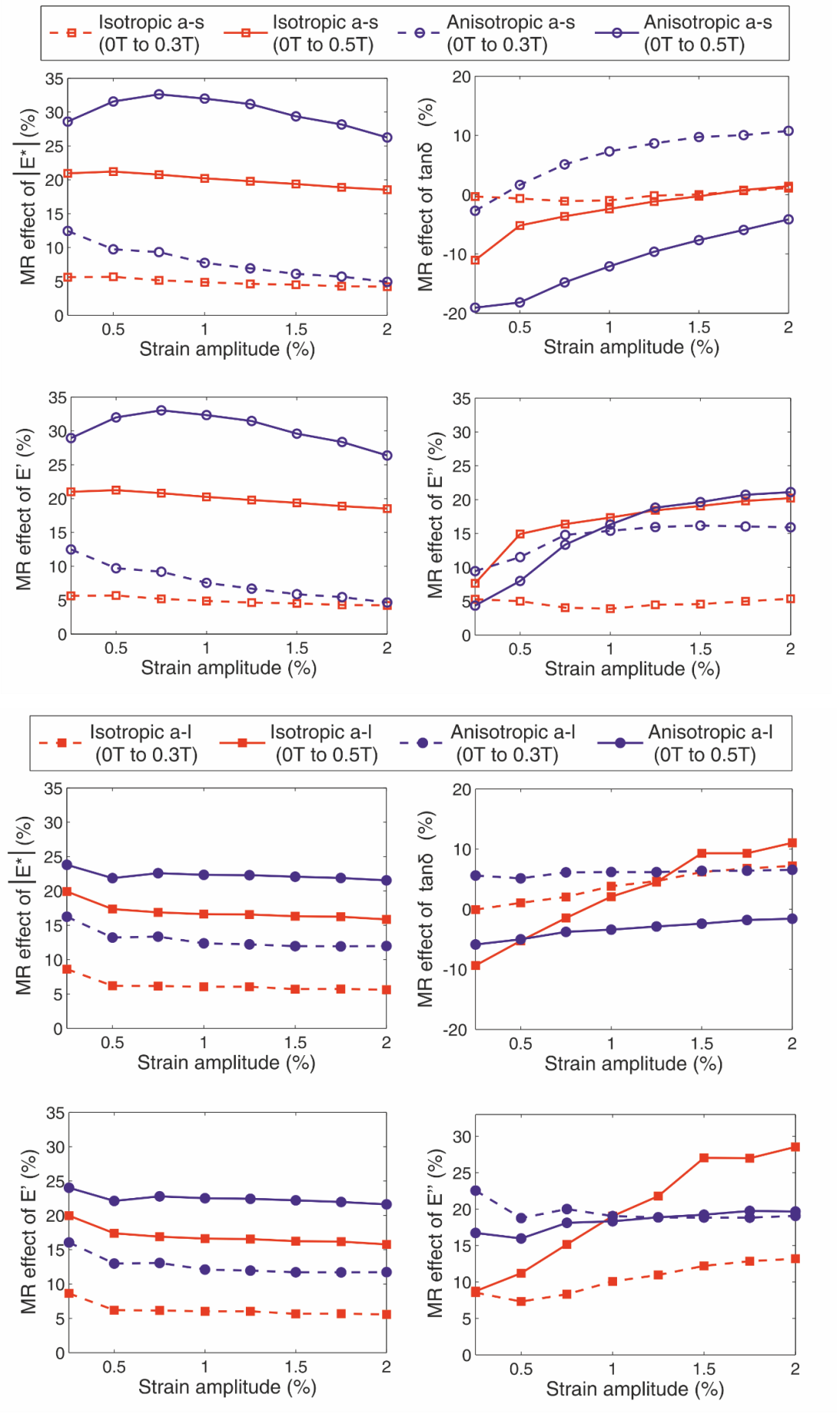

Figure 34: Relative MR effect of $|E^*|$, tanδ, E' and E'' in respect to strain amplitude (at 5Hz frequency and 10% prestrain).

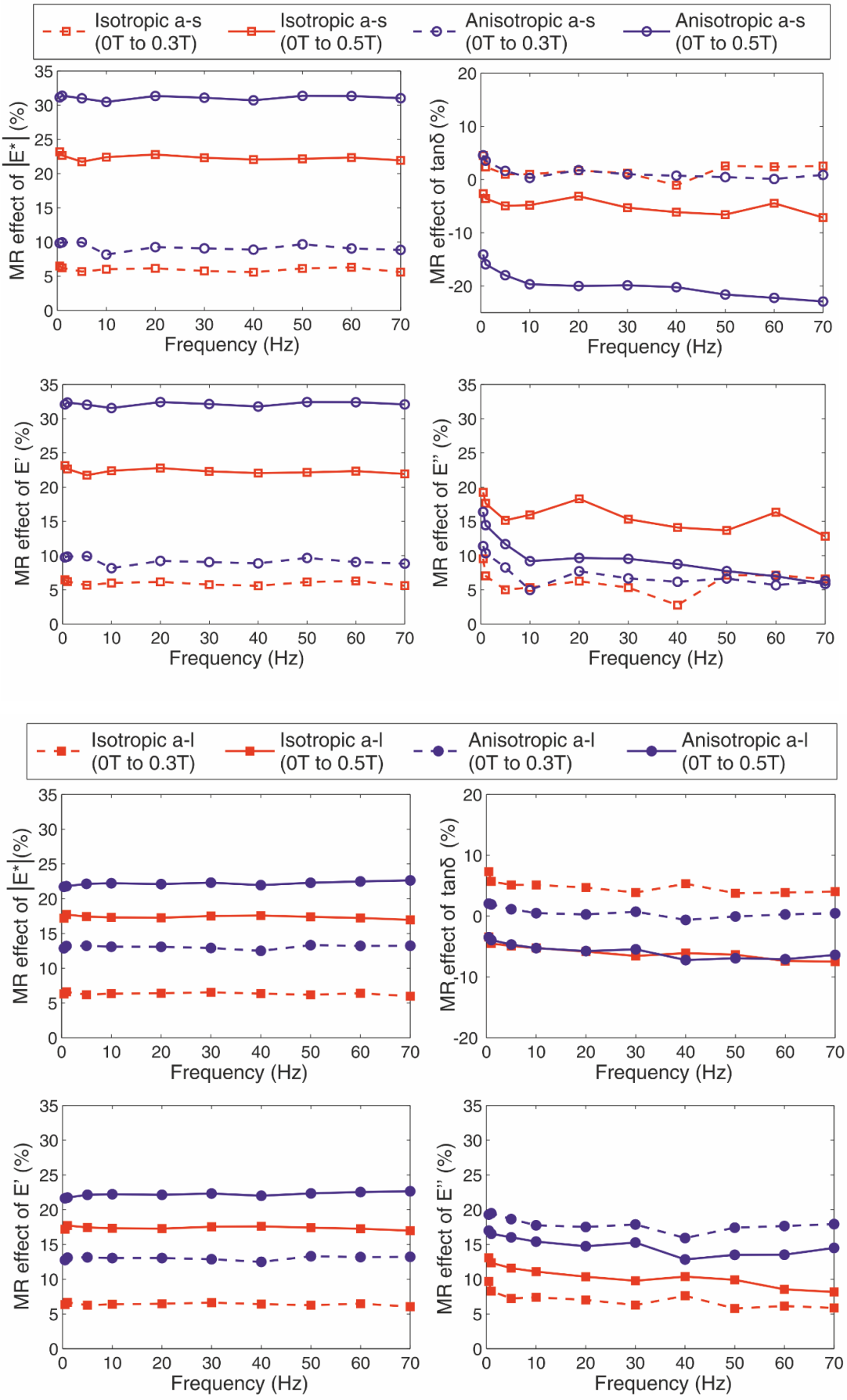

Figure 35: Relative MR effect of $|E^*|$, tanδ, E' and E'' in respect to frequency of all MRE samples (at 0.5% strain amplitude and 10% prestrain).

Magnetic field-static prestrain interaction

The static prestrain-magnetic field coupling effect (MR effect from 0T to 0.5T) is illustrated at Figure 36 for all MRE samples. For isotropic samples, MR effect of storage E' and loss E'' moduli increase both by 10% from 3% to 10% prestrain values so MR effect of tanδ is not influenced. For anisotropic MRE with large particles storage E' and loss E'' modulus MR effect decrease by 5% and 10 % respectively with increasing prestrain causing MR effect of tangent of the loss angle to decrease by 8%. On the other hand, MR effect of anisotropic MRE sample with small particles increases at small prestrain values to decrease later which agrees with the data published by Feng et al (Feng J 2015) for the same type of samples.

According to Feng et al (Feng J 2015), the variation of MR effect with increasing prestrain is due to movement of particles inside the matrix that alter the gap between them. As amplitude increases, particles come closer together and MR effect increases due to stronger magnetic forces between particles. After a point the particles start touching each other and MR effect decreases. A similar approach could explain the behaviour of isotropic MREs where it can be assumed that due to the original random position of particles they do reach the point of touching each other for the 3% to 10% prestrain range. In the case of the anisotropic a-l MRE, the large particles could start touching each other at lower prestrain values than anisotropic MRE with small particles thus, MR effect decreases during the prestrain range.

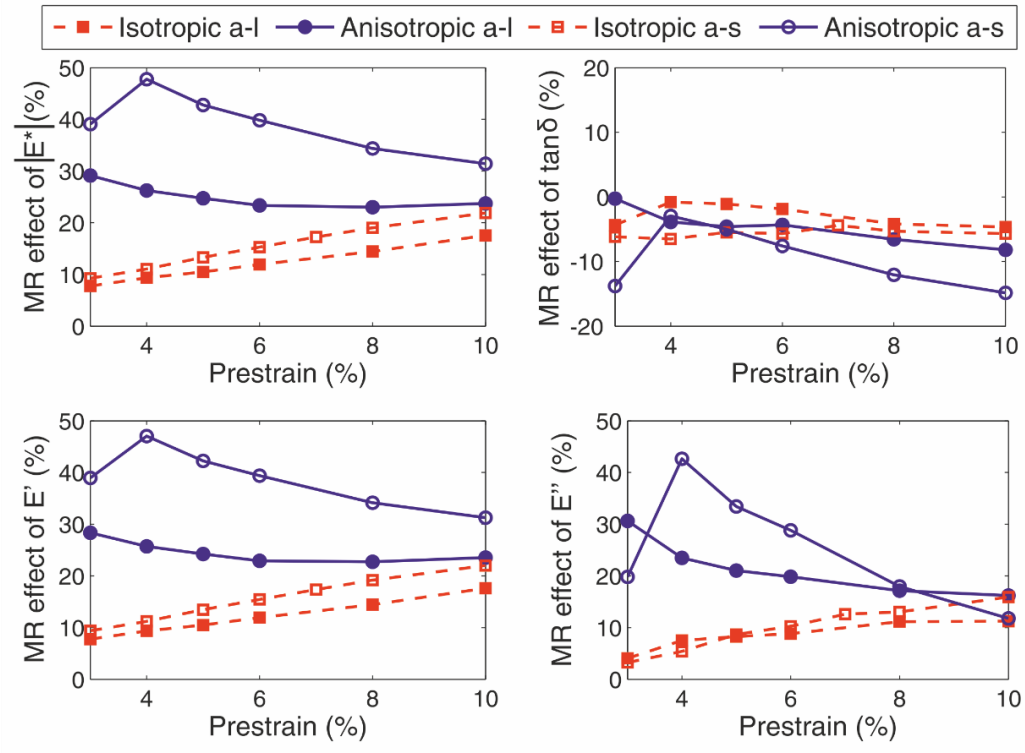

Figure 36: MR effect (from 0T to 0.5T) of $|E^*|$, tanδ, E' and E'' for all samples in respect to prestrain (at 0.5% strain amplitude and 5Hz frequency).

4.6 Influence of size and shape

Zero field dynamic mechanical properties

Disk, square, rectangular and ring shaped isotropic MR elastomers with different dimensions were manufactured to examine the influence of size and shape on dynamic stiffness and damping. Isotropic MREs with small particles (diameter 4-6 μm) were only considered in this study. Anisotropic MREs were not considered because it was impossible to ensure that all samples would cure under the same magnetic field and therefore, have comparable dynamic mechanical properties. It must be noted that all MRE isotropic samples mentioned in this section are of the same batch to avoid variability of measured stiffness mentioned in section (3.2.3). The results of the dynamic tests on disk and ring shaped MREs, under a compressive load of 5 Hz frequency, 0.5% strain amplitude and 10% prestrain are presented in Table 16.

Table 16: Characteristics of disk and ring MRE samples of height h, diameter D and inner diameter din (ring samples).

sample	h (mm)	D (mm)	S	$\|E^*\|$ (MPa)	$tan\delta$	$\|K^*\|$		Error of $\|K^*\|$	
						predicted	measured	absolute	%
a_1	6.25	29	1.17	11.93	0.076	623	1271	648	104%
a_2	12.5	29	0.56	6.1	0.068	311	310	0	0%
a_3	21	29	0.34	4.01	0.066	185	124	-61	-33%
a_4	12.5	56.5	1.14	6.6	0.064	1223	1343	120	10%
a_5	10.5	15.5	0.37	6.35	0.1	109	118	-8	-7%
a_6	14.5	41.5	0.7	5.82	0.074	569	534	-35	-6%
a_7	12.5	18.5	0.37	6.34	0.095	131	136	5	4%
r_1	16.5	Din= 23.5 D=54.5	0.5	6.21	0.073	702	720	-18	-3%
r_2	10.5	Din= 19.5 D=32.5	0.3	6.35	0.076	308	331	23	7%

The predicted dynamic stiffness refers to the stiffness calculated using the moduli of elasticity and tangent of the loss angle (E*=6.1MPa and tanδ=0,068) of the sample a_2 with the dimensions indicated by the BS ISO 4664:2011 standard, while the measured stiffness refers to the one really measured in the laboratory. It becomes obvious that the error between predicted and measured

stiffness is greater for relative thin samples. Keeping sample a_2 as a reference, dynamic stiffness is underestimated when height decreases (sample a_1) and is overestimated when it increases (sample a_3). When the height H remains the same but the diameter varies (samples a_2, a_4 and a_7), the measured dynamic stiffness is close to the predicted values. However, the same does not apply for tangent of loss angle tanδ since samples a_5 and a_7 that have a higher tanδ than the rest samples. For ring shaped MREs, the measured values of stiffness are very close to the calculated values because the shape factor is close to the one of reference sample a_2.

The storage E' and loss E'' moduli of elasticity (at 5 Hz frequency, 0.5% strain amplitude and 10% prestrain) in respect to shape factor S of all disk and ring MREs are illustrated in Figure 37. Both moduli of elasticity E' and E'' of samples a_1, a_2 and a_3 (that have same diameter) increase linearly with sample height. Samples a_2, a_4 and a_7 with the same height but different diameters have similar storage modulus E' like the rest of thick samples a_5 and a_6. However, samples a_7 and a_5, with the same shape factor S, have a higher loss modulus E'' that explains the higher values of tanδ mentioned in Table 16. Storage modulus E' and loss modulus E'' of ring samples r_1 and r_2 are very close to reference sample a_2.

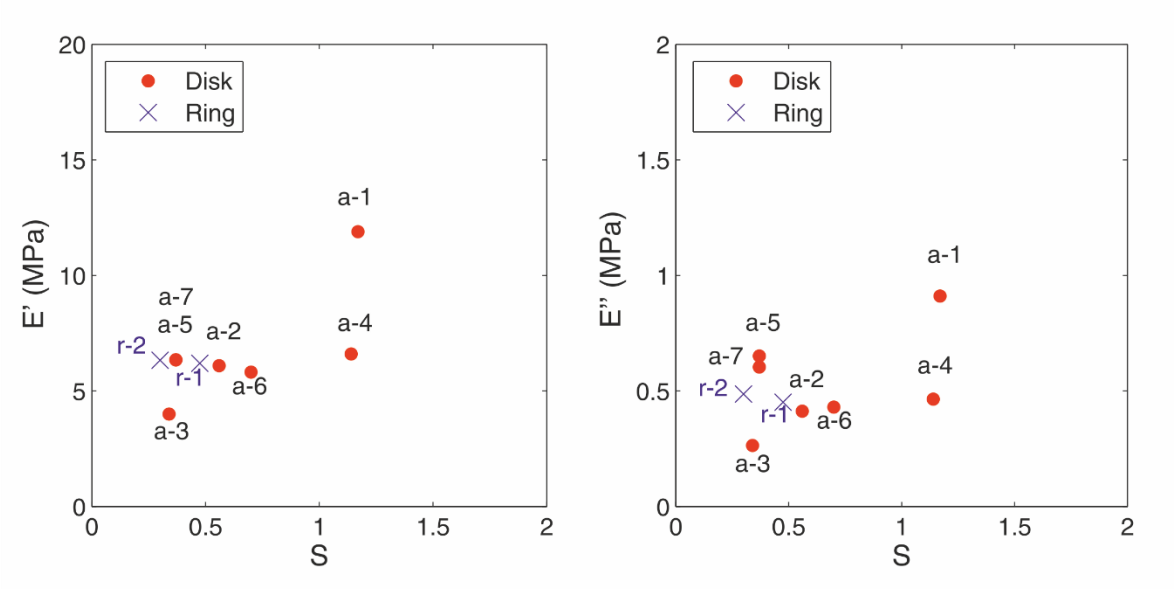

Figure 37: Dynamic moduli of elasticity E' and E'' of disk and ring isotropic MREs in respect to Shape Factor S (measured at 0.5% strain amplitude, 5Hz frequency and 10% static prestrain)

Similar results were observed for the square and rectangular MRE samples mentioned in Table 17. Again, the calculated dynamic stiffness of thin samples is underestimated (samples b_1, b_4, c_1 and c_2) while it is overestimated for long samples (sample b_3). The predicted dynamic stiffness of sample b_2 is very close to the measured one since it has similar shape factor S with reference sample a_2. Storage E' and loss E'' moduli of elasticity (at 5 Hz frequency, 0.5% strain amplitude and 10% prestrain) in respect to shape factor S are illustrated in Figure 38. Like disk samples, storage E' and loss modulus E'' values of square samples b_1, b_2 and b_3 (that have same side but

different heights) increase linearly with height while thin sample b_4 behaves differently. For rectangular samples, storage E' and loss modulus E'' values seem to increase linearly with shape factor while again, dynamic stiffness is underestimated for thin long samples.

Table 17: Characteristics of square and rectangular MRE samples of height h and sides H1 and H2.

sample	h (mm)	H1 (mm)	H2 (mm)	S	$\|E^*\|$ (MPa)	$tan\delta$	$\|K^*\|$		Error of $\|K^*\|$	
							predicted	measured	absolute	%
b_1	6.25	22	22	0.8	9.23	0.079	472	666	194	41%
b_2	10.5	22	22	0.5	6.66	0.074	284	299	18	6%
b_3	22	22	22	0.25	5.04	0.075	134	109	-25	-18%
b_4	5.5	34	34	1.6	14.5	0.08	1282	3070	1788	140%
c_1	5.5	34	20	1.2	7.33	0.075	790	950	160	20%
c_2	6.25	30	60.5	1.6	16.38	0.076	1771	4782	3011	170%
c_3	10.5	41	59.5	1.15	6.7	0.077	1417	1557	140	10%

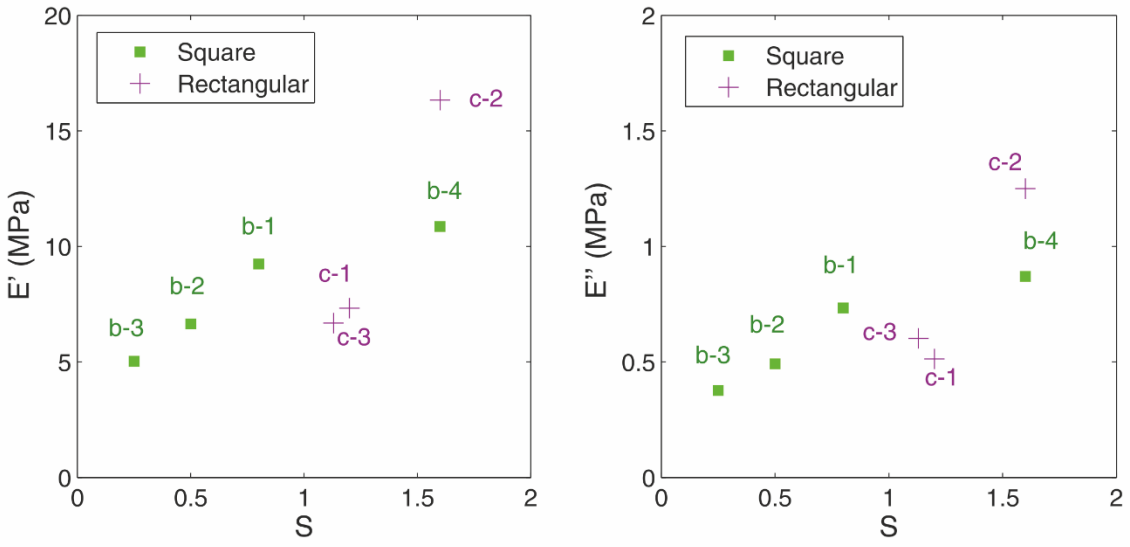

Figure 38: Dynamic moduli of elasticity E' and E'' of square and rectangular isotropic MREs in respect to shape factor S (measured at 0.5% strain amplitude, 5Hz frequency and 10% static prestrain).

All samples of same height disk a_5, ring r_2, square b_2 and rectangular c_3 have a low error percentage of dynamic stiffness although their shape factor is different. Therefore, their dynamic stiffness could be predicted by using the value of reference sample a_2 without needing a correction function. However, the same does not apply for thin samples disk a_1, square b_1 and rectangular c_2 where the error percentage of dynamic stiffness increases significantly with shape

factor. A correction function that depends on shape and shape factor should be considered for thin samples especially since for most practical application MREs would have a low height to ensure that the gap of the magnetic circuit would be as small as possible to be able to generate high magnetic flux values.

The variation of real K' and imaginary K'' components of dynamic stiffness in respect to strain amplitude and frequency for samples disk a-5, rectangular b-2, ring r-2, disk a-7 and reference sample a-2 are presented in Figure 39. Real K' and imaginary K'' components of dynamic stiffness in respect to strain amplitude and frequency of much stiffer samples disk a-1, disk a_4, rectangular c-3, square b-1 and ring r-1 is presented in Figure 40. All samples drop their real dynamic stiffness K' with increasing strain amplitude while the imaginary part K'' does not change like reference sample a-2. In a similar manner, all samples increase slightly their real dynamic stiffness K' with increasing frequency while, imaginary part of dynamic stiffness K'' increases for values up to 10Hz to decrease for later values. Therefore, the shape and size of the MRE does not influence the variation of dynamic stiffness with load amplitude and frequency.

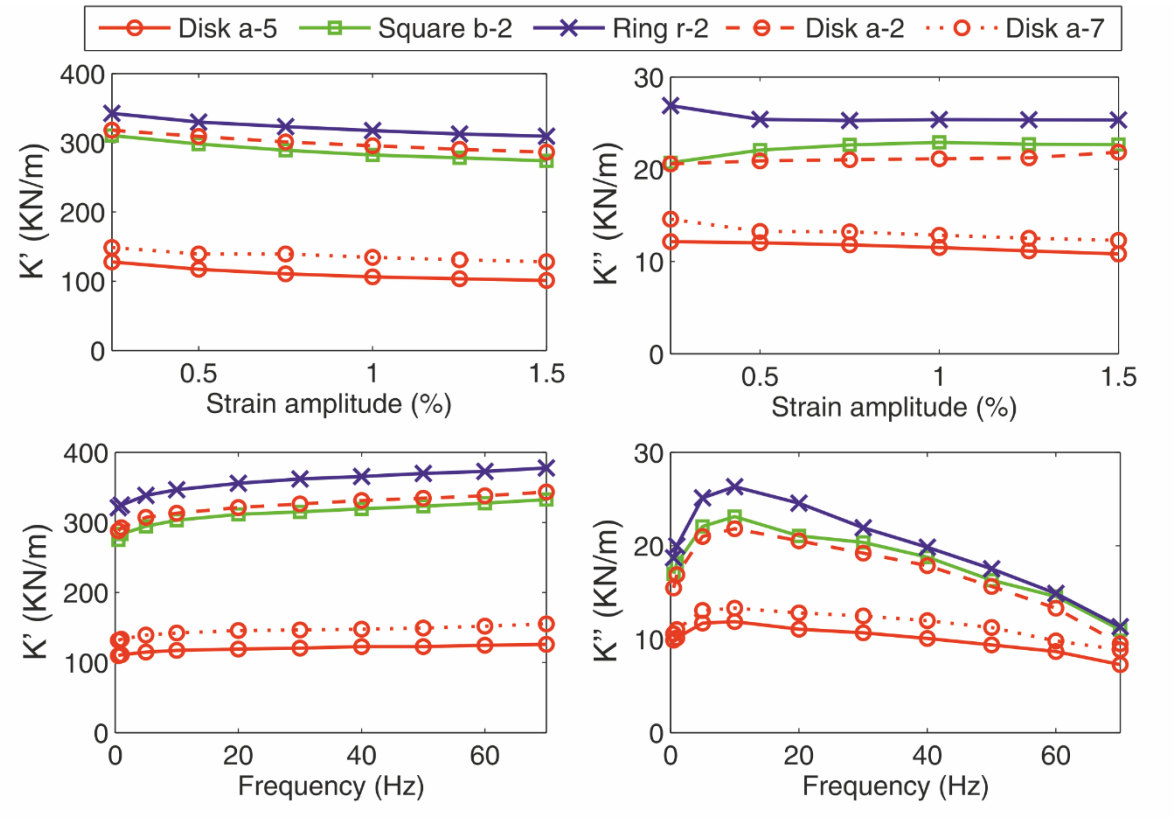

Figure 39: Zero field real K' and imaginary K'' components of dynamic stiffness for disc, rectangular and ring isotropic MRE samples with similar height in respect to strain amplitude (at 5Hz frequency and 10% static prestrain) and frequency (at 0.5%

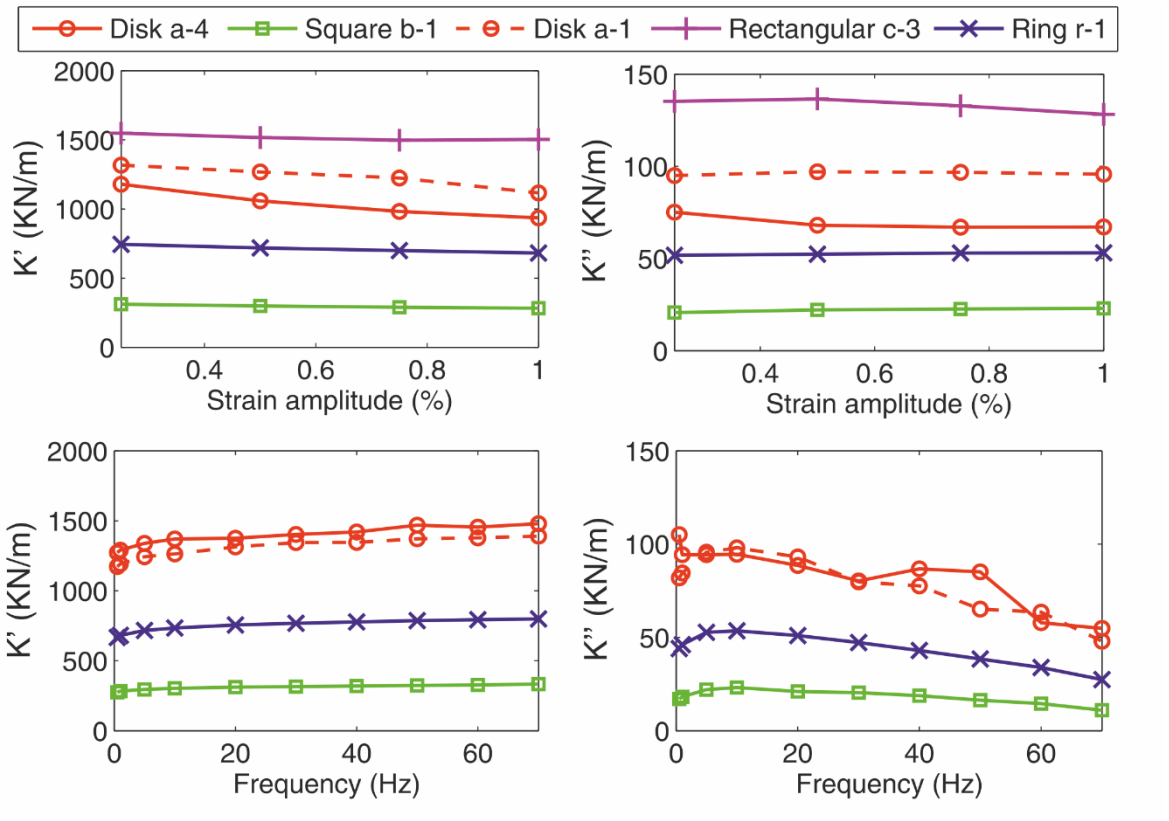

Figure 40: Zero field real K' and imaginary K'' components of dynamic stiffness for a-4, b-1, a-1, c-3 and r-1 samples in respect to strain amplitude (at 5Hz frequency and 10% static prestrain) and frequency (at 0.5% amplitude and 10% static prestrain).

Magnetorheological effect

The measured real K' and imaginary K'' dynamic compression stiffness of disk samples a-1,a-2, a3, square samples b-1,b-2, b3, ring sample r-2 and rectangular sample c-1 at zero field $K(0)$ as well as the absolute $K(B_x) - K(0)$ and relative $\frac{K(B_x)-K(0)}{K(0)}$ percentange increase (MR effect) when the samples are placed between a double pair of magnets are reported at Table 18. Since the samples are of different heights, the magnetic flux B_x created from the permanent magnets will be different for each sample resulting to a different MR effect. To be able to make safe conclusion on how the MRE sample size and shape influences MR effect, the term relative MR effect per 0.1T is used instead, assuming linear magnetic flux-MR effect behaviour.

Disk shaped MREs a_2, square sample b_2 and ring sample r_2 have the same real dynamic stiffness K' relative MR effect of 5% per 0.1T. However, thin samples disk a_1, square b_1 and ring r_1 have a 0.5% higher MR effect/0.1T while long samples a_3 and b_3 show a lower MR effect/0.1T due to the prestrain – MR effect coupling effect. The attraction force developed between the pair of permanent magnets is equivalent to an additional static compression force given by equation (3.2.1). The attraction forces are stronger when the magnets are close together thus, thin samples

are pre-compressed under a higher static force than the rest. Since isotropic MREs increase their MR effect with increasing static prestrain (section 5.5), the MR effect/ 0.1T for these samples also increases. The small variations recorded for the imaginary dynamic stiffness K'' are attributed to measurement error since the absolute increase is very low.

Table 18: Absolute and relative MR effect of isotropic MREs under a double pair of magnets.

Samples	Zero field		MR effect				B_x (T)	Relative MR effect per 0.1T	
			Absolute		Relative				
	$K(0)$ (KN/m)		$K(B_x)-K(0)$ (KN/m)		$\frac{K(B_x)-K(0)}{K(0)}$			$\frac{K(B_x)-K(0)}{K(0)} / 0.1T$	
	K'	**K''**	**K'**	**K''**	**K' (%)**	**K'' (%)**	**T**	**K' (%)**	**K'' (%)**
a_1	1267	97	348	17	28	17	0.5	5.5%	3.5%
a_2	309	21	68	3	22	14	0.42	5%	3.5%
a_3	123	8.1	19	1.1	15	14	0.33	4.5%	4%
b_1	665	53	179	9.5	27	18	0.5	5.5%	3.6%
b_2	298	22	66	4	22	18	0.44	5%	4%
b_3	108	7	14	0.85	13	12	0.31	4%	4%
r_2	330	25	70	4	21	16	0.44	5%	4%
c_1	946	68	255	15	27	20	0.51	5.5%	4%

The relative MR effect of real K' and imaginary K'' dynamic stiffness in respect to strain amplitude of disk samples a-1, a-2, a3, square samples b-1, b-2, b3, ring sample r-2 and rectangular sample c-1 are presented in Figure 41. The relative MR effect of real dynamic stiffness K' decreases with increasing strain amplitude in contrast to the relative MR effect of imaginary dynamic stiffness K'' that increases for all samples. Samples a-2, b-2 and r-2 have similar values of MR effect because they are of approximately the same height and thus, they are under a similar magnetic field. Therefore, shape and size does not influence the magnetic field- strain amplitude coupling effect. However, it should be noted that for most practical applications MRE samples would not be higher than 6mm for any magnetic circuit to be able to provide magnetic fields up to 0.5T.

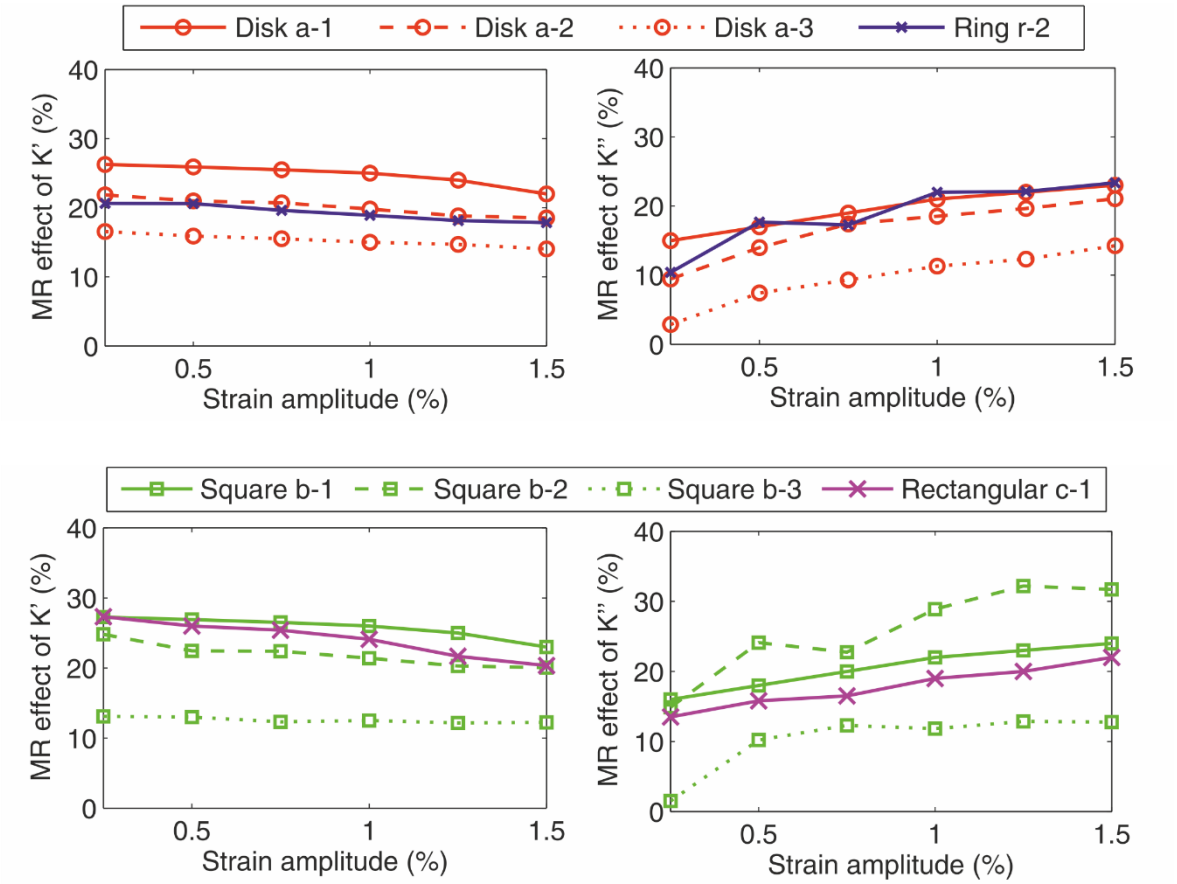

Figure 41: Relative MR effect of real K' and imaginary K'' dynamic stiffness of disk, square, rectangular and ring MRE samples under a double pair of permanent magnets (at 0.5% strain amplitude, 5Hz frequency and 10% static load).

4.7 Chapter summary

The main purpose of this chapter was to understand how the dynamic mechanical properties of isotropic and anisotropic MREs with small and large particles vary with strain amplitude, frequency, static prestrain and magnetic field intensity. In summary, the following conclusions are made:

Zero field dynamic mechanical properties

- Anisotropic MREs are three times stiffer and have two times higher damping capability than isotropic MREs. Dynamic compression modulus and tanδ of Isotropic sample with large particles are 10% higher than those of the isotropic sample with small particles, while for the anisotropic equivalents these number are 7% and 30% respectively.
- Storage E' and loss E'' moduli of all samples decrease with increasing strain amplitude. Storage modulus E' increases with increasing frequency while loss modulus E'' increases until about 10 Hz after which it decreases rapidly. No strain amplitude-frequency coupling effects were observed.
- Anisotropic MREs increase their storage E' and loss modulus E'' by 50% and 30% while isotropic MREs by 25% and 5% respectively when the applied prestrain varies from 2% to 10%. Thus, damping capability decreases with increasing prestrain.
- No static prestrain-dynamic amplitude coupling effects are observed.
- Dynamic stiffness of isotropic MREs depends greatly on the size and thickness of the elastomer but not on shape.

Magnetorheological effect

- The storage E' and loss E'' modulus MR effect are 21% and 15% for isotropic with small particles, 32% and 11 % for anisotropic with small particles, 17% and 11% for isotropic with large particles and 22% and 16% for anisotropic with large particles respectively.
- A strong MR effect-strain amplitude coupling effect is observed. MR effect of storage modulus E' decreases with increasing strain amplitude while MR effect of loss modulus E'' increases but at a different rate for each sample.
- MR effect does not vary with load frequency.
- For isotropic MREs, MR effect of both moduli increases linearly by 100% in the 3% to 10% static prestrain range. For anisotropic MRE with large particles MR effect of storage E' and loss E'' modulus decreases nonlinearly from 29% to 22% and from 30% to 18% respectively. For anisotropic MRE with small particles MR effect of storage E' and loss E'' modulus increase for prestrains up to 4% and then drop from 48% to 32% and 42% to 12% respectively.
- For isotropic MRE, MR effect is not influenced by the sample size and shape.

Chapter 5: Mechanical properties of composite MREs

5.1 Introduction

In practice, dynamic stiffness and damping of any elastomer can be increased by adding an amount of carbon black, varying from 10 to 50% per volume fraction, before curing. The same principle, regarding particle concentration, applies generally for MREs but with again another restriction. It has been well established that the maximum MR effect in silicon MREs is achieved when the particle/matrix material ratio is about 30% per volume or 70% per weight. Therefore, the optimum particle concentration for silicon MREs is fixed and the zero-field dynamic stiffness and damping cannot be adjusted without compromising MR effect. Another way to improve the isolation characteristics of isolators with high damping rubbers at high frequencies, is to place a second rubber with lower damping factor and stiffness in parallel. The combined elastomer will have lower stiffness but similar damping capability than the high damping rubber itself. This chapter examines the principle of combining isotropic and anisotropic MR elastomers in one composite, to adjust the zero-field dynamic properties of silicon MREs without compromising MR effect and make a composite anisotropic MRE (with particles aligned in different directions) with similar mechanical properties in those directions.

The experimental results of the static and dynamic compression tests in pure and composite MRE samples are presented in two parts. In the first part, disk-shaped isotropic/anisotropic composite MREs connected in parallel and series configurations were used to examine and compare the mechanical properties of isotropic/anisotropic composite MREs combined in parallel and series configurations. In addition, the possibility of using two MREs made of particles of small (4-6μm) and large (<220 μm) diameter connected in parallel to increase damping capability and how the mechanical properties can be tailored by changing the dimensions of each part is examined. In the second part cube shaped isotropic-anisotropic and anisotropic-anisotropic composite MRE samples were used to study the axial, transverse and longitudinal zero field static stiffness and dynamic stiffness K* of composite samples and verify that the mechanical properties can be estimated using the theoretical equations. Finally, the axial, transverse and longitudinal MR effect of isotropic-anisotropic and anisotropic-anisotropic composite MREs was examined in respect to strain amplitude.

5.2 Background theory

In general, when two different elastomers with complex moduli E_1^* and E_2^* respectively are connected in parallel or series configuration, as illustrated in Figure 42, the resulting elastomer will have a complex modulus E^* between E_1^* and E_2^* depending on the dimension of each part (Davey A B 1965) (similar to the rules of mixtures for composites).

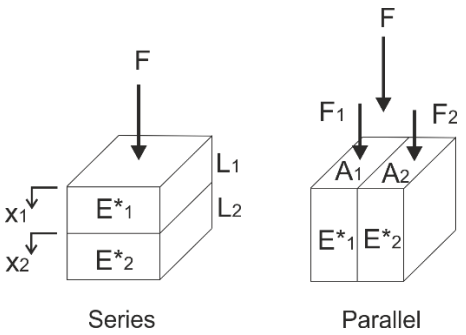

Figure 42: Two elastomers connected in parallel and series configurations

Parallel configuration

When a static compressive stress σ is applied on the composite rubber it will be distributed across the cross-sectional area A_1 and A_2 of each individual rubber.

$$\sigma = \sigma_1 + \sigma_2 = \frac{F}{A_1 + A_2} = \frac{F_1 + F_2}{A_1 + A_2} \tag{5.2.1}$$

The individual stress and force applied in each component is:

$$\sigma_1 = E_1\,\varepsilon \Rightarrow \frac{F_1}{A_1} = E_1\frac{x}{L_1} \Rightarrow F_1 = E_1\frac{A_1\,x}{L_1} \tag{5.2.2}$$

$$\sigma_2 = E_2\varepsilon \Rightarrow \frac{F_2}{A_2} = E_2\frac{x}{L_2} \Rightarrow F_2 = E_2\frac{A_2 x}{L_2} \tag{5.2.3}$$

Where $E_1\ and\ E_2$ are the static compressesion moduli of elasticity of the low loss and high tangent of the loss angle rubbers respectively. The compressive modulus of elasticity E of the composite rubber will be:

$$E = \frac{\sigma}{\varepsilon} = \frac{\frac{F_1 + F_1}{(A_1 + A_2)}}{\frac{x}{L}} = \frac{\frac{A_1E_1x}{L\,(A_1 + A_2)} + \frac{A_2E_2x}{L\,(A_1 + A_2)}}{\frac{x}{L}} = \frac{A_1E_1 + A_2E_2}{(A_1 + A_2)} = \frac{E_1 + aE_2}{1 + a} \tag{5.2.4}$$

Where $a = \frac{A_2}{A_1}$ is the area ratio. When a dynamic stress is applied to the composite rubber the material will have a complex modulus of elasticity E^*. Setting $E_1^* = E'_1 + j\,E''_1$ and $E_2^* = E'_2 + j\,E''_2$ as the complex moduli of elasticity of the low damping and the high damping rubber respectively and substituting to equation (A.4) the total modulus E^* becomes:

$$E^* = \frac{{E_1}^* + a{E_2}^*}{1+a} = \frac{(E'_1 + j\,E''_1) + \alpha(E'_2 + j\,E''_2)}{1+\alpha} = \frac{E'_1 + aE'_2}{1+a} + j\frac{E''_1 + a\,E''_2}{1+a} \quad (5.2.5)$$

The storage modulus E' of the combined rubber is the real part of the complex modulus E^*.

$$E' = \frac{E'_1 + aE'_2}{1+a} \quad (5.2.6)$$

While the loss modulus E'' is the imaginary part.

$$E'' = \frac{E''_1 + a\,E''_2}{1+a} \quad (5.2.7)$$

The tangent of the loss angle of the combined rubber will be:

$$tan\varphi = \frac{E''}{E'} = \frac{E''_1 + a\,E''_2}{E'_1 + a\,E'_2} \quad (5.2.8)$$

Series configuration

In the case where the two rubbers are combined in series the resulting static compression modulus is calculated as follows. When a stress σ is applied on the combined rubber the resulting strain ε will be the sum of the individual strains $\varepsilon_1, \varepsilon_2$ of each rubber component.

$$\varepsilon = \varepsilon_1 + \varepsilon_2 = \frac{x}{L_1 + L_2} = \frac{x_1 + x_2}{L_1 + L_2} \quad (5.2.9)$$

The individual strains $\varepsilon_1, \varepsilon_2$ and displacements x_1, x_2 in each component are:

$$\sigma = E_1\varepsilon_1 \Rightarrow \frac{F}{A} = E_1\frac{x_1}{L_1} \Rightarrow x_1 = \frac{F}{A}\frac{L_1}{E_1} \quad (5.2.10)$$

$$\varepsilon_2 = E_2\sigma \Rightarrow \frac{F}{A} = E_2\frac{x_2}{L_2} \Rightarrow x_2 = \frac{F}{A}\frac{L_2}{E_2} \quad (5.2.11)$$

Where $E_1\ and\ E_2$ are the static compression moduli of elasticity of the low and high damping rubbers and $L_1\ and\ L_2$ the individual lengths respectively. The static compression modulus of elasticity E of the combined rubber will be:

$$E = \frac{\sigma}{\varepsilon} = \frac{\frac{F}{A}}{\frac{x_1 + x_2}{L_1 + L_2}} = \frac{\frac{F}{A}}{\frac{F}{A}\frac{L_1}{E_1} + \frac{F}{A}\frac{L_2}{E_2}} = \frac{L_1 + L_2}{\frac{L_1}{E_1} + \frac{L_2}{E_2}} = \frac{(L_1 + L_2)E_1E_2}{L_1E_2 + L_2E_1} = \frac{(b+1)E_1E_2}{bE_2 + E_1} \quad (5.2.12)$$

Where $b = \frac{l1}{l2}$ is the ratio of the length of each rubber. When a dynamic stress is applied to the composite rubber the material will have a complex modulus of elasticity E^*. Setting ${E_1}^* = E'_1 +$

$j\,E''_1$ and $E_2{}^* = E'_2 + j\,E''_2$ as the complex moduli of elasticity of the low and high damping rubber respectively and substituting to equation (5.2.12) the total complex modulus E^* becomes:

$$\begin{aligned}
E^* &= \frac{(b+1)\,E_1{}^* E_2{}^*}{bE_2{}^* + E_1{}^*} = \frac{(b+1)(E'_1 + j\,E''_1)(E'_2 + j\,E''_2)}{b(E'_2 + j\,E''_2) + (E'_1 + j\,E''_1)} \\
&= (b+1)\frac{(E'_1E'_2 - E''_1E''_2) + j(E'_1E''_2 + E''_1E'_2)}{(bE'_2 + E'_1) + j\left(bE''_2 + E''_1\right)} \\
&= \frac{(1+b)}{(bE'_2 + E'_1)}\frac{(E'_1E'_2 - E''_1E''_2) + j(E'_1E''_2 + E''_1E'_2)}{1 + jR} \\
&= \frac{(1+b)}{(bE'_2 + E'_1)}\frac{(1 - jR)[(E'_1E'_2 - E''_1E''_2) + j(E'_1E''_2 + E''_1E'_2)]}{1 + R^2} \\
&= \frac{(1+b)}{(bE'_2 + E'_1)}\left[\frac{R(E'_1E''_2 + E''_1E'_2) - (E''_1E''_2 - E'_1E'_2)}{1 + R^2}\right. \\
&\left. + j\,\frac{R(E''_1E''_2 - E'_1E'_2) + (E'_1E''_2 + E''_1E'_2)}{1 + R^2}\right]
\end{aligned} \tag{5.2.13}$$

Where $b = \frac{l1}{l2}$ is the ratio of the length of each rubber and $R = \frac{E''_1 + bE''_2}{E'_1 + bE'_2}$.

The storage modulus E' of the combined rubber is the real part of the complex modulus.

$$E' = \frac{(1+b)}{(bE'_2 + E'_1)}\frac{R(E'_1E''_2 + E''_1E'_2) - (E''_1E''_2 - E'_1E'_2)}{1 + R^2} \tag{5.2.14}$$

While the loss modulus E'' is the imaginary part:

$$E'' = \frac{(1+b)}{(bE'_2 + bE'_1)}\frac{R(E''_1E''_2 - E'_1E'_2) + (E'_1E''_2 + E''_1E'_2)}{1 + R^2} \tag{5.2.15}$$

The tangent of the loss angle $tan\varphi$ of the combined rubber now becomes:

$$tan\varphi = \frac{E''}{E'} = \frac{R(E''_1E''_2 - E'_1E'_2) + (E'_1E''_2 + E''_1E'_2)}{R(E'_1E''_2 + E''_1E'_2) - (E''_1E''_2 - E'_1E'_2)} \tag{5.2.16}$$

With the storage modulus E’ and loss modulus E’’ known, the absolute value of compression modulus $|E^*|$ can be calculated using equation (5.2.17)

$$|E^*| = \sqrt{E'^2 + E''^2} \tag{5.2.17}$$

5.3 Details of experiment

MRE samples

For the first part of this chapter, we manufactured isotropic-anisotropic composite MRE disk samples with small particles in parallel and series configuration, as illustrated in Figure 43 under the name sample 2a and sample 1a respectively. For the series combination sample 2a, the length of each individual part is 6.25 mm half of the total 12.5 mm height. In the case of the parallel combination disk sample 1a, the inner diameter of the core was varied to give an anisotropic to isotropic part area ratio of 1/3, 2/3, 1 and 3 using both small and large particles, as shown in

Table 19. The outer diameter (d=29mm) and height (H=12.5mm) of all round samples were the same indicated by the BS:ISO 4664:2011 standard.

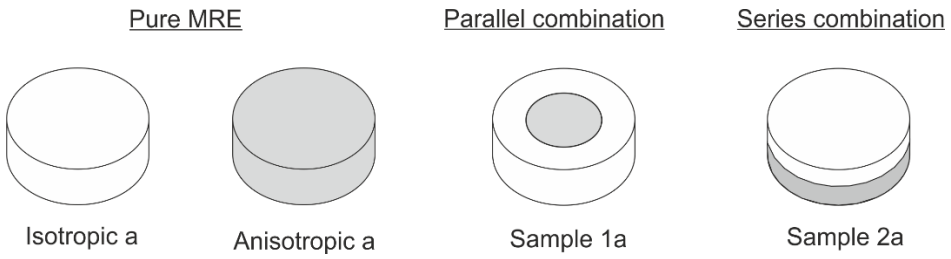

Figure 43: Pure isotropic and anisotropic MREs and isotropic-anisotropic parallel and series configuration composite MREs. The blank discs represent isotropic MREs while the grey anisotropic MREs.

The manufacturing process of the composite MR elastomers involves two stages. For sample 1a, anisotropic discs were first made in the appropriate aluminium moulds following the same process described in section 3.2. After they had cured they were placed inside of another aluminium mould and the isotropic MRE was poured to fill the gaps and left to cure again at room temperature, to achieve perfect adhesion. In a similar way, sample 2a was manufactured by cutting a pure anisotropic sample in the middle, place one half in the bottom of another aluminium mould and pure the isotropic MRE on top of it. All anisotropic parts of these disk samples are of the same height and thus, they were all cured under 0.5T magnetic flux density. The magnetic flux was produced using a set of cylindrical grades N42 neodymium permanent magnets of diameter 40mm and thickness 10mm (explained in detail in section 3.2).

In addition, cube samples of 22mm side combining isotropic and anisotropic MREs in parallel (sample 1b) and series (sample 2b) configurations and two anisotropic halves with particles aligned in different directions (sample 3 and sample 4) were manufactured, as shown in Figure 44. All samples were made using small particles. The cube shape allows for the axial, transverse and

longitudinal static K and dynamic stiffness K* of the composite MREs to be defined by simply rotating the sample. For example, the axial, transverse and longitudinal stiffness of square samples 3 and 4 can be defined as illustrated in Figure 45 and Figure 46.

Table 19: Physical characteristics of isotropic-anisotropic composite dikes.

	Name	**a**	**MRE core**		**MRE outer ring**	
			MRE type	**particles**	**MRE type**	**particles**
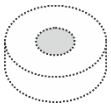	Sample 1a-1	1/3	Anisotropic	large	Isotropic	large
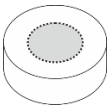	Sample 1a-2	2/3	Anisotropic	large	Isotropic	small
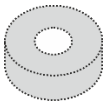	Sample 1a-3	3	Isotropic	large	Anisotropic	large
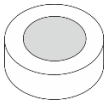	Sample 1a-4	1	Anisotropic	small	Isotropic	small
		b	**Top part**		**Bottom part**	
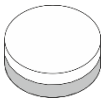	Sample 2a	1	Isotropic	small	Anisotropic	small

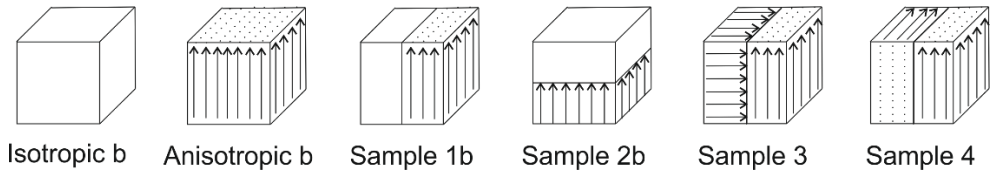

Figure 44: Square samples combining isotropic and anisotropic MREs. The blank blocks represent isotropic MREs while the arrows in the boxes represent the direction of the aligned chains in anisotropic MREs.

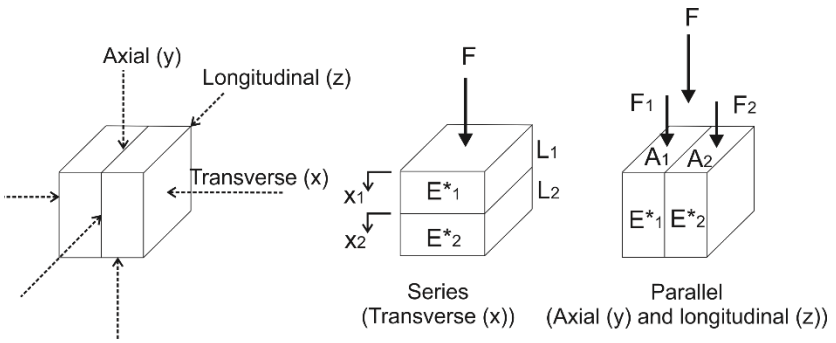

Figure 45: Definition of axial, longitudinal and transverse stiffness of square samples.

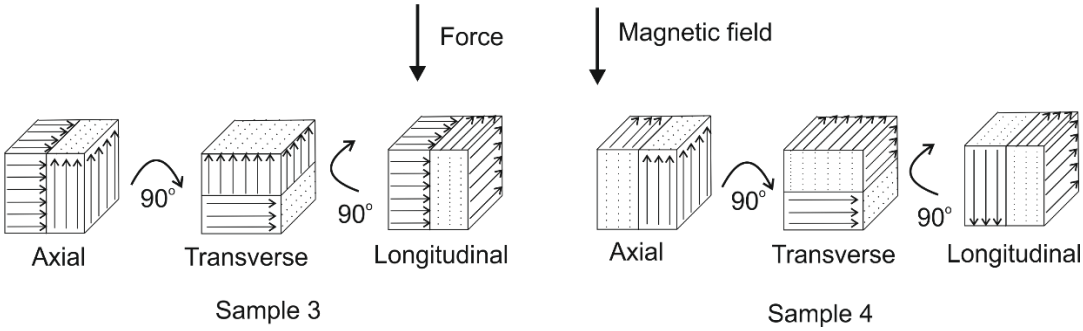

Figure 46: Defining axial, transverse and longitudinal mechanical characteristics of sample 3 and 4.

The manufacturing process of the composite MR elastomers involves two stages. First, pure isotropic and anisotropic cube samples were made. Samples 1b and 2b were manufactured by cutting a pure anisotropic sample in the middle, place one half in the bottom of the mould, pure MRE on top of it and let it cure at room temperature to form the isotropic part. Samples 3 and 4 were manufactured by again cutting an anisotropic sample in the middle, place one half in one side of the mould, pure MRE to fill the gap of the other side and then place the mould between the permanent magnets to cure the other anisotropic part. In this way, all anisotropic parts were cured under the same magnetic flux of 0.35T. The magnetic field during curing was produced using sets of cylindrical grade N42 neodymium permanent magnets of diameter 40mm and thickness 10 mm, as explained in detail in section 3.2.

Test setup

The static and dynamic tests were performed according to BS ISO 7743-1:2011 and BS ISO 4664-1:2011 standards respectively, using INSTRON PULS E1000 electromechanical dynamic tester and the experimental setup described in detail in section 4.2. Although, the BS ISO 7743-1:2011 standard requires the samples to be compressed up to 20% strain, this was not possible for anisotropic samples due to the load capacity of INSTRON E1000 machine. For this reason, the samples were compressed up to 15% strain and the compression modulus S_M (Secant modulus) is

measured at 5% and 15% strain instead of those at 10% and 20% indicated on the ISO standard. Young modulus E is then calculated $E = S_M(1 - \varepsilon)$ for 5% and 15% strain and the median value is reported. The magnetic field during testing was produced using permanent magnets as explained earlier in details in section 4.2.

Two types of dynamic loading cycles were performed at 0, 0.3 and 0.5T magnetic flux values for disk samples and 0, 0.2 and 0.35T for square samples. One amplitude sweep cycle, where the strain amplitude was increased from 0.25% to 1.5% at a constant frequency of 5 Hz, and a second frequency sweep cycle where the frequency was increased from 0.5Hz to 70 Hz at constant strain amplitude of 0.5%. The details of the compression test are mentioned in Table 20.

Table 20: Summary of test loading cycles for dynamic compression tests on composite MREs

<table>
<tr><th>Test</th><th colspan="2"></th><th>Magnetic field</th></tr>
<tr><td rowspan="3">Amplitude sweep</td><td>Strain Amplitude (%)</td><td>0.25,0.5,0.75,1,1.25,1.5
(50 loading cycles for each amplitude)</td><td rowspan="4">0,0.3,0.5 T for disk samples

0,0.2,0.35 T for square samples</td></tr>
<tr><td>Loading frequency</td><td>5 Hz
(at 5KHz sampling rate)</td></tr>
<tr><td>Prestrain</td><td>10 %</td></tr>
<tr><td rowspan="3">Frequency sweep</td><td>Strain Amplitude</td><td>0.5 %</td></tr>
<tr><td>Loading frequency (Hz)</td><td>0.5,1,5,10,20,30,40,50,60,70
(20,30,50,100,150,250,300,350,400,450 loading cycles for each corresponding frequency at 5KHz sampling rate) *</td></tr>
<tr><td>Prestrain</td><td>10 %</td></tr>
</table>

*The number of cycles was increased for each frequency in order to allow for the amplitude control feature of the wavematrix software to reach the desired amplitude with increasing frequency.

5.4 Isotropic and anisotropic MREs in parallel and series configurations

Zero field static mechanical properties

The results of the static compression test on the composite parallel and series combination samples are shown in Figure 47 along with the conventional pure isotropic a and anisotropic a MRE samples. The anisotropic a MRE is the stiffest while the isotropic a sample the softest of all. Samples 1a-4 and 2a lie between these two as expected, with the parallel combination sample 1a-4 being slightly stiffer than the series combination sample 2a. The static Young Modulus E of the composite samples can be estimated using equations 6.2.4 and 6.2.12 from the previous section, taking under consideration that E_1= compression modulus (Young modulus) of isotropic MRE, E_2= compression modulus (Young modulus) of anisotropic MRE. Table 21 presents the measured values of Young Modulus E, as well as the calculated values using the values of isotropic and anisotropic samples mentioned on Table 42. It can be seen that the theoretical equations can produce a good estimation of the static stiffness for some samples. This is mostly attributed to the variability of the stiffness values between sample batches. However, it becomes clear that the stiffness of each sample can by further tailored by selecting appropriate dimensions and particle size of each part.

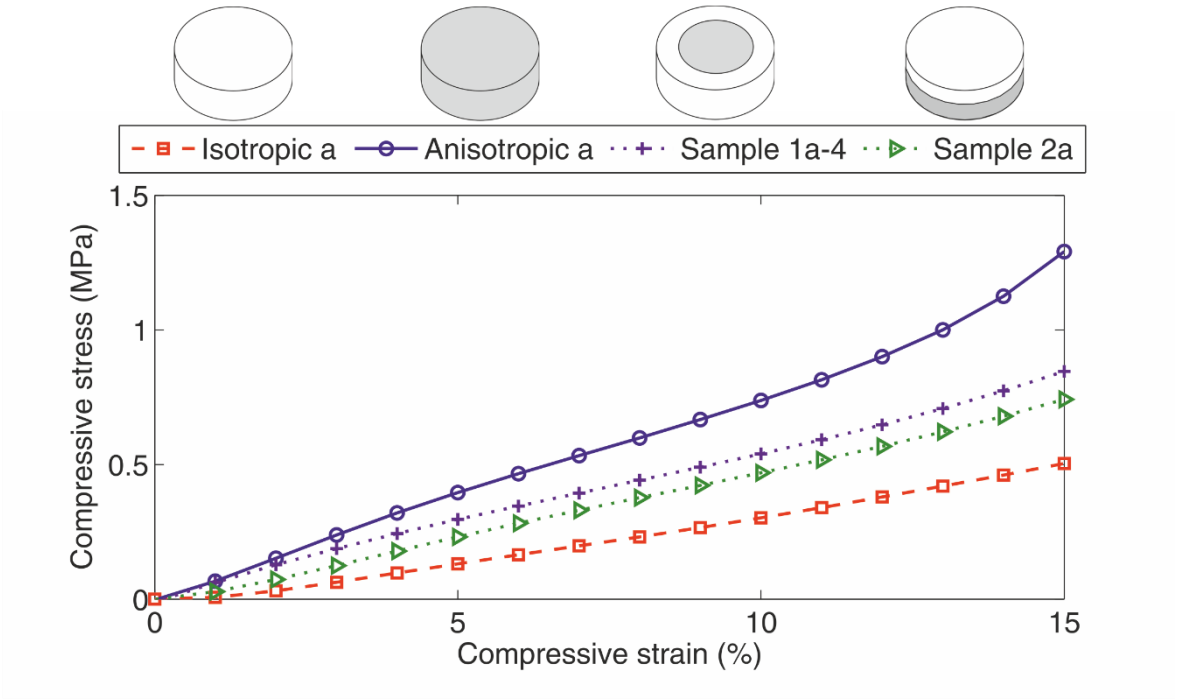

Figure 47: Static stress-strain curves for anisotropic a, isotropic a, composite sample 1a-4 and sample 2a MREs with small particles at zero field.

Table 21: Calculated and measured static Young Modulus E of disk pure and combined MREs.

Applied force (Parallel to particle alignment for anisotropic)		**Measured**	**Calculated**			
		E (MPa)	**E (MPa)**	**a**	**MRE core**	**MRE outside**
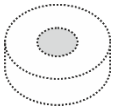	Sample 1a-1	4.72	4.67	1/3	Anisotropic large particles	Isotropic large particles
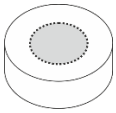	Sample 1a-2	3.3	4.8	2/3	Anisotropic large particles	Isotropic small particles
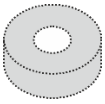	Sample 1a-3	6.2	5.9	3	Isotropic large particles	Anisotropic large particles
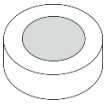	Sample 1a-4	5.2	4.7	1	Anisotropic small particles	Isotropic small particles
		E (MPa)	**E (MPa)**	**b**	**Bottom part**	**Top part**
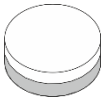	Sample 2a	4.7	4.3	1	Anisotropic small particles	Isotropic small particles

Zero field dynamic mechanical properties

The absolute modulus $|E^*|$, tangnent of loss factor tanδ, storage E' and loss E'' moduli of composite disk parallel (sample 1a-4) and series (sample 2a) configuration samples and the equivalent pure MREs in respect to strain amplitude, are shown in Figure 48. Pure anisotropic MRE is the stiffest elastomer with the highest tangent of the loss angle, isotropic MRE is the softest with the lower tangent of the loss angle, while absolute modulus $|E^*|$ and tangent of the loss angle $tan\delta$ of samples 1a and 2a are between the pure samples as expected. All samples decrease their storage E' and loss E'' modulus with increasing strain amplitude, but at a different rate that causes tangent of loss angle tanδ to increase slightly with strain amplitude. The decrease rate of both composite samples is between the ones of pure anisotropic and isotropic MREs. Combining anisotropic and isotropic MREs produces a new elastomer with higher damping capability than isotropic MRE and lower stiffness than anisotropic MRE without changing the general behaviour of the material.

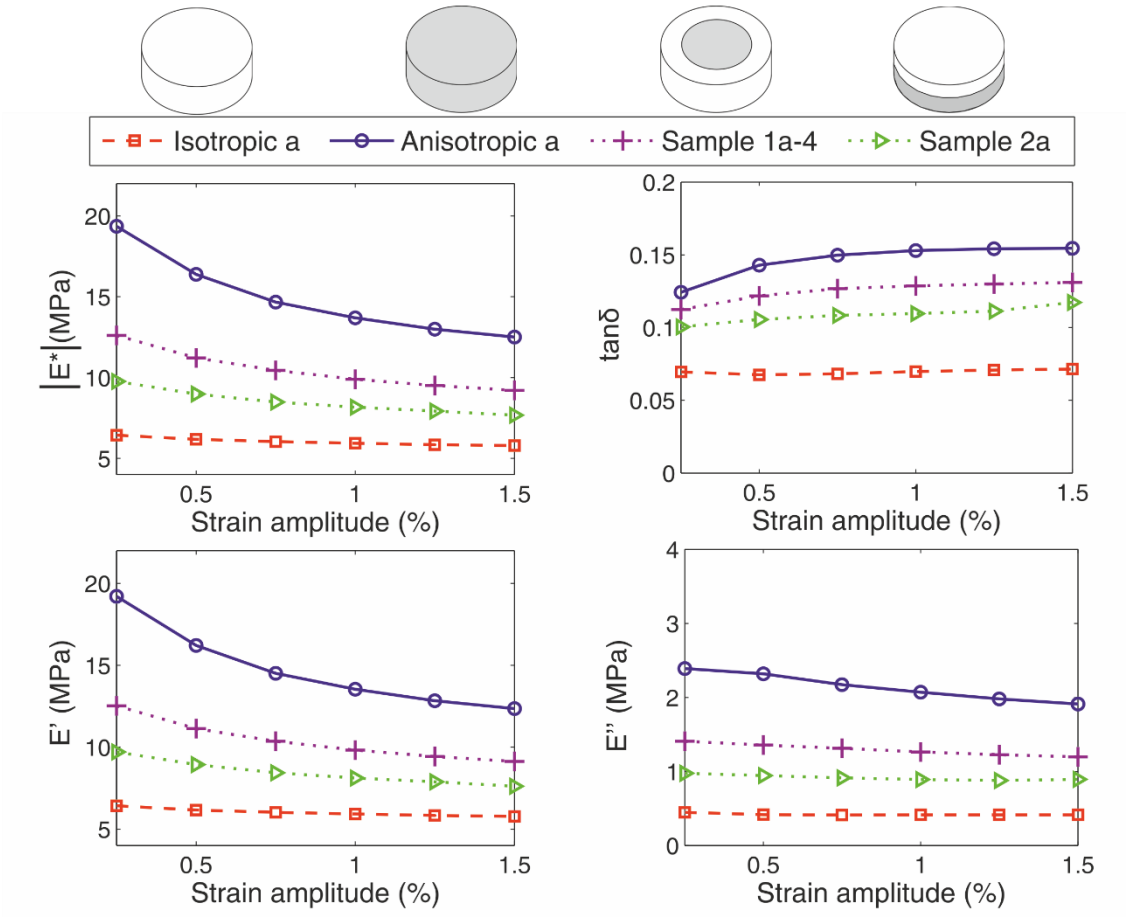

Figure 48: Zero field absolute modulus $|E^*|$ and tangent of the loss angle $tan\delta$ of pure isotropic, anisotropic, sample 1a-4 and sample 2a, at 5Hz frequency and 10% prestrain.

Figure 49 illustrates The absolute modulus $|E^*|$, tangnent of loss factor tanδ, storage E' and loss E'' moduli of all disk sample 1a MREs with an anisotropic core made of small or large particles. All samples decrease their storage E' and loss modulus E'' with increasing strain amplitude, like all MREs, but at a different rate. Composite samples 1a-1 and 1a-3, which are made of large particles, have higher absolute modulus $|E^*|$ than pure isotropic a-I sample but lower than pure anisotropic a-I MRE. Tangent of the loss angle tanδ of samples 1a-1 and 1a-3 increase for small strain amplitudes to decrease later for larger values similar to the pure anisotropic MRE with large particles. Sample 1a-2 has similar absolute modulus $|E^*|$ with 1a-4 but higher tanδ at small amplitudes because the core is made with anisotropic MRE with large particles that have a higher tanδ than the one with small particles. Tangent of the loss angle tanδ of sample 1a-2, which has one part with small particles and one with large, decrease with strain amplitude as a result of the contribution of each part.

The zero-field damping capability of a composite sample can be improved by using MREs with iron particles of different sizes. For example, consider samples 1a-2 and 1a-4 where the anisotropic to isotropic area ratio 'α' of sample 1a-2 was selected so to have similar dynamic stiffness to sample 1a-4 with unit area ratio. Using an anisotropic MRE core made of large particles to a cylinder

isotropic MRE made of small particles (sample 1a-2), increases tangent of the loss angle for small strains by 25% while keeping stiffness similar to the case where the anisotropic core was made of small particles (sample 1a-4). Therefore, it is possible to tailor the dynamic mechanical properties of composite MREs by selecting appropriate MRE material, iron particle size and dimensions of each part.

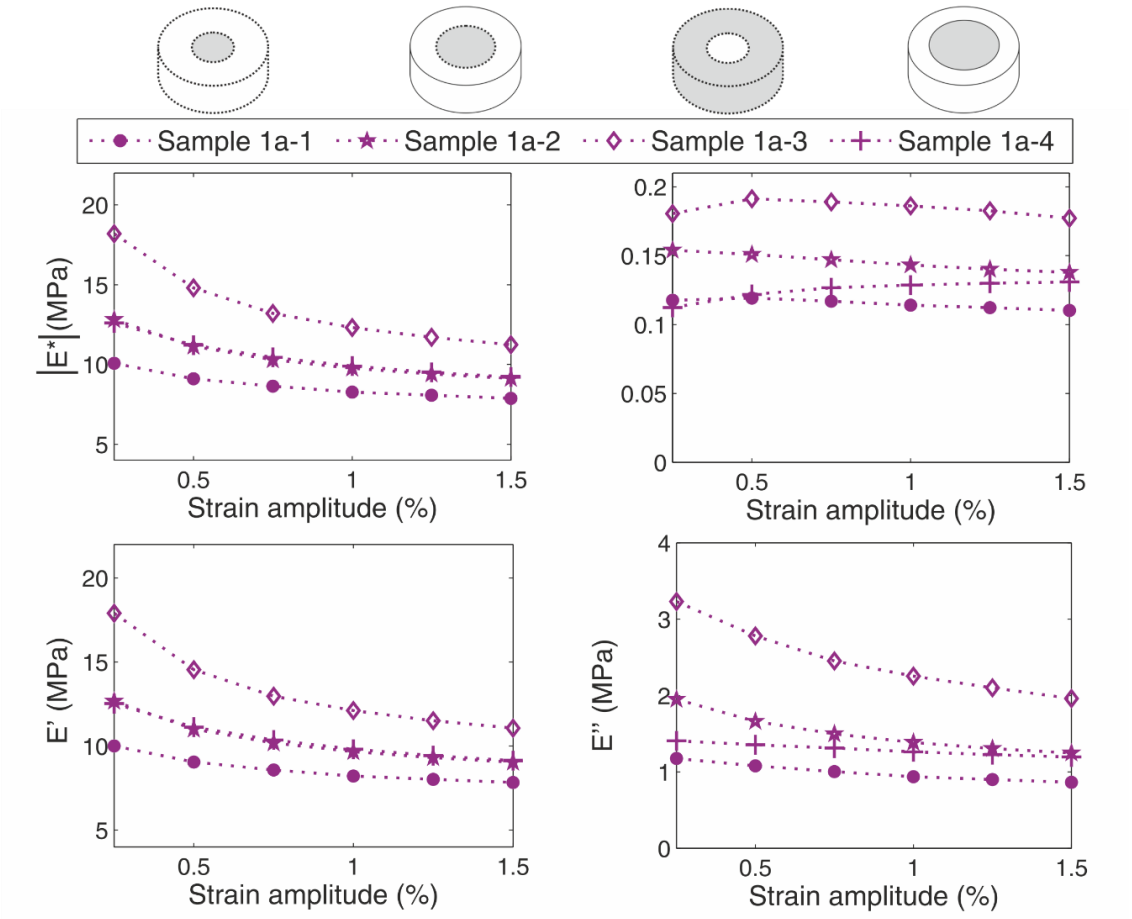

Figure 49: Zero field absolute modulus $|E^*|$ and tangent of the loss angle $tan\delta$ of all four parallel combination samples, at 5Hz frequency and 10% prestrain.

Dynamic compression absolute modulus $|E^*|$ and tangent of the loss angle $tan\delta$ of the composite samples can be estimated using equations (6.2.6) and (6.2.7) for the parallel configuration sample and (6.2.14) and (6.2.15) for the series configuration sample. Assuming, E'_1= storage modulus and E''_1= loss modulus of isotropic MRE, E'_2= storage modulus and E''_2 =loss modulus of anisotropic MRE and using the values mentioned in Table 22 (at 0.5% strain amplitude, 5Hz loading frequency and 10% prestrain), while

Table 23 presents the measured and calculated values of composite samples. The theoretical equations can thus, provide a good estimation for the actual measured data.

Table 22: Measured values of absolute modulus $|E^*|$ and tangent of the loss angle $tan\delta$ of pure disk MREs.

Sample		**Measured (0.5%, 5Hz)**				
		$\|E^*\|$ (MPa)	**tanδ**	**E' (MPa)**	**E''(MPa)**	**Particles**
Applied force (Parallel to particle alignment for anisotropic)	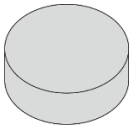	17.4	0.196	17.11	3.36	**Large**
		16.4	0.143	16.22	2.32	**Small**
	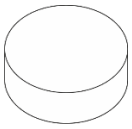	6.76	0.062	6.74	0.42	**Large**
		6.17	0.068	6.16	0.42	**Small**

Table 23: Measured and calculated values of absolute modulus $|E^*|$ and tangent of the loss angle $tan\delta$ of composite sample 1a and 2b MREs.

Applied force (parallel to particle alignment for anisotropic)		**Measured (0.5%,5Hz)**		**Calculated**				
		$\|E^*\|$	**tanδ**	**$\|E^*\|$**	**tanδ**	**a**	**MRE core**	**MRE outside**
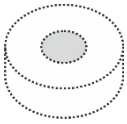	Sample 1a-1	9.1	0.12	9.5	0.13	1/3	Anisotropic large particles	Isotropic large particles
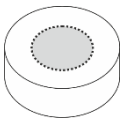	Sample 1a-2	11.3	0.15	10.8	0.15	2/3	Anisotropic large particles	Isotropic small particles
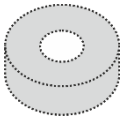	Sample 1a-3	14.8	0.19	14.96	0.17	3	Isotropic large particles	Anisotropic large particles
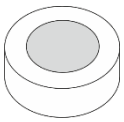	Sample 1a-4	11.2	0.12	11.38	0.12	1	Anisotropic small particles	Isotropic small particles
		$\|E^*\|$	**tanδ**	**$\|E^*\|$**	**tanδ**	**b**	**Bottom part**	**Top part**
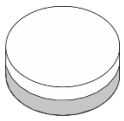	Sample 2a	8.9	0.1	9.04	0.09	1	Anisotropic small particles	Isotropic small particles

Magnetorheological effect

Figure 50 presents the relative MR effect (0T to 0.5T) of absolute modulus $|E^*|$, tangnent of loss angle tanδ, storage E' and loss E'' modulus of pure isotropic a-s, pure anisotropic a-s, parallel sample 1a-4 and series sample 2a composite MREs in respect to strain amplitude. Under a 0.5T magnetic field, parallel combination sample 1a-4 increases its storage modulus E' by 28% while series combination sample 2a by 27%. These values are very close to the 31% MR effect of pure anisotropic a-s sample and higher than the 21% MR effect of pure isotropic a-s sample. Loss modulus E'' and thus, the energy dissipated in each cycle increases with the application of the magnetic field but almost half the percentage of storage modulus E'. The mismatch of storage E' and loss E'' modulus MR effects results to a negative MR effect of tanδ for all samples that strongly depends on strain amplitude. Therefore, damping capability of all samples decreases slightly with increasing magnetic field and strain amplitude. However, the zero field values of loss modulus E'' are small and a 10% increase corresponds to a very small absolute value that could easily be considered a measurement error when calculating the area of the hysteresis loop to find loss angle δ.

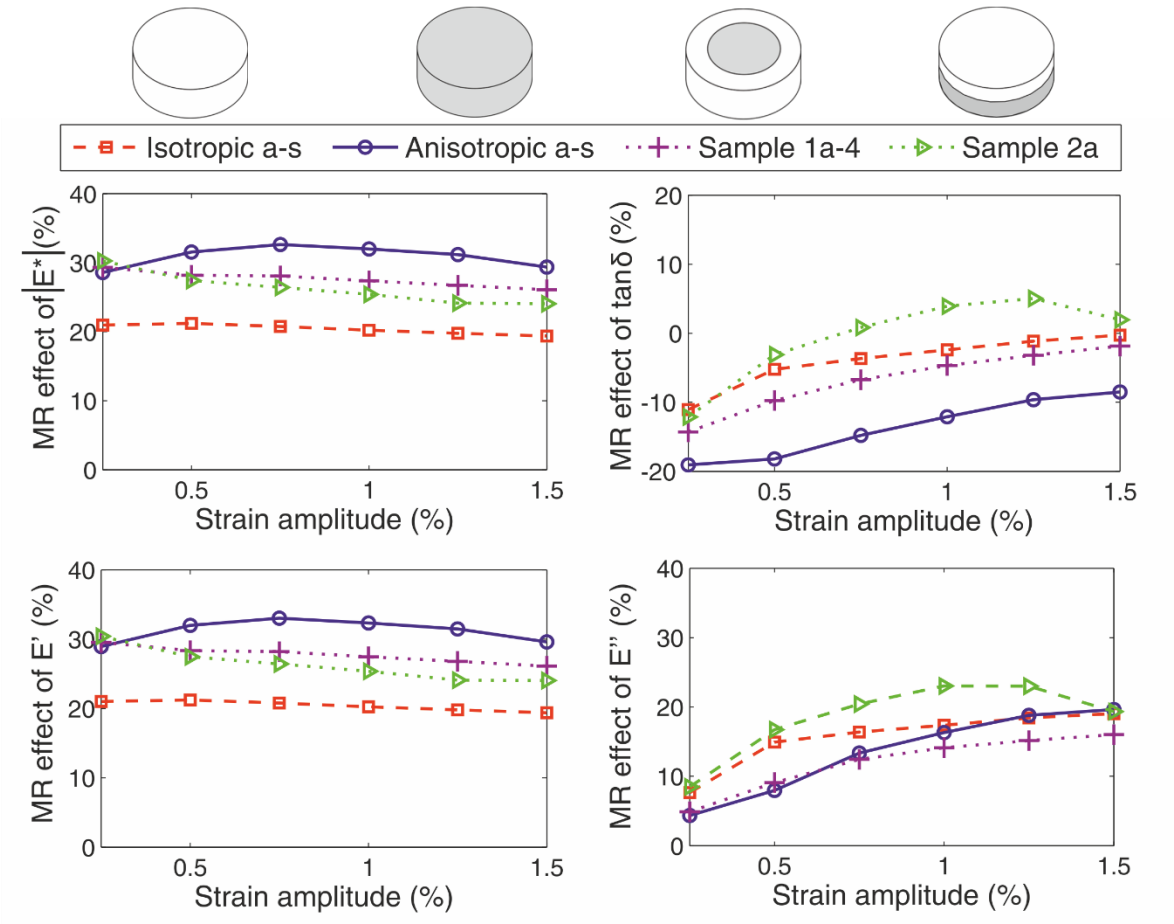

Figure 50: Relative MR effect (0T to 0.5T) of isotropic a-s, anisotropic a-s, sample 1a-4 and sample 2a in respect to strain amplitude (measured at 5Hz frequency and 10% prestrain).

Figure 51 presents the MR effect (0T to 0.5T) of absolute modulus $|E^*|$, tangnent of loss angle tanδ, storage E' and loss E'' of parallel configuration composite MRE samples 1a-1, 1a-2, 1a-3 and 1a-4 in respect to strain amplitude. When an external magnetic field of 0.5T is applied, the magnetic forces are developed between iron particles that force them to move inside the silicon matrix. Large particles need greater magnetic forces than small particles to move inside the matrix and align themselves parallel to the magnetic field. Therefore, MREs with large particles have a lower MR effect of storage modulus E' (measure of stiffness) but higher MR effect of loss modulus E'' since they need more energy to move. Under the same logic, sample 1a-4 has the highest MRE effect of storage modulus E' while, loss modulus E'' of samples 1a-1, 1a-2 and 1a-3, that have one part anisotropic MRE with large particles, increases two times more than sample 1a-4. The tangent of loss angle tanδ of samples 1a-1, 1a-2 and 1a-3 is not greatly influenced by the magnetic field since a 5% increase of the zero field value is negligible for real applications. The MR effect of samples 1a-1, 1a-2 and 1a-3 do not vary with strain amplitude in contrast to sample 1a-4, because MREs with large particles form more stable particle-elastomer structures. Thus, composite isotropic/anisotropic MREs behave like the equivalent anisotropic MRE they are made of.

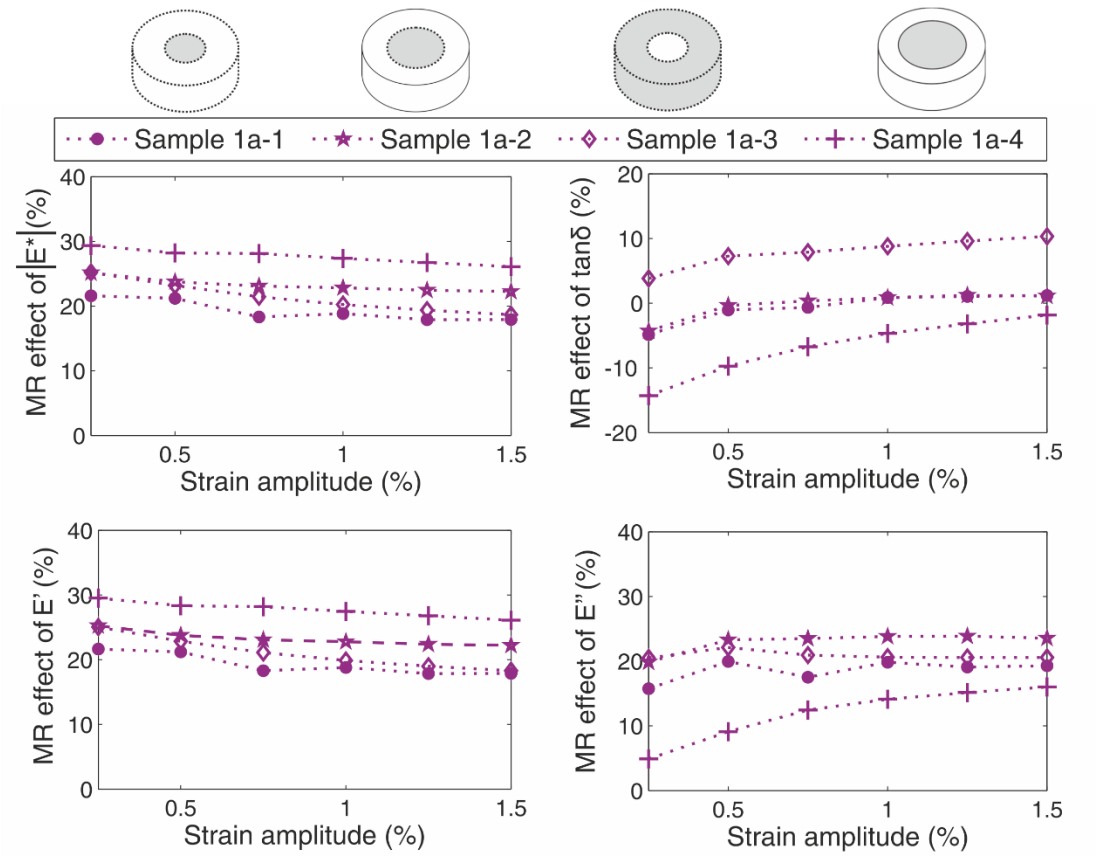

Figure 51: Relative MR effect (0T to 0.5T) of sample 1a-1, 1a-2, 1a-3 and 1a-4 in respect to strain amplitude (measured at 5Hz frequency and 10% prestrain).

5.5 Axial, transverse and longitudinal mechanical characteristics of composite samples

Zero field static mechanical properties

Figure 52 illustrates the axial load-displacement curves of the pure MRE square samples anisotropic b, isotropic b, and composite samples sample 1b, sample 2b and sample 3 with small particles. Since the square samples are of nonstandard dimensions, the results will be drawn regarding the compressive static stiffness rather than the Young modulus. Again, anisotropic MRE is much stiffer than isotropic MRE while their series (sample 2b) and parallel (sample 1b) combination samples have a similar axial stiffness that lies between the isotropic and anisotropic samples. Samples 3 and 4 also have a similar stiffness, although they consist of two anisotropic halves with their particles aligned in different directions. This is because when the particles are aligned perpendicular to the applied force in an anisotropic sample the elastomer has a similar stiffness with the isotropic one (Schubert G 2015), as can also be seen in Table 24.

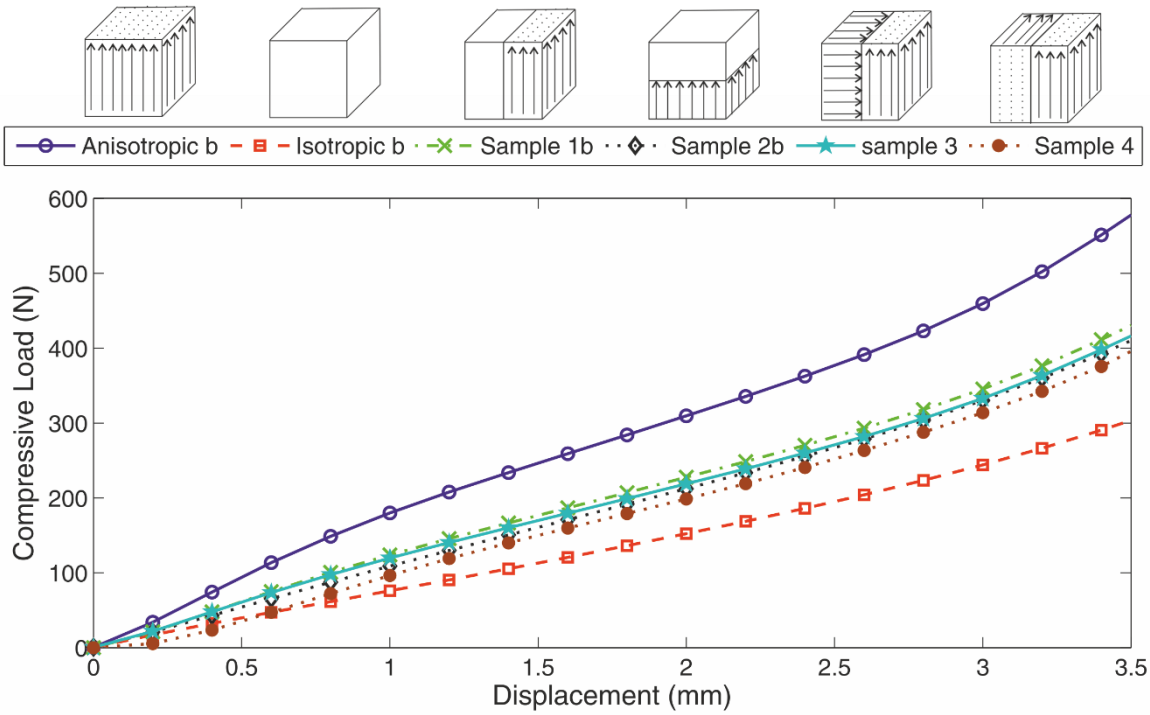

Figure 52: Static axial force-displacement curves for anisotropic b, isotropic b, composite sample 1b, sample 2b, sample 3 and sample 4 MREs with small particles at zero field.

The static compressive stiffness of the square composite samples can be estimated using equations (6.2.4) and (6.2.12), taking under consideration that:

$$E_1 = K_{iso}\frac{L_{iso}}{A_{iso}}, \qquad E_2 = K_{an}\frac{L_{an}}{A_{an}}, \qquad a = b = 1$$

Where E_1= compression modulus (Young modulus), K_{iso} =static stiffness, L_{iso}=length, A_{iso}=area of the isotropic sample, while E_2= compression modulus (Young modulus), K_{an} =static stiffness, L_{an}=length, A_{an}=area of the anisotropic sample and E= compression modulus, K= static stiffness, L=length, A=area of the combined sample. In this case since all samples have the same dimensions the moduli of elasticity in equations can be directly replaced by the equivalent stiffness.

Table 24: Measured and calculated static compression stiffness of square composite MREs with small particles at 2.2mm displacement (equivalent 10% strain).

Sample	**K (10%) Measured (KN/m)**	**Sample**	**K (10%) Measured (KN/m)**	**Sample**	**K (10%) Measured (KN/m)**	**Applied force**
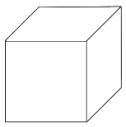	76.72	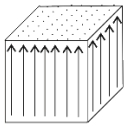	152.50	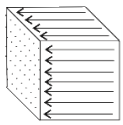	75.01	
K (10%) axial -p1 (KN/m)		**K (10%) transverse -p2 (KN/m)**		**K (10%) longitudinal- p3 (KN/m)**		
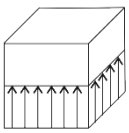	102.08	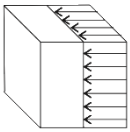	75.86	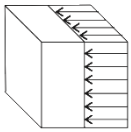	75.86	**Calculated**
	106.12		76.80		74.5	**measured**
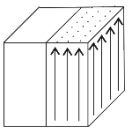	114.61	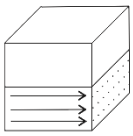	75.85	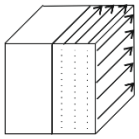	75.86	**Calculated**
	112.94		70.21		73.6	**measured**
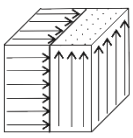	113.75	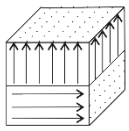	100.56	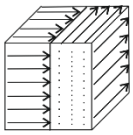	75.01	**Calculated**
	108.58		99.55		77.05	**measured**
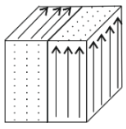	113.75	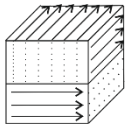	75.01	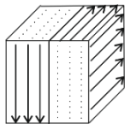	113.75	**Calculated**
	100.2		72.2		105.5	**measured**

Table 24 presents the measured and calculated values of the composite samples using the measured values of the square isotropic and anisotropic samples. It can be seen again, that the theoretical equations can produce a good estimation of static stiffness. When the particles of the anisotropic part are aligned perpendicular to the applied force, stiffness is similar to the pure isotropic sample. However, Sample 3 has almost similar axial and transverse stiffness while sample4 has the same axial and longitudinal stiffness. Therefore, it is possible to produce a composite MRE

with same zero field axial and transverse or axial and longitudinal stiffness depending on the actual loading conditions the rubber is subjected to.

Zero field dynamic mechanical properties

The zero field dynamic stiffness $|K^*|$ and tangent of the loss angle $tan\delta$ of pure isotropic b, anisotropic b MREs and their combinations cube samples 1b and 2b, in respect to the strain amplitude, are shown in Figure 53, while Figure 54 illustrates the influence of load frequency at 0.5% strain amplitude. The cube samples behave exactly like disk anisotropic a-s, isotropic a-s, sample 1a-4 and samples 2a MRE discussed in section 6.4. The pure anisotropic sample has the highest stiffness K* and tangent of the loss angle tanδ while pure isotropic the lowest, as expected. The parallel and series combination (sample 1b and 2b) have both similar stiffness values that lay between the different pure samples. The tangent of the loss angle tanδ of parallel combination (sample 1b) is much higher than the one of isotropic sample, almost approaching the value of the anisotropic MRE. The series combination (sample 2b) has a lower tangent of the loss angle tanδ but still higher than the isotropic sample itself. All samples drop their stiffness K* value while increasing their tangent of the loss angle tanδ with increasing strain amplitude. Increasing loading frequency, results to a slight increase of dynamic stiffness K* while tangent of the loss angle tanδ drops slightly for all samples.

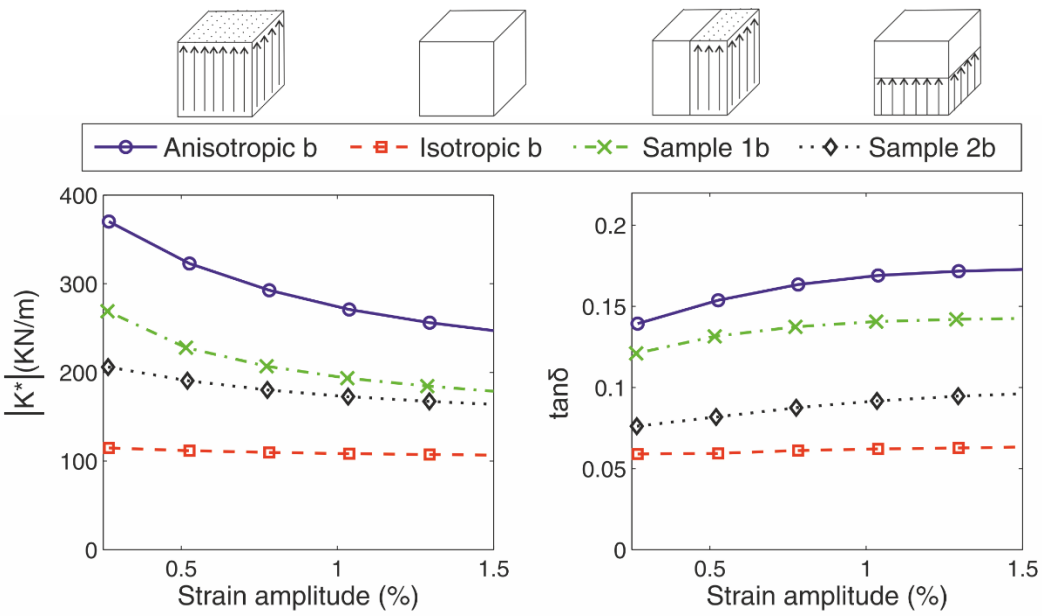

Figure 53: Zero field dynamic stiffness $|K^*|$ and tangent of the loss angle $tan\delta$ in respect to strain amplitude of pure isotropic b, anisotropic b, sample 1b and sample 2b (with small particles) at 5Hz frequency and 10% prestrain.

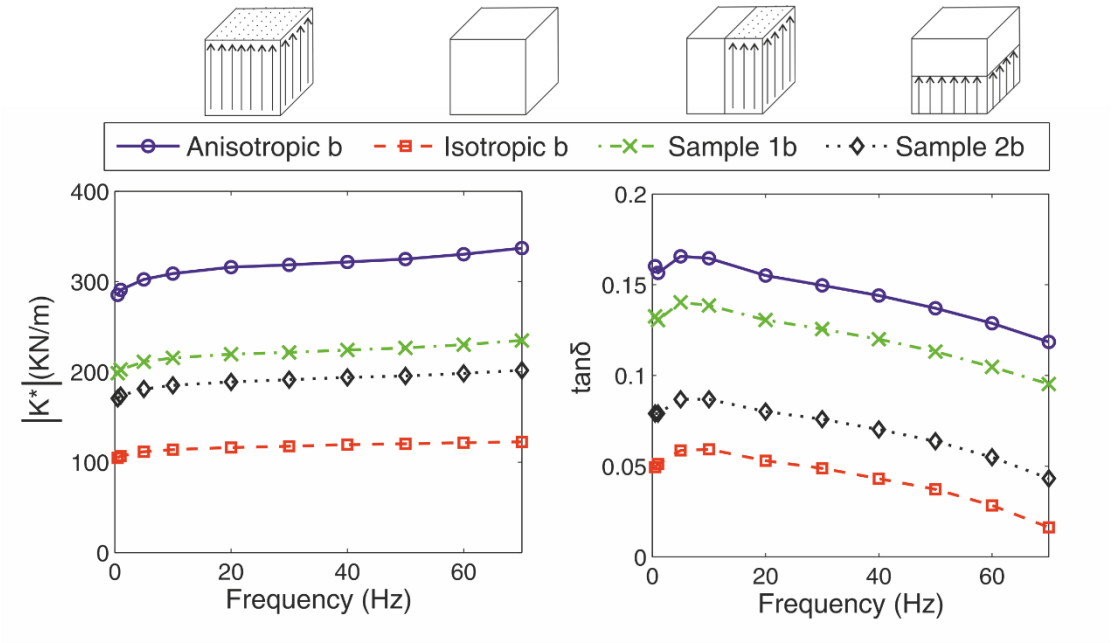

Figure 54: Zero field dynamic absolute stiffness $|K^*|$ and tangent of the loss angle $tan\delta$ in respect to frequency of pure isotropic b, anisotropic b, sample 1b and sample 2b (with small particles) at 0.5% strain amplitude and 10% prestrain.

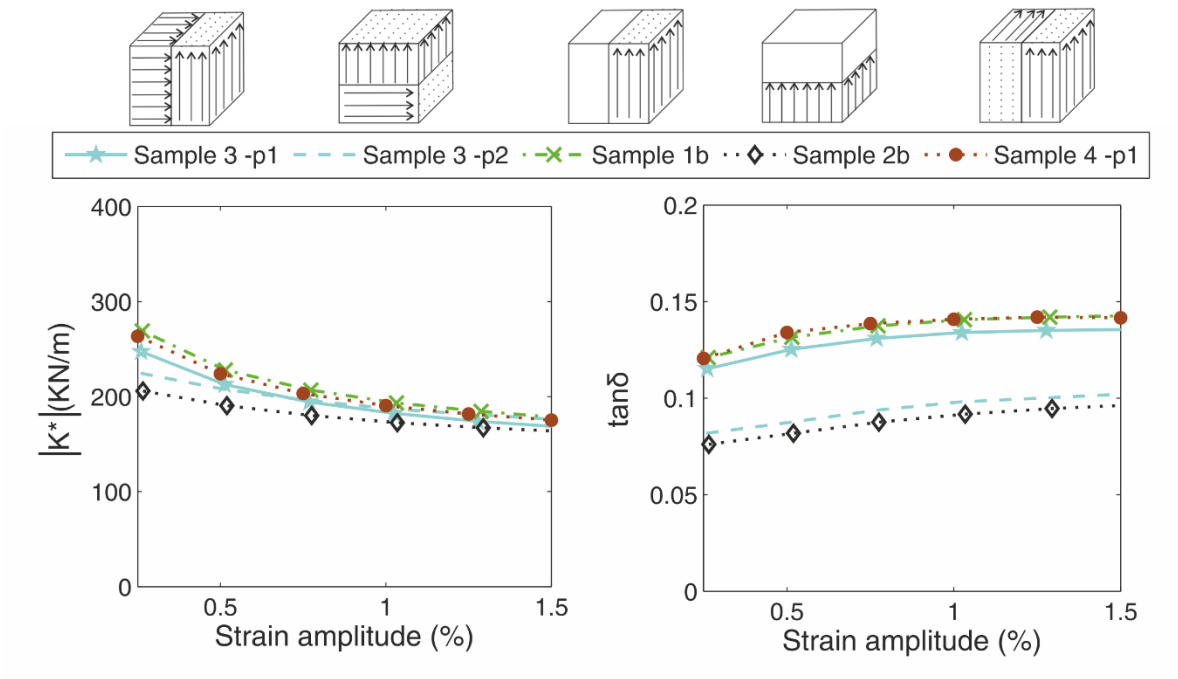

Figure 55: Zero field dynamic stiffness $|K^*|$ and tangent of the loss angle $tan\delta$ in respect of strain amplitude of sample 1b, sample 2b, sample 3-p1 (axial), sample 3-p2 (transverse) and sample 4-p1(axial) with small particles, at 5Hz frequency and 10% prestrain.

The variation of the axial dynamic mechanical properties of composite sample 3(p1), sample 4(p1), sample 2b and sample 1b along with the transverse dynamic mechanical properties of composite sample 3 (p2), in respect to strain amplitude and frequency, is illustrated in Figure 55 and Figure 56 respectively. Composite samples 3(p1), 4(p1) and 1b have similar axial dynamic stiffness and

tangent of loss angle tanδ while composite samples 3(p2) has similar transverse dynamic stiffness and tanδ to the axial dynamic stiffness and tanδ of sample 2b.

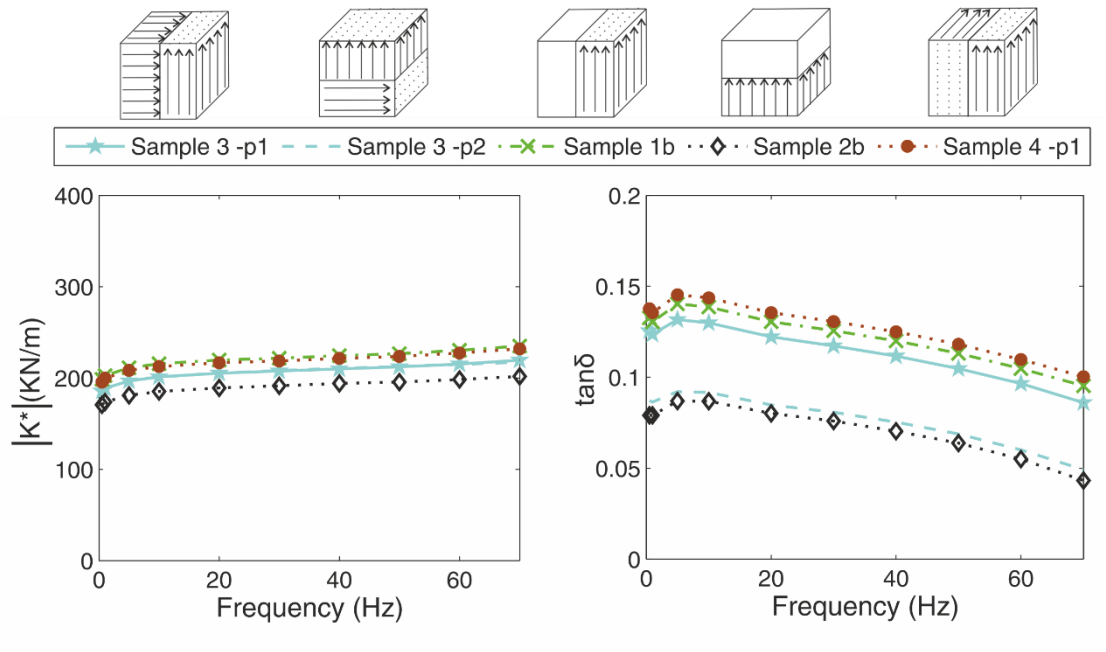

Figure 56: Zero field dynamic stiffness $|K^*|$ and tangent of the loss angle $tan\delta$ in respect of frequency of sample 1b, sample 2b and sample 3 (with small particles) at 0.5% strain amplitude and 10% prestrain.

The dynamic absolute stiffness $|K^*|$ of the square composite samples can be estimated using equations (6.2.6), (6.2.7), (6.2.14) and (6.2.15) taking under consideration that:

$$E'_1 = K'_{iso}\frac{L_{iso}}{A_{iso}}, \qquad E''_1 = K''_{iso}\frac{L_{iso}}{A_{iso}}, \qquad E'_2 = K'_{an}\frac{L_{an}}{A_{an}}, \qquad E''_2 = K''_{an}\frac{L_{an}}{A_{an}}$$

$$K' = E'\frac{A}{L}, \qquad K'' = E''\frac{A}{L}, \qquad |K^*| = \sqrt{K'^2 + K''^2}, \qquad \tan\delta = \frac{K''}{K'} \quad and \quad a = b = 1$$

Where E'_1= storage modulus, E''_1=loss modulus, K'_{iso} =real part of dynamic stiffness, K''_{iso} =imaginary part of dynamic stiffness, L_{iso}=length, A_{iso}=area of the isotropic sample, while E'_2= storage modulus, E''_2=loss modulus, K'_{an} =real part of dynamic stiffness, K''_{an} =imaginary part of dynamic stiffness, L_{an}=length, A_{an}=area of the anisotropic sample and E'= storage modulus, E''= loss modulus, K'= real part of dynamic stiffness, K''= imaginary part of dynamic stiffness, L=length, A=area of the combined sample. Table 26 presents the measured and calculated axial, transverse and longitudinal dynamic stiffness $|K^*|$ and tangent of the loss angle $tan\delta$ of all cube composite samples, using the values of pure anisotropic and isotropic samples of Table 25.

Table 25: Zero field measured dynamic stiffness $|K^*|$ and tangent of the loss angle $tan\delta$ of isotropic and anisotropic MREs with small particles at 0.5% strain amplitude, 5Hz frequency and 10% prestrain.

Applied force	Measured (0.5%, 5Hz)		Sample	Measured (0.5%, 5Hz)		Sample	Measured (0.5%, 5Hz)	
	$\|K^*\|$ (KN/m)	tanδ		$\|K^*\|$ (KN/m)	tanδ		$\|K^*\|$ (KN/m)	tanδ
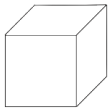	112	0.06	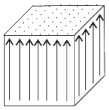	323	0.15		122	0.07

Table 26: Zero field measured and calculated $|K^*|$ and $tan\delta$ of composite MREs (at 0.5% strain amplitude, 5Hz frequency and 10% prestrain).

p1	Axial (0.5%, 5Hz)		p2	Transverse (0.5%, 5Hz)		p3	Longitudinal (0.5%, 5Hz)		Applied force
	$\|K^*\|$ (KN/m)	tanδ		$\|K^*\|$ (KN/m)	tanδ		$\|K^*\|$ (KN/m)	tanδ	
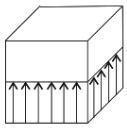	170	0.08	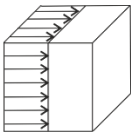	117	0.06	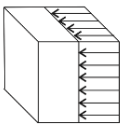	117	0.06	**Calculated**
	191	0.08		119	0.06		120	0.06	**Measured**
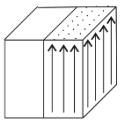	228	0.13	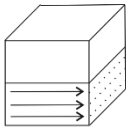	118	0.06	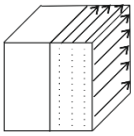	117	0.06	**Calculated**
	227	0.13		122	0.06		115	0.06	**Measured**
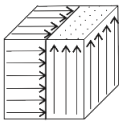	223	0.13	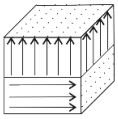	180	0.09	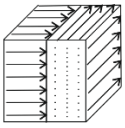	122	0.07	**Calculated**
	213	0.125		208	0.087		118	0.07	**Measured**
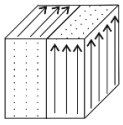	223	0.13	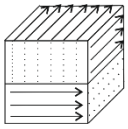	122	0.07	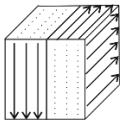	223	0.13	**Calculated**
	224	0.134		130	0.07		210	0.12	**Measured**

The two different MRE parts are combined in series or parallel configurations depending the direction of interest. For example, for the axial stiffness of sample 2b an isotropic part is considered in parallel to an anisotropic part with particles aligned in the same direction of the applied force. Axial stiffness of sample 2b can therefore be estimated by using the stiffness of isotropic b sample and the axial stiffness of anisotropic b sample in equation (6.2.6) setting area ratio α=1. However, for calculating the transverse stiffness the isotropic part is in series with the anisotropic part with particles aligned perpendicular to the applied force. In this case transverse stiffness of sample 2b is

estimated by using the stiffness of isotropic sample and the transverse stiffness of anisotropic sample, in equation (6.2.14) setting length ratio b=1. In a similar way, the longitudinal stiffness of sample 2b is estimated by using the stiffness of isotropic sample and the longitudinal stiffness of anisotropic sample, in equation (6.2.6) setting area ratio α=1. When the particles of anisotropic samples are not aligned in the same direction with the applied load, the stiffness and tangent of the loss angle of the MRE is similar to the isotropic sample like the transverse stiffness and tangent of the loss angle of samples 1b and 2b.

Magnetorheological effect

In order to evaluate the performance of the novel combined isotropic and anisotropic MREs, the effect of the magnetic field on the dynamic properties is examined. Figure 57 illustrates the axial and transverse dynamic stiffness $|K^*|$ and tangent of the loss angle $tan\delta$ of all MREs at 0T and 0.35T magnetic field. All samples increase their stiffness when the field is applied but tangent of the loss angle is not greatly influenced. Isotropic MRE has the lowest stiffness MR effect, similar to the one of the transverse stiffness of parallel configuration sample 1b and series configuration sample 2b. When the particles of the anisotropic part are aligned perpendicular to the applied force and magnetic field, the MRE behaves like an isotropic sample but has a slightly higher MR effect. Anisotropic MRE has the highest MR effect, like the one of the axial stiffness of parallel configuration sample 1b and series configuration sample 2b. Combining anisotropic and isotropic MREs in parallel and series configurations does not compromise the MR effect when the particles are aligned parallel to the applied magnetic field like pure anisotropic MRE.

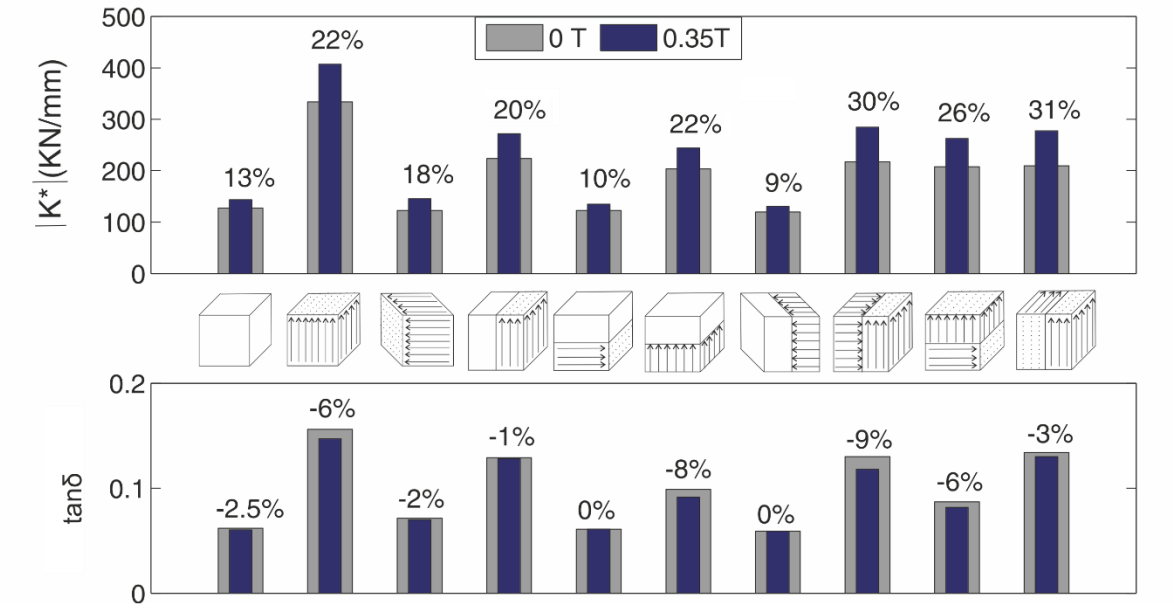

Figure 57: MR effect of axial and transverse dynamic stiffness $|K^*|$ and tangent of the loss angle $tan\delta$ of simple and composite square MREs at 0T and 0.35T measured at 0.5% strain amplitude, 5Hz frequency and 10% prestrain.

However, this is not the case for sample 3 and sample 4 that combine two anisotropic MREs with different particle alignment. In this case, the axial and transverse stiffness, along with the equivalent MR effect is similar and higher than even the anisotropic sample itself, which is attributed to the higher than isotropic MREs MR effect of anisotropic MREs with particles aligned perpendicular to the magnetic field. The tangent of the loss angle of the transverse position and equivalent MR effect is less than the one of the axial position, but the difference is not great. Combining two anisotropic MREs with different particle alignments produces a MRE with similar axial and transverse MR effect. This is highly desirable in applications where the elastomer is under multidirectional loading conditions. It also should be noted that MR effect of all square samples is higher than the one of disk samples when compared at the same magnetic field.

Magnetic field amplitude interaction

Figure 58 illustrates the MR effect of axial (p1), transverse (p2) and longitudinal (p3) dynamic stiffness $|K^*|$ and tangent of the loss angle $tan\delta$ of samples 1b, 2b, 3 and 4 in respect to strain amplitude, at 5Hz frequency and 10% prestrain. A strong magnetic field-strain amplitude coupling effect is observed when the particles of the anisotropic part are aligned parallel to the applied load and magnetic field. For these cases, MR effect of dynamic stiffness and tangent of the loss angle decreases with increasing strain amplitude. However, when the particle chains of the anisotropic part are aligned perpendicular to the applied load and magnetic field (sample1b-p2 and sample 2b-p2), the magnetic field-strain amplitude interaction is much weaker and the composite samples behave like a pure isotropic MRE (chapter 5). This behaviour is attributed to the destruction-reconstruction mechanism of the particle-matrix structure that occurs with increasing strain amplitude. This causes a disruption of the particle chain structure in anisotropic MREs that makes it more difficult for the particles to align under the influence of the magnetic field and thus dropping the MR effect.

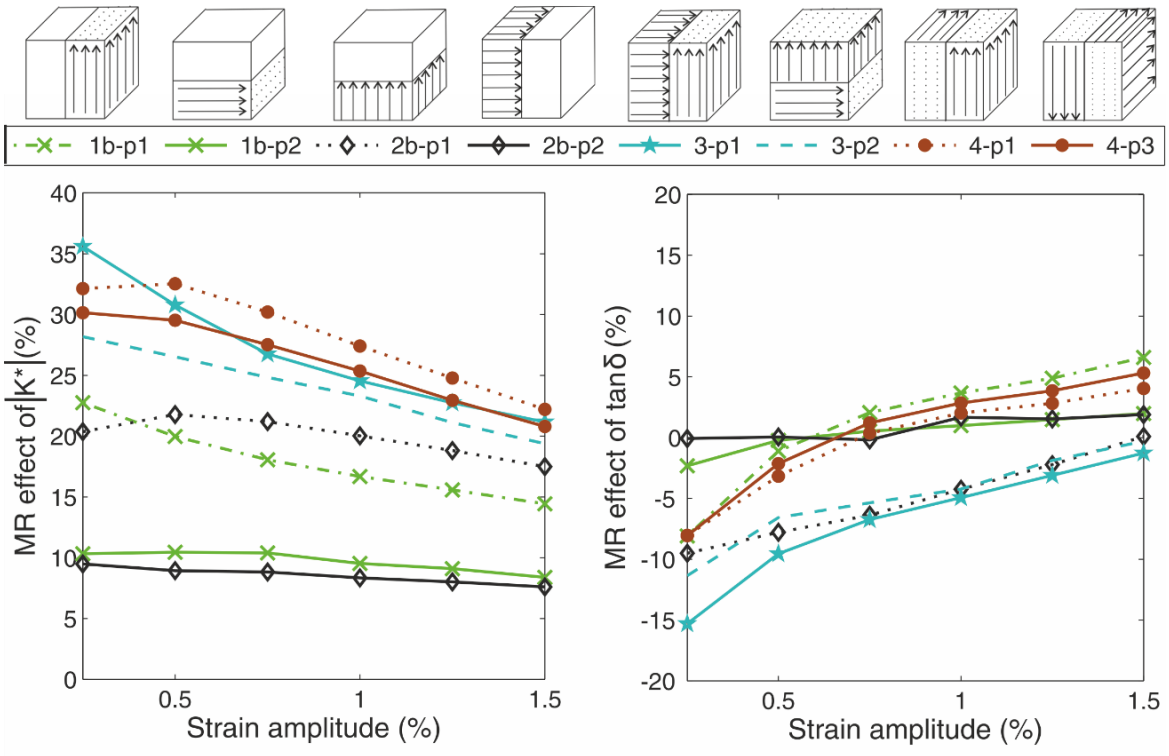

Figure 58: MR effect (0T to 0.35T) of dynamic stiffness $|K^*|$ and tangent of the loss angle $tan\delta$ of composite square samples in respect to strain amplitude (measured at 5Hz frequency and 10% prestrain).

5.6 Chapter summary

In this chapter, the principle of combining isotropic and anisotropic MREs in parallel and series configurations to improve the zero field mechanical properties of the material was examined. For this purpose, static and dynamic loading tests were performed under varying loading amplitude, frequency and magnetic field to determine the axial, transverse and longitudinal stiffness and damping of the new composite materials. The general behaviour of the new composite samples can be summarized by the following key points.

- Combining anisotropic and isotropic MREs in parallel and series, result to a new MRE with higher tangent of the loss angle than isotropic MRE by keeping stiffness lower than anisotropic MRE without compromising the MR effect. The isotropic-anisotropic disk MREs increased their dynamic stiffness by 29% compared to 32% and 21% for pure disk anisotropic and isotropic MREs respectively.
- The exact zero field stiffness and damping of the new composite samples can be tailored by selecting the dimensions of each part.
- Zero field stiffness and tangent of the loss angle can be further adjusted by selecting the particle size that each MRE part is made of.
- Combining two anisotropic MREs in parallel, one with particle chains aligned parallel to the applied load and field and the other perpendicular (along x axis), result to a new MRE with same axial and transverse stiffness and MR effect.
- Combining two anisotropic MREs in parallel, one with particle chains aligned parallel to the applied load and field and the other perpendicular (along z axis), result to a new MRE with same axial and longitudinal stiffness, tangent of the loss angle and MR effect.
- The cube composite samples with two anisotropic halves aligned in different directions, increase their dynamic stiffness by 30% while pure anisotropic by 22% and isotropic by 13%.
- The MR effect of tangent of loss angle $\tan\delta$ of pure anisotropic and anisotropic-anisotropic composite MREs is two times higher than the one of pure isotropic and composite isotropic-anisotropic MREs.
- A strong MR effect-strain amplitude coupling effect was observed especially for composite anisotropic-anisotropic MREs.

Chapter 6: Characterization of pure compression and inclined MRE isolator

6.1 Introduction

The engine room of a marine vessel is full of rotating, reciprocating and forging machines that generate huge amounts of noise and vibration. Except the main engine, a typical engine room will contain several generators, compressors, pumps, separators, refrigerators and auxiliary engines that vibrate constantly at different frequencies. In addition, the ship is a flexible structure subjected to random multidirectional loading conditions while travelling at sea. Therefore, it is important to mount all machines to efficient isolators that are responsible for two tasks. The first is to reduce the vibration and noise transmitted from the machine to the substrate (at high frequencies) and the second to ensure that the six modes of vibration system remains stable under sea movement (at low frequencies but high displacements). For this reason, the main engine is usually mounted on several isolators inclined by an angle to cope for the multidirectional loading conditions.

In a general mass-isolator system the equipment or machine is considered as a rigid body supported by isolators that has six modes of vibration and six natural frequencies one in each direction, as shown in Figure 59. In such arrangement, any random motion of the body maybe be resolved into three translations parallel to the OY, OX and OZ axis through the centre of gravity O and three rotations about these axis (Davey A B 1965) that are coupled to each other. These motions become uncoupled when the direction of the force causing them passes through the centre of gravity of the supporting isolators.

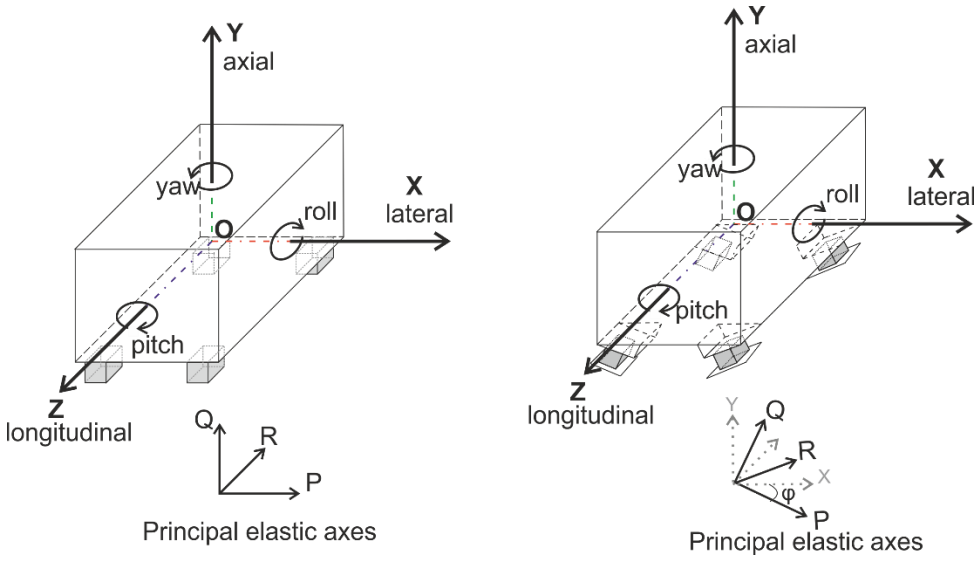

Figure 59: Diagram of a mass mounted on isolators in vertical and inclined positions.

Depending on the level of vibrations generated in each direction, the isolators can be placed, ideally symmetrically, to the vertical axial direction (under the body) or the horizontal longitudinal and lateral directions (against a wall or other fixed element) to achieve the desired reduction of vibrations. For large and heavy machines, like the ones found in marine industry, isolators are usually placed under the body in the axial direction to avoid stability problems. That means that the weight of the machine acts as a pure static compression load that will cause only a static deflection along the axial OY axis. The isolators will be always precompressed under the load of the machine, while the superimposed dynamic forces can be in any direction depending on loading conditions.

The natural frequencies of the system depend on the principal elastic axis stiffness ratios $\frac{k_p}{k_q}$ and $\frac{k_r}{k_q}$ of the mount and thus, the geometry of the elastomer and shape factor. The choice of mounting arrangement depends on the type of machine and loading conditions. When vertical exciting forces are of importance, like in reciprocating machines with vertical line of stroke, isolators working in pure compression mode are more effective. However, when dealing with horizontal exciting forces like in the case of reciprocating machines with horizontal line of stroke or rotating machines, isolators working in pure shear in the horizontal plane or the inclined arrangement should be preferred. For most common rubbers used in isolators, stiffness k_p and k_r can be estimated using shear modulus G and k_q by compression modulus E, taking under consideration the geometry of rubber mount and the appropriate shape correction function according to the shape factor and hardness of rubber.

However, for MREs this is not so simple due to the change in stiffness when the magnetic field is applied. The absolute increase will be different for each stiffness k_p, k_q and k_r and thus, modes that are uncoupled at zero field could become coupled when the magnetic field is applied. In this chapter, the composite isotropic/anisotropic and anisotropic/anisotropic MREs are tested in practice by examining the mechanical properties of a MRE prototype isolator working in pure compression and compression/shear (inclined) mode. The experimental data are then used to determine the principal elastic axis stiffness ratio $\frac{k_p}{k_q}$ and how this is influenced by the magnetic field.

6.2 Background theory

The general theory suggests that an unconstrained rigid body is free to move in six possible directions. Assuming an orthogonal OXYZ reference system where the origin O is the centre of gravity (as illustrate in Figure 60) these directions are lateral horizontal parallel to axis OX, longitudinal horizontal parallel to axis OZ, axial vertical parallel to axis OY and three rotations about these axis called here roll, pitch and yaw respectively.

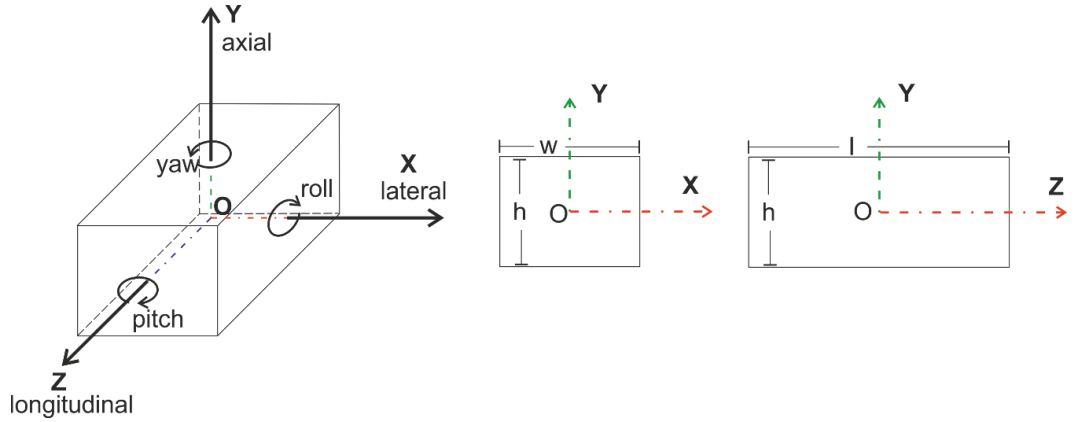

Figure 60: Diagram illustrating the six degrees of freedom of a rigid body.

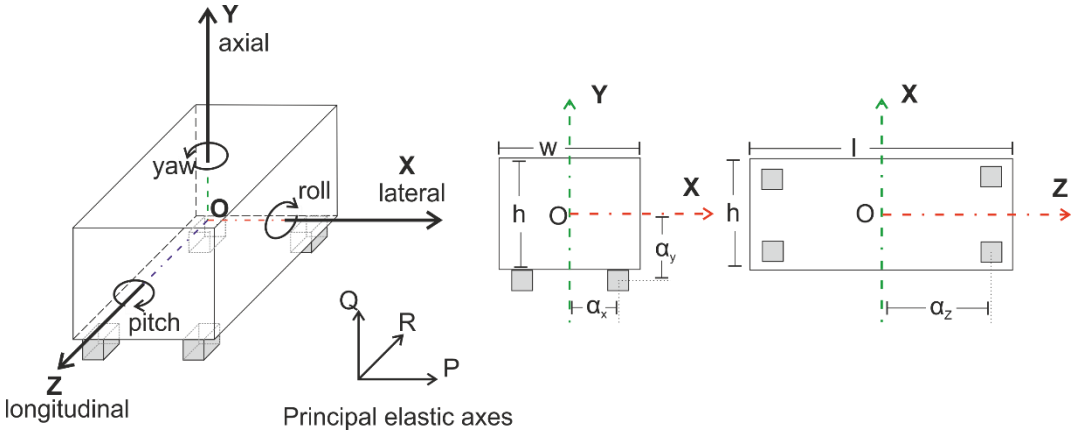

Figure 61: Diagram of a mass mounted in four isolators, where w=width, h=height, l=length of mass and α_x, α_y and α_z are the distances between the centre of gravity of body and isolator.

In a general mass-isolator system (illustrated in Figure 61) a rectangular block is mounted on four identical isolators with no motion restrictions and two planes of symmetry. The principal elastic axis Q, P, R of all isolators are orthogonal with reference axis X, Y, Z that coincide with the principal inertial axis of body. Therefore, a force applied on the OY axis will only cause a displacement on the same direction and therefore axial and yaw motion are considered uncoupled. However, the centre of gravity of the body O is much higher than the centre of gravity of the isolators (the direction of force does not pass through the centre of gravity of the isolators) and thus, any force applied along OX or OZ direction will cause translation along OX and OZ axis but also rotation about OZ and OX

axis respectively. Therefore, lateral translation and pitch motion are coupled motions like longitudinal translation and roll. Assuming x_x, x_y, x_z as the translational displacements of the centre of gravity of the body in the X,Y,Z directions, β_x, β_y , β_z the rotations of the body about those axis, u, v, w the translational displacements of the foundation and γ_x, γ_y , γ_z the rotations of the foundation, general equations of motion are:

$$[M]\begin{bmatrix}\ddot{x_x}\\ \ddot{x_y}\\ \ddot{x_z}\\ \ddot{\beta_x}\\ \ddot{\beta_y}\\ \ddot{\beta_z}\end{bmatrix}+[K]\begin{bmatrix}x_x-u\\ x_y-v\\ x_z-w\\ \beta_x-\gamma_x\\ \beta_y-\gamma_y\\ \beta_z-\gamma_z\end{bmatrix}+[C]\begin{bmatrix}\dot{x_x}-\dot{u}\\ \dot{x_y}-\dot{v}\\ \dot{x_z}-\dot{w}\\ \dot{\beta_x}-\dot{\gamma_x}\\ \dot{\beta_y}-\dot{\gamma_y}\\ \dot{\beta_z}-\dot{\gamma_z}\end{bmatrix}=\begin{bmatrix}F_x\\ F_y\\ F_z\\ M_x\\ M_y\\ M_z\end{bmatrix} \tag{6.2.1}$$

where: $[M]=\begin{bmatrix}m & 0 & 0 & 0 & 0 & 0\\ 0 & m & 0 & 0 & 0 & 0\\ 0 & 0 & m & 0 & 0 & 0\\ 0 & 0 & 0 & I_{xx} & -I_{xy} & -I_{xz}\\ 0 & 0 & 0 & -I_{yx} & I_{yy} & -I_{yz}\\ 0 & 0 & 0 & -I_{zx} & -I_{zy} & I_{zz}\end{bmatrix}$ is the mass matrix

The moments and products of inertia are defined as:

$$I_{xx}=\int_m (Y^2+Z^2)dm\ ,I_{yy}=\int_m (X^2+Z^2)dm\ \ ,I_{zz}=\int_m (Y^2+X^2)dm$$

$$I_{xy}=I_{yx}=\int_m XYdm\ ,I_{xz}=I_{zx}=\int_m XZdm\ \ ,I_{yz}=I_{zy}=\int_m YZdm$$

$$[K]=\begin{bmatrix}k_{11} & k_{12} & k_{13} & k_{14} & k_{15} & k_{16}\\ k_{21} & k_{22} & k_{23} & k_{24} & k_{25} & k_{26}\\ k_{31} & k_{32} & k_{33} & k_{34} & k_{35} & k_{36}\\ k_{41} & k_{42} & k_{43} & k_{44} & k_{45} & k_{46}\\ k_{51} & k_{52} & k_{53} & k_{54} & k_{55} & k_{56}\\ k_{61} & k_{62} & k_{63} & k_{64} & k_{65} & k_{66}\end{bmatrix}$$ is the stiffness matrix

Where the terms of stiffness matrix are defined as:

$$k_{11}=\sum k_{xx} \qquad k_{24}=k_{42}=\sum\left(k_{yz}a_y-k_{yy}a_z\right)$$

$$k_{12}=k_{21}=\sum k_{xy} \qquad k_{25}=k_{52}=\sum\left(k_{xy}a_z-k_{yz}a_x\right)$$

$$k_{13}=k_{31}=\sum k_{xz} \qquad k_{26}=k_{62}=\sum\left(k_{yy}a_x-k_{xy}a_y\right)$$

$$k_{14}=k_{41}=\sum\left(k_{xz}a_y-k_{xy}a_z\right) \qquad k_{33}=\sum k_{zz}$$

$$k_{15}=k_{51}=\sum(k_{xx}a_z-k_{xz}a_x) \qquad k_{34}=k_{43}=\sum\left(k_{yy}{a_z}^2+k_{zz}{a_y}^2-2k_{yz}a_ya_z\right)$$

$$k_{16}=k_{61}=\sum\left(k_{xy}a_x-k_{xx}a_y\right) \qquad k_{35}=k_{53}=\sum\left(k_{xz}a_ya_z+k_{yz}a_xa_z-k_{zz}a_ya_x-k_{xy}{a_z}^2\right)$$

$$k_{22} = \sum k_{yy} \qquad k_{36} = k_{63} = \sum\left(k_{xy}a_y a_z + k_{yz}a_x a_y - k_{yy}a_z a_x - k_{xz}{a_y}^2\right)$$

$$k_{23} = k_{32} = \sum k_{yz} \qquad k_{45} = k_{54} = \sum\left(k_{xy}a_x a_z + k_{xz}a_x a_y - k_{xx}a_y a_z - k_{yz}{a_x}^2\right)$$

$$k_{44} = \sum\left(k_{zz}a_y - k_{yz}a_z\right) \qquad k_{46} = k_{64} = \sum\left(k_{xx}{a_y}^2 + k_{yy}{a_x}^2 - 2k_{xy}a_x a_y\right)$$

$$k_{55} = \sum(k_{xz}a_z - k_{zz}a_x) \qquad k_{56} = k_{65} = \sum\left(k_{xy}a_y a_z + k_{yz}a_x a_y - k_{yy}a_z a_x - k_{xz}{a_y}^2\right)$$

$$k_{66} = \sum\left(k_{yz}a_x - k_{xz}a_y\right)$$

And the stiffness coefficients are defined:

$$\begin{gathered} k_{xx} = k_p cos^2\varphi_{xp} + k_q cos^2\varphi_{xq} + k_r cos^2\varphi_{xr} \\ k_{yy} = k_p cos^2\varphi_{yp} + k_q cos^2\varphi_{yq} + k_r cos^2\varphi_{yr} \\ k_{zz} = k_p cos^2\varphi_{zp} + k_q cos^2\varphi_{zq} + k_r cos^2\varphi_{zr} \\ k_{xy} = k_p cos\varphi_{xp} cos\varphi_{yp} + k_q cos\varphi_{xq} cos\varphi_{yq} + k_r cos\varphi_{xr} cos\varphi_{yr} \\ k_{xz} = k_p cos\varphi_{xp} cos\varphi_{zp} + k_q cos\varphi_{xq} cos\varphi_{zq} + k_r cos\varphi_{xr} cos\varphi_{zr} \\ k_{yz} = k_p cos\varphi_{yp} cos\varphi_{zp} + k_q cos\varphi_{yq} cos\varphi_{zq} + k_r cos\varphi_{yr} cos\varphi_{zr} \end{gathered} \tag{6.2.2}$$

Where φ_{xp}, φ_{xq}, φ_{xr} are the angles between principal axis of the resilient supporting element and X coordinate axis, φ_{yp}, φ_{yq}, φ_{yr} are the angles between principal axis of the resilient supporting element and Y coordinate axis and φ_{zp}, φ_{zq}, φ_{zr} are the angles between principal axis of the resilient supporting element and Z coordinate axis.

$$[C] = \begin{bmatrix} c_{11} & c_{11} & c_{13} & c_{14} & c_{15} & c_{16} \\ c_{21} & c_{22} & c_{23} & c_{24} & c_{25} & c_{26} \\ c_{31} & c_{32} & c_{33} & c_{34} & c_{35} & c_{36} \\ c_{41} & c_{42} & c_{43} & c_{44} & c_{45} & c_{46} \\ c_{51} & c_{52} & c_{53} & c_{54} & c_{55} & c_{56} \\ c_{61} & c_{62} & c_{63} & c_{64} & c_{65} & c_{66} \end{bmatrix} \text{ is the damping matrix}$$

Where the terms of damping matrix are defined as:

$$c_{11} = \sum c_{xx} \qquad c_{24} = c_{42} = \sum\left(c_{yz}a_y - c_{yy}a_z\right)$$

$$c_{12} = c_{21} = \sum c_{xy} \qquad c_{25} = c_{52} = \sum\left(c_{xy}a_z - c_{yz}a_x\right)$$

$$c_{13} = c_{31} = \sum c_{xz} \qquad c_{26} = c_{62} = \sum\left(c_{yy}a_x - c_{xy}a_y\right)$$

$$c_{14} = c_{41} = \sum\left(c_{xz}a_y - c_{xy}a_z\right) \qquad c_{33} = \sum c_{zz}$$

$$c_{15} = c_{51} = \sum(c_{xx}a_z - c_{xz}a_x) \qquad c_{34} = c_{43} = \sum\left(c_{yy}{a_z}^2 + c_{zz}{a_y}^2 - 2c_{yz}a_y a_z\right)$$

$$c_{16} = c_{61} = \sum\left(c_{xy}a_x - c_{xx}a_y\right) \qquad c_{35} = c_{53} = \sum\left(c_{xz}a_y a_z + c_{yz}a_x a_z - c_{zz}a_y a_x - c_{xy}{a_z}^2\right)$$

$$c_{22} = \sum c_{yy} \qquad c_{36} = c_{63} = \sum\left(c_{xy}a_y a_z + c_{yz}a_x a_y - c_{yy}a_z a_x - c_{xz}{a_y}^2\right)$$

$$c_{23} = c_{32} = \sum c_{yz} \qquad c_{45} = c_{54} = \sum\left(c_{xy}a_x a_z + c_{xz}a_x a_y - c_{xx}a_y a_z - c_{yz}{a_x}^2\right)$$

$$c_{44} = \sum\left(c_{zz}a_y - c_{yz}a_z\right) \qquad c_{46} = c_{64} = \sum\left(c_{xx}{a_y}^2 + c_{yy}{a_x}^2 - 2c_{xy}a_x a_y\right)$$

$$c_{55} = \sum\left(c_{xz}a_z - c_{zz}a_x\right) \qquad c_{56} = c_{65} = \sum\left(c_{xy}a_y a_z + c_{yz}a_x a_y - c_{yy}a_z a_x - c_{xz}{a_y}^2\right)$$

$$c_{66} = \sum\left(c_{yz}a_x - c_{xz}a_y\right)$$

And the damping coefficients are defined:

$$\begin{aligned} c_{xx} &= c_p cos^2\varphi_{xp} + c_q cos^2\varphi_{xq} + c_r cos^2\varphi_{xr} \\ c_{yy} &= c_p cos^2\varphi_{yp} + c_q cos^2\varphi_{yq} + c_r cos^2\varphi_{yr} \\ c_{zz} &= c_p cos^2\varphi_{zp} + c_q cos^2\varphi_{zq} + c_r cos^2\varphi_{zr} \\ c_{xy} &= c_p cos\varphi_{xp} cos\varphi_{yp} + c_q cos\varphi_{xq} cos\varphi_{yq} + c_r cos\varphi_{xr} cos\varphi_{yr} \\ c_{xz} &= c_p cos\varphi_{xp} cos\varphi_{zp} + c_q cos\varphi_{xq} cos\varphi_{zq} + c_r cos\varphi_{xr} cos\varphi_{zr} \\ c_{yz} &= c_p cos\varphi_{yp} cos\varphi_{zp} + c_q cos\varphi_{yq} cos\varphi_{zq} + c_r cos\varphi_{yr} cos\varphi_{zr} \end{aligned} \tag{6.2.3}$$

when the reference axis X, Y, Z are selected to coincide with the principal inertial axis of the body then $I_{xy} = I_{xz} = I_{zy} = 0$. When the principal elastic axis P, Q, R or all resilient support elements are orthogonal with reference axis X, Y, Z then:

$$k_{xx} = k_p,\ k_{yy} = k_q,\ k_{zz} = k_r \text{ and } k_{xy} = k_{xz} = k_{yz} = 0$$

$$c_{xx} = c_p,\ c_{yy} = c_q,\ k_{zz} = c_r \text{ and } c_{xy} = c_{xz} = c_{yz} = 0$$

The translational natural frequency in the Y axis f_Y and the rotational natural frequency about the Y axis $f_{n\beta_y}$, assuming linear behaviour are given by equations (6.2.4) (Harris C M 2002).

$$f_Y = \frac{1}{2\pi}\sqrt{\frac{4k_q}{m}} \quad and \quad f_{\beta_y} = \frac{1}{2\pi}\sqrt{\frac{4k_p}{m}\left(\frac{\alpha_z}{\rho_y}\right)^2 + \frac{4k_r}{m}\left(\frac{\alpha_x}{\rho_y}\right)^2} \tag{6.2.4}$$

Where $\rho_y = \sqrt{I_y/m}$ is the radius of gyration around the Y axis. The natural frequencies in the coupled modes $f_{X\beta_z}$ (lateral translation and pitch) and $f_{Z\beta_x}$ (Longitudinal translation and roll) are:

$$\left(\frac{f_{X\beta_z}}{f_Y}\right)^2 = \frac{1}{2}\left(A \pm \sqrt{A^2 - 4\frac{k_p}{k_q}\frac{{\alpha_x}^2}{{\rho_z}^2}}\right) \quad and \quad A = \frac{k_p}{k_q}\left(1 + \frac{{\alpha_y}^2}{{\rho_z}^2}\right) + \frac{{\alpha_x}^2}{{\rho_z}^2}$$

$$\left(\frac{f_{Z\beta_x}}{f_Y}\right)^2 = \frac{1}{2}\left\{B \pm \sqrt{B^2 - 4\frac{k_r}{k_q}\frac{{\alpha_z}^2}{{\rho_x}^2}}\right\} \quad and \quad B = \frac{k_r}{k_q}\left(1 + \frac{{\alpha_y}^2}{{\rho_x}^2}\right) + \frac{{\alpha_z}^2}{{\rho_x}^2} \tag{6.2.5}$$

Where $\rho_x = \sqrt{I_x/m}$, $\rho_z = \sqrt{I_z/m}$ is the radius of gyration around the X and Z axis respectively while I_x and I_z are the relevant moments of inertia. Stiffness elements k_p, k_q and k_r are defined as the equivalent stiffness corresponding to the principal elastic axis P, Q, R and in this case $k_p = k_x$, $k_q = k_y$ and $k_r = k_z$.

For these motions to become uncoupled, more isolators must be placed horizontally along the longitudinal and lateral directions between the body and a wall. When this is not possible, inclined isolators can be used to decouple the vibration modes (Jerome 2002). A mass mounted on inclined isolators system is illustrated in Figure 62. By arranging the supports in an inclined position, it is possible to make all the natural modes of vibration independent or decoupled. If the isolators are inclined in one plane then only the modes of vibration on that plane are decoupled. For example, the isolators shown in Figure 62 are inclined in the XY plane to decouple lateral translation and pitch motion. This is achieved when the line of action OOi converge on the centre of gravity or on the horizontal line passing through it.

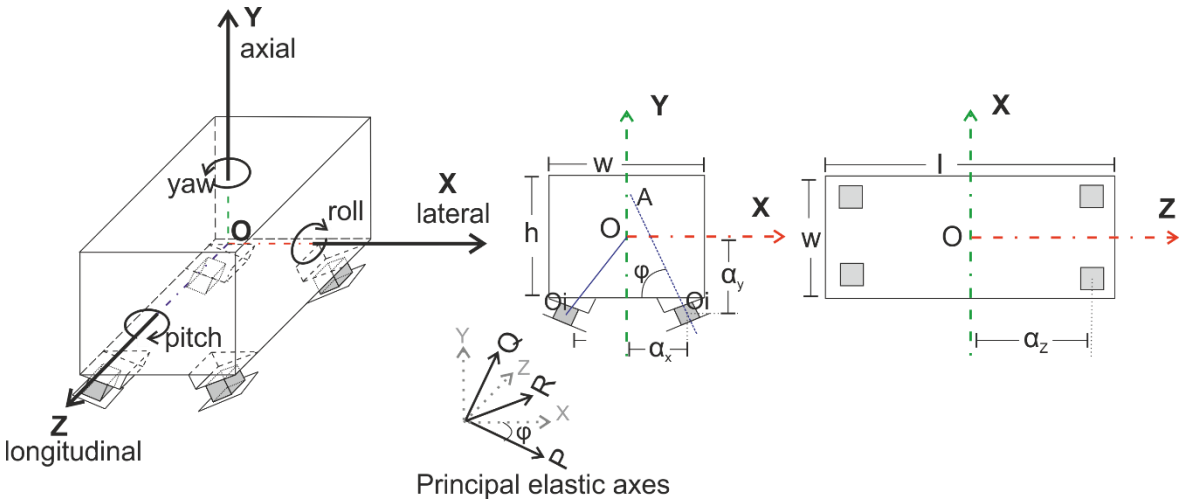

Figure 62: Diagram of a mass mounted in four inclined isolators, where w=width, h=height, l=length of mass, ϕ is the inclination angle and α_x, α_y and α_z are the distances between the centre of gravity of body and isolator.

For the system shown in Figure 62 the mass is supported by four identical isolators located symmetrically about the Y axis while the principal elastic axis Q, P, R are at an angle ϕ with the coordinate axis X, Y, Z. Planes XY and ZY are both planes of symmetry thus, axial translation and yaw rotation are decoupled from other modes. Assuming the principal elastic axis Q, P, R to be the main coordinate system and linear behaviour the natural frequencies in the axial translation f_Y (Y direction) and yaw rotation f_{β_y} are given by equations (6.2.6) (Harris C M 2002).

$$f_Y = \frac{1}{2\pi}\sqrt{\frac{4\left(k_p \sin^2\varphi + k_q \cos^2\varphi\right)}{m}}$$
$$f_{\beta_y} = \frac{1}{2\pi}\sqrt{\frac{4}{m}\left(k_p \cos^2\varphi + k_q \sin^2\varphi\right)\left(\frac{\alpha_z}{\rho_y}\right)^2 + \frac{4}{m}k_r\left(\frac{\alpha_x}{\rho_y}\right)^2} \quad (6.2.6)$$

Where, $\rho_y = \sqrt{I_y/m}$ is the radius of gyration around the Y axis. The natural frequencies in the coupled modes $f_{X\beta_z}$ (lateral translation and pitch) and $f_{Z\beta_x}$ (Longitudinal translation and roll) are:

$$\left(\frac{f_{X\beta_z}}{f_q}\right)^2 = \frac{1}{2}\left[A \pm \sqrt{A^2 - 4\frac{k_p}{k_q}\frac{{\alpha_x}^2}{{\rho_z}^2}}\right]$$
$$A = \left(\frac{k_p}{k_q}\cos^2\varphi + \sin^2\varphi\right)\left[1 + \left(\frac{\alpha_y}{\rho_z}\right)^2\right] + \left(\frac{k_p}{k_q}\sin^2\varphi + \cos^2\varphi\right)\left(\frac{\alpha_x}{\rho_z}\right)^2$$
$$+ 2\left(1 - \frac{k_p}{k_q}\right)\left|\frac{\alpha_x}{\rho_z}\right| sin\varphi\, cos\varphi \quad (6.2.7)$$
$$\left(\frac{f_{X\beta_z}}{f_q}\right)^2 = \frac{1}{2}\left[B \pm \sqrt{B^2 - 4\frac{k_r}{k_q}\left(\frac{k_p}{k_q}\sin^2\varphi + \cos^2\varphi\right)\frac{{\alpha_z}^2}{{\rho_x}^2}}\right]$$
$$B = \frac{k_r}{k_q}\left[1 + \left(\frac{\alpha_y}{\rho_x}\right)^2\right] + \left(\frac{k_p}{k_q}\sin^2\varphi + \cos^2\varphi\right)\left(\frac{\alpha_z}{\rho_x}\right)^2$$

Where $f_q = \frac{1}{2\pi}\sqrt{\frac{4k_q}{m}}$ is a mathematical term used for convenience. The conditions of decoupling the lateral (X direction) and pitch modes are defined by equation (6.2.8) (Harris C M 2002). If longitudinal translation and roll motion were to be uncoupled, the isolators should be inclined in the YZ plane.

$$\frac{k_q}{k_p} = \frac{\frac{\alpha_x}{\alpha_y} + tan\varphi'}{\frac{\alpha_x}{\alpha_y} - cot\varphi'} \quad (6.2.8)$$

When equation (6.2.8) is satisfied the decoupled natural frequencies for lateral translation f_X and pitch rotation f_{β_z} are given from equations:

$$f_X = \frac{1}{2\pi}\sqrt{\frac{4\left(k_p \sin^2\varphi' + k_q \cos^2\varphi'\right)}{m}}, \quad f_{\beta_z} = \frac{1}{2\pi}\frac{\alpha_x}{\rho_z}\sqrt{\frac{4k_q k_p}{m\left(k_q \sin^2\varphi' + k_p \cos^2\varphi'\right)}} \quad (6.2.9)$$

6.3 Details of experiment

MRE samples

Following the same procedure with the one mentioned in section (3.2) the simple MRE samples isotropic c, anisotropic c, parallel (sample 1c and sample 3c) and series (sample 2c) combination configuration were made as shown in Figure 63. Sample 3c consists of four anisotropic parts, two with particle alignment parallel to the axial direction and two perpendicular to it. The dimensions of these samples were 20mm length and 34mm depth to fit exactly on the area of each left of the electromagnet core. The height was set to 5mm to achieve a small gap in the magnetic circuit and thus, a higher magnetic field. All anisotropic MREs were cured under a magnetic flux of 0.51 T that was produced by a double pair of permanent magnets. Therefore, these set of anisotropic samples were cured under a higher magnetic field than anisotropic a sample and is expected to have different mechanical properties.

Composite samples were manufactured in two steps. For sample 1c, a cured anisotropic c sample was cut in 4 pieces of 8.5 mm x20mm each. Two of these parts when then placed back to the aluminium mould and the isotropic MRE was poured to fill the gaps. For sample 3c, a cured anisotropic c sample was cut in 4 pieces of 5mm x 34mm each. Two of these pieces were then rotated by 90^0 (so that the particles were aligned in the longitudinal direction) and placed back to the mould. New anisotropic MRE was poured to fill in the gaps and the mould was left to cure again under a double set of permanent magnets as described in section (3.2). For sample 2c, the isotropic half was first made and after it had cured it was placed back to the mould and the anisotropic part was poured on top. The sample was then left to cure under a double set of magnets.

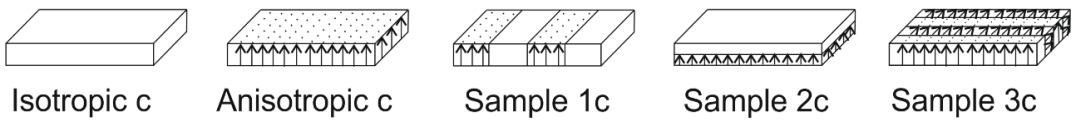

Figure 63: MRE samples

Test setup

Both static and dynamic loading tests were performed using INSTRON PULS E1000 electromechanical dynamic tester for a range of frequencies and load amplitudes. The samples where first preloaded under static load for four cycles to avoid the Mullins effect and then the dynamic loading cycles where performed under a static force. Two types of dynamic loading cycles were carried out at 0.06, 0.12 and 0.19 T magnetic flux values corresponding to 1,2 and 3 Amps electric current fed to the electromagnet. One amplitude sweep cycle, where the displacement amplitude increased from 0.025 to 0.15mm at a constant frequency of 5 Hz, and a second frequency

sweep cycle where the frequency was increased from 0.5Hz to 70 Hz at constant displacement amplitude of 0.05mm. The details of the dynamic test are mentioned in Table 27. The displacement amplitude and frequency sweep cycles for both pure compression and inclined isolators were performed under a static load of 80N. Since the pure compression isolator is much stiffer than the inclined one, the displacement amplitude was swept from 0.02mm to 0.08mm to get the same range of dynamic force values for both cases.

Table 27: Summary of test loading cycles for dynamic tests.

<table>
<tr><th>Test</th><th colspan="2"></th><th>Magnetic field</th></tr>
<tr><td rowspan="5">Amplitude sweep</td><td colspan="2">Displacement amplitude (mm)</td><td rowspan="10">1Amp=60 mT
2Amp=120 mT
3Amp=190 mT</td></tr>
<tr><td>Pure compression</td><td>0.02,0.04,0.06,0.08</td></tr>
<tr><td>Inclined</td><td>0.025,0.05,0.075,0.1,0.125,0.15</td></tr>
<tr><td>Loading frequency</td><td>5 Hz</td></tr>
<tr><td>Static load</td><td>80N</td></tr>
<tr><td rowspan="3">Frequency sweep</td><td>Displacement Amplitude</td><td>0.05 mm</td></tr>
<tr><td>Loading frequency (Hz)</td><td>0.5,1,5,10,20,30,40,50,60,70*</td></tr>
<tr><td>Static load</td><td>80N</td></tr>
<tr><td rowspan="3">Transmissibility</td><td>Displacement Amplitude</td><td>0.05 mm</td></tr>
<tr><td>Frequency range</td><td>1 to 70Hz</td></tr>
<tr><td>Static load</td><td>80N</td></tr>
</table>

*The number of cycles was increased for each frequency in order to allow for the amplitude control feature of the wavematrix software to reach the desired amplitude with increasing frequency.

6.4 Pure compression MRE isolator

Zero field device characterization

The static load-displacement curves of all samples at zero field are presented in Figure 64. As expected anisotropic MRE is the hardest while isotropic the softest. Parallel configuration composite samples 1c and 3c have similar static stiffness while series configuration sample 2c is slightly softer as theory indicates. The stiffness of parallel sample 3c is slightly higher than sample 1c due to its half anisotropic part with chains aligned perpendicular to the direction of the applied load that is slightly stiffer than pure isotropic MRE. These agree with the results of the compression tests on cube samples presented in chapter 5.

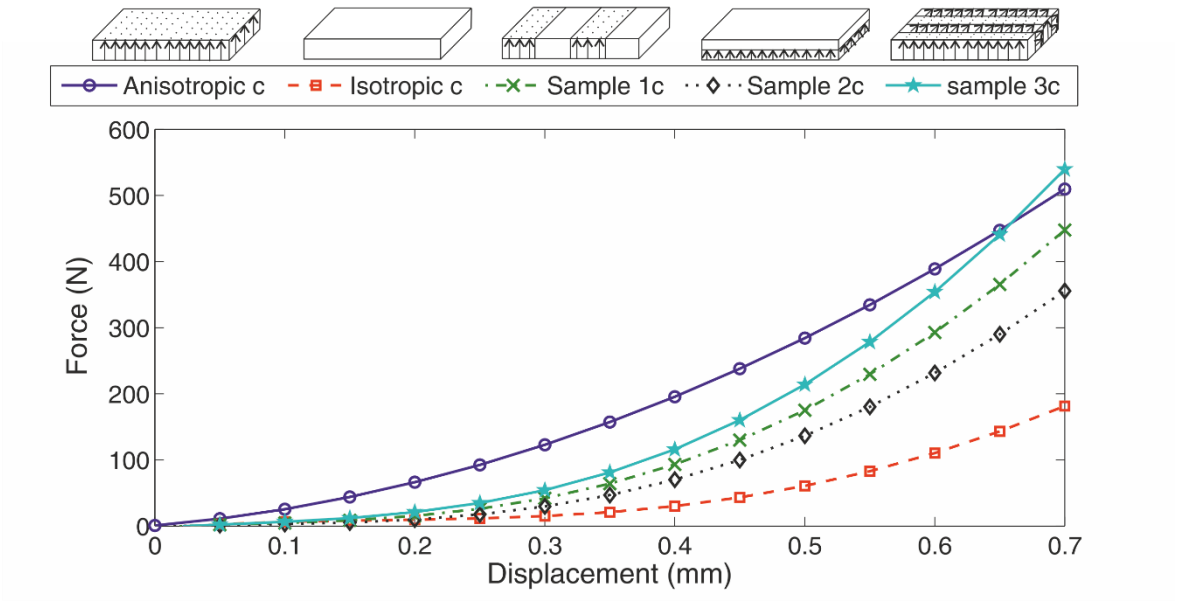

Figure 64: Static force-displacement curves of pure compression isolator using anisotropic c, isotropic c, sample 1c sample 2c and sample 3c MREs.

The variation of zero field dynamic stiffness $|K^*|$, real K' and K'' imaginary component of dynamic stiffness and tangent of the loss angle $tan\delta$ with increasing displacement amplitude for all samples is illustrated in Figure 65. Dynamic stiffness $|K^*|$ decreases with increasing amplitude while tangent of the loss angle tanδ increases. These agree with the results of the compression tests on cube samples presented in chapter 5. As expected, the isolator with anisotropic MREs has the highest stiffness while composite samples sample 1c and 3c show similar dynamic stiffness values. However, the isolator with pure isotropic MRE has a higher dynamic stiffness than the isolator with the composite samples. This is because the 80N static load causes different static deformation (prestrain) for each type of MRE sample, as shown in Table 28

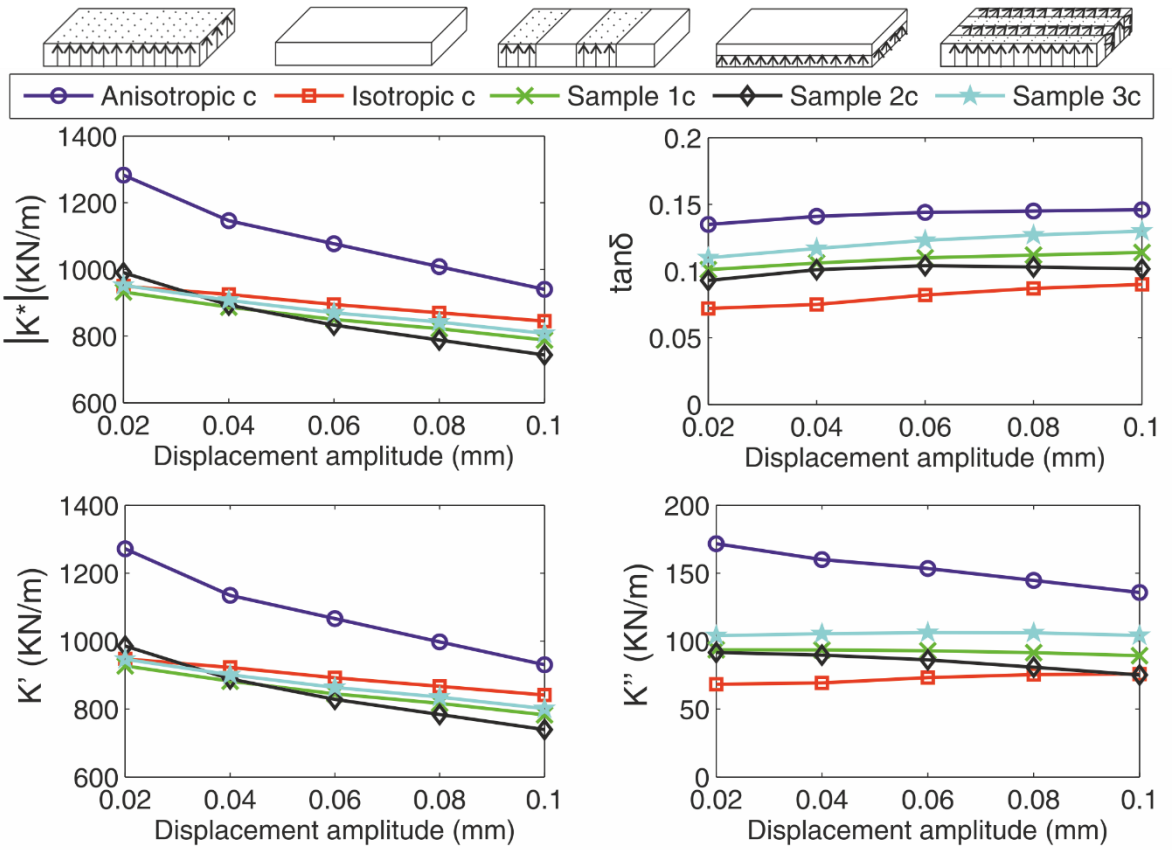

Figure 65: Zero field mechanical properties of compression isolator, in respect to displacement amplitude (at 5Hz frequency and 80N static load)

Table 28: Static deflection and prestrain under 80N static force for compression isolator.

	At 0T and 80N static load		
MRE sample	**Static deflection**	**prestrain**	**Static K**
Anisotropic c	0.25 mm	5%	320 KN/m
Isotropic c	0.5 mm	10%	160 KN/m
Sample 1c	0.34 mm	6.8%	235 KN/m
Sample 2c	0.39 mm	7.8%	205 KN/m
Sample 3c	0.33 mm	6.6%	242 KN/m

Using equations from section (5.2) the static stiffness of composite samples with equal parts of isotropic and anisotropic MREs (α=b=1) are:

Samples 1c and 3c in compression isolator: $K = \frac{K_{iso\_c}+aK_{an\_c}}{1+a} = \frac{320+160}{2} = 240$ KN/m

Sample 2c in compression isolator: $K = \frac{(b+1)K_{iso\_c}K_{an\_c}}{bK_{an\_c}+K_{iso\_c}} = \frac{2*320*160}{320+160} = 213$ KN/m

Where K_{iso_c} and K_{an_c} are the static stiffnesses of isotropic c and anisotropic c samples in pure compression isolator, mentioned in Table 28, respectively. As described analytically in section (4.4), the dynamic stiffness under pure compression load increases greatly with increasing prestrain values. Isotropic MREs are much softer than composite samples and thus, the static deformation caused by the 80N load is much higher leading to dynamic stiffness values similar to composite samples. Because sample 2c is softer it is pre compressed by 1% more than sample 1c under the same 80N static force. Thus, dynamic stiffness of sample 2c becomes as high as the dynamic stiffness of samples 1c and 3c. Tangent of loss factor tanδ of composite samples is between the ones of isotropic and anisotropic MREs as expected.

The variation of dynamic stiffness $|K^*|$, real K' and K'' imaginary component of dynamic stiffness and tangent of the loss angle tanδ with increasing loading frequency is illustrated in Figure 66. Dynamic stiffness $|K^*|$ and real component of dynamic stiffness K' rises slightly with increasing frequency, while tangent of the loss angle tanδ and imaginary component of dynamic stiffness K'' increases until about 10Hz to decrease slowly for higher frequency values. The results agree with the ones presented in chapter 5 regarding pure compression tests in anisotropic, isotropic and their combination composite samples.

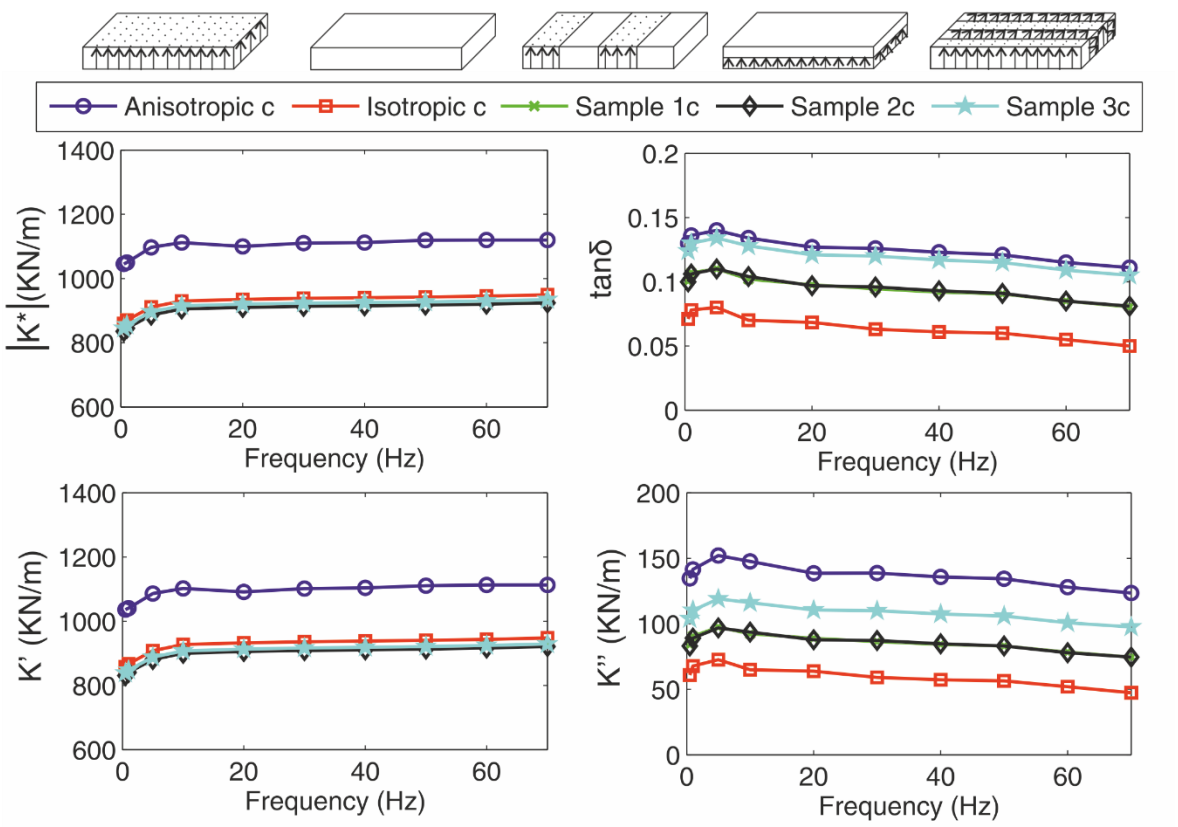

Figure 66: Zero field mechanical properties of compression isolator, in respect to frequency (at 0.05mm displacement amplitude and 80N static load).

Effect of magnetic field

The magnetorheological effect of real K' and imaginary K'' components of dynamic stiffness of all samples in the pure compression isolator at 0.04mm displacement amplitude is shown in Figure 67. The MR effect of dynamic stiffness $|K^*|$, real K' and K'' imaginary component of dynamic stiffness and tangent of the loss angle tanδ in respect to displacement amplitude Xo and current I fed to the electromagnet for isotropic c, anisotropic c and composite samples 1c, 2c and 3c is presented in Figure 68, Figure 69, Figure 70, Figure 71 and Figure 72 respectively. Isotropic MRE showed the lowest MR effect of 38% at 3 Amps. The MR effect of isotropic/anisotropic parallel sample 1c is 50% that is between the isotropic and anisotropic MREs. Anisotropic, series isotropic/anisotropic sample 2c and anisotropic/anisotropic sample 3c have all similar MR effect of about 65% for both components of dynamic stiffness.

MR effect of both components of dynamic stiffness decreases as displacement amplitude increases for all samples while MR effect of imaginary component of dynamic stiffness K'' is 5 % higher of MR effect of real component of dynamic stiffness K' for all samples except isotropic MRE. The result is a 5% positive MR effect of tanδ for all samples except isotropic MRE where it becomes negative at -5 %, which does not vary with increasing magnetic field or strain amplitude. Therefore, damping capability of all samples is not affected from the magnetic field.

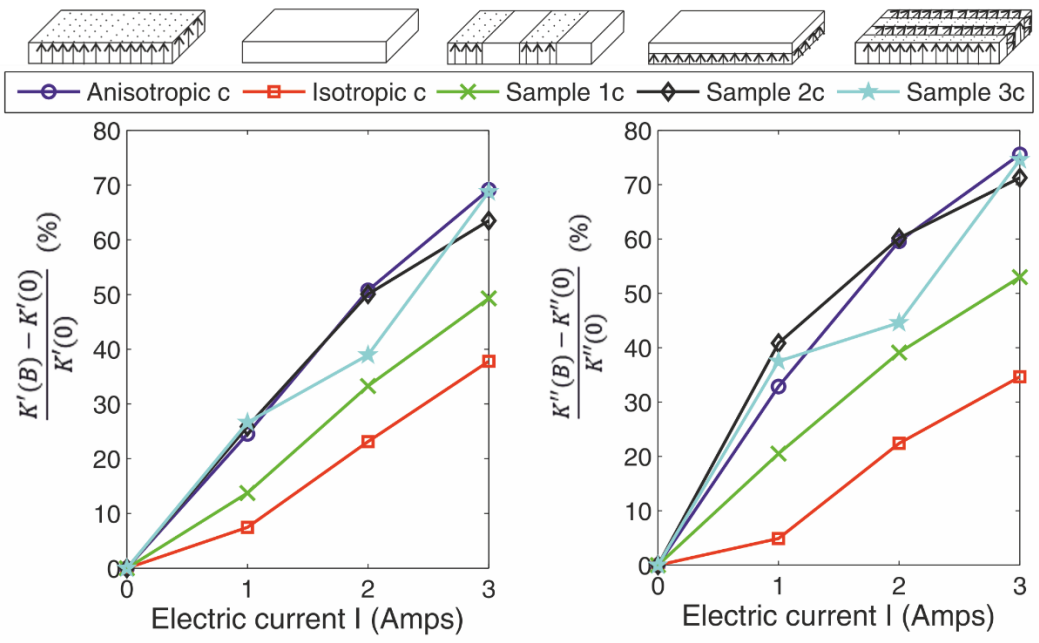

Figure 67: MR effect of real K' and K'' imaginary component of dynamic stiffness (compression) for all samples in respect to electric current I (at 0.04mm displacement amplitude, 5Hz frequency and 80N static force).

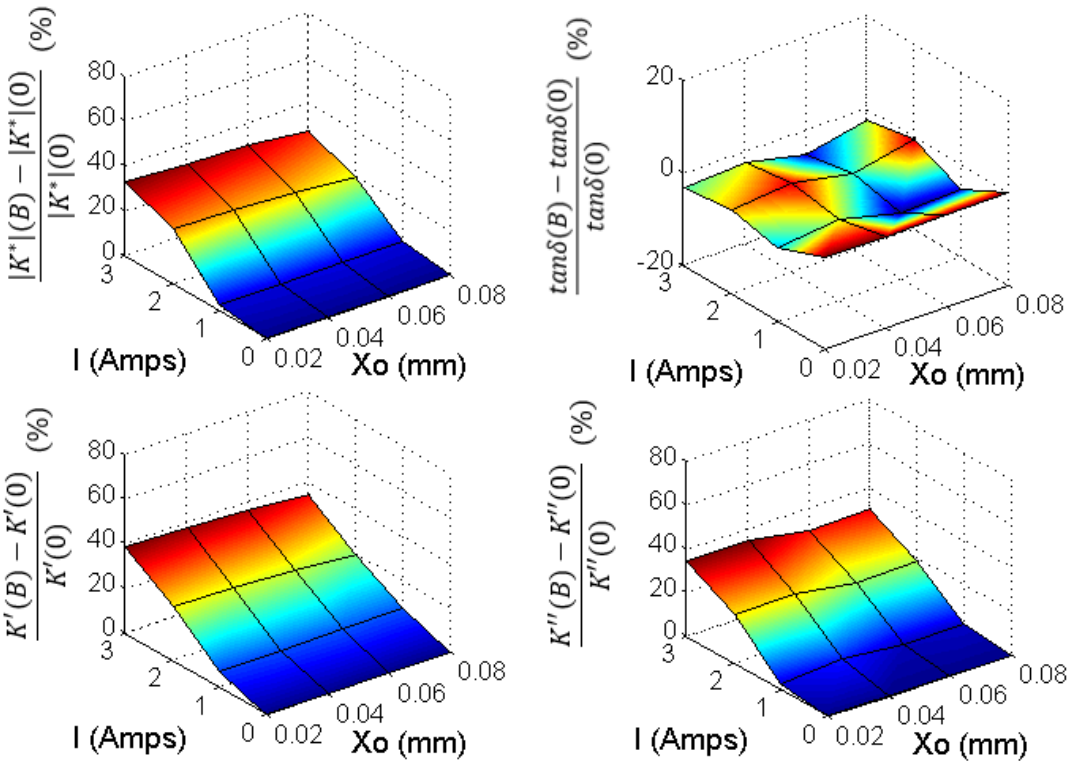

Figure 68: MR effect of isotropic c MRE (compression) in respect to displacement amplitude Xo and electric current I (at 5Hz and 80N static force).

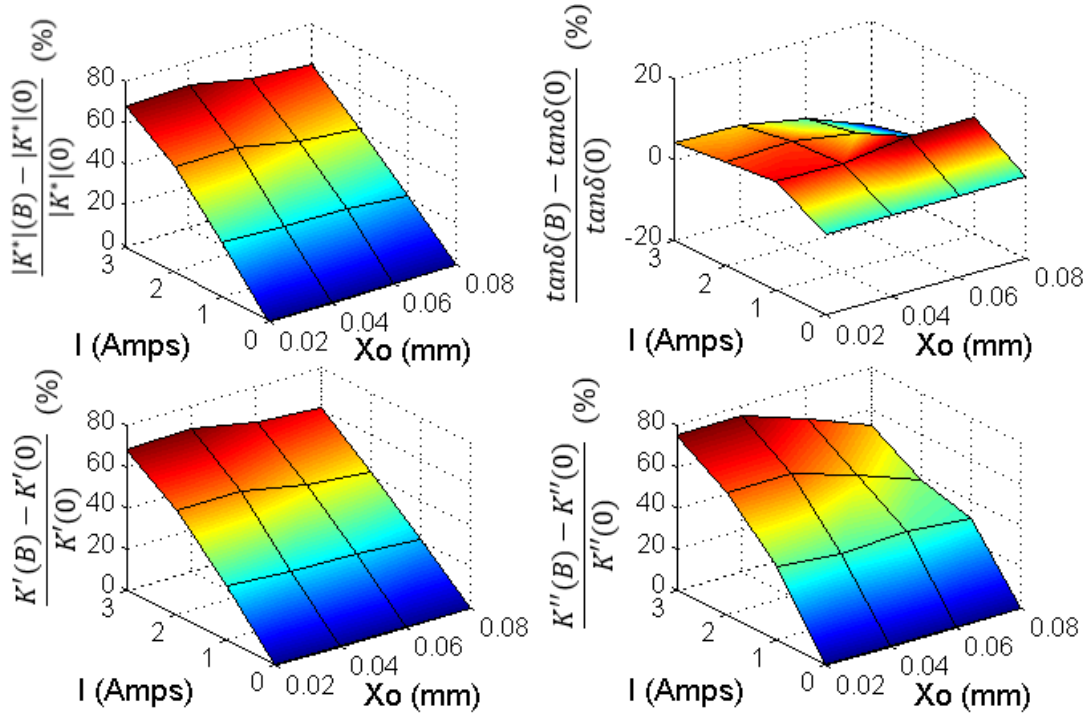

Figure 69: MR effect of anisotropic c MRE (compression) in respect to displacement amplitude Xo and electric current I (at 5Hz and 80N static force).

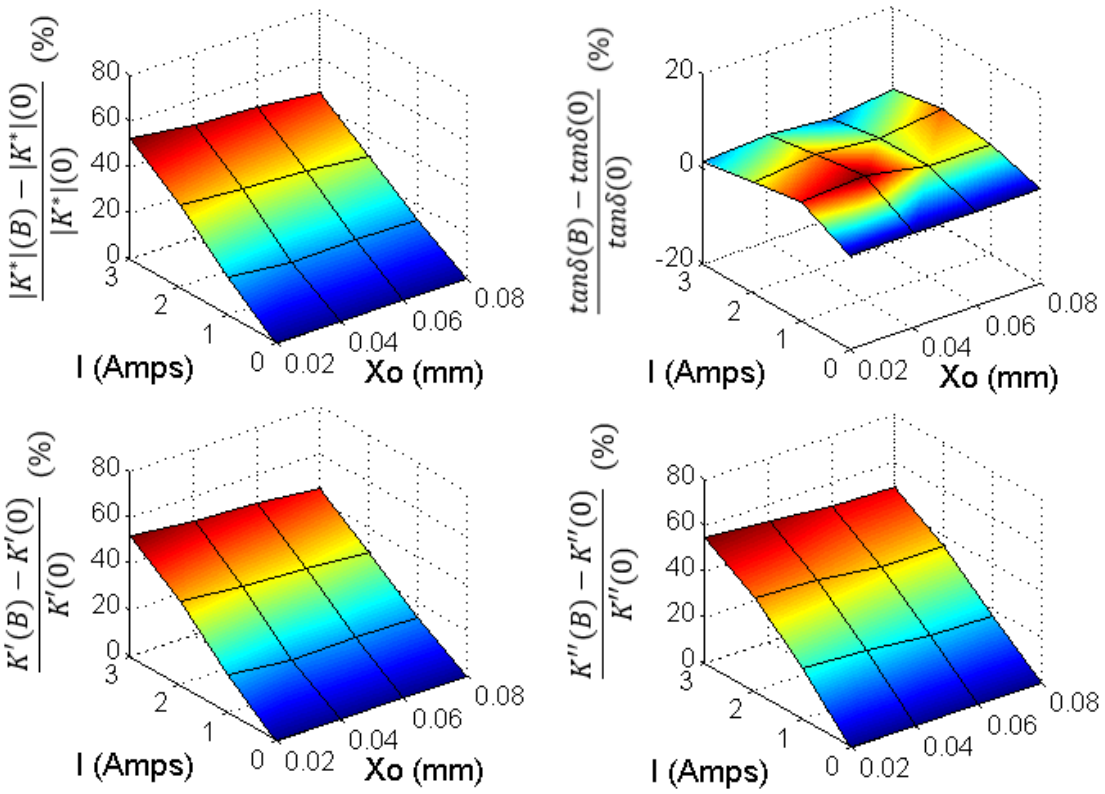

Figure 70: MR effect of parallel configuration composite sample 1c MRE (compression) in respect to displacement amplitude Xo and electric current I (at 5Hz and 80N static force).

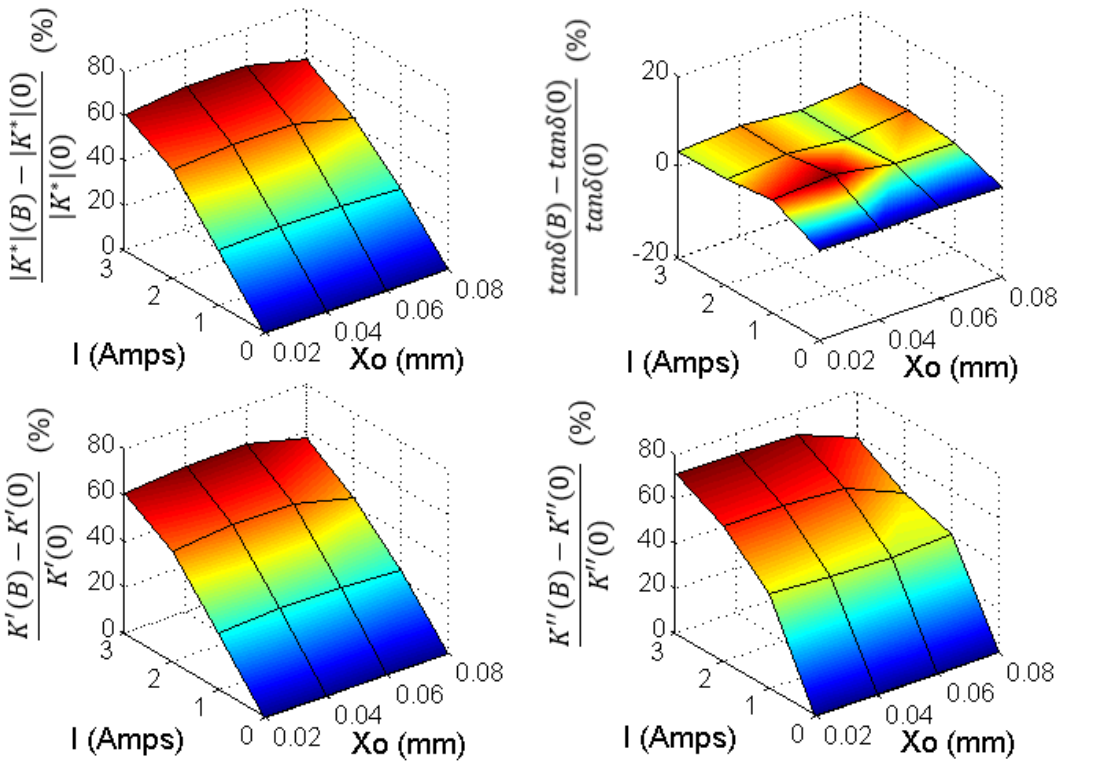

Figure 71: MR effect of series configuration composite sample 2c MRE (compression) in respect to displacement amplitude Xo and electric current I (at 5Hz and 80N static force).

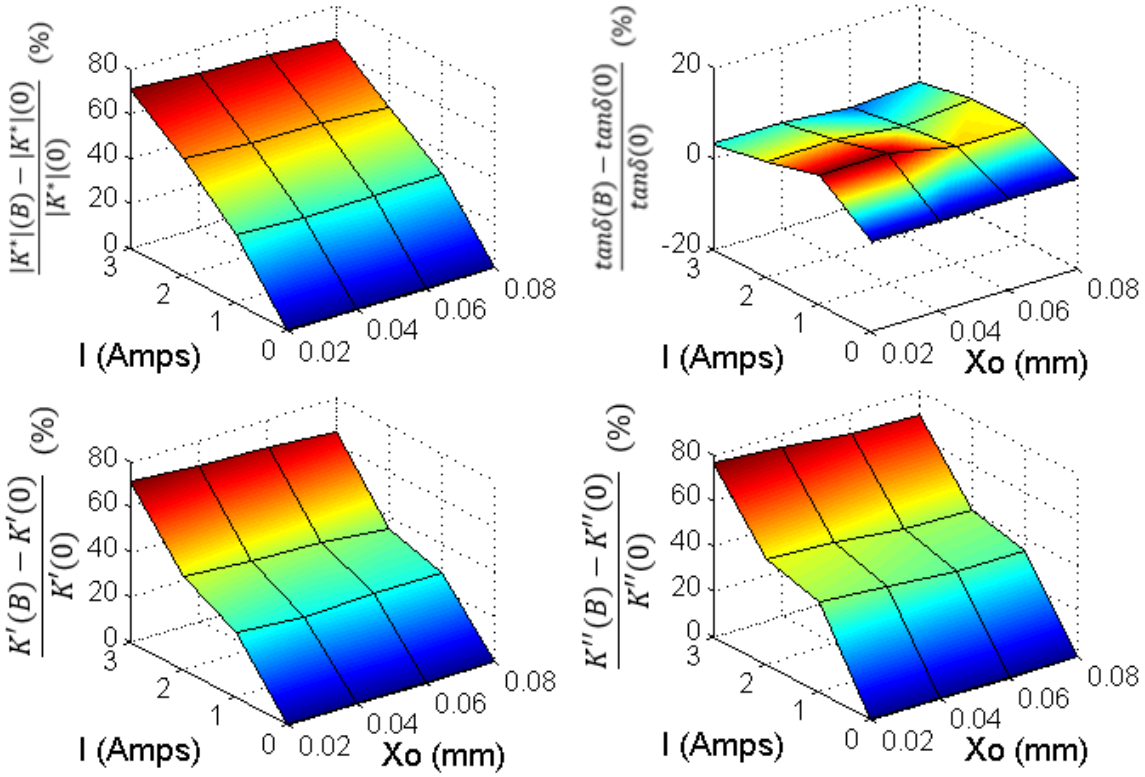

Figure 72: MR effect of parallel configuration composite sample 3c MRE (compression) in respect to displacement amplitude Xo and electric current I (at 5Hz and 80N static force).

On-off operation

Figure 73 illustrates the displacement and load time sequences of pure compression isolator with anisotropic c MRE samples under 80N static load, 30N dynamic load and 1Hz frequency. The second graph corresponds to the actual displacement data recorded, where the change in the static displacement with the applied field is obvious. The last graph illustrates only the dynamic displacement when the static component was subtracted. The effect of the magnetic field is instant and irreversible in both on and off stages. However, the variation of the static stiffness in such a test configuration where there are no movement constrictions in the axial direction is the dominant trend.

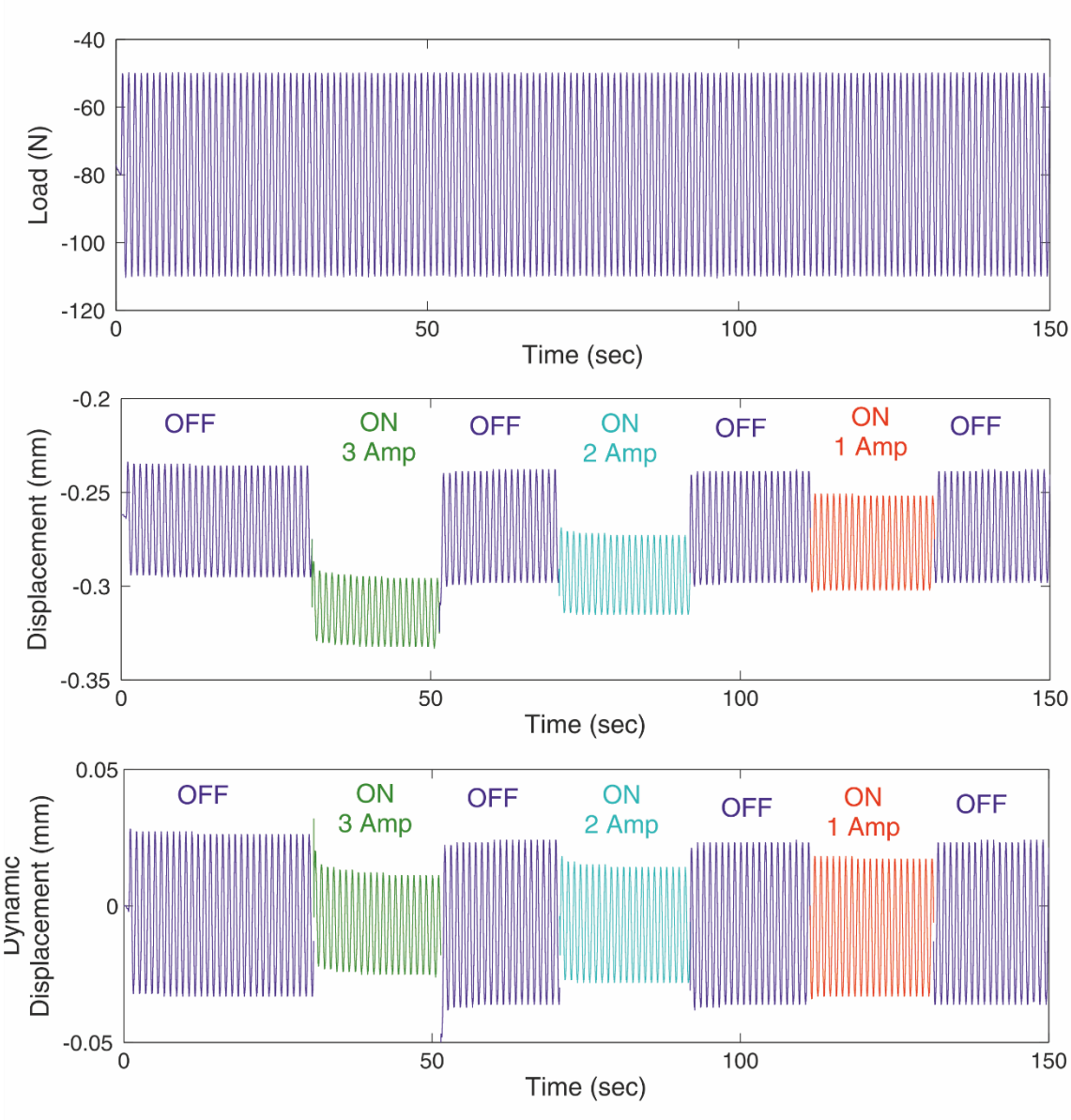

Figure 73: Displacement and load time sequences of pure compression isolator with anisotropic c MRE samples under 30N dynamic load and 1Hz frequency.

Figure 74 illustrates a zoomed version of the previous force and displacement time sequences when the 3 Amps electric current is switched on and off again. The transition period from zero to three amps is smooth and reversible regarding both static and dynamic displacement. Figure 75 illustrates the dynamic load amplitude, displacement amplitude and dynamic stiffness amplitude $|K^*|$ when the 3 Amps electric current is switched on and off. These values are provided from Instron Puls DMA calculation software and are in respect to cycles (one full period) since dynamic stiffness needs one full cycle to be calculated. In this test the load frequency was 5Hz thus, one cycle is 0.2sec. The anisotropic compression isolator needs 11 cycles or 2.2 seconds to reach a steady state when the current is switched on and off again.

However, the time response of the MRE isolator depends mostly on the speed and accuracy of the power source that provides the current to the electromagnet and the magnetic circuit of the electromagnet itself. When the power source cannot provide a stabilized electric current or needs more time to reach a stable level the response of the isolator will be slower or even unstable. In addition, if the magnetic circuit has high losses it will need more time to produce a stable magnetic field especially in the case of AC electric current or when the DC electric current is switched on and off very fast.

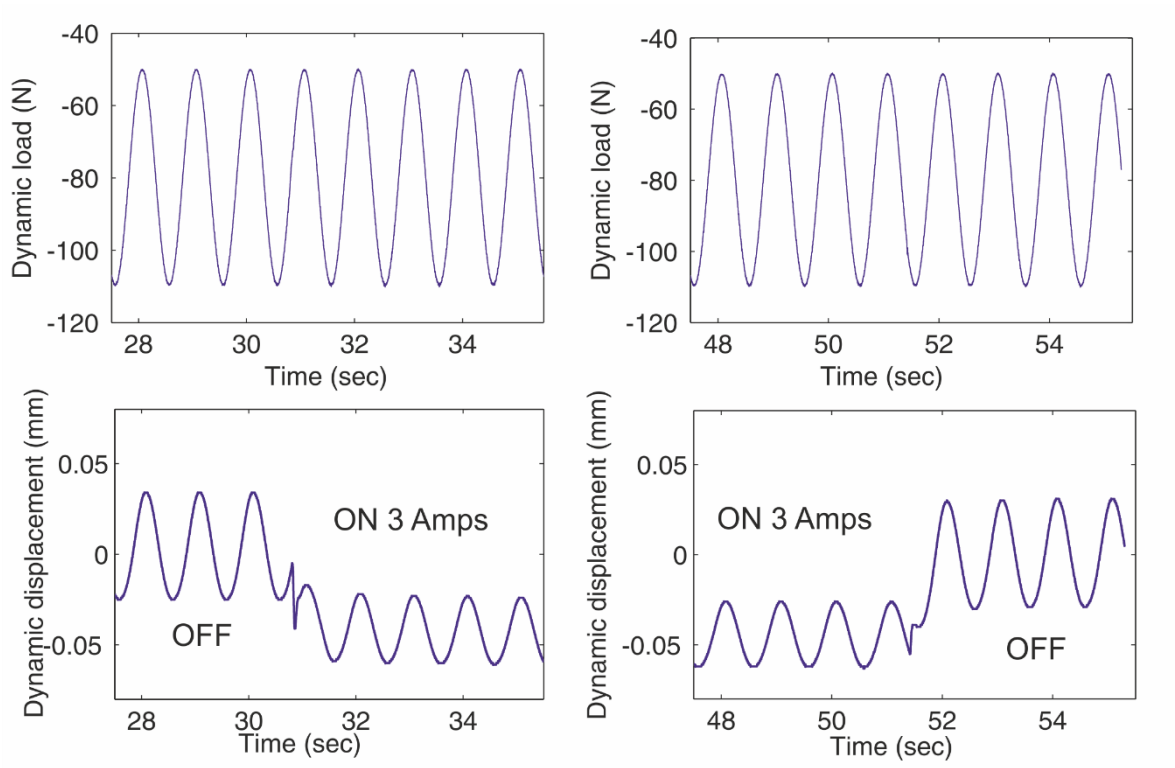

Figure 74: Dynamic load and displacement of compression anisotropic MRE isolator at the time when the electric current is switched on and off (at 30N amplitude and 1Hz frequency).

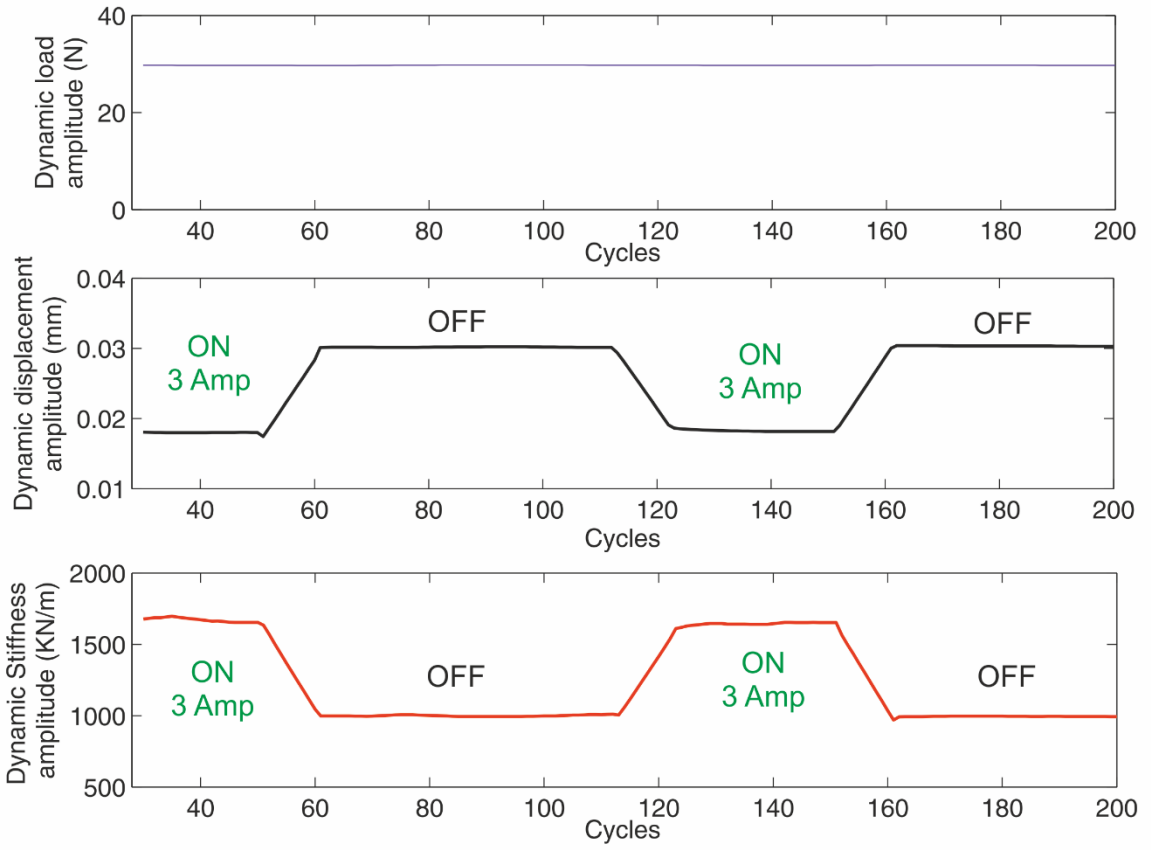

Figure 75: Dynamic force amplitude (5 Hz frequency), displacement amplitude and stiffness of compression isolator with anisotropic MREs in an ON-OFF operation. One cycle is 0.2 sec.

6.5 Inclined MRE isolator

Zero field device characterization

The zero-field static force-displacement curves for all samples in the inclined isolator are presented in Figure 76. Isotropic c MRE is the softest followed by isotropic/anisotropic series configuration sample 2c and then parallel configuration sample 2c. In the case of inclined isolator composite sample 3c has the same static stiffness with anisotropic sample. This is due to the direction of the particles in each anisotropic part (part 1 and 2) as illustrated in Figure 77. When a vertical force F is applied to the 45^0 inclined isolator, the MRE is subjected to equal shear and compression load components Fs and Fc respectively. Part 1 of MRE sample 3c has its particles aligned perpendicular to the shear force Fs and parallel to the compression force Fc, while part 2 the other way around.

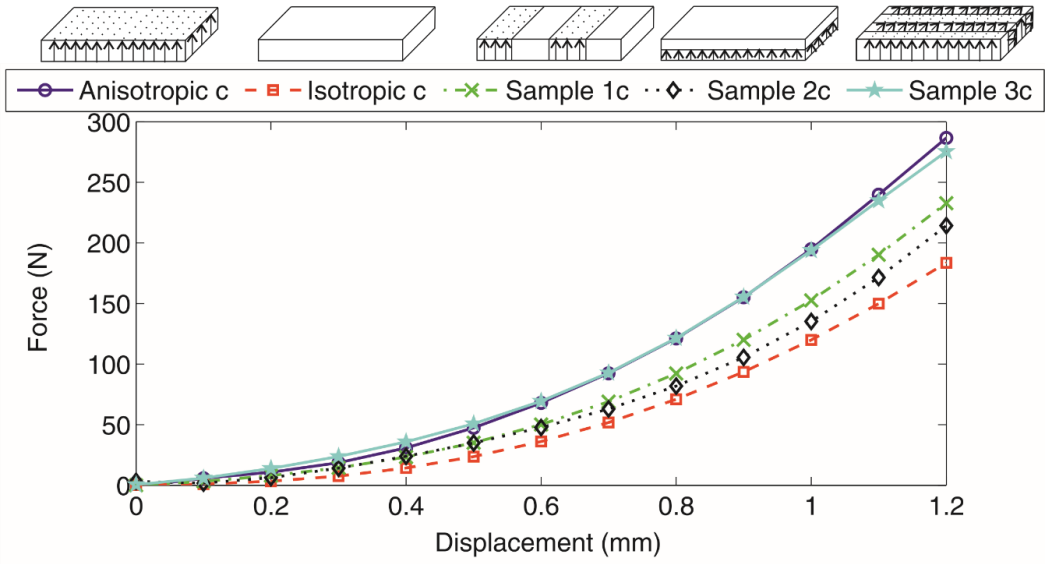

Figure 76: Zero field static stiffness-displacement curves of inclined isolator using anisotropic c, isotropic c, sample 1c sample 2c and sample 3c MREs.

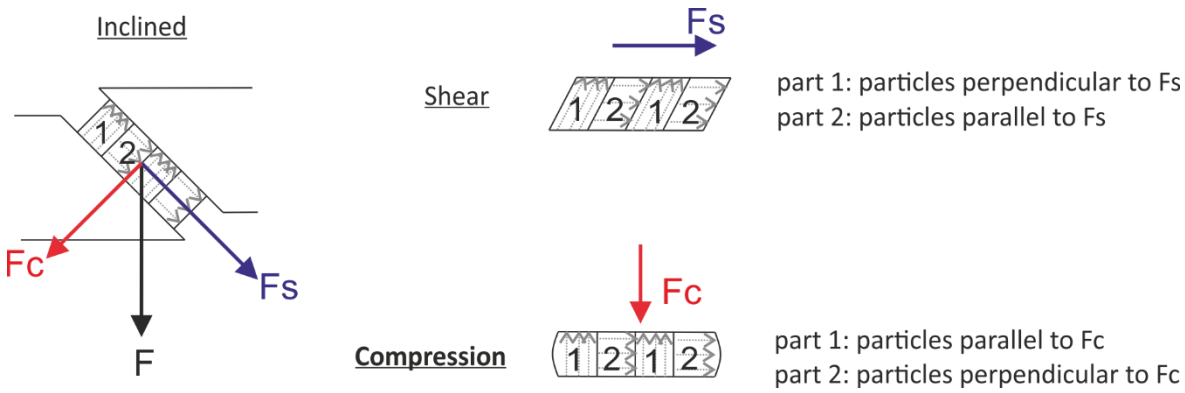

Figure 77: Diagram of loading modes of composite sample 3c in inclined isolator

In pure compression, the stiffness of anisotropic MREs with particles perpendicular to the direction of the applied compression force is close to the pure isotropic sample (section 5.5). However, this

is not valid under shear loading conditions. It has been reported that the zero-field shear modulus G of anisotropic MREs with particles aligned perpendicular to the applied shear force is higher than the one with particles aligned parallel to the direction of the shear force (Boczkowska A 2012), (Schubert G 2015). For composite MRE sample 3c this means that shear stiffness of part 2 will be higher than the stiffness of part 1 as well as the pure anisotropic c sample. Thus, composite sample 3c has higher stiffness in shear than pure anisotropic c MRE but lower in compression. Since in inclined isolator the MRE is subjected to both shear and compression forces, the total static stiffness of sample 3c becomes equal to the pure anisotropic sample.

The variation of zero field dynamic stiffness $|K^*|$, real K' and imaginary K'' components of dynamic stiffness and tangent of the loss angle $tan\delta$ with increasing displacement amplitude for isotropic c, anisotropic c and composite samples 1c, 2c and 3c are illustrated in Figure 78. Dynamic stiffness $|K^*|$ decreases with increasing amplitude while tangent of the loss angle tanδ increases. These results are expected since MR elastomers under pure shear loading conditions behave in a similar manner to pure compression (Opie S 2011). The isolator with anisotropic MREs has the highest dynamic stiffness, the one with isotropic the lowest and all composite MREs have a similar dynamic stiffness that is between pure isotropic and anisotropic values. This is attributed to the different prestrain caused by 80N static force that affects the value of zero field compression dynamic stiffness.

In this case, the static deflections caused by 80N static force are much higher than the pure compression isolator. However, dynamic stiffness is not as sensitive to static prestrain because the dynamic shear stiffness component is independent of prestrain. The inclined isolator with anisotropic MRE is pre compressed by 0.19 mm more than the inclined isolator with isotropic MRE while for the pure compression isolator the equivalent difference was 0.25mm.

For samples 1c and 2c in inclined isolator:

Sample 1c in inclined isolator: $$K = \frac{K_{iso\_in} + aK_{an\_in}}{1+a} = \frac{123+95}{2} = 109$$

Sample 2c in inclined isolator: $$K = \frac{(b+1)K_{iso\_in}K_{an\_in}}{bK_{an\_in}+K_{iso\_in}} = \frac{2*123*95}{123+95} = 107$$

Where K_{iso_in} and K_{an_in} are the static stiffness's of isotropic c and anisotropic c samples in inclined isolator, mentioned in Table 29. Static stiffness of anisotropic/anisotropic sample 3c cannot be predicted form the above equations since it is equal to the stiffness of pure anisotropic sample. Thus for the composite samples under combined shear/compression loads the static and dynamic stiffness can not be predicted accurately by simple equations (5.2.4),(5.2.5), (5.2.12) and (5.2.13).

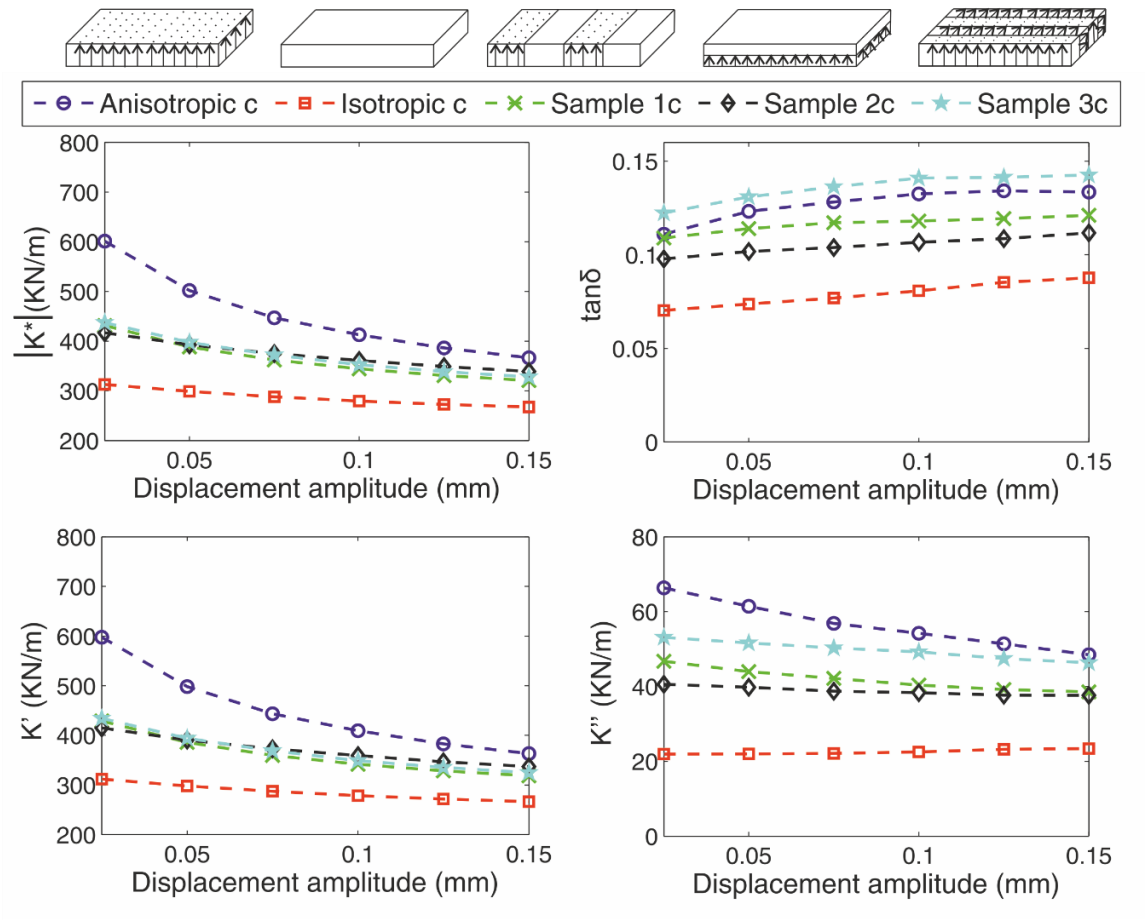

Figure 78: Zero field mechanical properties of inclined isolator will isotropic c, anisotropic c, sample 1c, sample 2c and sample 3c in respect to displacement amplitude (at 5Hz frequency and 80N static load)

Table 29: Static deflection and prestrain caused to inclined isolator by 80N static force.

	Inclined isolator		
MRE sample	**Static deflection**	**prestrain**	**Static K**
Anisotropic c	0.65 mm	13%	123 (KN/mm)
Isotropic c	0.84 mm	17%	95 (KN/mm)
Sample 1c	0.75 mm	15%	107 (KN/mm)
Sample 2c	0.78 mm	16%	103 (KN/mm)
Sample 3c	0.65 mm	13%	123 (KN/mm)

Composite anisotropic/anisotropic sample 3c has the same real dynamic stiffness K' with isotropic/anisotropic samples 1c and 2c but the imaginary component of dynamic stiffness K'' is 40% higher. As a result, tangent of loss angle tanδ becomes 10% greater than the anisotropic

sample itself. Therefore, composite sample 3c has the same zero field static stiffness, same dynamic stiffness and higher tangent of loss angle tanδ with anisotropic MRE.

The variation of dynamic stiffness $|K^*|$, real K' and K'' imaginary component of dynamic stiffness and tangent of the loss angle tanδ with increasing load frequency are illustrated in Figure 79. Dynamic stiffness $|K^*|$ rises slightly with increasing frequency, while tangent of the loss angle increases until about 10Hz to decrease slowly for higher frequency values. The results agree with the ones presented in previous section (6.3) regarding pure compression isolator. Therefore, in respect to load frequency the inclined isolator behaves in the same manner with the pure compression isolator.

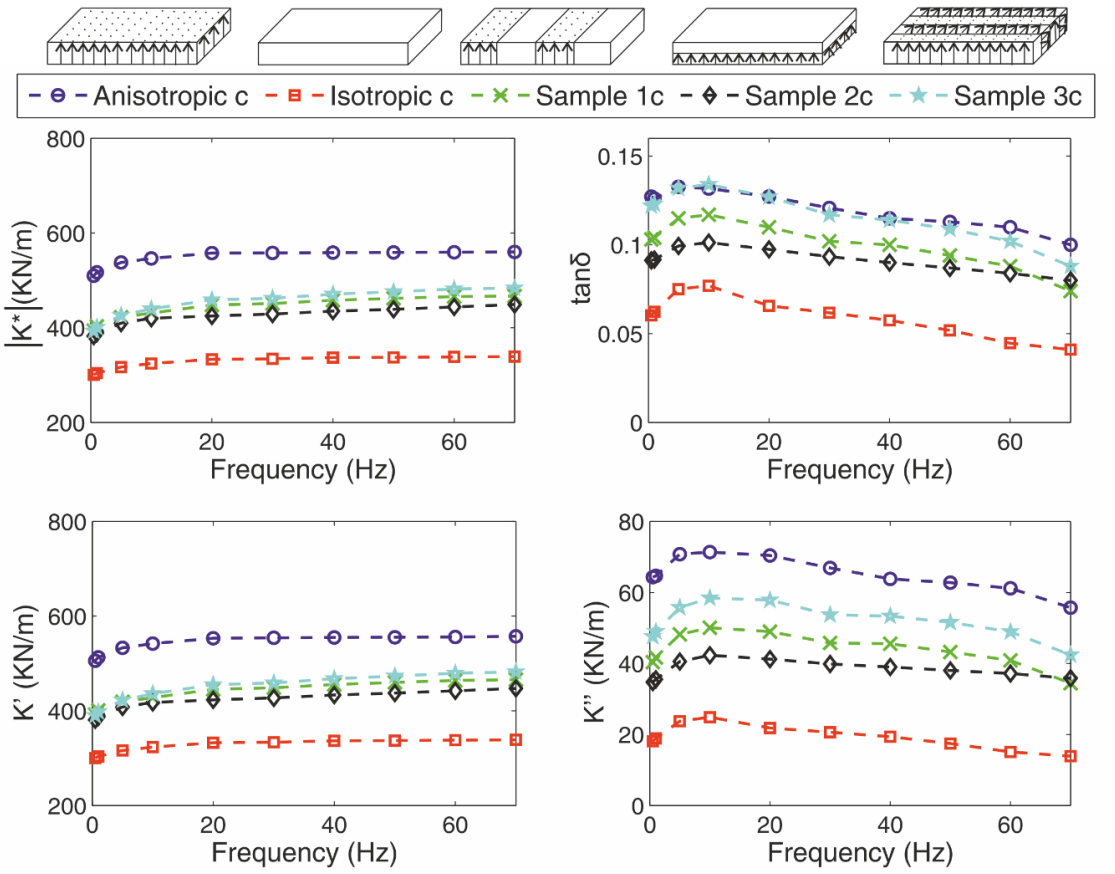

Figure 79: Zero field mechanical properties of inclined isolator will isotropic c, anisotropic c, sample 1c, sample 2c and sample 3c in respect to frequency (at 0.05mm displacement amplitude and 80N static load)

Magnetorheological effect

The increase in static stiffness, measured at 80N static force, for all samples when the electromagnet is fed with 1, 2 and 3 Amps Electric current is presented in Table 30. In this case where the MREs are under combined shear/compression loading conditions, the highest MR effect is observed for the isotropic/anisotropic series composite MRE sample 2c. The isotropic MRE follows then while the anisotropic MRE has the lowest MR effect of all. Isotropic/anisotropic sample 1c has the same MR effect with anisotropic MRE while the MR effect of anisotropic/anisotropic composite sample 3c is 11% higher than the one of the anisotropic sample.

The effect of the magnetic field on dynamic stiffness $|K^*|$, real K' and imaginary K'' components of dynamic stiffness and tangent of the loss angle $tan\delta$ is presented in Figure 80. Dynamic stiffness of all samples increases significantly with increasing magnetic field while imaginary component of dynamic stiffness K'' has a higher MR effect than the real component K'. The highest MR effect, of 48% for K' and 68% for K'', is observed for the pure anisotropic c sample and the lowest of 26% and 30% respectively for the isotropic MRE. Anisotropic-isotropic series configuration composite sample 2c has the same MR effect of real component of dynamic stiffness K' with anisotropic MRE but a 10% lower MR effect of imaginary K'' dynamic stiffness. Anisotropic/anisotropic parallel configuration sample 3c has the same MR effect with anisotropic MRE for both components of dynamic stiffness.

Table 30: Static stiffness MR effect of pure compression and inclined MRE isolator device.

	Static stiffness at 80 N (KN/mm)				**MR effect (%)**		
Current I (A)	**0**	**1 A**	**2 A**	**3 A**	**1 A**	**2 A**	**3 A**
Anisotropic c	123	136	170	206	11	38	68
Isotropic c	95	132	165	195	39	74	105
Sample 1c	107	120	150	182	12	41	70
Sample 2c	103	121	173	227	17	68	120
Sample 3c	123	145	175	223	18	49	81

The variation of MR effect in respect to displacement amplitude Xo and electric current I for anisotropic, isotropic, sample 1c, sample 2c and sample 3c is presented in Figure 81, Figure 82, Figure 83, Figure 84 and Figure 85 respectively. The MR effect of dynamic stiffness increases with increasing displacement amplitude while there is a strong MR effect of tanδ– displacement

amplitude coupling effect. For all samples, MR effect of the dynamic stiffness is lower than the one for the pure compression isolator but the MR effect of tangent of loss angle tanδ is higher.

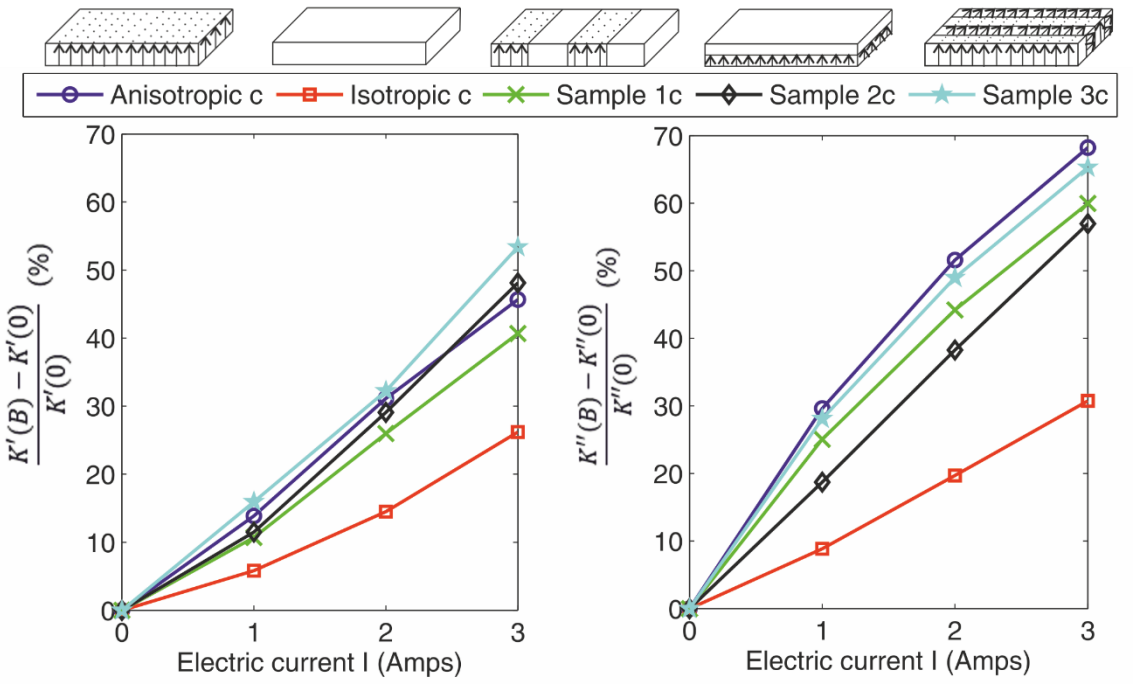

Figure 80: MR effect of real K' and K'' imaginary component of dynamic stiffness (inclined) for all samples in respect to electric current I (at 0.04mm displacement amplitude, 5Hz frequency and 80N static force).

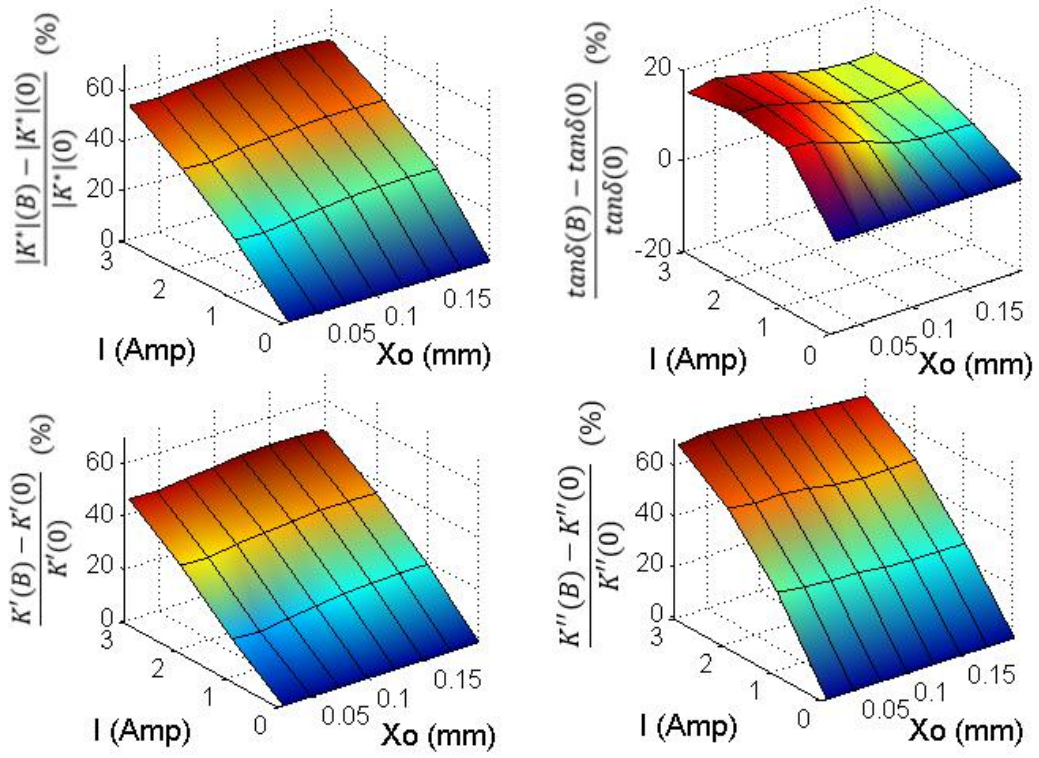

Figure 81: MR effect of anisotropic c MRE (inclined) in respect to displacement amplitude Xo and electric current I (at 5Hz and 80N static force).

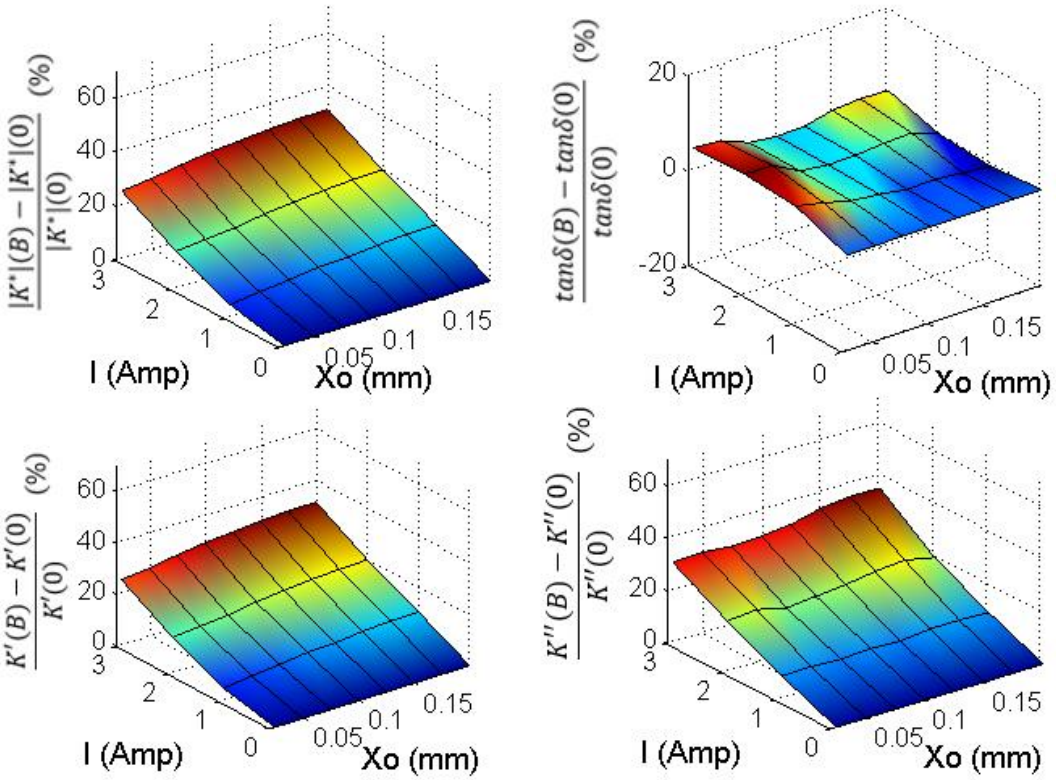

Figure 82: MR effect of isotropic c MRE (inclined) in respect to displacement amplitude Xo and electric current I (at 5Hz and 80N static force).

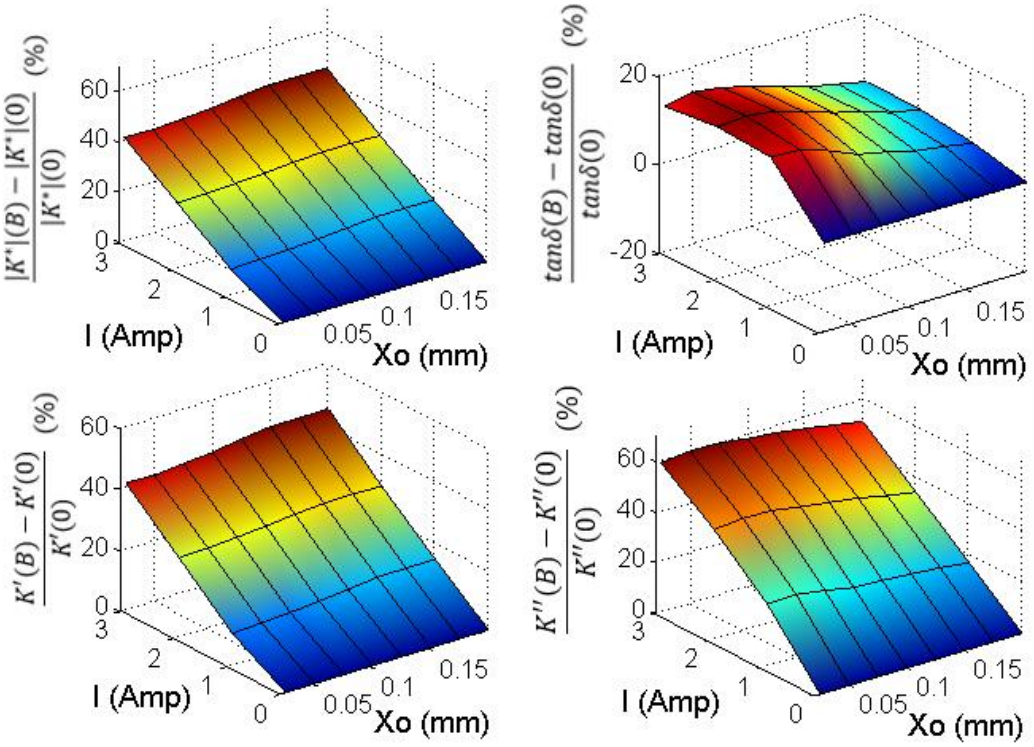

Figure 83: MR effect of parallel configuration composite sample 1c MRE (inclined) in respect to displacement amplitude Xo and electric current I (at 5Hz and 80N static force).

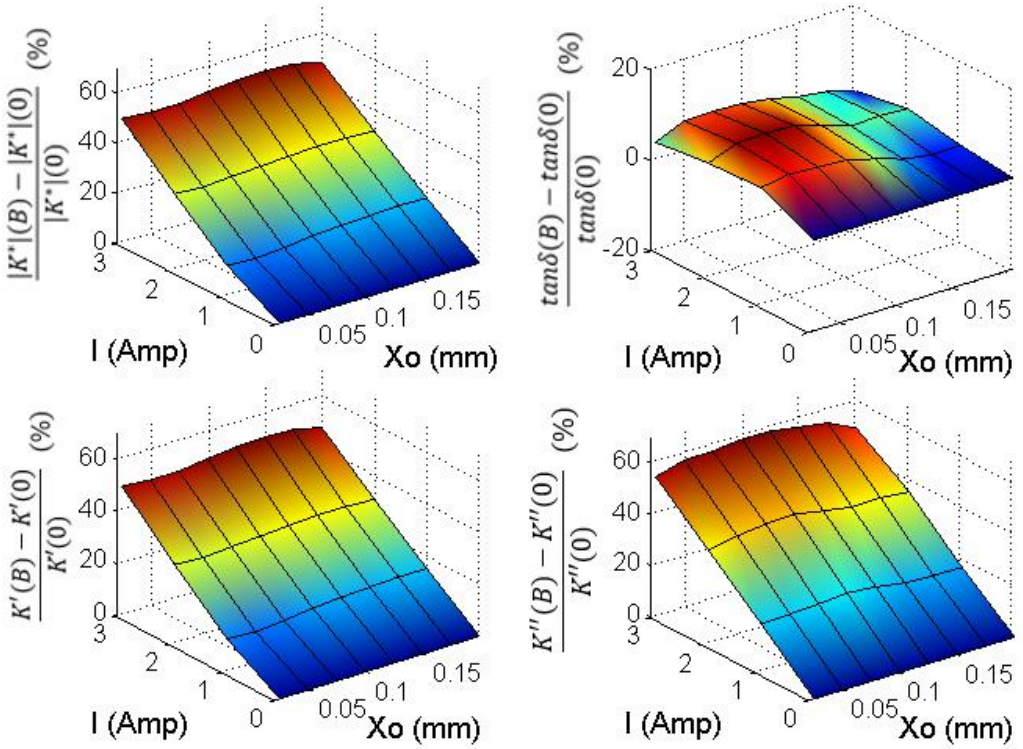

Figure 84: MR effect of series configuration composite sample 2c MRE (inclined) in respect to displacement amplitude Xo and electric current I (at 5Hz and 80N static force).

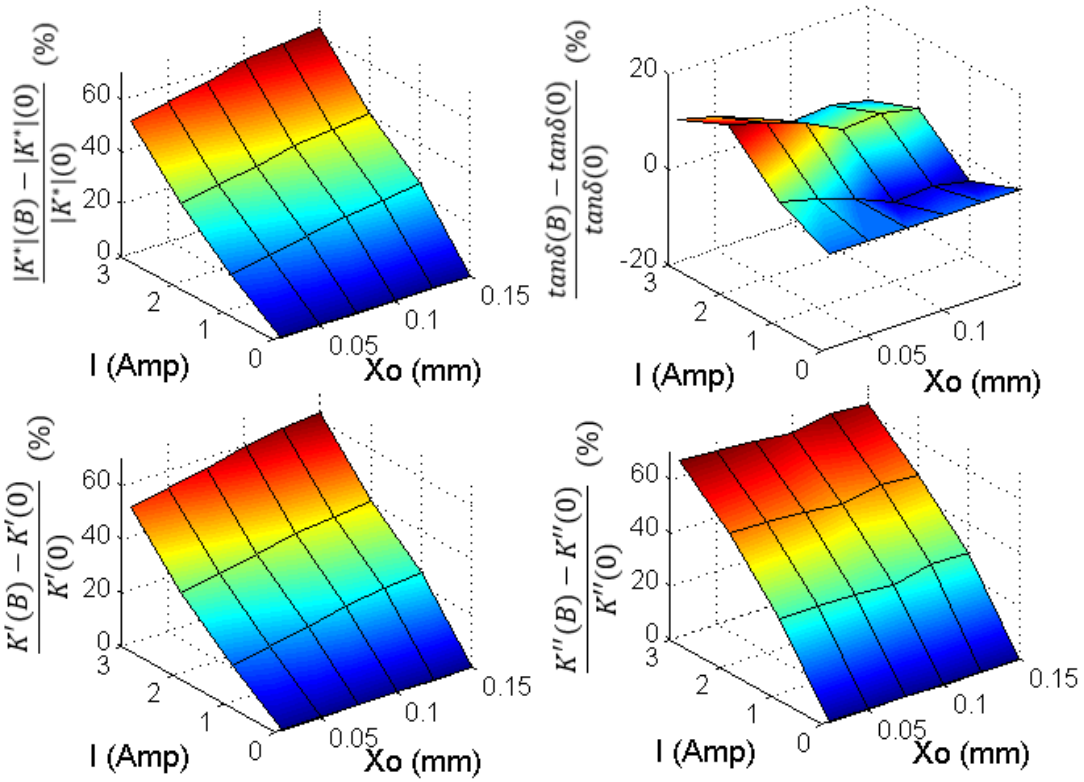

Figure 85: MR effect of composite sample 3c MRE (inclined) with two anisotropic parts in respect to displacement amplitude Xo and electric current I (at 5Hz and 80N static force).

On-off operation

Figure 86 illustrates the displacement and load time sequences of pure compression isolator with anisotropic c MRE samples under 80N static load, 15N dynamic load amplitude and 5Hz frequency. The second graph corresponds to the actual displacement channel recorded, while the third graph illustrates only the dynamic displacement when the static component was subtracted. The effect of the magnetic field is instant and irreversible in both on and off stages as shown in the last graph. However, the variation of the static stiffness is again the dominant trend although the change is less than the pure isotropic isolator case.

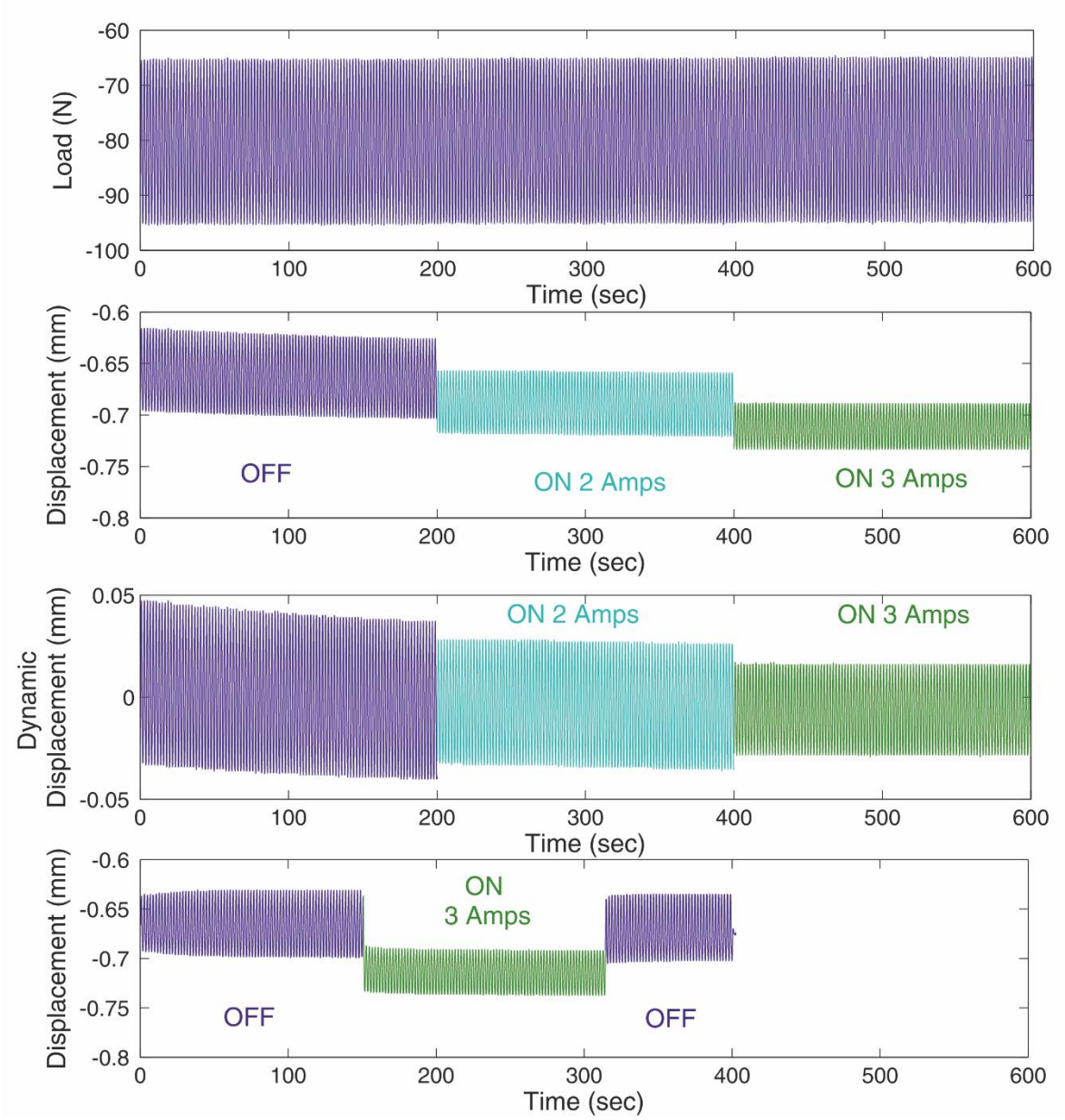

Figure 86: Displacement and load time sequences of inclined isolator with anisotropic c MRE samples under 15N dynamic load and 5Hz frequency.

Figure 87Figure 74 illustrates a zoomed version of the previous force and displacement time sequences when the 3 Amps electric current is switched on and off again. The transition period from zero to three amps is smooth and reversible regarding both static and dynamic displacement. Figure 88 illustrates the dynamic load amplitude, displacement amplitude and dynamic stiffness amplitude $|K^*|$ of the same signals when the 3Amps electric current is switched on and off. These values are provided from Instron Puls DMA calculation software and are in respect to cycles (one full period) since dynamic stiffness needs one full cycle to be calculated. In this test load frequency was 5Hz thus, one cycle is 0.2sec. The anisotropic inclined isolator needs 7 cycles or 1.4 seconds to reach a steady state when the current is switched on and off again.

Compared to the 11cycles or 2.2 seconds rise time of the anisotropic compression MRE isolator, the inclined configuration is much faster. This could be due to the smaller dynamic stiffness or the design of the magnetic circuit. In the inclined isolator the top part is made from laminated sheets like the rest of core but in the compression isolator the top part is a low carbon solid steel bar that has higher losses. The magnetic field produced in the gap where the MRE samples are placed will be similar for both isolators, but the magnetic circuit of the compression isolator is slower.

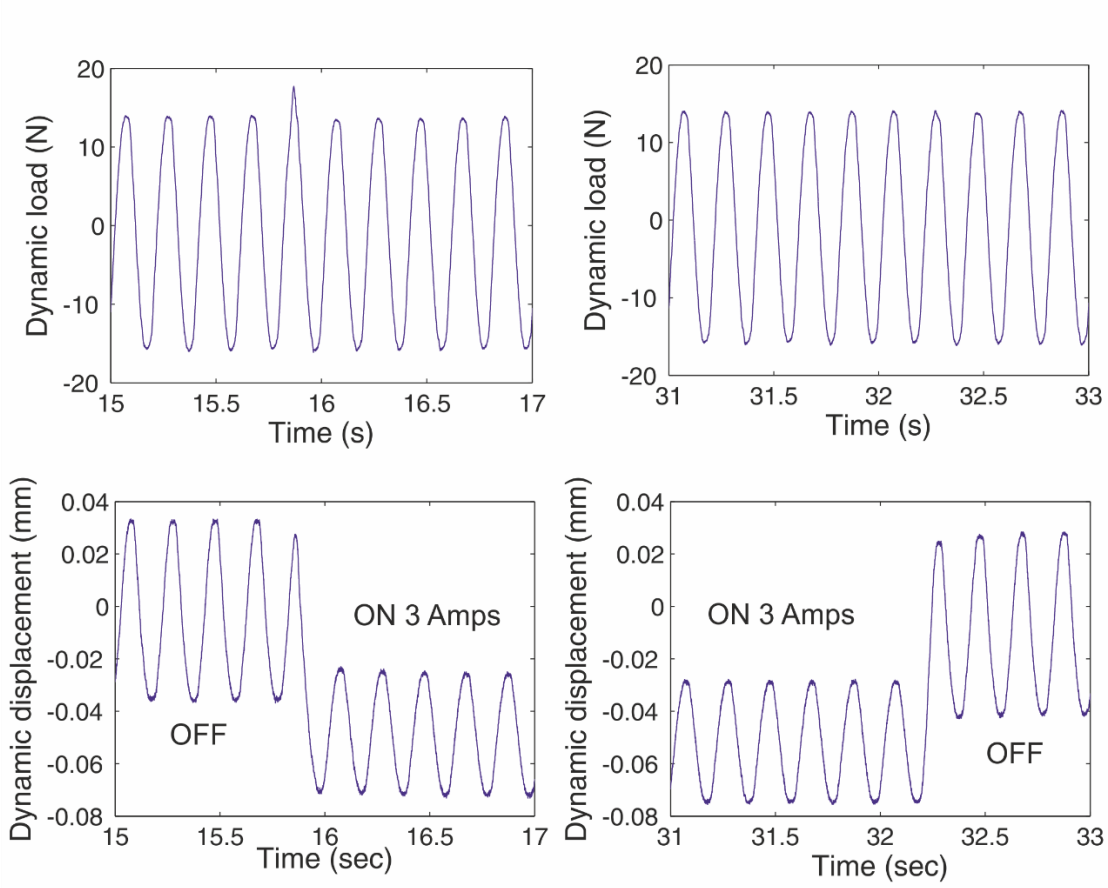

Figure 87: Dynamic load and displacement of inclined anisotropic MRE isolator at the time when the electric current is switched on and off.

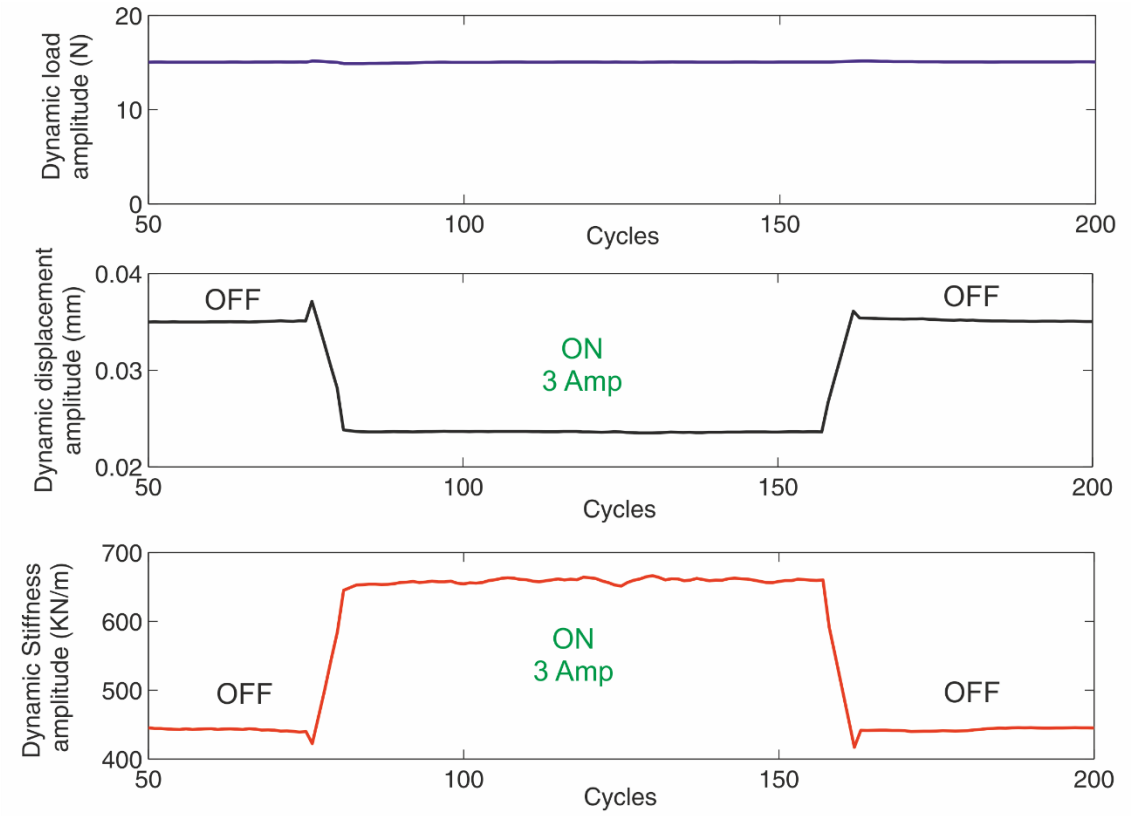

Figure 88: Dynamic force amplitude (5 Hz frequency), displacement amplitude and stiffness of inclined isolator with anisotropic MREs in an ON-OFF operation.

6.6 Principal elastic dynamic stiffness ratio of inclined isolator

In the inclined test system used in this study, there are two planes of symmetry around the longitudinal Z and the lateral X axis. Thus, translational motion in the axial direction (Y axis) and yaw rotation are decoupled from the other modes. Assuming a plane defined by axis X and Y coordinate system (as illustrated in Figure 89) where all forces and displacement are restricted (no rotations), the components of force and displacement on X and Y axis are defined as F_x, F_y, δ_x and δ_y respectively. The equations of motion for the MR elastomers can be found by setting in the general system equations (6.2.1) all moments, rotations and substrate movements to zero.

$$\begin{bmatrix} F_x \\ F_y \end{bmatrix} = \begin{bmatrix} k_{11} & k_{12} \\ k_{21} & k_{22} \end{bmatrix} \begin{bmatrix} \delta_x \\ \delta_y \end{bmatrix} + \begin{bmatrix} c_{11} & c_{12} \\ c_{21} & c_{22} \end{bmatrix} \begin{bmatrix} \dot{\delta}_x \\ \dot{\delta}_y \end{bmatrix} \tag{6.6.1}$$

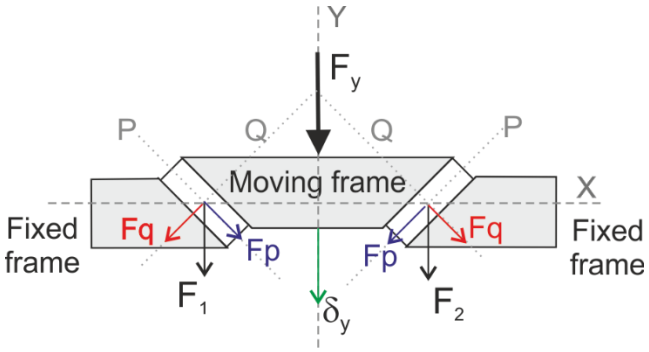

Figure 89: Forces on the inclined isolator

Where $k_{11} = 2k_{xx}$, $k_{12} = k_{21} = 2k_{xy}$, $k_{22} = 2k_{yy}$ and $c_{11} = 2c_{xx}$, $c_{12} = c_{21} = 2c_{xy}$, $c_{22} = 2c_{yy}$. For each MRE, principal stiffness $k_{xx} = F_{xx}/d_x$ is defined as the ratio of the applied force in the x direction F_{xx} to the resulting displacement when the rubber is constrained to deflect only in the x direction, and $k_{yy} = F_{yy}/d_y$ as the ratio of the applied force in the Y direction F_{yy} to the resulting displacement when the rubber is constrained to deflect only in the **Y** direction. Due to the inclined position there are two additional coupling stiffness elements, $k_{xy} = F_{xy}/d_y$ defined as the ratio of the force that has to be applied in the **x** direction F_{xy} to cause a unit displacement in the **Y** direction when the isolator is constrained to deflect only in the **y** direction and $k_{yx} = F_{yx}/d_x$ defined as the ratio of the force that has to be applied in the **Y** direction F_{yx} to cause a unit displacement in the **X** direction when the isolator is constrained to deflect only in the **X** direction. The principal and coupling damping elements are defined accordingly.

When the principal elastic axis P, Q are selected as the new coordinate system, the stiffness and damping coefficients in the original XY system can be expressed in terms of principal stiffness and damping elements k_p, c_p and k_q , c_q (Harris C M 2002).

$$
\begin{aligned}
k_{xx} &= k_q \cos^2\theta + k_p \sin^2\theta \\
k_{yy} &= k_q \sin^2\theta + k_p \cos^2\theta \\
k_{xy} &= k_{yx} = \left(k_q - k_p\right)\sin\theta\cos\theta \\
c_{xx} &= c_q \cos^2\theta + c_p \sin^2\theta \\
c_{yy} &= c_q \sin^2\theta + c_p \cos^2\theta \\
c_{xy} &= c_{yx} = \left(c_q - c_p\right)\sin\theta\cos\theta
\end{aligned}
\tag{6.6.2}
$$

Where θ is the inclination angle. For θ=45^0 the forces applied to each principal elastic axis Q and P are equal $F_q = F_p$ and the above equations (6.5.2) become:

$$
\begin{aligned}
k_{xx} = k_{yy} = \frac{k_q + k_p}{2} \quad , \quad k_{xy} = k_{yx} = \frac{\left(k_q - k_p\right)}{2} \\
c_{xx} = c_{yy} = \frac{c_q + c_p}{2} \quad , \quad c_{xy} = c_{yx} = \frac{\left(c_q - c_p\right)}{2}
\end{aligned}
\tag{6.6.3}
$$

In this case, the only acting force is a compression force in the axial (Y axis) direction F_y that causes a translational displacement δ_y in the same direction thus, $F_x = \delta_x = 0$. Substituting equations (6.5.3) to force-deflection equations (6.5.1) for two rubber samples and setting $F_x = \delta_x = 0$ we get:

$$
F_y = 2k_{yy}\delta_y + 2c_{yy}\dot{\delta_y} = \left(k_q + k_p\right)\delta_y + \left(c_q + c_p\right)\dot{\delta_y} \tag{6.6.4}
$$

And in mass (m)- inclined MRE isolator system the natural frequency would be $f_Y = \frac{1}{2\pi}\sqrt{\frac{\left(k_p + k_q\right)}{m}}$.

In the case of the pure compression isolator where the MREs are subjected again to a force acting in the axial direction (Y) F'_y that causes a translational displacement δ'_y in the same direction, the equation of motion is:

$$
F'_y = 2k_y\delta'_y + 2c_y\dot{\delta'_y} = 2\,k_q\delta'_y + 2\,c_q\dot{\delta'_y} \tag{6.6.5}
$$

And in mass (m)- compression MRE isolator system the natural frequency would be $f'_Y = \frac{1}{2\pi}\sqrt{\frac{2k_q}{m}}$.

The above equations are valid for a linear system where k_q, c_q and k_p, c_p are independent of load amplitude, frequency and static prestrain. The principal stiffness and damping ratios k_p/k_q and c_p/c_q could then be easily determined by equations (6.6.5) and (6.6.4) and the experimental data presented in sections (6.3) and (6.4) since the MRE samples and electromagnet used in both cases were the same. However, pure compression stiffness coefficient k_q depends on static prestrain and load amplitude. When an 80N static load applied on the inclined isolator the load

corresponding to the principal stiffness axis $F_q = F\ sin45 = F\frac{\sqrt{2}}{2} = 57N$. The pure compression stiffness and damping coefficients k_q and c_q to be used in equation (6.5.4) is the one for 57N static force and $\delta_y = \delta_y sin45 = 0.035mm$ dynamic displacement. The shear stiffness and damping coefficients k_p and c_p can then be found by equations $K' = k_q + k_p$ and $K'' = \omega(c_q + c_p)$ where K' and K'' are the real and imaginary components of the inclined isolator and are presented in Table 31. The principal stiffness and damping ratios k_p/k_q and c_p/c_q for isotropic and composite sample 1c increase with increasing magnetic field while for sample 2c they decrease. Samples 1c and 3c showed the greatest variation of stiffness ratio with magnetic field while sample 2c the lowest.

Table 31: Principal stiffness coefficient for all samples

		Compression (57N, 0.035mm)		**Inclined (80N,0.05mm)**					
I (Amps)		$\boldsymbol{k_q}$	$\boldsymbol{\omega c_q}$	$\boldsymbol{K'}$	$\boldsymbol{K''}$	$\boldsymbol{k_p}$	$\boldsymbol{\omega c_p}$	$\boldsymbol{\frac{k_q}{k_p}}$	$\boldsymbol{\frac{c_q}{c_p}}$
0	Isotropic	231	17.5	342	27.24	111	10.74	2.08	1.63
1		261	19.7	369.7	30.1	108.7	10.4	2.40	1.89
2		286.5	21.4	401.2	31.46	114.7	10.06	2.50	2.13
0	Anisotropic	320	40	500	62	180	22	1.78	1.82
1		400	51	580	81	180	30	2.22	1.70
2		475	64	693	96	218	32	2.18	2.00
0	Sample 1c	282.8	30.5	423	48	140.2	17.5	2.02	1.74
1		330.5	37.25	460	55	129.5	17.75	2.55	2.10
2		410	45.5	514	62.5	104	17	3.94	2.68
0	Sample 2c	225	18.75	409	42.3	184	23.55	1.22	0.80
1		252.3	22.5	452	51.5	199.7	29	1.26	0.78
2		271.9	25	524	60	252.1	35	1.08	0.71
0	Sample 3c	285	32	394.2	51.6	109.2	19.6	2.61	1.63
1		356	42.5	457	56	101	13.5	3.52	3.15
2		427.5	46.5	521	77	93.5	30.5	4.57	1.52

6.7 Discussion

The load-displacement hysteresis curves of anisotropic MREs in pure compression and inclined isolators, under 0.08mm (1.6% strain) and 0.02 (4% strain) mm displacement amplitudes are presented in Figure 90. For small displacement values, less than 1% strain amplitude, the hysteresis curves are pure ellipses and the MREs are behaving in a linear manner. As displacement amplitude increases, the hysteresis curves become distorted and the MRE behaves in a nonlinear manner. In the case of the 45 degrees inclined isolator the MRE is subjected to equal compression and shear loads but since all rubbers behave more linearly under pure shear than pure compression, the hysteresis curves of the inclined isolator are closer to an ellipse compared to those of the pure compression isolator at 0.08mm displacement amplitude. Thus, the inclined MRE isolator can behave in a linear manner for higher displacements than the pure compression isolator. Isotropic and composite MREs show the same behaviour.

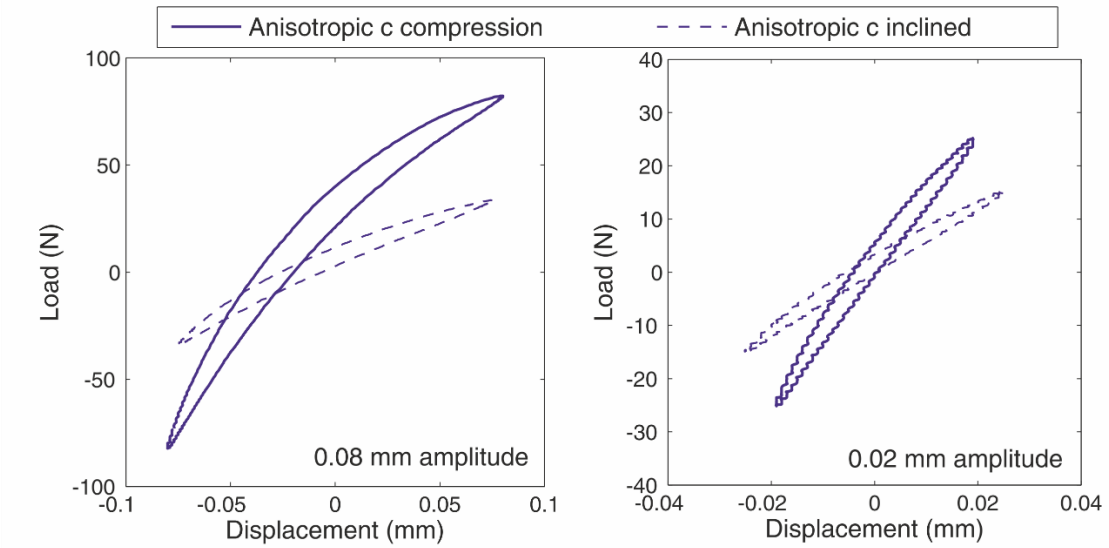

Figure 90: Zero field load-displacement hysteresis curves of pure compression and inclined isolator with anisotropic c MRE sample at 0.08mm and 0.02mm displacement amplitude (at 5Hz frequency and 80N static load)

Under pure compression the particles of anisotropic MREs are aligned in the same direction of the applied force and magnetic field, while for the inclined setup system the particle chains are in the same direction with the applied magnetic flux but in 45 degrees angle with the direction of the applied force as Figure 91 illustrates. If the principal elastic axis Q, P are chosen as reference, the compression component of the applied force $F_q = F\ sin\theta$ will be parallel to the direction of the magnetic flux and particle alignment while the shear component $F_p = F\ cos\theta$ perpendicular. However, if the force is applied in the lateral x direction the MRE in the compression isolator will work in pure shear mode with the force being perpendicular to the direction of the magnetic flux and particle alignment. In the inclined isolator, the movement of the top part is constrained by the

frame of the electromagnet and a force applied in the x direction will only cause a compressive force that is in 45 degrees with the particle alignment and magnetic flux. Therefore, the magnetorheological effect will be different than the one of pure compression for all samples and cannot be defined by this experimental setup system.

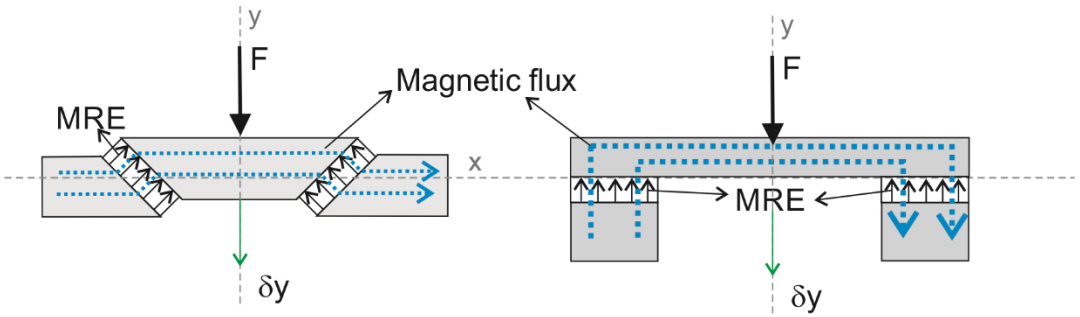

Figure 91: Magnetic flux direction of the inclined and compression isolator with anisotropic MRE

6.8 Chapter summary

In this chapter, the composite isotropic/anisotropic and anisotropic/anisotropic MREs were tested in practice by examining the mechanical properties of a MRE prototype isolator working in pure compression and compression/shear (inclined) mode. The experimental data were then used to determine the principal elastic axis stiffness ratio $\frac{k_p}{k_q}$ and how this is influenced by the magnetic field. The general behaviour of the composite samples in pure compression and shear /compression mixed mode isolator can be summarized as:

- MR effect of dynamic stiffness is higher in pure compression isolator than the inclined isolator.
- MR effect of tangent of loss angle tanδ is higher in inclined isolator than pure compression.
- The effect of the magnetic field is instant and irreversible in both on and off stages.
- For the pure compression isolator, Isotropic MRE showed the lowest MR effect of 38% at 3 Amps while the MR effect of isotropic/anisotropic parallel sample 1c is 50%. Anisotropic, series isotropic/anisotropic sample 2c and anisotropic/anisotropic sample 3c have all similar MR effect of about 65% for both components of dynamic stiffness. MR effect of both components of dynamic stiffness decreases as displacement amplitude increases while damping capability is not affected from the magnetic field.
- For the inclined isolator, imaginary component of dynamic stiffness K'' has a higher MR effect than the real component K'. The highest MR effect, of 48% for K' and 68% for K'', is observed for the pure anisotropic c sample and the lowest of 26% and 30% respectively for the isotropic MRE. Anisotropic/isotropic series configuration composite sample 2c has the same MR effect of K' with anisotropic MRE but a 10% lower MR effect K''. Anisotropic/anisotropic parallel configuration sample 3c has the same MR effect with anisotropic MRE for both components of dynamic stiffness.
- In the inclined isolator composite sample 3c has the same zero field static stiffness, lower dynamic stiffness, higher tanδ and same MR effect with anisotropic MRE.
- The principal elastic axis stiffness $\frac{k_p}{k_q}$ and damping ratio $\frac{c_p}{c_q}$ changes with the magnetic field for all samples.

Chapter 7: Simulation of a single degree of freedom mass – MRE inclined isolator system

7.1 Introduction

The last chapter of the theses is focused on examining how the inclined and compression MRE isolators can find applications in the marine industry and present the advantages of the combined isotropic/anisotropic and anisotropic/anisotropic MREs in practical applications. In more detail the purpose of this chapter is to:

- Produce a dynamic force and electric current dependent viscoelastic model of the inclined and compression MRE isolator. Since the model is about the device itself the electric current supplied to the electromagnet was used as a variable instead of magnetic field, so the dynamics of the power supply are also included.
- Simulate the force and displacement transmissibility of a single degree of freedom mass-MRE isolator system of all the MRE samples to compare their performance.
- Examine the principle of using the inclined MRE isolator to improve stability of a mass-isolator system under loading conditions that represent ship motion by varying the translational and rotational static stiffness.
- Examine the possible performance of MREs as base isolators for a marine oil separator when a simple ON-OFF control strategy is used to shift the natural frequency and decrease transmitted vibrations during starting up and closing stages.

7.2 Force dependent viscoelastic model of MRE isolator

The aim of this section is to provide a viscoelastic model capable of predicting the static and dynamic response of the compression and inclined MRE isolator presented in chapter 6. Thus, taking also under consideration the general conclusion of the tests performed in chapter 4 the following assumptions were made:

- Dynamic stiffness and damping depend on:
  - Amplitude of dynamic load
  - Magnetic field. Since the model is about the isolator device as a system the values of the electric current I supplied to the electromagnet are used as a variable instead of magnetic field *B*.
- There is a strong magnetic field-load amplitude coupling effect
- There is a strong magnetic field-static load coupling effect

The following were ignored:

- Effect of frequency on dynamic properties.
- The weak static load-dynamic load amplitude coupling effect.
- The weak load amplitude-frequency coupling effect.
- The weak magnetic field-frequency coupling effect.
- The effect of static prestrain

The variation of dynamic stiffness and damping with static strain is modelled only for one applied load amplitude value, while it is assumed to follow the same curve for all other amplitudes but with different absolute values.

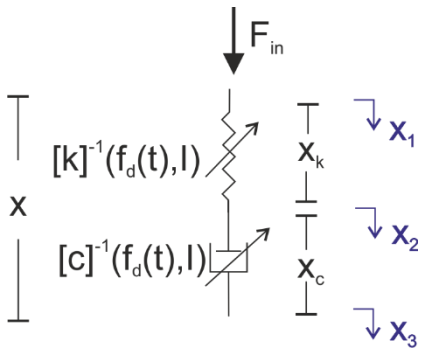

Figure 92: Nonlinear dynamic force dependent model

The basic idea behind the model is to use a nonlinear spring $k_1$and dashpot c_1 in the Maxwell chain to represent the strong dependence on input force and magnetic field as well as their coupling effects. To express dynamic stiffness K* as a function of the applied force $f(t)$ rather than the displacement $x(t)$ the Maxwell element dashpot c and spring k are replaced by mobility $[c]^{-1}$ and

receptance $[k]^{-1}$ respectively that depend on dynamic force $f_d(t)$, electric current I and static load f_{st}. Assuming the MRE isolator is always prestressed under a static force f_{st} where a general dynamic force $f_d(t)$ is superimposed, the total displacement $x(t)$ will be the sum of the static displacement x_{st} caused by the static force and the dynamic one $x_d(t)$ due to the dynamic force.

$$x(t) = x_{st} + x_d(t) \tag{7.2.1}$$

Since both MRE isolators exhibit a non-linear static force-displacement behaviour, the static displacement can be expressed as two polynomial functions. The first one represents the static displacement caused by the static force at zero field and the second represents the change on the static displacement when the magnetic field is applied.

$$x_{st} = \sum_{j=1}^{J_{st}} kst_j {f_{st}}^j + \sum_{j=1}^{J_{Bst}} kI_j I^j f_{st} \tag{7.2.2}$$

Where kst_j and kst_{ij} are parameters to be defined by the experimental data.

The total dynamic displacement that the MR elastomer undergoes under the applied force will be the sum of the dynamic displacements at each branch.

$$x_d(t) = x_k + x_c \tag{7.2.3}$$

where $x_k = x_2 - x_1$ and $x_c = x_3 - x_2$ are the relative displacements on the spring k and dashpot c. The use of receptance and mobility allows the nonlinear elements of Kelvin chain to be functions of the applied force instead of displacement. Assuming polynomial functions, $[k]^{-1}$ and $[c]^{-1}$ can be expressed as functions of applied dynamic force and electric current.

$$[k]^{-1} = g_{0fd}\big(f_d(t)\big) + g_{Bfd}(f_d(t), I) \tag{7.2.4}$$

$$[c]^{-1} = z_{0fd}\big(f_d(t)\big) + z_{Bfd}(f_d(t), I) \tag{7.2.5}$$

The first terms of the above equations represent the dependence of dynamic stiffness and damping on force amplitude at zero field. Assuming polynomial functions we get:

$$g_{0fd}\big(f_d(t)\big) = \sum_{ik=0}^{N_k} ra_{ik} f_d(t)^{ik} \tag{7.2.6}$$

$$z_{0fd}\big(f_d(t)\big) = \sum_{ic=0}^{N_c} ma_{ic} f_d(t)^{ic} \tag{7.2.7}$$

Where ra_{ik} and ma_{ic} are model parameters that depend on the dynamic force $f_d(t)$ and N_k and N_c are integers. These parameters can be extracted by curve fitting to the zero field experimental

data. The second terms $[k]_B{}^{-1}(f_d(t),\mathrm{I})$ and $[c]_B{}^{-1}(f_d(t),\mathrm{I})$ represent the influence of the magnetic field on dynamic stiffness and damping. Assuming again polynomial functions we get:

$$g_{Bfd}(f_d(t),I)=\sum_{ikB=0}^{N_{kB}}\left(\sum_{jk=1}^{J_k} r_{ikBjk}I^{jk}\right)f_d(t)^{ikI} \tag{7.2.8}$$

$$z_{Bfd}(f_d(t),I)=\sum_{icB=0}^{N_{cB}}\left(\sum_{jc=1}^{J_c} m_{icBjc}I^{jc}\right)f_d(t)^{icI} \tag{7.2.9}$$

Where r_{ikBjk} and m_{icBjc} are model parameters and N_{kB}, J_k , N_{cB}, J_c are integers. These parameters are also extracted by curve fitting to the experimental data. The differential equations of each element are:

$$x_k(t)=[k]^{-1}\,f_d(t)=\mathrm{g}_r(f_d(t),\mathrm{I}) \tag{7.2.10}$$

$$\dot{x_c}=[c]^{-1}f_d(t)=\mathrm{z}_m(f_d(t),\mathrm{I}) \tag{7.2.11}$$

Functions $\mathrm{g}_r(f_d(t),\mathrm{I})$ and $\mathrm{z}_m(f_d(t),\mathrm{I})$ are now:

$$\begin{aligned}\mathrm{g}_r(f_d(t),\mathrm{I},f_{st}) &=\left(g_{0fd}\left(f_d(t)\right)+g_{Bfd}(f_d(t),I)\right)f_d(t)=\\ &=\sum_{ik=0}^{N_k} ra_{ik}f_d(t)^{ik+1}+\sum_{ikB=0}^{N_{kB}}\left(\sum_{jk=1}^{J_k} r_{ikBjk}I^{jk}\right)f_d(t)^{ikB+1}\end{aligned} \tag{7.2.12}$$

$$\begin{aligned}\mathrm{z}_m(f_d(t),\mathrm{I},f_{st}) &=\left(z_{0fd}\left(f_d(t)\right)+z_{Bfd}(f_d(t),I)\right)f_d(t)\\ &=\sum_{ic=0}^{N_c} ma_{ic}f_d(t)^{ic+1}+\sum_{ikB=0}^{N_{kB}}\left(\sum_{jk=1}^{J_k} r_{ikBjk}I^{jk}\right)f_d(t)^{ikB+1}\end{aligned} \tag{7.2.13}$$

To acquire the differential equation of the model, the Laplace transforms of equations (7.2.10), and (7.2.11) are used:

$$X_k(s)=G_r(s) \tag{7.2.15}$$

$$X_c(s)=\frac{Z_m(s)}{s} \tag{7.2.16}$$

And substituting the above equations to the Laplace transform of equation (7.2.3) we get:

$$X_d(s)=X_k(s)+X_c(s)=G_r(s)+\frac{Z_m(s)}{s}\Rightarrow$$

$$s\,X_d = s\,G_r(s) + Z_m(s) \tag{7.2.17}$$

Taking the inverse Laplace transform of equation (7.2.17) we get the differential equation.

$$\dot{x_d} = \mathrm{g}_r(f_d, \mathrm{B}) + \mathrm{z}_m(f_d(t), \mathrm{I}) \tag{7.2.18}$$

Equation (7.2.18) requires the first derivative of function $\mathrm{g}_r(f_d(t), \mathrm{I})$. Differentiating equation (7.2.12) we get:

$$\dot{\mathrm{g}_r}(f_d, \mathrm{I}) = \left[\sum_{ik=1}^{N_k} (ik+1)\, r a_{ik} f_d(t)^{ik} \dot{f_d} + \sum_{ikB=1}^{N_{kB}} \left(\sum_{jk=0}^{J_k} r_{ikBjk} I^{jk}\right) (ikB+1)\, f_d(t)^{ikB}\, \dot{f_d}\right] \tag{7.2.19}$$

- **Assuming the input signal to be a harmonic force** $f_d(t) = f_0\omega^n \sin(\omega t)$

When the input signal is assumed to be a general harmonic force of $f_0\omega^n$ amplitude given by equation (7.2.20), the resulting harmonic displacement $x(t)$ (of amplitude x_0) will be out of phase with the input signal by an angle ϕ called the loss angle. For a nonlinear material it will not be a pure sinusoidal signal but contain higher harmonics $x(t) = \sum_{n=1}^{L} x_0 \sin(n\omega t + \varphi_n)$.

$$f_d(t) = f_0\omega^n \sin(\omega t) \tag{7.2.20}$$

Where n denotes the exponent of input excitation. When n=0, the force input is harmonic with constant amplitude while when n=2 it can represent the force excitation from a rotating machine with an eccentric mass. For harmonic inputs with amplitude values corresponding to less than 1% strain amplitude the harmonic balance method is valid. Thus, the higher harmonics can be ignored and only the fundamental frequency becomes of importance. The resulting dynamic displacement becomes:

$$\begin{aligned} x_d(t) &= x_0 \sin(\omega t + \varphi) = x_0 \sin\varphi \cos(\omega t) + x_0 \cos\varphi \sin(\omega t) \\ &= x_f \cos(\omega t) + x_s \sin(\omega t) \end{aligned} \tag{7.2.21}$$

To solve the system analytically, the Ritz-Galerking (Guo P F 2012) method is used where an approximate solution to the differential equation is assumed and the solution is found by minimizing the integrated error function over a specified time period $t \in [t1, t2]$.

$$J = \int_{t1}^{t2} e(t)^2 dt \tag{7.2.22}$$

The error function $e(t)$ to be minimized is:

$$\dot{x_d} - \dot{g_r}(f_d, \mathrm{I}) - \mathrm{z}_m(f_d(t), \mathrm{I}) = e(t) \tag{7.2.23}$$

The individual displacement components can then be obtained by solving the following set of equations:

$$\frac{\partial J}{\partial x_f} = \int_{t1}^{t2} 2 * e(t) \frac{\partial e(t)}{\partial x_f} = 0 \qquad \frac{\partial J}{\partial x_s} = \int_{t1}^{t2} 2 * e(t) \frac{\partial e(t)}{\partial x_s} = 0 \tag{7.2.24}$$

The partial derivatives $\frac{\partial e(t)}{\partial x_f}$ and $\frac{\partial e(t)}{\partial x_s}$ become:

$$\frac{\partial e(t)}{\partial x_f} = -\omega \sin(\omega t) \qquad \frac{\partial e(t)}{\partial x_s} = \omega \cos(\omega t) \tag{7.2.25}$$

The displacement components are acquired by substituting equations (7.2.23) and (7.2.25) to (7.2.24) and integrate for one period (from $t_1 = 0$ to $t_2 = 2\pi/\omega$). Equations (7.2.13) and (7.2.19) are polynomial functions that contain odd number trigonometric power functions that will drop out during integration. For this purpose, the integration is broken down in two parts from $t_1 = 0$ to $t_2 = \pi/\omega$ and $t_1 = \pi/\omega$ to $t_2 = 2\pi/\omega$, one for each semiperiod, making sure that the input signal is inversed for the negative semi period. From experimental data it was found that the behaviour of the material could be described accurately for all samples by setting $N_k = 3,\ N_c = 2,\ N_{kB} = 1, N_{cB} = 1, J_k = 2, J_c = 3$. The equations now become:

$$g_{0fd}\big(f_d(t)\big) = ra_0 + ra_1 f_d(t)^1 + ra_2 f_d(t)^2 + ra_3 f_d(t)^3 \tag{7.2.26}$$

$$g_{0fst}(f_{st}) = rst_1 {f_{st}}^1 + rst_2 {f_{st}}^2 + rst_3 {f_{st}}^3 \tag{7.2.27}$$

$$g_{Bfd}\big(f_d(t)\big) = (r_{01} I + r_{02} I^2) + (r_{11} I + r_{12} I^2) f_d(t)^1 \tag{7.2.28}$$

$$z_{Bfd}\big(f_d(t)\big) = (m_{01} I + m_{02} I^2 + m_{03} I^3) + (m_{11} I + m_{12} I^2 + m_{13} I^3) f_d(t)^1 \tag{7.2.29}$$

The system of equations was solved in Matlab using the symbolic toolbox and the fsolve function (Appendix A). The solution for one period becomes:

$$\begin{aligned} x_s = (ra_0 + r_{01} I + r_{02} I^2) f_0 \omega^n + \frac{8}{3\pi}(ra_1 + r_{11} I + r_{12} I^2)(f_0 \omega^n)^2 \\ + \frac{3}{4}(ra_2)(f_0 \omega^n)^3 + \frac{32}{15\pi}(ra_3)(f_0 \omega^n)^4 \end{aligned} \tag{7.2.30}$$

$$x_f = -\frac{1}{\omega}\Big[(ma_0 + m_{01}I + m_{02}I^2 + m_{03}I^3)f_0\omega^n + \frac{8}{3\pi}(ma_1 + m_{11}I + m_{12}I^2 + m_{13}I^3)(f_0\omega^n)^2 + \frac{3}{4}(ma_2)(f_0\omega^n)^3\Big] \quad (7.2.31)$$

Model linearization

For harmonic inputs with a certain force amplitude value $f_0\omega^n$, that correspond to less than 1% strain amplitude, the system can be considered linear. In the linearized system $[k]^{-1}$ and $[c]^{-1}$ are replaced by the equivalent receptance $\left[k_{eq}\right]^{-1}$ and mobility $\left[c_{eq}\right]^{-1}$ respectively, that are functions of the applied dynamic force amplitude $f_0\omega^n$, static load f_{st} and magnetic field B. The equivalent stiffness and dashpot are:

$$\left[k_{eq}\right]^{-1}(f_0\omega^n, \mathrm{I}) = g_{0f0}(f_0\omega^n) + g_{Bf0}(f_0\omega^n, I) \quad (7.2.32)$$

$$\left[c_{eq}\right]^{-1}(f_0\omega^n, \mathrm{I}) = z_{0f0}(f_0\omega^n) + z_{Bf0}(f_0\omega^n, I) \quad (7.2.33)$$

Where the amplitude dependent equations now become:

$$g_{0f0}(f_0\omega^n) = \sum_{ik=0}^{N_k} ra'_{ik}(f_0\omega^n)^{ik} \qquad z_{0f0}(f\omega^n) = \sum_{ic=0}^{N_c} ma'_{ic}(f_0\omega^n)^{ic} \quad (7.2.34)$$

And

$$g_{Bf0}(f_0\omega^n, I) = \sum_{ikB=0}^{N_{kB}} \left(\sum_{jk=1}^{J_k} r'_{ikBjk} I^{jk} \right) (f_0\omega^n)^{ikB} \quad (7.2.35)$$

$$z_{Bf0}(f_0\omega^n, I) = \sum_{icB=0}^{N_{cB}} \left(\sum_{jc=1}^{J_c} m'_{icBjc} I^{jc} \right) (f_0\omega^n)^{icB} \quad (7.2.36)$$

In this case the solution to the system becomes:

$$x_s = (ra'_0 + r'_{01}I + r'_{02}I^2)f_0\omega^n + (ra'_1 + r'_{11}I + r'_{12}I^2)(f_0\omega^n)^2 + (r'a_2)(f_0\omega^n)^3 + (r'a_3)(f_0\omega^n)^4 = \left[k_{eq}\right]^{-1}(f_0\omega^n, \mathrm{B})f_0\omega^n \quad (7.2.37)$$

$$x_f = -\frac{1}{\omega}[(ma'_0 + m'_{01}I + m'_{02}I^2 + m'_{03}I^3)f_0\omega^n + (ma'_1 + m'_{11}I + m'_{12}I^2 + m'_{13}I^3)(f_0\omega^n)^2 + (ma'_2)(f_0\omega^n)^3] = -\frac{1}{\omega}\left[c_{eq}\right]^{-1}(f_0\omega^n, \mathrm{I})f_0\omega^n \quad (7.2.38)$$

Where $ra'_1 = \frac{8}{3\pi}ra_1, ra'_2 = \frac{3}{4}ra_2, ra'_3 = \frac{32}{15\pi}ra_1$ and $ma'_1 = \frac{8}{3\pi}ma_1,\ ma'_2 = \frac{3}{4}ma_2$The same principle apply for the magnetic dependent parameters.

7.3 Parameter extraction and model validation

After defining the equations of the model in the previous chapter, the procedure of determining all the parameters by curve fitting to the experimental data presented on chapter 6 follows. The parameter extraction method is performed in the following steps:

1. Parameters of static equation $\sum_{j=1}^{J_{Bst}} kI_j I^j f_{st}$ are defined by setting J_{Bst}=2

Isotropic

Compression: kI_1*=0.002*, kI_2*=0.008*

Inclined: kI_1*=0.4826*, kI_2*=-0.02204*

Anisotropic

Compression: kI_1*=0.03514*, kI_2*=0*

Inclined: kI_1*=0.125*, kI_2*=0.075*

Sample 1

Compression: kI_1*=0.0105*, kI_2*=0.0115*

Inclined: kI_1*=0.1303*, kI_2*=0.06184*

Sample 2

Compression: kI_1*=0.066*, kI_2*=-0.013*

Inclined: kI_1*=0.1757*, kI_2*=0.07961*

Sample 3

Compression: kI_1*=0.01*, kI_2*=0.013*

Inclined: kI_1*=14.05*, kI_2*=6.368*

2. The dynamic amplitude and magnetic field dependent parameters are extracted using surface fitting toolbox of matlab in the form of the following arrays (example for anisotropic MRE isolator is shown in Appendix A2).

$$req = [ra'_0 \quad r'_{01} \quad r'_{02} \quad ra'_1 \quad r'_{11} \quad r'_{12} \quad ra'_2 \quad ra'_3]$$

$$meq = [ma'_0 \quad m_{01} \quad m'_{02} \quad ma'_1 \quad m'_{11} \quad m'_{12} \quad ma'_2 \quad ma'_3]$$

Isotropic

Compression

req =[0.00103587103058268 1.79825025564022e-06 -2.30466559233385e-09
4.31347057023736e-13 -7.99907656209759e-05 -9.50858866044892e-06
8.80720171803219e-08 1.09047589982836e-08]

meq =[-7.07235452317028e-05 -3.85886450709802e-07 4.10389692596989e-10

-4.44701334210588e-06 1.43047719063004e-05 -3.09888536772647e-06
4.82521684338851e-08 -6.78744365861371e-08 1.40780576517799e-08]

Inclined

req =[0.00282239425720900 2.34251679238024e-05 -2.72002682190518e-07
1.74742740659535e-09 -0.000110241307795260 -3.02535470029390e-05 -
4.34453622186435e-06 8.11556578060433e-07]

meq =[-0.000207014649801837 -1.79134124775320e-06 2.84840616561721e-09

-1.38251183036623e-05 1.32035437019622e-05 -1.52711746490617e-06
1.12739193244048e-06 -5.24291723241899e-07 7.84071543897332e-08]

Anisotropic

Compression

req =[0.000589021817970268 9.83230811378498e-06 -1.09735295893093e-07
4.89379112490672e-10 -0.000262969685304389 4.61037441263455e-05
1.67692604992172e-07 -1.07307193544496e-07]

meq =[-7.32735063840740e-05 -8.36702838099236e-07 5.01684455867378e-09
1.08470847273274e-05 1.60253566280896e-05 -4.64446393833591e-06 -
1.71187414177365e-07 8.94928763353093e-08 -1.55463278780071e-08]

Inclined

req =[0.00168972350678578 4.34663584263923e-05 -4.78266254688414e-07
2.35128322788845e-09 -0.000337186568964790 2.67714774893017e-05

-5.13940415759776e-06 9.40163934087295e-07]

meq =[-0.000193266457799236 -4.81051502626398e-06 3.19126109942259e-08 -
4.52116948657233e-05 5.46109245990808e-05 -1.00815253146594e-05
1.59438231880634e-06 -1.03062985241853e-06 1.78416300890113e-07]

Sample 1

Compression

req =[0.00100771180160571 3.65798312079208e-06 -8.02287808067005e-09
4.81663854388781e-12 -0.000184438452593717 1.62609405267314e-05
2.50761040889082e-08 -5.24378218261484e-08]

meq =[-0.000105947527079151 -4.25398712254291e-07 4.82604405368612e-10
7.54370423358824e-06 9.49953540621025e-06 -1.94754224264328e-06 -
3.30585580415542e-08 -1.69911087617543e-08 3.70673602549684e-09]

Inclined

req =[0.00214602792990812 3.87331741009252e-05 -4.44809834606600e-07
2.36286024007953e-09 -0.000257807952334912 -1.27483696394968e-06 -
4.57579764763075e-06 7.67688658524488e-07]

meq =[-0.000208239900363976 -3.76933856912337e-06 2.12859229726663e-08 -
6.11470178420710e-05 5.37500645217646e-05 -9.12903737552744e-06
1.81681385259888e-06 -1.02212043597187e-06 1.70537397964099e-07]

Sample 2

Compression

req =[0.000891163472410508 6.99619129929362e-06 -1.81690211081701e-08
1.29073051587080e-11 -0.000312196171665165 6.31180104457131e-05 -
5.02923915216259e-07 -1.38405572879025e-07]

meq =[-9.83033357371639e-05 -4.30366093490193e-07 5.14068348352131e-10
2.61045325693091e-05 1.99431482297828e-06 -1.25798397500532e-06 -
8.54511410753508e-08 3.54057135947273e-09 7.93646305903151e-10]

Inclined

req =[0.00190207243827528 3.16193522493809e-05 -3.26507528077420e-07
1.51903462731127e-09 -0.000253471543463312 -5.39543799224320e-06 -
3.46373641113165e-06 5.84410486525860e-07]

meq =[-0.000183858433929019 -4.03477425625874e-06 2.27083691231863e-08 -
2.70773576144433e-05 4.01203397449577e-05 -7.09745729015581e-06
1.32818257992192e-06 -8.13196109002374e-07 1.42670026148870e-07]

Sample 3:

compression

req=[0.00101799582503055 2.36531884288672e-06 -4.28450771866724e-09
2.05372769288458e-12 -0.000311844629163691 4.99339995291308e-05
1.28580696438005e-07 -5.37246612210750e-08]

meq = [-0.000118963603184620 -3.51506438112479e-07 3.74944159041136e-10
3.78370708971371e-05 -7.43886064004629e-06 9.84918919712280e-07

-9.60664277437765e-08 2.22162886841789e-08 -3.35071145541844e-09]

Inclined

req=[0.00200255286924732 4.43278396053266e-05 -7.86901217066570e-07
3.54028625905949e-09 -0.000603631418696466 5.49879247414060e-05
5.14962792327169e-06 -7.02068084948004e-07]

meq = [-0.000248313806071125 -5.78436191567050e-06 5.88020844614220e-08
0.000118746595751670 -7.33387146696521e-05 1.73385095313312e-05

-2.23898094760982e-07 3.27281179307831e-07 -1.16531508597134e-07]

The model was validated using the experimental data from chapter 6 during the compression and inclined isolator characterization stage using Instron PULS tester in displacement control. Thus, the tests were performed using displacement as an input signal and the input of the model was the force amplitude corresponding to the displacement amplitude. To make the results more visually attractive five periods of the signals at each displacement amplitude were selected and connected to make a single waveform. The figures shown are only for the compression and inclined isolator with anisotropic MRE, but the same results apply for the rest of samples.

Figure 93 illustrates the simulated and experimental zero field displacement response under a dynamic force of 12, 21, 29, 36, 44 and 51N amplitude, that correspond to 0.025, 0.05, 0.075, 0.1, 0.125 and 0.15mm displacement amplitudes, for the anisotropic MRE inclined isolator. Figure 94 presents the equivalent response of the anisotropic MRE compression isolator under 26, 46, 64 and 81 N dynamic force amplitude, that correspond to 0.02, 0.04, 0.06 and 0.08 mm displacement amplitudes. As force amplitude increases, the displacement response becomes distorted due the MRE nonlinear behaviour. However, the model ignores higher harmonics and produces a pure sine wave causing loss of accuracy for higher force amplitude values that correspond to strains higher than 1%.

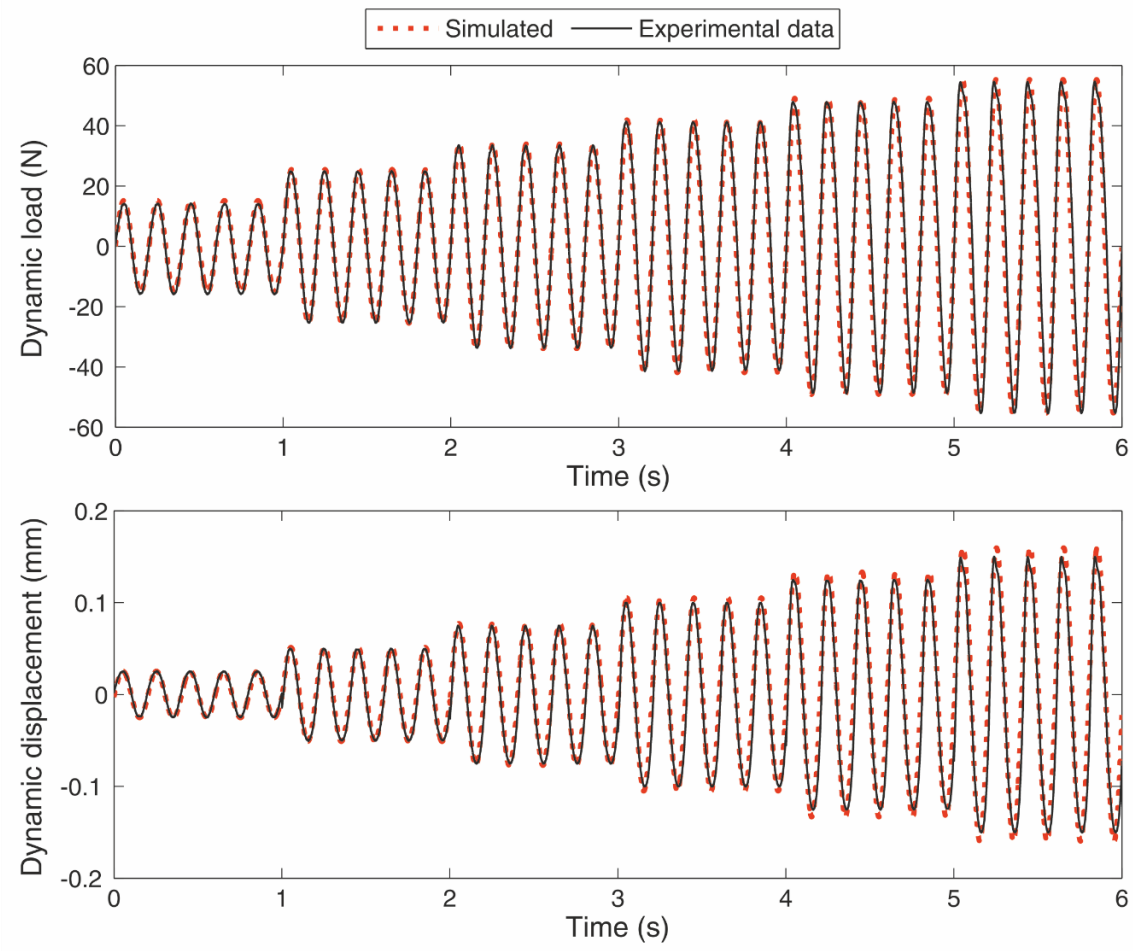

Figure 93: Simulated and experimental data of dynamic load and displacement for the anisotropic inclined isolator (at 12, 21, 29, 36, 44 and 51N dynamic force amplitude, 5Hz frequency and 80N static load).

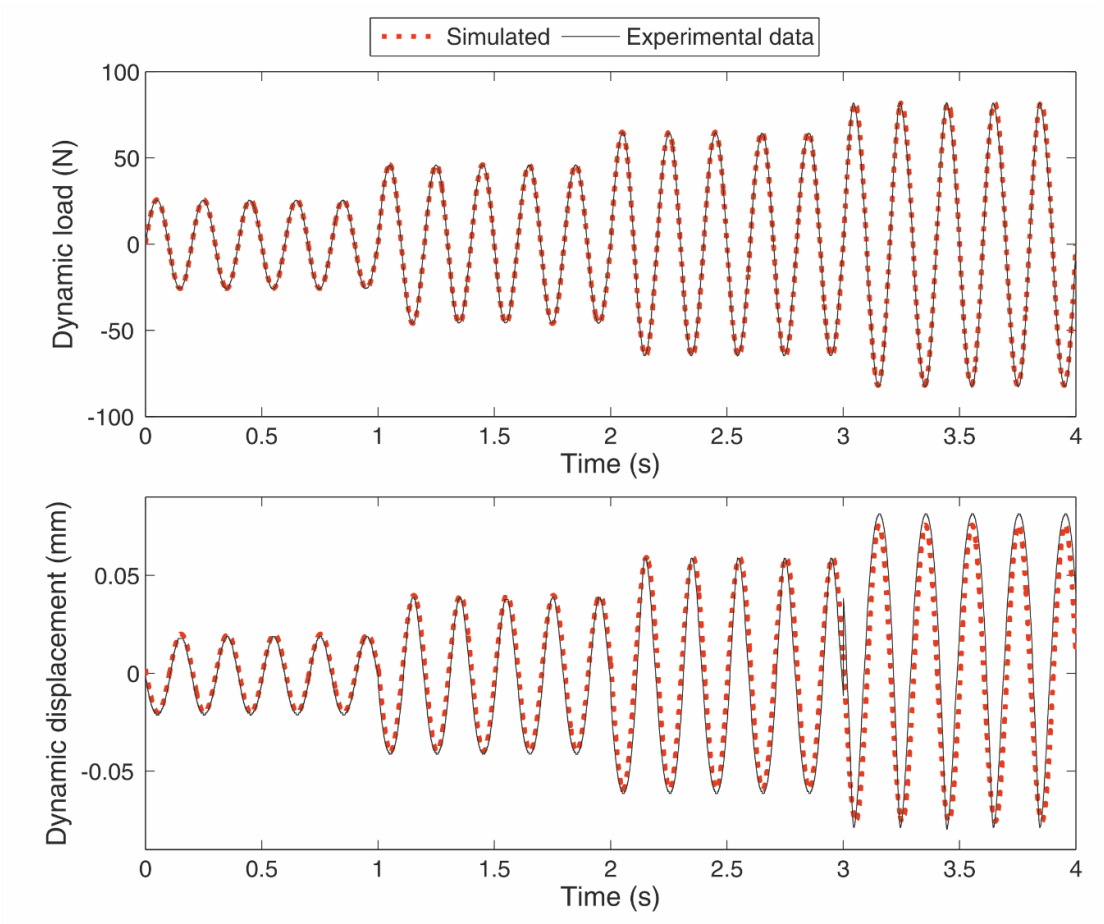

Figure 94: Simulated and experimental data of dynamic load and displacement for the anisotropic compression isolator (at 26, 46, 64 and 81 N dynamic force amplitudes, 5Hz frequency and 80N static load).

Figure 95 illustrates the stead state dynamic response for 0, 1 and 2 Amps electric current for the anisotropic MRE compression isolator under a dynamic displacement of 0.02mm amplitude. All characterization tests were performed using displacement as an input signal since Instron PULS is more accurate in displacement control. In this case the input of the model was the force amplitude corresponding to 0.02mm displacement amplitude when the electromagnet was fed with 0, 1 and 2 Amps electric current. The model can predict the variation of both dynamic and static displacements with the magnetic field. It is shown that static displacement increases by 0.07 mm when the electromagnet is fed with 2 Amps while for 3 Amps it increases to 0.1mm corresponding to 1.4% and 2% static strain.

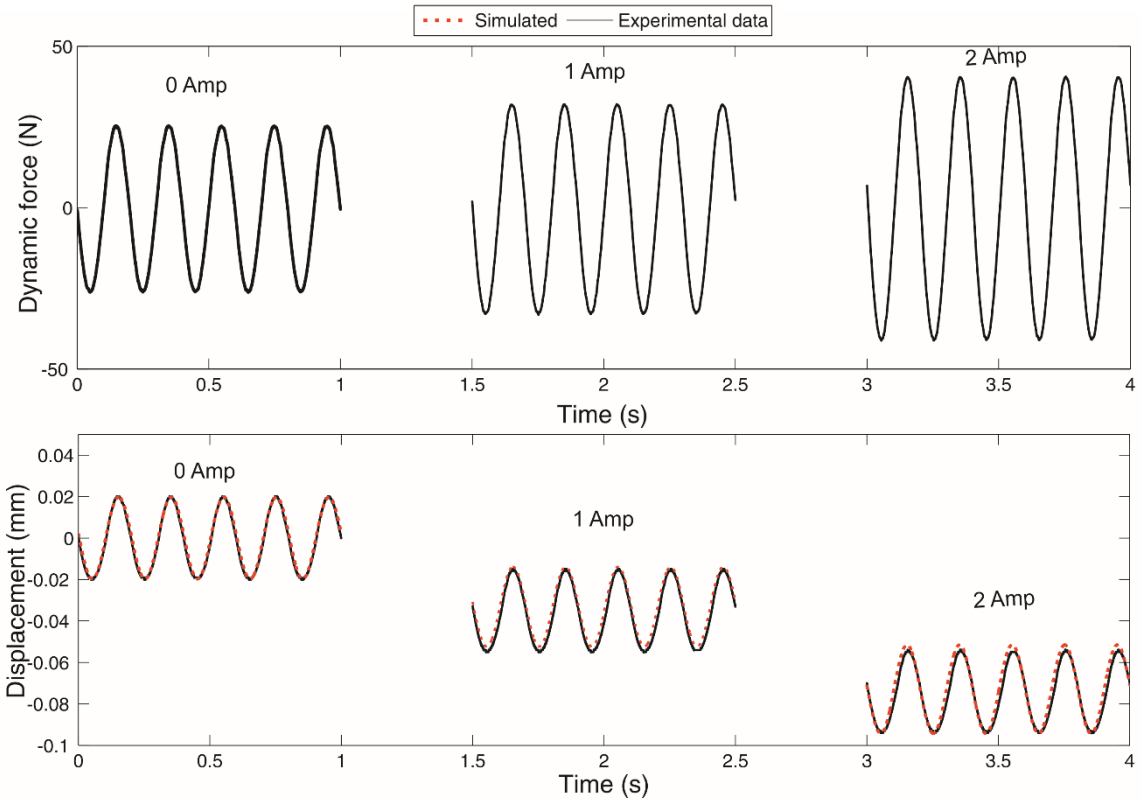

Figure 95: Simulated and experimental data of dynamic load and displacement for the anisotropic compression isolator (at 26, 32 and 41N load amplitude corresponding to 0.02mm displacement amplitude at 0 ,1 and 2 Amps electric current, 5Hz frequency and 80N static load).

7.4 Transmissibility of a single degree of freedom mass-MRE isolator system

- **Direct force excitation (n=0)**

Figure 96 presents a mass damper single degree of freedom system that can be equivalent of an engine of mass m mounted through an MRE isolator to a rigid foundation. When the input force is assumed harmonic with an amplitude causing less than 1% strain in the isolator the linearized model can be used instead. In the linearized system $[k]^{-1}$ and $[c]^{-1}$ are replaced by the equivalent receptance $\left[k_{eq}\right]^{-1}$ and mobility $\left[c_{eq}\right]^{-1}$ respectively, that are functions of the applied dynamic force amplitude $f_0$static load f_{st} and electric current.

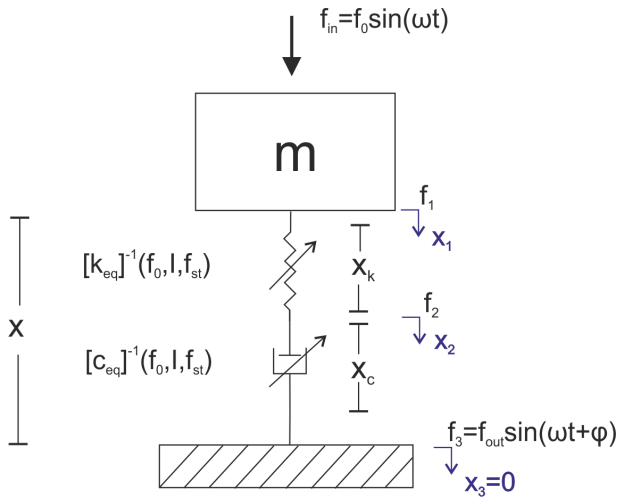

Figure 96: Single degree of freedom mass MRE isolator system where the excitation is a force applied on the mass supported by an MRE isolator in a rigid foundation

When a force $f_{in}(t)$ is applied to the mass the transmitted force to the substrate is $f_{out}(t)$. The total displacement of the mass is:

$$x(t) = x_1 - x_3 = x_k(t) + x_c(t) \tag{7.4.1}$$

Where $x_k(t) = x_1 - x_2$and $x_c(t) = x_2 - x_3$ are the relative displacements on the spring k, and dashpot c The differential equations of each branch are:

$$f_{out}(t) = f_2(t) = f_1(t) = f_{in}(t) - m\ddot{x}_1 \tag{7.4.2}$$

$$x_k(t) = \left[k_{eq}\right]^{-1} f_{out}(t) = \left[k_{eq}\right]^{-1}(f_{in}(t) - m\ddot{x}) \tag{7.4.3}$$

$$\dot{x_c} = \left[c_{eq}\right]^{-1} f_{out}(t) = \left[c_{eq}\right]^{-1}(f_{in}(t) - m\ddot{x}) \tag{7.4.4}$$

When a harmonic force force $F_{in}(t) = f_0 \sin \omega t$ is applied to the mass, the transmitted force to the substrate is $f_{out}(t)$. The displacement response is $x(t) = x_0 \sin(\omega t + \varphi) = x_f \cos(\omega t) + x_s \sin(\omega t)$ while equation (7.3.2) becomes:

$$\begin{aligned} F_{out} = F_{in} - m\ddot{x} &= F_0 \sin \omega t + m\omega^2 x_f \cos(\omega t) + m\omega^2 x_s \sin(\omega t) \\ &= (F_0 + m\omega^2 x_s)\sin \omega t + m\omega^2 x_f \cos(\omega t) \end{aligned} \tag{7.4.5}$$

Therefore, the force transmitted to the substrate $F_{out} = |F_{out}| \sin(\omega t + \theta)$ will have an amplitude $|F_{out}|$and be out of phase by an angle θ.

$$|F_{out}| = \sqrt{(f_0 + m\omega^2 x_s)^2 + \left(m\omega^2 x_f\right)^2} \tag{7.4.6}$$

$$\Theta = \tan^{-1}\left(\frac{m\omega^2 x_f}{F_0 + m\omega^2 x_s}\right) \tag{7.4.7}$$

$$TFF = \frac{|F_{out}|}{|F_{in}|} = \frac{\sqrt{(F_0 + m\omega^2 x_s)^2 + \left(m\omega^2 x_f\right)^2}}{F_0} \tag{7.4.8}$$

To solve the system analytically the Ritz-Galerkin method can be used again to determine the components of the displacement x_s and x_f. The error function, the integral of which must be minimized in this case is

$$\dot{x} - \dot{x_k} - \dot{x_c} = e(t) \tag{7.4.9}$$

Where:

$$\dot{x_k}(t) = \left[k_{eq}\right]^{-1} \omega\left((F_0 + m\omega^2 x_s)\cos \omega t - m\omega^2 x_f \sin(\omega t)\right) \tag{7.4.10}$$

$$\dot{x_c} = \left[c_{eq}\right]^{-1} f_{out}(t) = \left[c_{eq}\right]^{-1}\left((F_0 + m\omega^2 x_s)\sin \omega t + m\omega^2 x_f \cos(\omega t)\right) \tag{7.4.11}$$

$$\dot{x} = \omega x_s \cos(\omega t) - \omega x_f \sin(\omega t) \tag{7.2.12}$$

The individual displacement components can then be obtained by solving the following set of equations:

$$\frac{\partial J}{\partial x_f} = \int_{t1}^{t2} 2e(t)\frac{\partial e(t)}{\partial x_f} = 0 \qquad \frac{\partial J}{\partial x_s} = \int_{t1}^{t2} 2e(t)\frac{\partial e(t)}{\partial x_s} = 0 \tag{7.4.13}$$

The partial derivatives $\frac{\partial e(t)}{\partial x_f}$ and $\frac{\partial e(t)}{\partial x_s}$ become:

$$\frac{\partial e(t)}{\partial x_f} = -\omega\left[\left(1 - m\omega^2\left[k_{eq}\right]^{-1}\right)\sin(\omega t) + m\omega^2 \frac{\left[c_{eq}\right]^{-1}}{\omega} \cos(\omega t)\right] \tag{7.4.14}$$

$$\frac{\partial e(t)}{\partial x_s} = \left(1 - m\omega^2 \left[k_{eq}\right]^{-1}\right)\cos(\omega t) - m\omega^2 \frac{\left[c_{eq}\right]^{-1}}{\omega} \sin(\omega t)$$

The displacement components of the solution are acquired by substituting equations (7.4.11) to (7.4.13) to equation (7.2.14) and then the latter along with equations (7.4.16) to (7.4.15) and integrating for one period (from $t_1 = 0$ to $t_2 = 2\pi/\omega$). These calculations were done using MATLAB's symbolic maths toolbox (Appendix A). The resulting components of the displacement are:

$$x_f = -\frac{\frac{\left[c_{eq}\right]^{-1}}{\omega}}{\left(m\omega^2 \frac{\left[c_{eq}\right]^{-1}}{\omega}\right)^2 + \left(1 - m\omega^2 \left[k_{eq}\right]^{-1}\right)^2} F_0 \tag{7.4.15}$$

$$x_s = \frac{\left[k_{eq}\right]^{-1}\left(1 - m\omega^2 \left[k_{eq}\right]^{-1}\right) - m\omega^2 \left(\frac{\left[c_{eq}\right]^{-1}}{\omega}\right)^2}{\left(m\omega^2 \frac{\left[c_{eq}\right]^{-1}}{\omega}\right)^2 + \left(1 - m\omega^2 \left[k_{eq}\right]^{-1}\right)^2} F_0 \tag{7.4.16}$$

Substituting equations (7.4.17) and (7.4.18) to equation (7.4.5) the force transmitted to the substrate becomes:

$$\begin{aligned} F_{out} = &\left(\frac{1 - m\omega^2 \left[k_{eq}\right]^{-1}}{\left(m\omega^2 \frac{\left[c_{eq}\right]^{-1}}{\omega}\right)^2 + \left(1 - m\omega^2 \left[k_{eq}\right]^{-1}\right)^2} F_0\right) \sin \omega t \\ &+ \left(-\frac{m\omega^2 \frac{\left[c_{eq}\right]^{-1}}{\omega}}{\left(m\omega^2 \frac{\left[c_{eq}\right]^{-1}}{\omega}\right)^2 + \left(1 - m\omega^2 \left[k_{eq}\right]^{-1}\right)^2} F_0\right) \cos(\omega t) \end{aligned} \tag{7.4.17}$$

The force transmissibility TFF of the system is:

$$TFF = \frac{|F_{out}|}{|F_{in}|} = \frac{1}{\sqrt{\left(m\omega^2 \frac{\left[c_{eq}\right]^{-1}}{\omega}\right)^2 + \left(1 - m\omega^2 \left[k_{eq}\right]^{-1}\right)^2}} \tag{7.4.18}$$

$$\Theta = \tan^{-1}\left(\frac{\frac{[c_{eq}]^{-1}}{\omega}}{(m\omega^2)^{-1} - [k_{eq}]^{-1}}\right) \tag{7.4.19}$$

While the force-displacement response TDF of the system is:

$$TDF = \frac{|x|}{|F_{in}|} = \frac{\sqrt{(x_s)^2 + (x_f)^2}}{F_0} \tag{7.4.20}$$

The force transmissibility curves of anisotropic, isotropic, sample 1, sample 2 and sample 3 compression and inclined isolators (calculated using equation (7.4.18)) in respect to zero field frequency ratio $\frac{f}{fn}$ are presented in Figure 97, Figure 98, Figure 99, Figure 100 and Figure 101 respectively. As the electric current *I* fed to the electromagnet increases, dynamic stiffness increases and the natural frequency fn increases as well. Damping is relatively low and not greatly influenced by the magnetic field. Low damping causes high transmissibility values at resonance indicating a damping ratio of about 0.05. The stiffening of the material with the magnetic field reduces force transmissibility at higher frequencies especially for the compression isolator that has a higher MR effect than inclined isolator. However, the inclined isolator increases its natural frequency almost linearly with the electric current for all MRE samples while this is not the case for the compression isolator with anisotropic, sample 2 and sample 3 MREs.

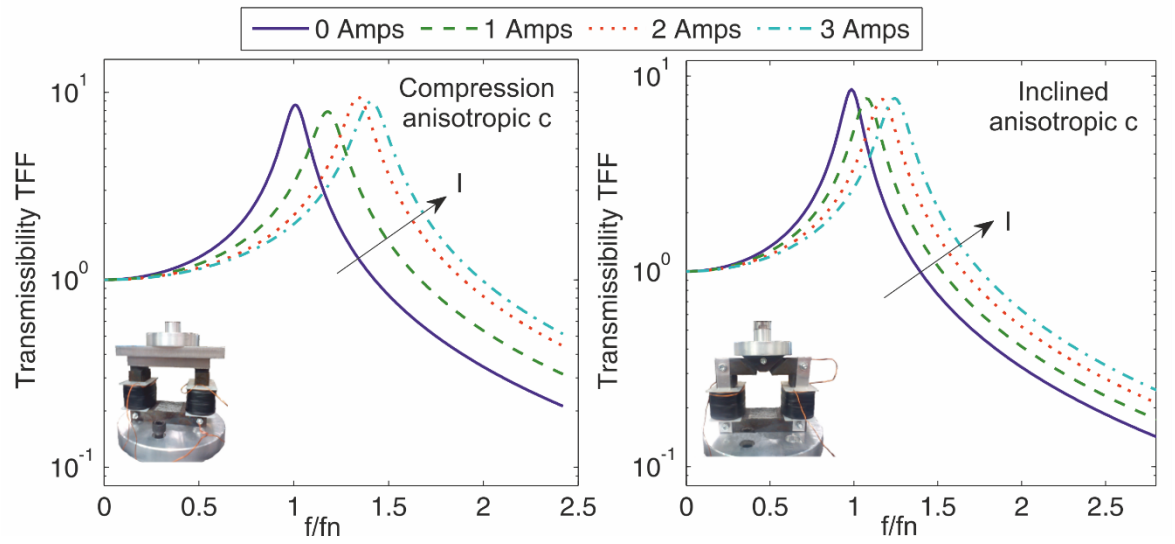

Figure 97: Force transmissibility TFF of anisotropic MRE compression and inclined isolator at 0, 1, 2 and 3 Amps electric current fed to the electromagnet in respect to zero field frequency ratio f/fn (at 30N amplitude force and m=8Kg).

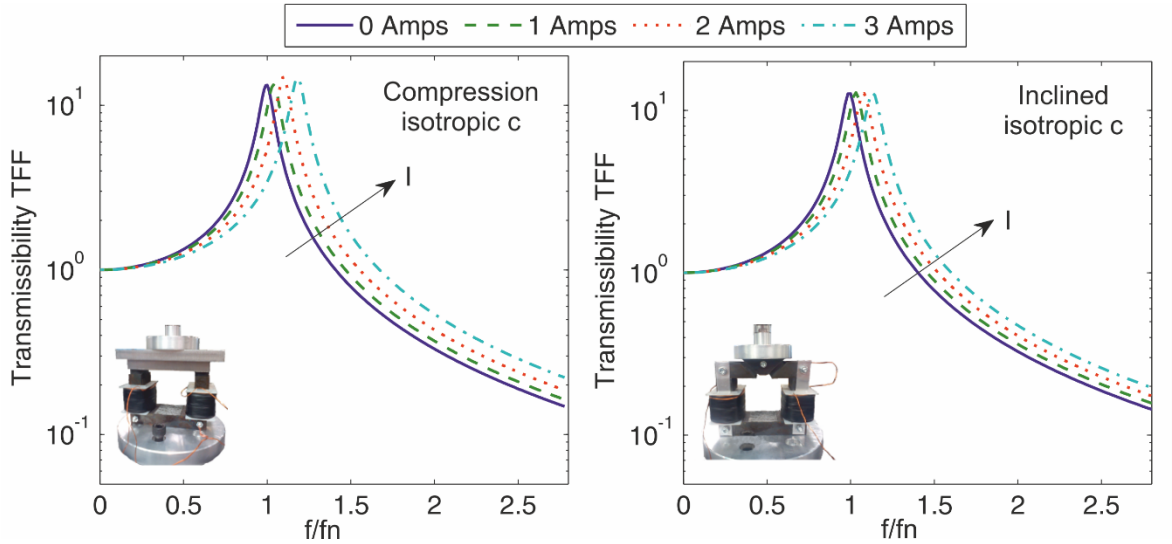

Figure 98: Force transmissibility TFF of isotropic MRE compression and inclined isolator at 0, 1, 2 and 3 Amps electric current fed to the electromagnet in respect to zero field frequency ratio f/fn (at 30N amplitude force and m=8Kg).

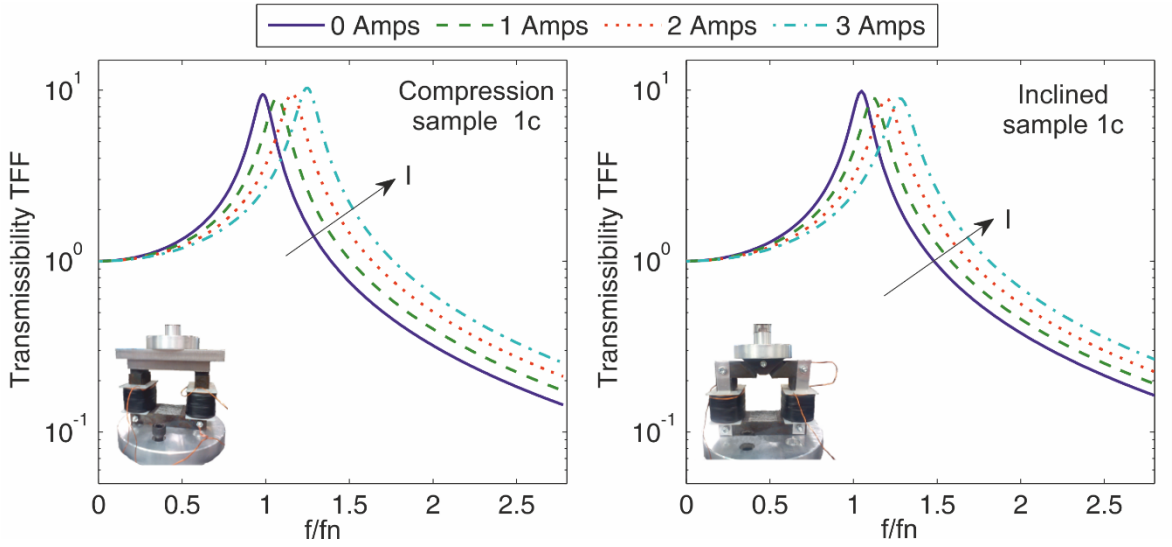

Figure 99: Force transmissibility TFF of sample 1c (isotropic/anisotropic parallel combination) MRE compression and inclined isolator at 0, 1, 2 and 3 Amps electric current fed to the electromagnet in respect to zero field frequency ratio f/fn (at 30N amplitude force and m=8Kg).

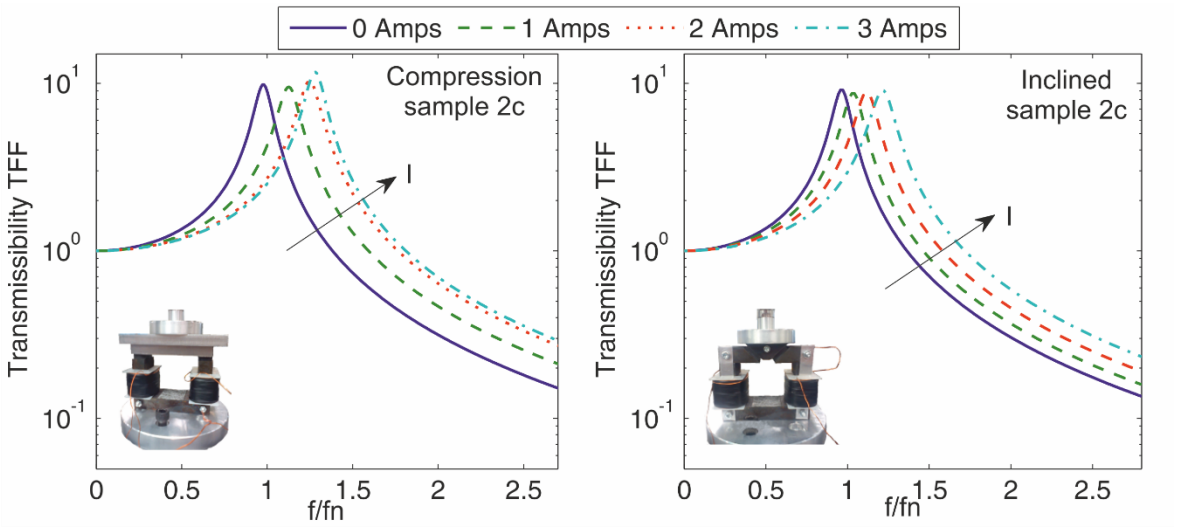

Figure 100: Force transmissibility TFF of sample 2c (isotropic/anisotropic series combination) MRE compression and inclined isolator at 0, 1, 2 and 3 Amps electric current fed to the electromagnet in respect to zero field frequency ratio f/fn (at 30N amplitude force and m=8Kg).

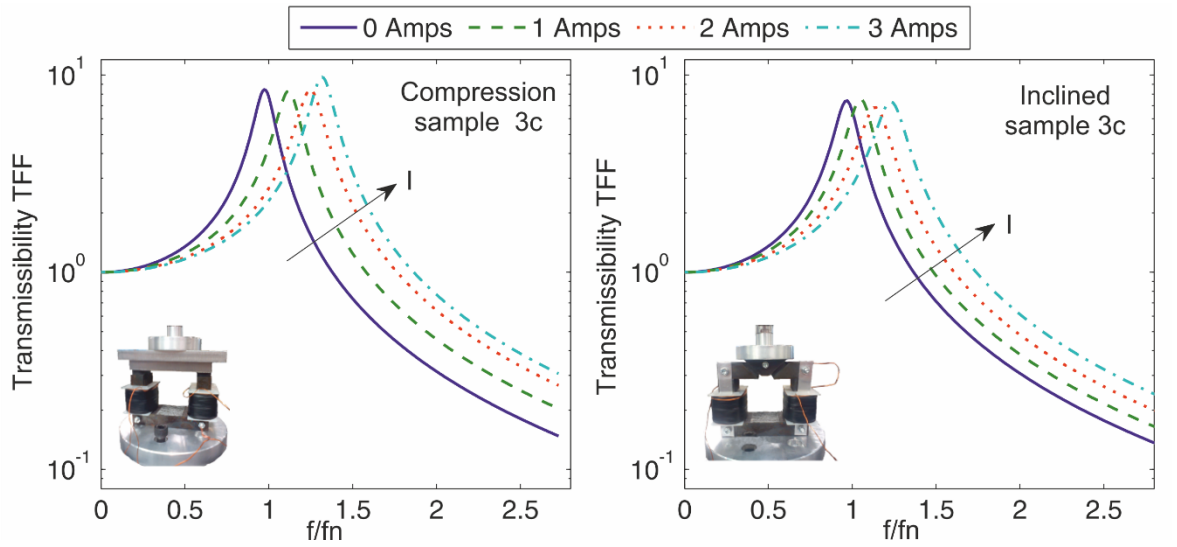

Figure 101: Force transmissibility TFF of sample 3c (anisotropic/anisotropic parallel combination) MRE compression and inclined isolator at 0, 1, 2 and 3 Amps electric current fed to the electromagnet in respect to zero field frequency ratio f/fn (at 30N amplitude force and m=8Kg).

- **Support acceleration excitation (n=2)**

Figure 102 presents a mass damper single degree of freedom system that can be equivalent of an engine of mass m mounted through an MRE isolator to a non-rigid foundation. Assuming a harmonic base excitation $x_3(t) = x_{in}\sin\omega t$, then the ground acceleration will be $\ddot{x_3}(t) = -\omega^2 x_{in}\sin\omega t$. The force acting on the isolator is the inertial force $f_3(t) = -m\ddot{x_3}(t) = m\omega^2 x_{in}\sin\omega t$ resisting the ground acceleration, which is a harmonic force of amplitude $m\omega^2 x_{in}$. For harmonic inputs with displacement amplitude value x_{in}, that correspond to less than 1% strain amplitude, the system can be considered linear. In the linearized system $[k]^{-1}$ and $[c]^{-1}$ are replaced by the equivalent receptance $\left[k_{eq}\right]^{-1}$ and mobility $\left[c_{eq}\right]^{-1}$ respectively, that are functions of the force amplitude $m\omega^2 x_{in}$ applied to the substrate, static load f_{st} and electric current I.

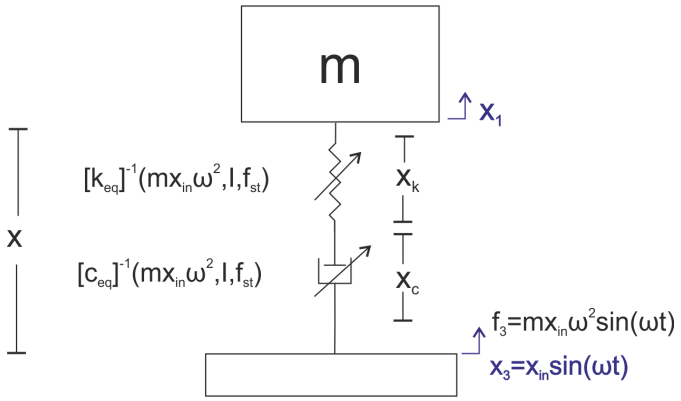

Figure 102: Single degree of freedom mass MRE isolator system where the excitation is due to a movement of the foundation

The steady state displacement response of the MRE isolator is:

$$x(t) = x_1(t) - x_3(t) = x_f\cos(\omega t) + x_s\sin(\omega t) \tag{7.4.21}$$

The total displacement the mass undergoes is:

$$x_1(t) = x(t) + x_3(t) = x_f\cos(\omega t) + (x_s + x_{in})\sin(\omega t) \tag{7.4.22}$$

The differential equations are:

$$x(t) = x_k(t) + x_c(t) \tag{7.4.23}$$

$$x_k(t) = \left[k_{eq}\right]^{-1}\left(-m\ddot{x_3}(t) - m\ddot{x_1}(t)\right) \tag{7.4.24}$$

$$\dot{x_c}(t) = \left[c_{eq}\right]^{-1}\left(-m\ddot{x_3}(t) - m\ddot{x_1}(t)\right) \tag{7.4.25}$$

To solve the system analytically the Ritz-Galerkin method can be used again to determine the components of the displacement x_s and x_f. The error function, the integral of which must be minimized in this case is

$$\dot{x}(t) - \dot{x_k}(t) - \dot{x_c}(t) = e(t) \tag{7.4.26}$$

Where:

$$\dot{x_k}(t) = \left[k_{eq}\right]^{-1}\left(-m\ddot{x_3}(t) - m\ddot{x_1}(t)\right) \tag{7.4.27}$$

$$\dot{x}(t) = \omega x_s \cos(\omega t) - \omega x_f \sin(\omega t) \tag{7.4.28}$$

$$\ddot{x_3}(t) = -\omega^2 x_{in}\sin\omega t \qquad \dddot{x_3}(t) = -\omega^3 x_{in}\cos\omega t \tag{7.4.29}$$

$$\ddot{x_1}(t) = -\omega^2 x_f \cos(\omega t) - \omega^2(x_s + x_{in})\sin(\omega t) \tag{7.4.30}$$

$$\dddot{x_1}(t) = \omega^3 x_f \sin(\omega t) - \omega^3(x_s + x_{in})\cos(\omega t) \tag{7.4.31}$$

The individual displacement components can then be obtained by solving the following set of equations:

$$\frac{\partial J}{\partial x_f} = \int_{t1}^{t2} 2e(t)\frac{\partial e(t)}{\partial x_f} = 0 \qquad \frac{\partial J}{\partial x_s} = \int_{t1}^{t2} 2e(t)\frac{\partial e(t)}{\partial x_s} = 0 \tag{7.4.32}$$

The partial derivatives $\frac{\partial e(t)}{\partial x_f}$ and $\frac{\partial e(t)}{\partial x_s}$ become:

$$\frac{\partial e(t)}{\partial x_f} = \omega\left[-\left(1 + m\omega^2\left[k_{eq}\right]^{-1}\right)\sin(\omega t) + m\omega^2\frac{\left[c_{eq}\right]^{-1}}{\omega}\cos(\omega t)\right] \tag{7.4.33}$$

$$\frac{\partial e(t)}{\partial x_s} = \left(1 + m\omega^2\left[k_{eq}\right]^{-1}\right)\cos(\omega t) + m\omega^2\frac{\left[c_{eq}\right]^{-1}}{\omega}\sin(\omega t) \tag{7.4.34}$$

The displacement components of the solution are acquired by substituting equations (7.4.26), (7.2.23) and (7.4.27) to equation (7.2.28) and then the latter along with equations (7.4.30) to (7.4.29) and integrating for one period (from $t_1 = 0$ to $t_2 = 2\pi/\omega$). In this case the solution to the system becomes:

$$x_f = -\frac{\frac{\left[c_{eq}\right]^{-1}}{\omega}}{\left(m\omega^2\frac{\left[c_{eq}\right]^{-1}}{\omega}\right)^2 + \left(1 - m\omega^2\left[k_{eq}\right]^{-1}\right)^2} m\omega^2 x_{in} \tag{7.4.35}$$

$$x_s = \frac{\left[k_{eq}\right]^{-1}\left(1 - m\omega^2\left[k_{eq}\right]^{-1}\right) - m\omega^2\left(\frac{\left[c_{eq}\right]^{-1}}{\omega}\right)^2}{\left(m\omega^2\frac{\left[c_{eq}\right]^{-1}}{\omega}\right)^2 + \left(1 - m\omega^2\left[k_{eq}\right]^{-1}\right)^2} m\omega^2 x_{in} \tag{7.4.36}$$

The absolute displacement transmissibility TDD of the system is:

$$TDD = \frac{|x_1|}{|x_3|} = \frac{\sqrt{(x_s - x_{in})^2 + \left(x_f\right)^2}}{x_{in}} = \frac{1}{\sqrt{\left(1 - m\omega^2\left[k_{eq}\right]^{-1}\right)^2 + \left(m\omega^2\frac{\left[c_{eq}\right]^{-1}}{\omega}\right)^2}} \tag{7.4.37}$$

$$\Theta = \tan^{-1}\left(-\frac{m\omega^2\frac{\left[c_{eq}\right]^{-1}}{\omega}}{1 + m\omega^2\left[k_{eq}\right]^{-1}}\right) \tag{7.4.38}$$

While the relative displacement transmissibility of the system is:

$$TDR = \frac{|x|}{|x_3|} = \frac{|x_1 - x_3|}{|x_3|} = \frac{1}{\sqrt{\left(1 - m\omega^2\left[k_{eq}\right]^{-1}\right)^2 + \left(m\omega^2\frac{\left[c_{eq}\right]^{-1}}{\omega}\right)^2}} - 1 \tag{7.4.39}$$

The absolute displacement transmissibility curves of anisotropic, isotropic, sample 1, sample 2 and sample 3 compression and inclined isolators (calculated using equation (7.4.37)) in respect to zero field frequency ratio $\frac{f}{fn}$ are presented in Figure 103, Figure 104, Figure 105, Figure 106 and Figure 107 respectively. As the electric current *I* fed to the electromagnet increases, dynamic stiffness increases and the natural frequency fn increases as well. Damping is relatively low and not greatly influenced by the magnetic field. The displacement transmissibility curves are different at high frequencies from force transmissibility curves presented earlier due to the increase of force amplitude with frequency and the amplitude-magnetic field coupling effects. This is more pronounced for the anisotropic compression MRE isolator because its dynamic stiffness decreases faster with increasing amplitude.

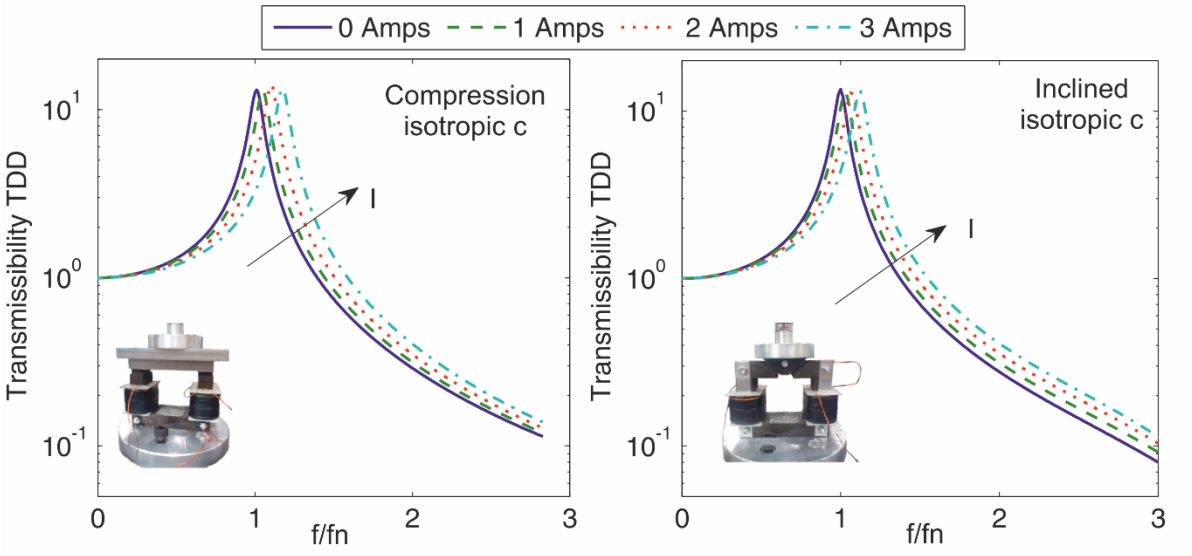

Figure 103: Displacement transmissibility TFF of isotropic MRE compression and inclined isolator at 0, 1, 2 and 3 Amps electric current fed to the electromagnet in respect to zero field frequency ratio f/fn (at 30N amplitude force and m=8Kg).

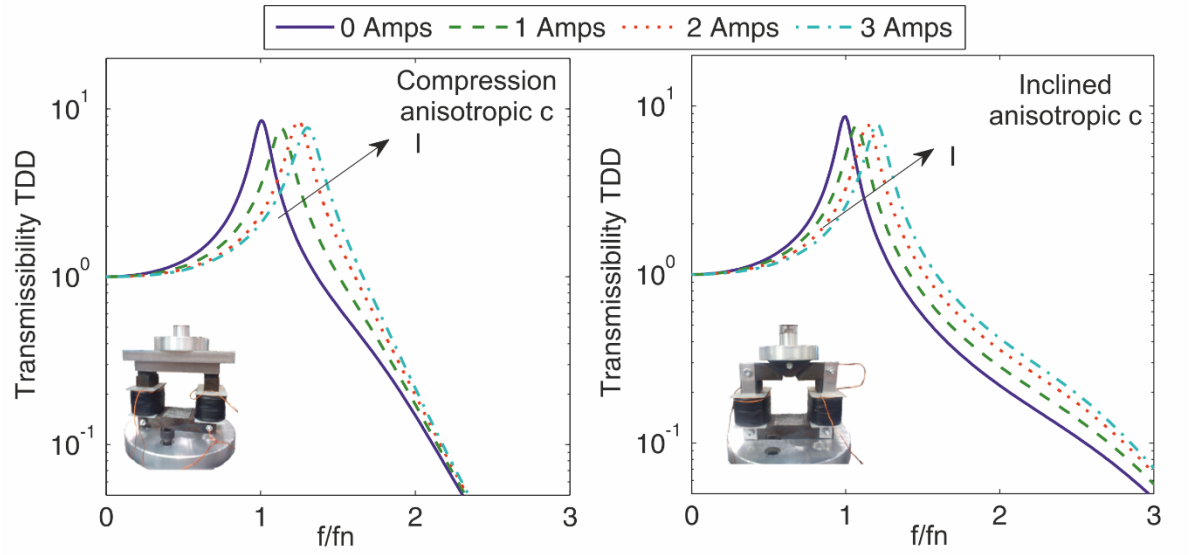

Figure 104: Displacement transmissibility TFF of anisotropic MRE compression and inclined isolator at 0, 1, 2 and 3 Amps electric current fed to the electromagnet in respect to zero field frequency ratio f/fn (at 30N amplitude force and m=8Kg).

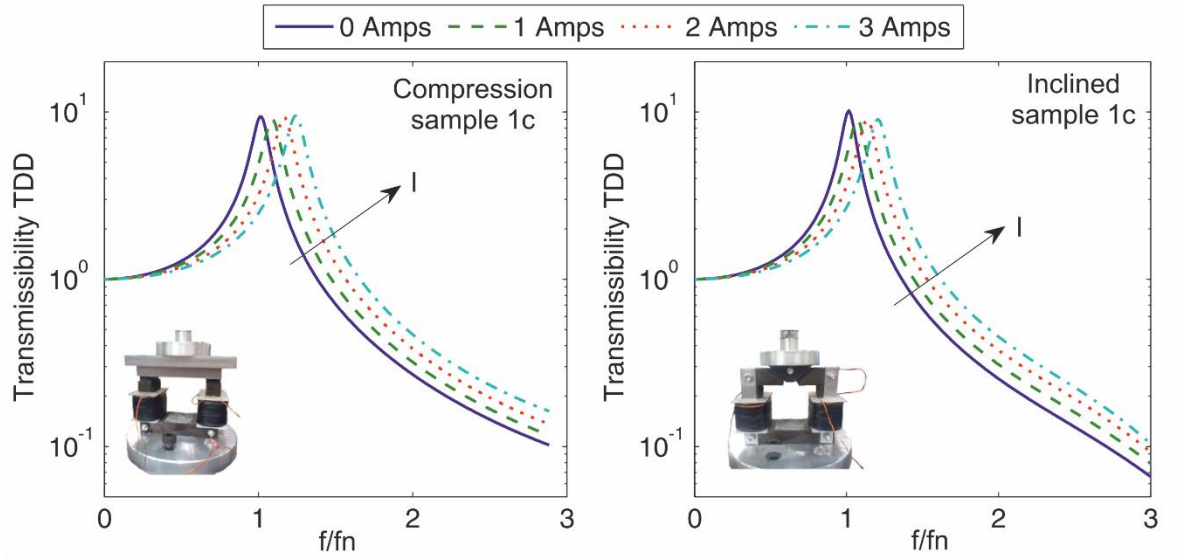

Figure 105: Displacement transmissibility TFF of sample 1c (isotropic/anisotropic parallel combination) MRE compression and inclined isolator at 0, 1, 2 and 3 Amps electric current fed to the electromagnet in respect to zero field frequency ratio f/fn (at 30N amplitude force and m=8Kg).

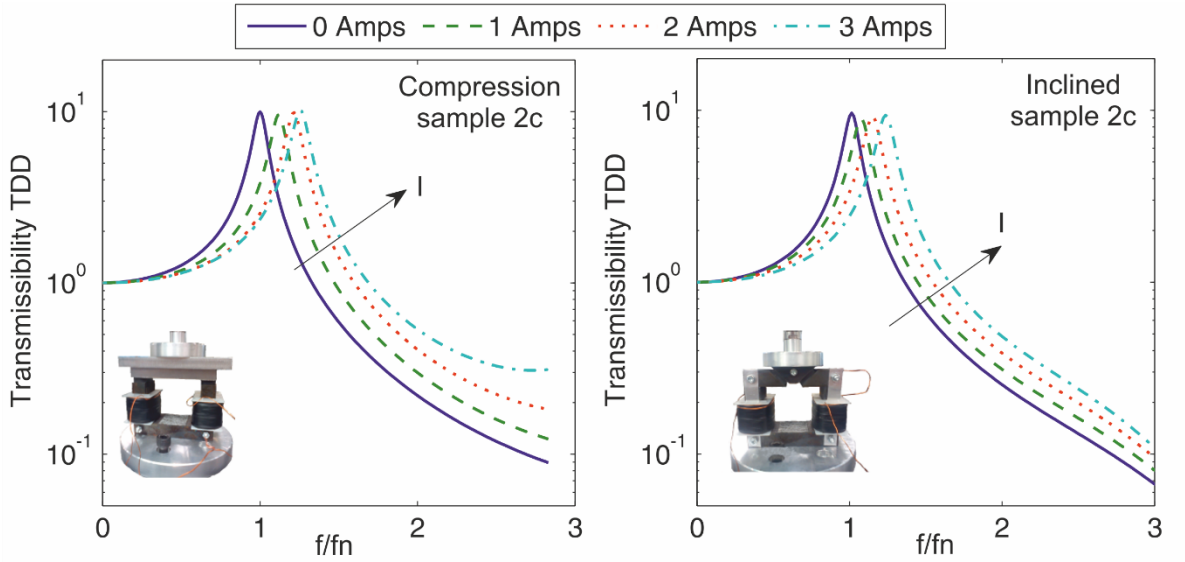

Figure 106: Displacement transmissibility TFF of sample 2c (isotropic/anisotropic series combination) MRE compression and inclined isolator at 0, 1, 2 and 3 Amps electric current fed to the electromagnet in respect to zero field frequency ratio f/fn (at 30N amplitude force and m=8Kg).

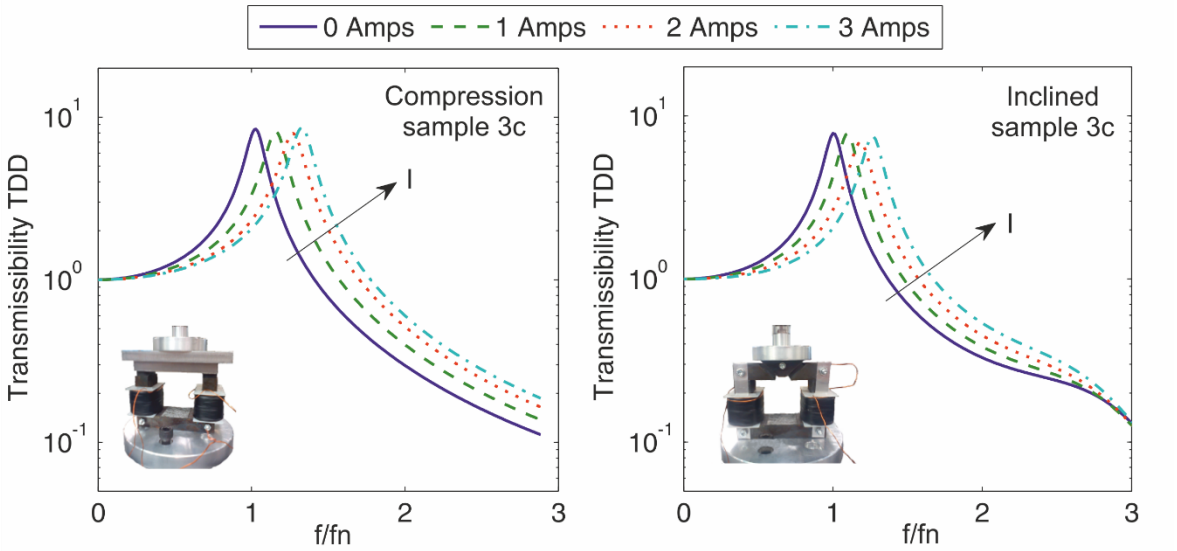

Figure 107: Displacement transmissibility TFF of sample 3c (anisotropic/anisotropic parallel combination) MRE compression and inclined isolator at 0, 1, 2 and 3 Amps electric current fed to the electromagnet in respect to zero field frequency ratio f/fn (at 30N amplitude force and m=8Kg).

7.5 Stability of a mass-inclined MRE isolator system

In many marine mass-isolator systems, stability is equally important as isolation efficiency. Such a system could be the main propulsion engine that is usually connected to the propeller shaft through an elastic coupling. During heavy sea, ship motion could cause severe misalignment between the engine and the shaft line making the system unstable. Marine propulsion engines are usually mounted on inclined isolators with natural frequencies below 15Hz, that provide efficient isolation at engine operating frequencies. However, roll, pitch and yaw ship motion have very low frequencies that could be in the early amplification area of transmissibility curves. Thus, the stiffness of the isolators must be high enough to ensure low displacements under sea motion (stability) but still low enough to provide adequate isolation. A solution to this problem is the use of active isolation systems where natural frequency is increased when stability becomes an issue while sacrificing isolation efficiency at higher frequencies. MRE isolators could be used for this purpose.

This section examines the principle of using the inclined MRE isolator to improve stability of a mass-isolator system under loading conditions that represent ship motion. The theoretical mass-inclined MRE isolator system is presented in Figure 108. The mass represents an engine supported in two identical MRE inclined isolators arranged in the Z direction with two planes of symmetry. At equilibrium the system is excited only by $F_{in}(t) = f_o \sin(2\pi f_1 t)$ acting in the vertical direction when it is rotated by an angle $u_{in}(t)$ about the Z axis due to sea motion and the isolators provide sufficient isolation. The important part in this section is to present how the configuration of the combined MRE samples influences stiffness in more than one direction and if MRE isolator can be used to control stability. Thus, only the anisotropic/anisotropic parallel combination sample 3c and isotropic/anisotropic series combination sample 2c MREs are considered.

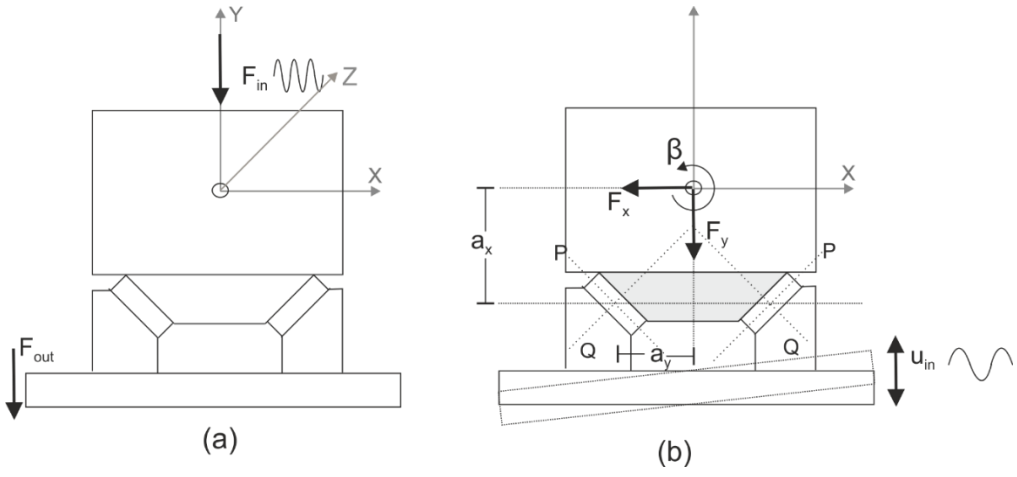

Figure 108: Mass-inclined MRE isolator system a) at equilibrium state under force excitation b) under rotation about the Z axis

The displacement of each isolator in the y direction is assumed $u(t) = u_1(t) - u_{in}(t) = u_f \cos(\omega t) + u_s \sin(\omega t)$, where $u_1(t)$ is the displacement of the mass. The force transmitted to the substrate and the dynamic displacement components u_f and u_s are given by equations (7.4.18), (7.4.15) and (7.4.16) for $\left[c_{eq}\right]^{-1}$ and $\left[k_{eq}\right]^{-1}$ at f_o amplitude and 0 Amps electric current. The rotation motion is equivalent to applying the following forces to the mass centre of gravity [L He et al. 2014]:

$$\begin{aligned} F_x &= mg \sin(u(t)) \\ F_y &= mg \cos(u(t)) \end{aligned} \tag{7.5.1}$$

Where u(t) is the rotation angle. The system has two planes of symmetry thus, the forces applied in the Y direction cause displacements *y* only in the same direction while translational displacement *x* on the X axis and rotational displacement *β* about the Z axis are coupled motions. Therefore, force component F_x causes a rotational displacement β and the equations of motion for the system with two isolators are:

$$m\ddot{x} + 2{k_x}^* x - 2{k_x}^* a_y \beta = F_x \tag{7.5.2}$$

$$m\ddot{y} + 2{k_y}^* y = F_y \tag{7.5.3}$$

$$I_z \ddot{\beta} + 2{k_\beta}^* \beta - 2{k_x}^* a_y x = 0 \tag{7.5.4}$$

Where I_z is the moment of inertia about the z axis, ${k_x}^*$ and ${k_y}^*$ are complex dynamic stiffnesses in the X, Y axis, ${k_\beta}^*$ is complex rotational stiffness about the Z axis and a_y is defined in Figure 108. Rotation angle frequency f_2 is very low and the MRE isolator operates in the zero-isolation region where damping is negligible. Thus, the system behaves as a static one and the second order differential terms can be ignored. When the principal elastic axis P, Q are selected as the new coordinate system, the stiffness in the original OXY system can be expressed in terms of principal stiffness elements k_p and k_q (Harris C M 2002) (for the specific MRE inclined isolator $\theta = 45^0$).

$$k_x = k_q \cos^2\theta + k_p \sin^2\theta = \frac{k_q + k_p}{2} \tag{7.6.5}$$

$$k_y = k_q \sin^2\theta + k_p \cos^2\theta = \frac{k_q + k_p}{2} \tag{7.6.6}$$

$$k_\beta = \frac{{a_x}^2 k_q\, k_p}{k_q \sin^2\theta + k_p \cos^2\theta} = \frac{2{a_x}^2 k_q\, k_p}{k_q + k_p} \tag{7.6.7}$$

Where, k_x and k_y are static stiffnesses in the X, Y axis, k_β is static rotational stiffness about the Z axis and a_x is defined in Figure 108. Substituting equations (7.6.6) to (7.6.3) and (7.6.5), (7.6.7) to (7.6.2) and (7.6.4) we get:

$$y = \frac{F_y}{2k_y}, \qquad x = \frac{F_x}{2k_x}\frac{k_\beta}{k_\beta - {a_y}^2 k_x}, \qquad \beta = \frac{F_x a_y}{(2k_\beta - {a_y}^2 2k_x)} \tag{7.6.8}$$

For the inclined MRE isolator $\frac{k_q}{k_p}$ ratio varies with the magnetic field due to the change of stiffness in the direction of the applied field as explained in detail is (section 6.6). The next step is to define principle static stiffness $\frac{k_q}{k_p}$ ratio at different magnetic fields. Assuming m=16Kg, each isolator will be support 8Kg each (which corresponds to the applied static force during characterization stage at chapter 6), the results for sample 2c and sample 3c MREs are presented at Table 32. Vertical stiffness k_y is found from the model of the inclined isolator for Fst=80N while stiffness Kq is found from the model of the compression isolator for $F_{st} = 80\sin(45) = 57N$. Anisotropic/anisotropic parallel combination sample 3 MRE isolator has a much higher stiffness ratio than isotropic/anisotropic series combination sample 2 isolator. Stiffness ratio decreases with electric current for both types while for the isotropic/anisotropic series combination sample 2c the stiffness in shear k_p becomes greater than stiffness k_q after 2 Amps. This is because the static MR effect in shear, and thus the inclined isolator, is higher than the pure compression one.

Table 32: Principal Static stiffness ratio for sample 2c and 3c MREs

	Sample 2c				**Sample 3c**			
I (Amps)	***Kq (57N)*** (KN/mm)	k_y **(80N)** (KN/mm)	***Kp*** (KN/mm)	k_q/k_p	***Kq (57N)*** (KN/mm)	k_y **(80N)** (KN/mm)	***Kp*** (KN/mm)	k_q/k_p
0	119	103	87	1.37	182	123	64	2.84
1	140	121	102	1.37	206	145	84	2.45
2	151	173	195	0.77	237	175	113	2.1
3	167	227	287	0.58	257	223	189	1.36

The displacements the mass undergoes at 20 degrees inclination angle and assuming $a_y = 0.7a_x$ is presented at Table 33. At zero electric current vertical displacement y is higher for sample 2c inclined isolator but horizontal and rotational displacements x and β are smaller. As the electric current increases and the isolator becomes stiffer all displacements decrease to similar values at 3 Amps electric current. Thus, both MRE isolators are effective at decreasing displacements caused

by severe sea motion while ensuring that transmitted vibrations remain to an acceptable level. In addition, the combined MRE configuration and anisotropic/isotropic or anisotropic/anisotropic ratio can be adjusted to control $\frac{k_q}{k_p}$ and thus, zero field static stiffness in the X, Y axis k_x, k_y and k_β static rotational stiffness about the Z axis. When the electric current is increased the transmitted vibrations to the substrate also increase but if the natural frequency of the isolator is selected correctly the increase at high frequencies will not be a problem.

Table 33: Static x, y and β displacements assuming $a_y = 0.7a_x$ and 20^0 inclination angle.

	Sample 2c				**Sample 3c**			
I (Amps)	$\boldsymbol{k_\beta}$ (KN/mm)	$\boldsymbol{y}$ (mm)	$\boldsymbol{x}$ (mm)	$\boldsymbol{\beta}$	$\boldsymbol{k_\beta}$ (KN/mm)	$\boldsymbol{y}$ (mm)	$\boldsymbol{x}$ (mm)	$\boldsymbol{\beta}$
0	100.4 ${a_x}^2$	0.73	0.52	$0.38/a_x$	95 ${a_x}^2$	0.61	0.61	$0.55/a_x$
1	118 ${a_x}^2$	0.62	0.45	$0.33/a_x$	119 ${a_x}^2$	0.52	0.47	$0.4/a_x$
2	170.6 ${a_x}^2$	0.43	0.31	$0.22/a_x$	153 ${a_x}^2$	0.43	0.35	$0.28/a_x$
3	212 ${a_x}^2$	0.33	0.25	$0.19/a_x$	218 ${a_x}^2$	0.34	0.25	$0.18/a_x$

7.6 Base isolator for a marine separator

To examine the possible performance of MREs in a real system, the example of a base isolator for an Alfa Laval MAB 104 marine oil separator will be considered. Oil separators are present in all modern ships and are responsible for generating a great amount of vibration. Their role is to clean the dirty oil of the main engines from water and solid particles and recycle it. The separation procedure is achieved by a fast-rotating bowl using the principal of the centrifugal force and the difference in the specific weights of oil and water. In the end of every operation cycle the discs inside the bowl rises and the clean oil, water and sludge is pushed out through appropriate pipes. The bowl is rotated by a vertical driving device which is driven by a horizontal device connected to a motor. If the bowl or the vertical and horizontal shafts are misaligned, or the ball bearings of the driving devices are damaged, the vibrations generated by the machine will increase significantly. To design an isolator for a specific application we must first determine the frequency range that we want the isolation to occur, the amount of isolation desired at that frequency and the load distribution.

- **System characteristics**

The MAB 104 machine weights approximately 150 Kg and generates a maximum vibration level of 9mm/s when fully used. The speeds of rotation for the motor shaft and bowl for 50 Hz electric current supply are 1500 rpm and 7500 rpm respectively. The frequencies at which vibrations are most likely to occur in this case are the rotating frequencies of the driving devices at 25 Hz and 125 Hz. The machine has four base isolators and assuming even weight distribution, each one will have to support 37.5 Kg. The detailed load distribution however is not known. In general, the isolator will always be compressed by the weight of the machine. Table 34 summarizes the general vibration characteristics of the MAB 104 system.

Part	**Characteristics**	
Bowl and vertical driving device	Speed of rotation:	7500 rpm
	Frequency of rotation:	125 Hz
Horizontal driving device	Speed of rotation:	1500 rpm
	Frequency of rotation:	25 Hz
Vibration level:	9 mm/s	
Corresponding vibration displacement	At 25 Hz:	0.06 mm
	At 125 Hz:	0.011 mm
Start-up and closing time:	2-3 min	

Table 34: Vibration characteristics of MAB 104 system

The selection of an appropriate isolator in the industry is made based on the following steps:

1. *Determine the load on each mount.*

As mentioned above each isolator will have to support 37.5 Kg or approximately 375 N.

2. *Determine the lower frequency the vibrations are likely to occur.*

The frequencies of the horizontal and vertical rotation systems are:

$$f_{vib1} = \frac{RPM}{60\ sec/min} = \frac{1500}{60} = 25\ Hz, \quad f_{vib2} = \frac{RPM}{60\ sec/min} = \frac{7500}{60} = 125\ Hz \quad (7.6.1)$$

The selection of the mount should therefore be based on the lower frequency of 25 Hz, however the required stiffness and natural frequency will be calculated for both frequencies to gain a better understanding of the isolation system.

3. *Calculate the natural frequency for the desired level of isolation.*

Assuming minimum desired isolation of 80%, the corresponding transmissibility value will be 0.2. From the general transmissibility equation for the frequencies of interest we have:

$$T = \frac{1}{\left(\frac{\omega}{\omega_n}\right)^2 - 1} = \frac{1}{\left(\frac{f}{f_n}\right)^2 - 1} \Rightarrow f_n = \frac{f}{\sqrt{\frac{1}{T} + 1}} \quad (7.6.2)$$

$$f_{n1} = \frac{25}{\sqrt{\frac{1}{0.2} + 1}} = 10\ Hz, \quad f_{n2} = \frac{125}{\sqrt{\frac{1}{0.2} + 1}} = 51\ Hz \quad (7.6.3)$$

4. *Calculate the static deflection to obtain the desired natural frequency.*

From the general equation of the natural frequency:

$$f_n = \frac{1}{2\pi}\sqrt{\frac{K}{m}} = \frac{1}{2\pi}\sqrt{\frac{\frac{F}{x_s}}{m}} \Rightarrow {f_n}^2 = \left(\frac{1}{2\pi}\right)^2 \frac{F}{m x_s} \Rightarrow x_s = \left(\frac{1}{2\pi}\right)^2 \frac{g}{{f_n}^2} \quad (7.6.4)$$

$$x_{s1} = \frac{9.8}{(2\pi 10)^2} = 2.48\ mm, \quad x_{s2} = \frac{9.8}{(2\pi 51)^2} = 0.1\ mm \quad (7.6.5)$$

5. *Calculate the required stiffness to obtain the desired natural frequency.*

$$K_1 = \frac{load\ per\ mount}{static\ deflection} = \frac{375}{x_{s1}} = \frac{375}{2.48\ mm} = 151.2\ KN/m \quad (7.6.6)$$

$$K_2 = \frac{load\ per\ mount}{static\ deflection} = \frac{375}{x_{s2}} = \frac{375}{0.1\ mm} = 3750\ KN/m \quad (7.6.7)$$

6. Select a mount and recalculate the transmissibility using the stiffness of the actual mount.

The mount that can offer an acceptable level of isolation for this case should have a stiffness or spring rate less than the calculated one and a maximum load rating greater than the calculated. These rules apply when selecting a mount from the ones on offer in the industry, but the situation is different when designing the isolator from the beginning. In that case there is another general rule to follow. The static strain should not be more than 5% when the isolator works in compression while it can be much higher for shear. The design of the dimensions of the rubber as well as selection of the rubber itself will have to deal with all the requirements. Figure 109 illustrates one out of the total four antivibration mounts of MAB 104 separator. The device consists of a cylindrical elastomer (3) made of Neoprene rubber placed inside two iron caps (4, 5). The elastomer has an outer and inner diameter of 50 mm and 20 mm respectively and a height of 15 mm.

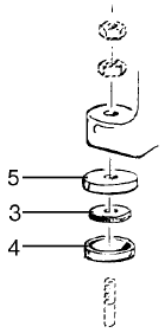

Figure 109: Anti vibration mount for MAB 104 Alfa Laval separator.

The forces caused by the misaligned rotating parts of the separator will subject the device in both shear and compression load components while the movement of the bowl in the end of every cycle induces an additional compression load. In this example, we focus in reducing the vibrations transmitted from the machine to the shell in the vertical direction. The effective area that the load is distributed is:

$$A = \pi\left(r_{outside}^2 - r_{inside}^2\right) = \pi\left(\left(\frac{50}{2}\right)^2 - \left(\frac{20}{2}\right)^2\right) = 1650\ mm^2 \qquad (7.6.8)$$

This corresponds to a stress value of:

$$\sigma_{st} = \frac{F}{A} = \frac{375}{1650\ mm^2} = 0.227\ \ MPa \qquad (7.6.9)$$

The next step is to determine the static displacement the load of the machine causes. Figure 110 presents the static displacement-force curves of the neoprene rubber tested in the laboratory. The displacement and calculated strain for 375N compressive load are:

$$x_{st} = 0.43\ mm\,, \qquad \varepsilon_{st} = \frac{x_{st}}{L}\ 100 = \frac{0.43mm}{15mm}\ 100 = 2.86\% \qquad (7.6.10)$$

The strain is therefore much smaller than the maximum 5% static strain rule. The static stiffness for that load is:

$$K_{st} = \frac{F_{st}}{x_{st}} = \frac{375}{0.43mm} = 872.1\ 10^3 \tag{7.6.11}$$

Using the static displacement to calculate the natural frequency from equation (9.2.6) we get:

$$f_n = \frac{1}{2\pi}\sqrt{\frac{g}{x_s}} = \frac{1}{2\pi}\sqrt{\frac{9.8}{0.43}} = 24\ Hz \tag{7.6.12}$$

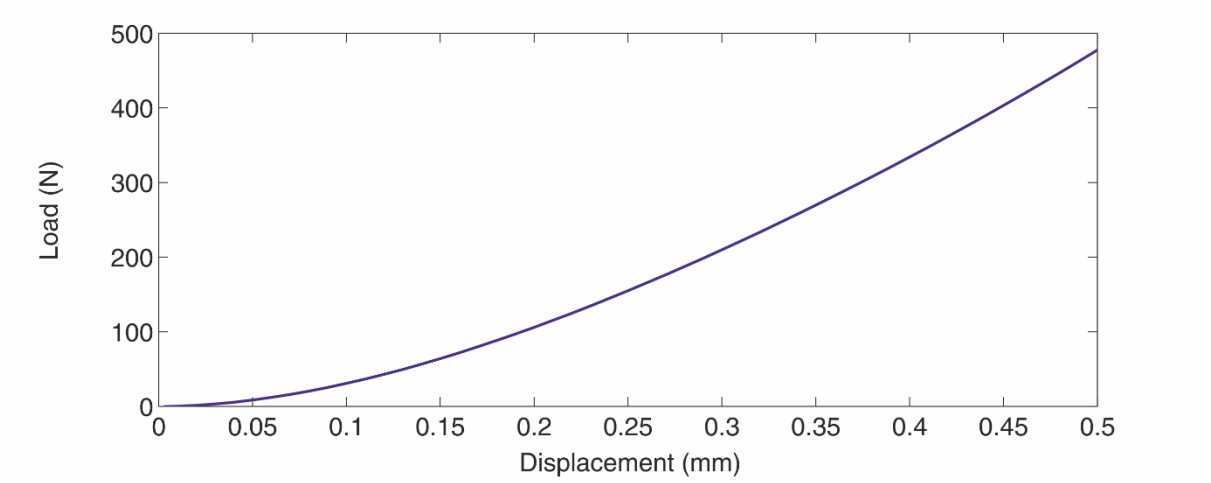

Figure 110: Static load-displacement curves for Neoprene rubber isolator

The above natural frequency will provide efficient isolation at the frequency of 125Hz but for the frequency of 25Hz the isolator is in the amplification stage. The specific mount was therefore designed to provide isolation at the higher frequency of 125Hz where probably the vibrations are more significant due to the movement of the horizontal shaft system. However, for rubber isolator the dynamic stiffness is always larger than the static one and thus, the actual natural frequency is greater than 24Hz. Thus, dynamic loading tests were performed under 3% static strain and 0.05mm dynamic displacement amplitude (0.34% dynamic strain) to find dynamic stiffness and damping. The dynamic properties of Neoprene rubber isolator are mentioned in Table 35. The extracted stiffness was then used to determine the new natural frequency of the Neoprene rubber. The new natural frequency is 7Hz higher than the one calculated using the static stiffness value.

$$f_{ndynamic} = \frac{1}{2\pi}\sqrt{\frac{K_{dynamic}}{m}} = \frac{1}{2\pi}\sqrt{\frac{1414\ 10^3}{37.5}} = 31\ Hz \tag{7.6.13}$$

Table 35: Isolation properties of Neoprene rubber isolator

<table>
<tr><td colspan="4">Isolator characteristics</td></tr>
<tr><td rowspan="9">Neoprene rubber</td><td>Weight supported:</td><td colspan="2">37.5 Kg or ≈375 N</td></tr>
<tr><td>Area of rubber isolator:</td><td colspan="2">1650 mm^2</td></tr>
<tr><td>Height:</td><td colspan="2">15 mm</td></tr>
<tr><td>Static displacement</td><td colspan="2">0.43 mm</td></tr>
<tr><td>Corresponding static strain:</td><td colspan="2"><3 %</td></tr>
<tr><td>Static stiffness:</td><td colspan="2">872 K</td></tr>
<tr><td>Natural frequency:</td><td colspan="2">24 Hz (calculated using the static stiffness value)
31 Hz (calculated using the dynamic stiffness value)</td></tr>
<tr><td>Storage modulus:</td><td>12.8 MPa</td><td rowspan="3">At 3% static strain, 60N* load amplitude (0.051* mm displacement, 0.34% strain) and 5Hz</td></tr>
<tr><td>Dynamic stiffness:</td><td>1414 KN/m</td></tr>
<tr><td>Damping factor:</td><td>0.17</td></tr>
</table>

* Assuming 80% isolation, corresponding displacement input is 0.05mm for 0.01 mm vibration displacement at 125Hz (corresponding to 9mm/s).

- **Scaling up the MRE isolators**

The possibility of replacing the existing neoprene mounts of the MAB104 marine oil separator with an MRE isolator is discussed next. The first step is to examine if the MRE isolator can support the weight of the machine assuming maximum 5% static strain at 375 N static force. This load is too high for the small-scale test MRE isolators examined in chapter 6 thus, larger isolators are needed to cope with the load. However, for the MR effect to be high the gap between the top and base parts of the magnetic circuit, where the MREs are placed, must be as small as possible. This practically means that the height of the MREs cannot be increased while the dimensions of the magnetic circuit must be chosen wisely for the device to be stable.

Of course, scaling up the MRE isolator means increasing the size of the magnetic circuit and rewiring the coil to produce the same magnetic flux for the same values of electric current. This is straightforward when the gap between the magnetic circuit (Height of the MREs H) and $\frac{L}{w}$ ratio remain the same. Changing the length and width will increase the effective area ($L * W$) and the efficiency of the electromagnet but the height of the electromagnet itself will also have to be increased for the coils to be effective. The new coil will need less turns to produce the same magnetic flux, but the copper wire will be longer with higher resistance thus, the power dissipated by the electromagnet will increase as its size increases. As a conclusion, scaling up the MRE isolator means scaling up the whole device while keeping the height of MREs at 5mm.

Making the MREs larger by keeping the height stable will increase shape factor S and affect significantly the zero-field dynamic modulus E as shown in section 4.6. Table 36 presents the results of three rectangular isotropic MREs with 1.15, 1.2 and 1.6 shape factors. The dynamic tests were performed under 0.5% dynamic load, 5Hz frequency and 10% static prestrain while static modulus E was measured at 5% static strain. Sample c_1 has the similar dimension with the MREs used in the isolator device and is used as a reference sample. Both dynamic and static modulus increase linearly with shape factor according to the shape function correction equations (7.6.14) and (7.6.15) respectively. These equations are used later to estimate the actual stiffness of the scaled isolator. The compression MRE isolator is much stiffer than the inclined one and can handle greater loads. Therefore, the compression MRE isolator case will be examined first for all MRE samples.

Design parameters

Thus, it was decided to scale up the MRE isolators assuming:

- The height of the MREs is set to H=5mm
- Maximum static strain of 5% for the compression isolator and 15% for the inclined.
- Maximum natural frequency of 51 Hz.
- The length to width ratio is set to 1.7 (same with the test isolator $\frac{L}{w} = \frac{34mm}{20mm} = 1.7$).
- The magnetic flux (and MR effect) remains the same for the same values of the electric current.
- The static and dynamic moduli of elasticity increase as size increases according to equations (7.6.14) and (7.6.15) for all MRE samples where E_{ref}, E^*_{ref} and S_{ref} refer to the original small-scale MRE isolator tested in the laboratory.

Table 36: Dynamic $|E^*|$ and static E modulus of rectangular isotropic MREs used for scaling up

sample	**h** (mm)	**W** (mm)	**L** (mm)	**S**	$\|\boldsymbol{E^*}\|$ (MPa)	$\boldsymbol{tan\delta}$	**E Static**
c_1	5.5	20	34	1.2	7.33	0.075	3.3
c_2	6.25	30	60.5	1.6	16.38	0.076	5.2
c_3	10.5	41	59.5	1.15	6.7	0.077	3.1
Dynamic modulus $\boldsymbol{E^* = E^*_{ref}(1 + 3(S - S_{ref}))}$ **(7.6.14)**							
Static modulus $\boldsymbol{E = E_{ref}(1 + 1.44(S - S_{ref}))}$ **(7.6.15)**							

Table 37: Static load design properties of compression isolator for 37.5 Kg weight

	X (mm)	Strain ε (%)	Static E (MPa)	K (KN/m)	Stress σ (MPa)	Fn (Hz)	Area (mm^2)	S	L	w	h
									(mm)		
Neoprene	*0.43*	*2.86*	*7.94*	*872*	*0.227*	*24*	*1650*	*0.5*	*Ring*		*15*
Isotropic											
Test device	*0.89*	*17*	*1.61*	*421*	*0.275*	*17*	*1360*	*1.3*	*20*	*34*	*5*
Scaled	0.28	5.6	1.61	1340	0.908	30	4130	2.2	35	59	5
Shape factor correction	0.12	2.45	3.7	3125	0.908	46	4130	2.2	35	59	5
	0.24	4.7	2.77	1562	0.132	32	2842	1.8	29	49	5
Anisotropic											
Test device	*0.57*	*11.4*	*3.26*	*658*	*0.275*	*21*	*1360*	*1.3*	*20*	*34*	*5*
Scaled	0.23	4.6	3.26	1630	0.151	33	2484	1.7	27	46	5
Shape factor correction	0.15	3	5.13	2500	0.151	41	2484	1.7	27	46	5
	0.22	4.5	4.2	1800	0.19	35	1968	1.5	24	41	5
Sample 1 (anisotropic/isotropic parallel combination)											
Test device	*0.66*	*13*	*2.1*	*568*	*0.275*	*20*	*1360*	*1.3*	*20*	*34*	*5*
Scaled	0.25	5	2.1	1500	0.106	32	3520	2	32	55	5
Shape factor correction	0.13	2.52	4.2	2884	0.106	44	3520	2	32	55	5
	0.22	4.5	3.3	1800	0.151	35	2484	1.7	27	46	5
Sample 2 (anisotropic/isotropic series combination)											
Test device	0.71	14.2	1.9	528	0.275	19	1360	1.3	20	34	5
Scaled	0.28	5.6	1.9	1340	0.106	30	3520	2	32	55	5
Shape factor correction	0.14	2.8	3.8	2680	0.106	42	3520	2	32	55	5
	0.25	5	3	1500	0.151	32	2484	1.7	27	46	5
Sample 3 (anisotropic/anisotropic parallel combination)											
Test device	0.61	12.2	2.3	615	0.275	20	1360	1.26	20	34	5
Scaled	0.23	4.6	2.3	1630	0.106	33	3520	2	32	55	5
Shape factor correction	0.11	2.3	4.6	3260	0.106	47	3520	2	32	55	5
	0.25	5	3.3	1500	0.164	32	2288	1.6	26	44	5

Table 37 presents the static stiffness and strain caused to the original test MRE isolator (1st Light blue highlighted row) under a static load of 375N, the scaled-up isolator with no shape factor correction (2nd row) that deflects less than 0.25mm under 375N and the previously scaled up isolator with shape factor corrected stiffness (3nd grey highlighted row). When the shape factor correction is considered, the actual stiffness of the scaled-up isolator is higher than the one predicted using the modulus of the test device E_{ref} and a smaller size isolator can be used instead as the last row (purple highlighted row) indicates. Considering cost as an extra parameter the smallest scaled-up MRE isolator should be preferred. Thus, the isolators with anisotropic and sample 3 MREs are considered for further study.

The next step is to examine the natural frequency and isolation efficiency of the scaled-up anisotropic and sample 3 MRE isolators. Table 38 presents the dynamic stiffness and natural frequency of the scaled-up isolators with dimensions defined at the previous static load design stage. Storage modulus E' of simple scaled isolator (2nd row) is slightly higher than the one of the test device (1st blue highlighted row) to account for the variation of dynamic stiffness with input force amplitude. For example, for the anisotropic compression isolator the 4.37 value corresponds to the modulus of the test device for 0.03 MPa stress or 41N. In this case when the shape factor correction is considered, the predicted dynamic stiffness becomes much higher and so does the natural frequency of the device.

Table 38: Dynamic properties of compression isolator for 60N force amplitude

	tan	E' (MPa)	K' (KN/m)	Stress (MPa)	Fn (Hz)	T (125Hz)	Area (mm^2)	S	L (mm)	w (mm)	h (mm)
	Anisotropic										
Test device	*0.12*	*4.13*	*1124*	*0.044*	*27*	*0.05*	*1360*	*1.3*	*20*	*34*	*5*
Scaled	*0.12*	*4.37*	*1720*	*0.030*	*34*	*0.08*	1968	1.5	24	41	5
Shape factor correction	*0.12*	*6.99*	*2751*	*0.030*	*43*	*0.13*	1968	1.5	24	41	5
	Sample 3 (anisotropic/anisotropic parallel combination)										
Test device	0.12	3.21	873	0.044	24	0.04	*1360*	*1.3*	*20*	*34*	*5*
Scaled	0.12	3.35	1533	0.026	32	0.07	2288	1.6	26	44	5
Shape factor correction	0.12	6.36	2913	0.026	44	0.13	2288	1.6	26	44	5

The static and design properties for the inclined isolator with anisotropic and sample 3 MREs are presented in Table 39 and

Table 40 respectively. The inclined isolator works both in compression and shear loading modes and thus, higher static displacements are acceptable. However, it still needs to become larger than the pure compression isolator to meet the 15% maximum static strain design rule. Unlike the pure compression isolator case, anisotropic and sample 3 inclined MRE isolators have similar static stiffness and are scaled-up to the same size. However, sample 3 MRE inclined isolator has lower natural frequency and higher tanδ values.

Table 39: Static load design properties of inclined isolator for 37.5 Kg weight

	X (mm)	Strain ε (%)	Static E (MPa)	K (KN/m)	Stress σ (MPa)	Fn (Hz)	Area (mm^2)	S	L	w	h
									(mm)		
Anisotropic											
Test device	*1.8*	*36*	*0.76*	*208*	*0.275*	*12*	*1360*	*1.3*	*20*	*34*	*5*
Scaled	1.25	25	0.76	300	0.19	14	1968	1.5	24	41	5
Shape factor correction	0.96	20	0.99	390	0.19	16	1968	1.5	24	41	5
	0.64	13	1.18	586	0.151	20	2484	1.7	27	46	5
Sample 3 (anisotropic/anisotropic parallel combination)											
Test device	1.85	37	0.74	203	0.275	12	1360	1.3	20	34	5
Scaled	1.1	22	0.74	341	0.164	15.2	2288	1.6	26	44	5
Shape factor correction	0.66	13	1.15	571	0.151	20	2484	1.7	27	46	5

Table 40: Dynamic properties of inclined isolator for 60 N force amplitude

	tan	E' (MPa)	K' (KN/m)	Stress (MPa)	Fn (Hz)	T (125Hz)	Area (mm^2)	S	L (mm)	w (mm)	h (mm)
	Anisotropic										
Test device	0.12	1.19	324	0.044	15	0.014	*1360*	*1.3*	*20*	*34*	*5*
Scaled	0.12	1.37	372	0.024	16	0.016	2484	1.7	27	46	5
Shape factor correction	0.12	3	1497	0.024	32	0.07	2484	1.7	27	46	5
	Sample 3 (anisotropic/anisotropic parallel combination)										
Test device	0.14	1.42	385	0.044	16	0.017	*1360*	*1.3*	*20*	*34*	*5*
Scaled	0.14	1.34	665	0.024	21	0.03	2484	1.7	27	46	5
Shape factor correction	0.14	2.95	1464	0.024	31	0.07	2484	1.7	27	46	5

Important notes

- The same shape factor correction function was used for both inclined and compression isolators assuming that they behave in a similar way when scaled-up. This assumption may not be accurate because the inclined isolator is working in both shear and compression modes and it is usually assumed that shear modulus is not affected by size or shape. The estimated static and dynamic stiffness considering shape factor correction might be higher than the real ones.
- The corresponding static strain at each isolator is close to the one the 80N static force caused during characterization stage thus the static prestrain effect on dynamic properties is ignored.

- **Force transmissibility under rotating moment excitation**

In the previous section we examined the zero-field static and dynamic properties of the MRE isolators. In this section we will consider how we can vary the magnetic field in the MRE isolators to reduce the force transmitted to the substrate during start-up and stopping periods. The user manual of MAB 104 separator states that the start-up time is 2-3 min depending on maximum load. During these periods the system will pass through its natural frequency where the transmitted force will increase significantly. The system is modelled as a mass supported by 4 isolators and excited by a moment $M = M_0\omega^2\sin(\omega t)$ as shown in Figure 111.

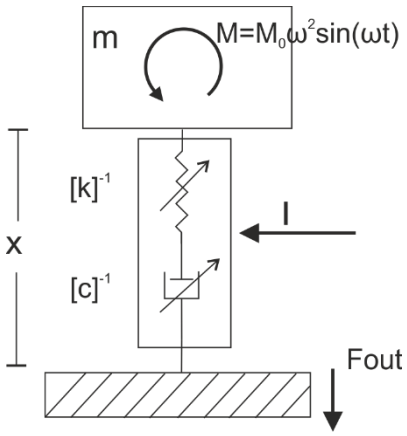

Figure 111: Model of mass-MRE isolator system under rotating moment excitation

Simulation parameters and assumptions:

- System takes 180 sec (3 min) to reach steady operation at 125Hz.
- Only the force transmitted in the vertical direction is of interest.
- $M_0 = 0.1e-3$ (corresponding to approximately 62N amplitude at 125Hz)

- Mass: m=150 Kg
- 4 identical MRE isolators with two planes of symmetry supplied with the same electric current I that depend on amplitude $M_0\omega^2$ and electric current I.

The system is equivalent with the direct force excitation system described in section 7.4 by substituting $f_0 = M_0\omega^2$. The force transmissibility equation therefore is:

$$TFF = \frac{|F_{out}|}{|F_{in}|} = \frac{1}{\sqrt{\left(m\omega^2\frac{[c]}{\omega}^{-1}\right)^2 + (1 - m\omega^2[k]^{-1})^2}} \tag{7.6.16}$$

And the force transmitted:

$$F_{out} = \left(\frac{1 - m\omega^2[k]^{-1}}{\left(m\omega^2\frac{[c]}{\omega}^{-1}\right)^2 + (1 - m\omega^2[k]^{-1})^2} A\, M_0\omega^2\right)\sin\omega t + \left(-\frac{m\omega^2\frac{[c]}{\omega}^{-1}}{\left(m\omega^2\frac{[c]}{\omega}^{-1}\right)^2 + (1 - m\omega^2[k]^{-1})^2} A\, M_0\omega^2\right)\cos(\omega t) \tag{7.6.17}$$

Where:

$$[c]^{-1} = 4\,\frac{1}{SF}\left[c_{eq}\right]^{-1}(A\, M_0\omega^2, I) \quad , \quad [k]^{-1} = 4\,\frac{1}{SF}\left[k_{eq}\right]^{-1}(A\, M_0\omega^2, I) \tag{7.6.18}$$

$SF = \frac{K'\,(scaled\ with\ SF\ correction)}{K'(test\ device)}$ and $A = \frac{area\ of\ original\ test\ device}{area\ of\ the\ scaled\ isolator}$ are scaling factors to adjust the values calculated by the model for the test device isolator to the new size of the MRE isolator of interest. A scaling factor is needed because the model parameters were defined using force and displacement than stress and strain and the force inserted to the model has to be adjusted based on the stress it would cause to the test device.

The force transmissibility of the system with the Neoprene rubber is illustrated in Figure 112. The maximum transmitted force at resonance is 23N at 31Hz. The force transmissibility curves of compression and inclined isolator with anisotropic and sample 3 MREs at zero and 3 Ampere electric current supplied to the electromagnet are shown in Figure 113 and Figure 114 respectively. The force transmissibility was simulated using the linearized model but taking under consideration the effect of force amplitude and the force amplitude-magnetic field coupling effects on dynamic properties. In Figure 113, sample 3 MRE compression isolator is shown to have a lower natural frequency than the anisotropic compression isolator which is the opposite of what is mentioned in

Table 38 where the natural frequency was calculated for 60N force amplitude. In a similar way, in Figure 114 the anisotropic inclined MRE isolator is shown to have a higher natural frequency than sample 3 inclined isolator in contrast to the values of Table 40. This is because the force transmissibility curves consider a moment as excitement force where amplitude increases with frequency and anisotropic MRE behaves differently than sample 3 with varying force amplitude as presented in detail is section 6.4.

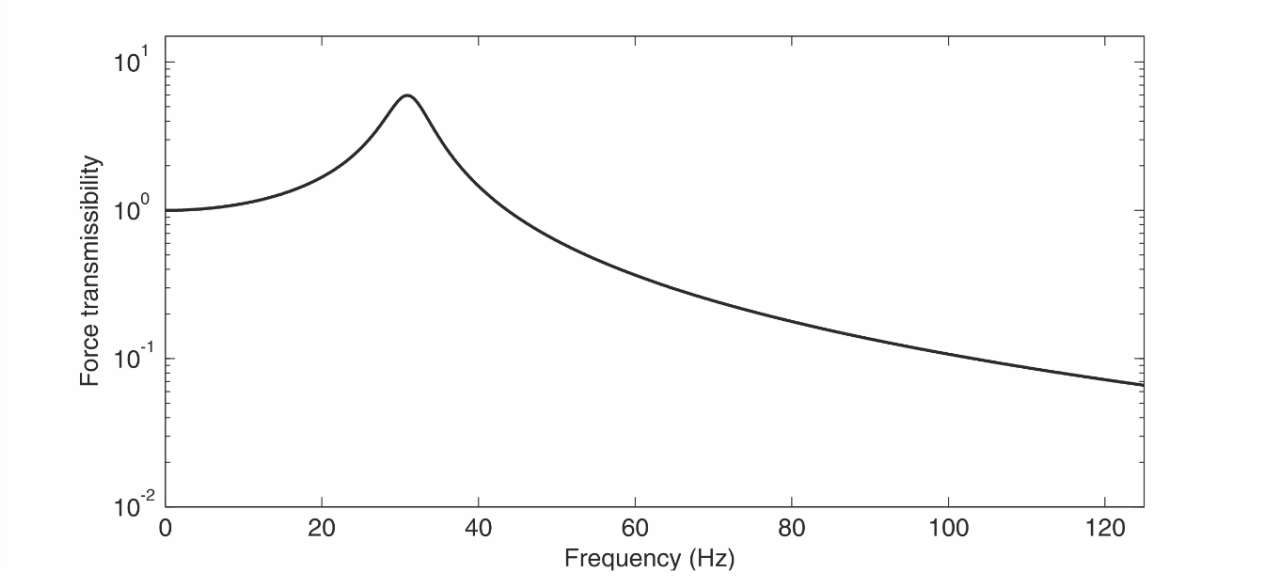

Figure 112: Linear force transmissibility of Neoprene rubber mounts for K'=4*1414 KN/mm, tanδ=0.17 and m=150 Kg.

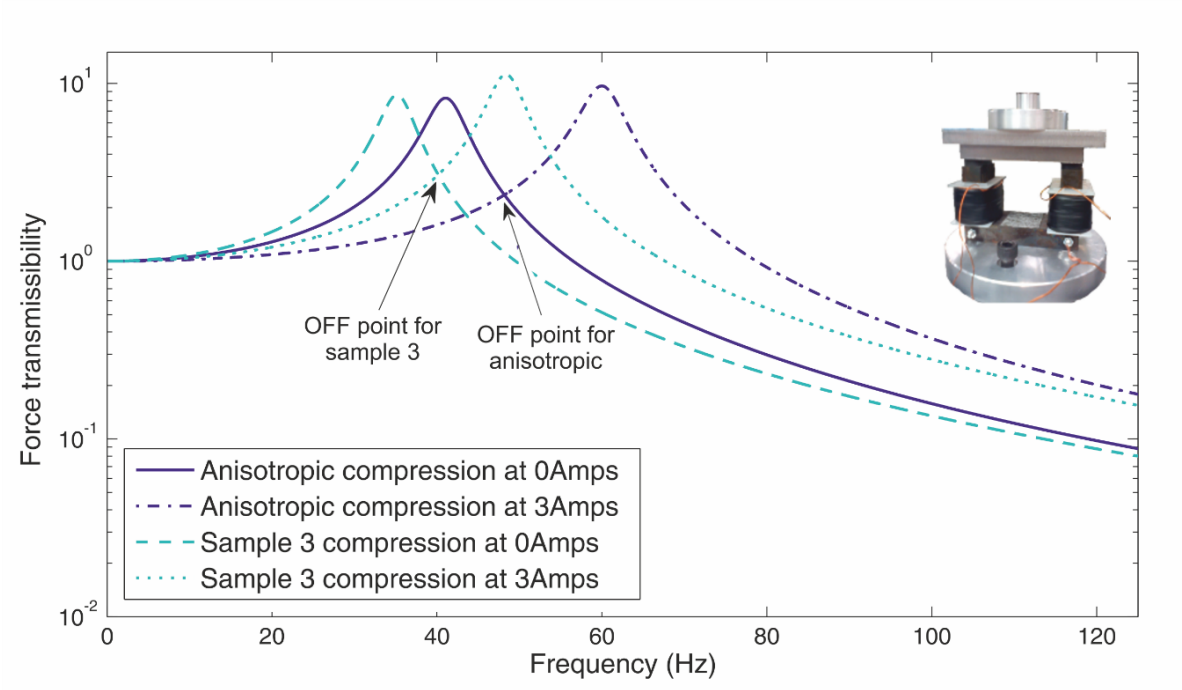

Figure 113: Force transmissibility of anisotropic and sample 3 compression isolator at 0 and 3 Amps in respect to frequency (using the linearized force and electric current depended model).

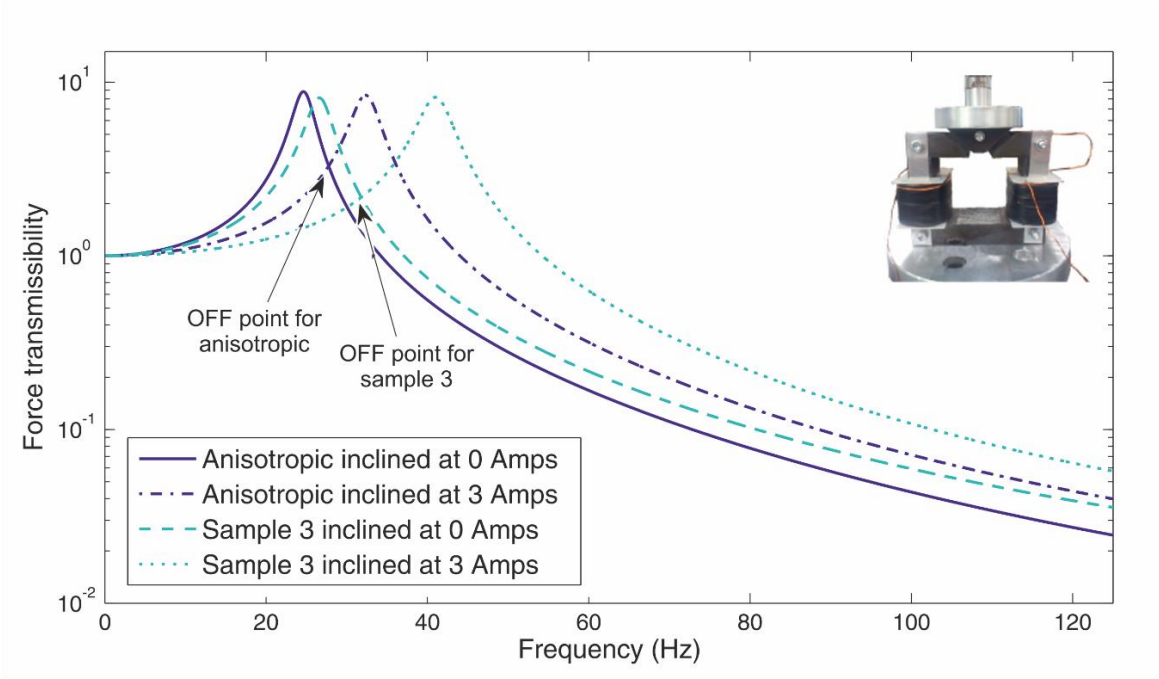

Figure 114: Force transmissibility of anisotropic and sample 3 inclined isolator at 0 and 3 Amps in respect to frequency (using the linearized force and electric current depended model).

The situation becomes interesting when the magnetic field is applied and force amplitude-magnetic field coupling effects are present. The natural frequency, maximum transmitted force at resonance and force transmitted at 125Hz at 0 and 3 Amps are presented in Table 41. Anisotropic compression isolator shows the highest MR effect but not the best isolation efficiency. However, it is a much smaller device compared to the rest and since magnetic materials are expensive, size of the magnetic circuit should not be underestimated when considering MREs. Both inclined MRE isolators are of the same size and show similar isolation characteristics but sample 3 inclined isolator has a higher MR effect and lower transmitted force values.

Table 41: Isolation characteristics at zero field and 3 Amps electric current

	Natural frequency (Hz)		**Transmitted force (125 Hz) (N)**		**Maximum transmitted force Fout (N)**		**MR effect* (%)**
	0 (Amps)	*3 (Amps)*	*0 (Amps)*	*3 (Amps)*	*0 (Amps)*	*ON-OFF control*	*ON-OFF control*
Neoprene	31	-	2	-	23	-	-
Anisotropic compression isolator	41	60	3.7	7.7	59	15	75%
Sample 3 compression isolator	35	48	2.9	5.7	25	12	52 %
Anisotropic inclined isolator	25	32	1	1.7	15	7	44%
Sample 3 inclined isolator	27	42	1.2	2	12	5	58%

*MR effect defined as $\frac{F_{out}(ON-OFF)-F_{out}(0)}{F_{out}(0)} x100$

- **Control strategy**

The control law is a simple ON-OFF operation when the electric current is applied for a predefined period during starting operation. The main idea is to supply 3 Amps electric current to the electromagnet some seconds after starting time well before the amplification stage starts at zero field. The electric current is switched back to zero when the amplification stage at zero field has passed and before the amplification stage at 3 Amps current starts. Since the starting time is a predefined operation no feedback control is needed. The control system can be programmed to switch the MRE isolator ON and OFF at standard times every time the machine starts a starting up or stopping cycle with no feedback needed. Figure 115 and Figure 116 illustrate the force transmitted to the substrate at 0, 3 Amps and when the on-off control strategy is implemented during the 3min (180 sec) starting time for anisotropic compression and sample 3 inclined isolator respectively (MRE isolators with the highest MR effect).

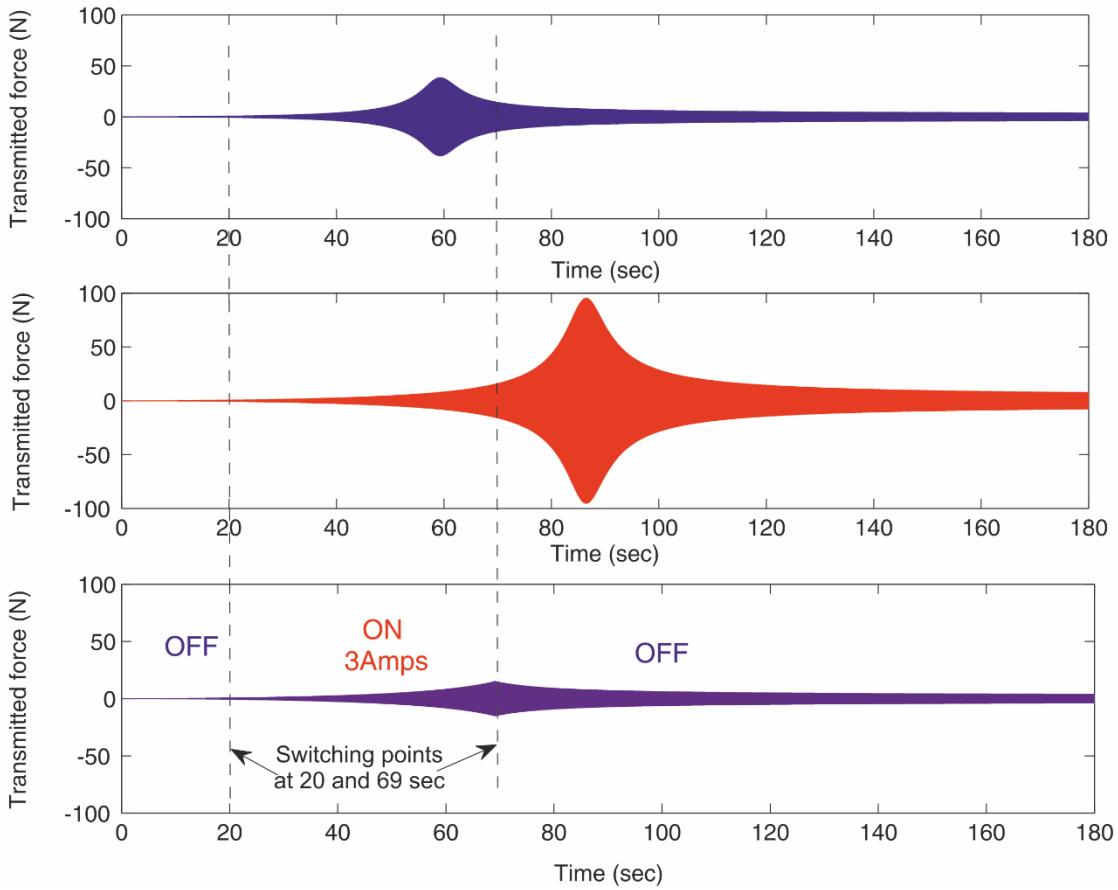

Figure 115: Transmitted force of anisotropic compression isolator at 0, 3Amps and ON-OFF control in respect to time. With ON-OFF control, maximum transmitted force decreases from 59N (at zero field) to 15N.

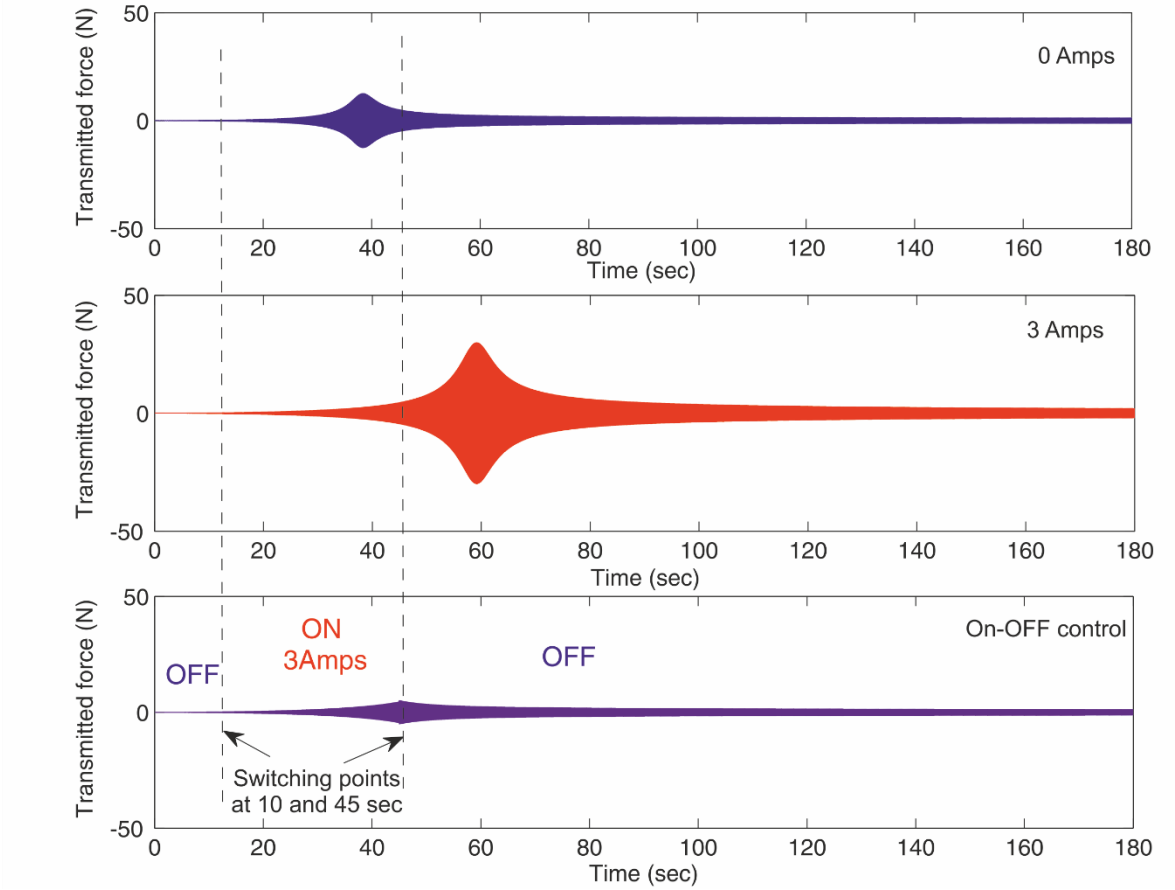

Figure 116: Transmitted force of sample 3 inclined isolator at 0, 3Amps and ON-OFF control in respect to time. With ON-OFF control, maximum transmitted force decreases from 12.5N (at zero field) to 5N.

In terms of isolation efficiency in the full frequency range sample 3 inclined isolator has a better performance than anisotropic compression isolator although the latter has higher MR effect. In addition, the 3 Amps electric current needs to be on for 35 sec to provide efficient isolation for sample 3 inclined isolator while the equivalent time for the anisotropic compression is 49 sec. Thus, it will consume less energy while the magnetic circuit will generate less heat. However, sample 3 inclined isolator is larger than anisotropic compression and operates at higher static strain values. Switching ON periods of this semi-active control system are well above the response time of the MRE isolators and long enough not to expect high losses on the magnetic circuit but still for real applications a cooling system for the electromagnet is needed.

7.7 Chapter summary

In this final chapter, a force dependent Maxwell viscoelastic model was used to describe the behaviour of the inclined and compression MRE isolators and to simulate the force and displacement transmissibility of a single degree of freedom mass-inclined isolator system. The principle of using the inclined MRE isolator to improve stability of a marine engine under loading ship motion was examined for Anisotropic/anisotropic sample 3c and anisotropic/isotropic sample 2c MRs was also examined along with the efficiency of MREs as base isolators for a marine oil separator. The general conclusions can be summarized as:

- Anisotropic/anisotropic sample 3c and anisotropic/isotropic sample 2c inclined isolators are effective at decreasing displacements caused by severe sea motion while ensuring that transmitted vibrations remain to an acceptable level.
- The combined MRE configuration and anisotropic/isotropic or anisotropic/anisotropic ratio can be adjusted to control $\frac{k_q}{k_p}$ and thus, zero field static stiffness in the X, Y axis k_x, k_y and k_β static rotational stiffness about the Z axis.
- When the mounts of a marine oil separator are replaced from MRE isolators and simple ON-OFF control strategy is used to shift the natural frequency during starting up and closing stages, the transmitted force can be reduced up to 75%.
- MREs are amazing.

Chapter 8: Conclusion

Magnetorheological elastomers (MRE) are a category of smart materials that can adjust their mechanical properties according to the intensity of an external magnetic field. The aim of this project is to develop new magnetorheological elastomers with improved isolation efficiency for applications in the marine industry. A two-component room-temperature vulcanization silicon rubber was used as the rubber matrix. For the filler particles, I selected two types of iron particles, one with an average diameter lower than 220 μm (Sigma-Aldrich) and the other with average diameter of 4-6 μm (Sigma-Aldrich), referred as large and small particles respectively. The experimental results showed that the pure isotropic MRE made of large (diameter< 220μm) particles has similar zero field dynamic properties but a slightly lower MR effect than the isotropic MRE made of small (diameter 4-6μm) particles. The anisotropic MRE with large particles is slightly stiffer but have higher damping than the equivalent sample with small particles but their MR effect is 10% lower. A strong MR effect-strain amplitude coupling effect was observed for all samples except anisotropic MREs with large particles that tend to form more stable matrix-particles structures. In addition, the effect of size and shape of isotropic MREs on the dynamic mechanical properties was examined for the first time. The dynamic stiffness of isotropic MREs depends greatly on the size and thickness of the elastomer but not on shape while the MR effect is not influenced by the sample size and shape.

The possibility of combining isotropic and anisotropic MREs in parallel and series configurations to a novel composite MRE as an easy way to tailor its dynamic mechanical properties was then examined. The new composite MRE has higher tangent of the loss angle tanδ than isotropic MRE by keeping stiffness lower than anisotropic MRE without compromising the MR effect. Under a 0.5T magnetic field, pure anisotropic and isotropic MREs increased their storage modulus E' by 31% and 21% respectively while their parallel and series combination composite MREs by 27% and 28% respectively. The exact stiffness and damping capability of composite samples can be tailored by selecting the dimensions of each part and the particle size that each MRE part is made of. For example, using an anisotropic MRE core made of large particles to a cylinder isotropic MRE made of small particles, increases tangent of the loss angle for small strains by 25% while keeping stiffness the same with the case where the anisotropic core is made of small particles. However, there is a 5% compromise on the MR effect.

Combining two anisotropic MREs in parallel, one with particle chains aligned parallel to the applied load and field and the other perpendicular (along x axis), result to a new MRE with same axial and transverse stiffness and MR effect. Combining two anisotropic MREs in parallel, one with particle chains aligned parallel to the applied load and field and the other perpendicular (along z axis), result to a new MRE with same axial and longitudinal stiffness, tangent of the loss angle and MR

effect. The composite isotropic/anisotropic and anisotropic/anisotropic MREs were tested in practice by examining the mechanical properties of a MRE prototype isolator working in pure compression and compression/shear (inclined) mode.

The experimental data were then used to determine the principal elastic axis stiffness ratio $\frac{k_p}{k_q}$ and how this is influenced by the magnetic field. The MR effect of dynamic stiffness is higher in pure compression isolator than the inclined isolator. For example the anisotropic MRE increases its dynamic stiffness by 68% in the compression isolator while for the inclined the percentage drops to 55%. In the inclined isolator composite anisotropic/anisotropic sample 3c has the same zero field static stiffness, lower dynamic stiffness, higher tanδ and same MR effect with anisotropic MRE. Thus, this type of MRE can offer better isolation efficiency than the rest samples. The principal elastic axis stiffness $\frac{k_p}{k_q}$ and damping ratio $\frac{c_p}{c_q}$ changes with the magnetic field for all samples. More tests are needed to define in detail the mechanism behind this phenomenon in application where the MRE would be subjected to multi directional forces.

Finally, a force dependent Maxwell viscoelastic model is used to describe the behaviour of the inclined and compression MRE isolators. The model can predict the magnetic field- strain amplitude coupling effects while the linearized version allows for an easy parameter fitting method and was used to simulate the force and displacement transmissibility of a single degree of freedom mass-inclined and mass-compression isolator system. In addition, two possible applications for the MRE isolators in the marine industry are discussed. The first examines the principle of using MRE inclined isolators to maintain alignment of a marine engine during changing sea states. It was shown, that the MRE inclined isolator can reduce significantly translational and rotational displacements of the mass caused by sea motion. The second example presents the design process of an MRE base isolator that can be controlled by a simple on-off operation to decrease transmitted vibrations during starting up and closing stages. In this example the problem of scaling up the isolator is also addressed.

Appendices

Appendix A Matlab functions

A.1 Functions for solving the system

- **Function to solve the model equation**

```
function [axf,axs,sol] = calc_model( )
syms f0 fst xs xf w t B
syms ra0 ra1 ra2 ra3 ma0 ma1 ma2 ma3 m
syms rst0 rst1 rst2 rst3 mst0 mst1 mst2 mst3
syms r01 r02 r03 r11 r12 r13 r21 r22 r23 r31 r32 r33
syms m01 m02 m03 m11 m12 m13 m21 m22 m23 m31 m32 m33
f=f0*sin(w*t);
x=xs*sin(w*t)+xf*cos(w*t);
dx=diff(x,t);
g0fd=ra0+ra1*f+ra2*f^2+ra3*f^3;
g0fst=rst0+rst1*fst+rst2*fst^2+rst3*fst^3;
gBfd=(r01*B+r02*B^2+r03*B^3)+(r11*B+r12*B^2+r13*B^3)*f+(r21*B+r22*B^2+r23
*B^3)*(f^2)+(r31*B+r32*B^2+r33*B^3)*(f^3);
z0fd=ma0+ma1*f+ma2*f^2+ma3*f^3;
z0fst=mst0+mst1*fst+mst2*fst^2+mst3*fst^3;
zBfd=(m01*B+m02*B^2+m03*B^3)+(m11*B+m12*B^2+m13*B^3)*f+(m21*B+m22*B^2+m23
*B^3)*(f^2)+(m31*B+m32*B^2+m33*B^3)*(f^3);
gr=g0fd+gBfd+g0fst;
zm=z0fd+zBfd+z0fst;
xk=gr*f;
dxc=zm*f;
dxk=diff(xk,t);
% error functions
e=dx-dxc-dxk;
%partial differentials
axf=diff(e,xf);
axs=diff(e,xs);
%solution
a1=2*e*axf;
a2=2*e*axs;
fa1=int(a1,t,0,pi/w);
fa2=int(a2,t,0,pi/w);
eqns = [2*fa1 == 0,2*fa2 == 0 ];
S = solve(eqns);
sol = [S.xf; S.xs];
end
```

- **Function to solve the linear system under force excitation**

```
function [sol] = calc_system4( )
% excitation force applied to the mass fin=f0*sin(w*t);
syms f0 fst xs xf w t B m
syms ra0 ra1 ra2  ma0 ma1 ma2
syms rst0 rst1 rst2 rst3 mst0 mst1 mst2 mst3
syms r01 r02 r03 r11 r12 r13 r21 r22 r23 r31 r32 r33
syms m01 m02 m03 m11 m12 m13 m21 m22 m23 m31 m32 m33
fin=f0*sin(w*t);
x=xs*sin(w*t)+xf*cos(w*t);
dx=diff(x,t);
ddx=diff(dx,t);
```

```
fout=(fin-m*ddx);
f=f0;
g0fd=ra0+ra1*f+ra2*f^2;
g0fst=rst0+rst1*fst+rst2*fst^2+rst3*fst^3;
    gBfd=(r01*B+r02*B^2+r03*B^3)+(r11*B+r12*B^2+r13*B^3)*f+(r21*B+r22*B^2+
    r23*B^3)*(f^2)+(r31*B+r32*B^2+r33*B^3)*(f^3);
    z0fd=ma0+ma1*f+ma2*f^2;
    z0fst=mst0+mst1*fst+mst2*fst^2+mst3*fst^3;
    zBfd=(m01*B+m02*B^2+m03*B^3)+(m11*B+m12*B^2+m13*B^3)*f+(m21*B+m22*B^2+
    m23*B^3)*(f^2)+(m31*B+m32*B^2+m33*B^3)*(f^3);
    gr=g0fd+gBfd+g0fst;
    zm=z0fd+zBfd+z0fst;
    xk=gr*fout;
    dxc=zm*fout;
    dxk=diff(xk,t);
    % error functions
    e=dx-dxc-dxk;
    %partial differentials
    axf=diff(e,xf);
    axs=diff(e,xs);
    %solutions
    a1=2*e*axf;
    a2=2*e*axs;
    fa1=int(expand(a1),t,0,pi/w);
    fa2=int(expand(a2),t,0,pi/w);
    eqns = [2*fa1 == 0,2*fa2 == 0 ];
    S = solve(eqns);
    sol = [S.xf; S.xs];
    end
```

- **Function to solve the system under base excitation**

```
function [S1,S2] = calc_system5( )
    % excitation movement of the support x3=xin*sin(w*t);
syms xin fst xs xf w t B m
syms ra0 ra1 ra2 ma0 ma1 ma2
syms rst0 rst1 rst2 rst3 mst0 mst1 mst2 mst3
syms r01 r02 r03 r11 r12 r13 r21 r22 r23 r31 r32 r33
syms m01 m02 m03 m11 m12 m13 m21 m22 m23 m31 m32 m33
x3=xin*sin(w*t);
f3=m*(w^2*xin*sin(w*t);
x=xs*sin(w*t)+xf*cos(w*t);
dx=diff(x,t);
f=f3;
g0fd=ra0+ra1*f+ra2*f^2;
g0fst=rst0+rst1*fst+rst2*fst^2+rst3*fst^3;
gBfd=(r01*B+r02*B^2+r03*B^3)+(r11*B+r12*B^2+r13*B^3)*f+(r21*B+r22*B^2+
r23*B^3)*(f^2)+(r31*B+r32*B^2+r33*B^3)*(f^3);
z0fd=ma0+ma1*f+ma2*f^2;
z0fst=mst0+mst1*fst+mst2*fst^2+mst3*fst^3;
zBfd=(m01*B+m02*B^2+m03*B^3)+(m11*B+m12*B^2+m13*B^3)*f+(m21*B+m22*B^2+
m23*B^3)*(f^2)+(m31*B+m32*B^2+m33*B^3)*(f^3);
gr=g0fd+gBfd+g0fst;
zm=z0fd+zBfd+z0fst;
xk=gr*f;
dxc=zm*f;
dxk=diff(xk,t);
% error functions
e=dx-dxc-dxk;
%partial differentials
axf=diff(e,xf);
```

```
axs=diff(e,xs);
%solutions
a1=2*e*axf;
a2=2*e*axs;
fa1=int(expand(a1),t,0,pi/w);
fa2=int(expand(a2),t,0,pi/w);
   S1 = solve(2*fa1==0,xf);
   S2 = solve(2*fa2==0,xs);
  End
```

A.2 Function to extract the amplitude dependent model parameters

```
function [req_i,meq_i] = an_param_inc_T( )
%% Anisotropic MRE in inclined isolator (linear case)
%%  0 amp
I0=[0 0 0 0 0 0 0 0];
F_0=1000.*[0.012213008 0.021347563 0.029298048 0.036578842 0.043707403
0.050518826 0.0572317 0.063177287];
x_0=[0.026203152 0.051858968 0.07716023 0.101893439 0.127103547
0.151905433 0.176386686 0.197899713];
tan_0=[0.110206681 0.11676846 0.119959143 0.120438546 0.121388775
0.121080096 0.117041977 0.115559423];
LA_0=atand(tan_0);
M=length(x_0);
for i=1:M;
xs0(i)=x_0(i)*cosd(LA_0(i));
xf0(i)=x_0(i)*sind(LA_0(i));
end
%% 1 amp
I1=[1 1 1 1 1 1 1 1];
F_1=1000.*[0.01411168 0.02440916 0.033866999 0.042874816 0.051671306
0.060112293 0.06793943 0.075047647];
x_1=[0.026347001 0.051950582 0.07725871 0.102298133 0.12695996
0.151772051 0.174933463 0.196666453];
tan_1=[0.126122593 0.132917331 0.133832478 0.132473276 0.130715119
0.129164838 0.12443329 0.122636042];
LA_1=atand(tan_1);
M=length(x_1);
for i=1:M;
xs1(i)=x_1(i)*cosd(LA_1(i));
xf1(i)=x_1(i)*sind(LA_1(i));
end
;
%% 2 Amp
I2=[2 2 2 2 2 2 2 2];
F_2=1000.*[0.016188017 0.028084807 0.038973006 0.049246187 0.059380151
0.068735427 0.077754231 0.085939766];
x_2=[0.026154598 0.051841573 0.077334408 0.102378095 0.127488967
0.151125876 0.175135878 0.1977405];
tan_2=[0.127969419 0.134976783 0.136957713 0.135562807 0.133988959
0.131886047 0.127677829 0.126670018];
LA_2=atand(tan_2);
M=length(x_2);
for i=1:M;
xs2(i)=x_2(i)*cosd(LA_2(i));
xf2(i)=x_2(i)*sind(LA_2(i));
end

%% 3 Amp
I3=[3 3 3 3 3 3 3 3];
```

```
F_3=1000.*[0.017880701 0.031006938 0.04305478 0.054493661 0.06532582
0.075948387 0.085618329 0.094115747];
x_3=[0.02610191 0.051680262 0.077265145 0.102501723 0.126770042
0.151201966 0.174155143 0.195237638];
tan_3=[0.12595826 0.134847796 0.137083676 0.136237103 0.13458637
0.132858249 0.127824641 0.12645756];
LA_3=atand(tan_3);
M=length(x_3);
for i=1:M;
xs3(i)=x_3(i)*cosd(LA_3(i));
xf3(i)=x_3(i)*sind(LA_3(i));
end

%% MR effect
MR_xs=[(xs0) (xs1) (xs2) (xs3)];
MR_xf=[(xf0) (xf1) (xf2) (xf3)];
F=[F_0 F_1 F_2 F_3];
I=[I0 I1 I2 I3];

%% Fit xf
[xData, yData, zData] = prepareSurfaceData( F, I,(-MR_xf./F) );
ft =
fittype( '((m00+m01*y+m02*y^2+m03*y^3)+(m10+m11*y+m12*y^2+m13*y^3)*x+m20*
(x^2))', 'independent', {'x', 'y'}, 'dependent', 'z' );
opts = fitoptions( ft );
opts.Display = 'Off';
opts.Lower = [-Inf -Inf -Inf -Inf -Inf -Inf -Inf -Inf -Inf];
opts.StartPoint = [0 0 0 0 0 0 0 0 0];
opts.Upper = [Inf Inf Inf Inf Inf Inf Inf Inf Inf];
[fitMR_xf, gof] = fit( [xData, yData], zData, ft, opts );
m00_i=fitMR_xf.m00;
m10_i=fitMR_xf.m10;
m20_i=fitMR_xf.m20;
m01_i=fitMR_xf.m01;
m02_i=fitMR_xf.m02;
m03_i=fitMR_xf.m03;
m11_i=fitMR_xf.m11;
m12_i=fitMR_xf.m12;
m13_i=fitMR_xf.m13;
meq_i=[m00_i m10_i m20_i m01_i m02_i m03_i m11_i m12_i m13_i];
% Fit xs
[xData, yData, zData] = prepareSurfaceData( F, I, MR_xs./F );
ft =
fittype( '(r00+r01*y+r02*y^2)+(r10+r11*y+r12*y^2)*x+r20*x^2+r30*x^3',
'independent', {'x', 'y'}, 'dependent', 'z' );
opts = fitoptions( ft );
opts.Display = 'Off';
opts.Lower = [-Inf -Inf -Inf -Inf -Inf -Inf -Inf -Inf -Inf];
opts.StartPoint = [0 0 0 0 0 0 0 0 0];
opts.Upper = [Inf Inf Inf Inf Inf Inf Inf Inf Inf];
[fitMR_xs, gof] = fit( [xData, yData], zData, ft, opts );
r00_i=fitMR_xs.r00;
r10_i=fitMR_xs.r10;
r20_i=fitMR_xs.r20;
r30_i=fitMR_xs.r30;
r01_i=fitMR_xs.r01;
r02_i=fitMR_xs.r02;
r11_i=fitMR_xs.r11;
r12_i=fitMR_xs.r12;
req_i=[r00_i r10_i r20_i r30_i r01_i r02_i r11_i r12_i];
end
```

Appendix B Zero field static mechanical properties

The static compression tests were performed following the directions of the BS ISO 7743:2011 standard ('Rubber, volcanized or thermoplastic-Determination of compression stress-strain properties'). The zero field stress-strain curves for the four different samples are illustrated in Figure 117. Anisotropic MREs are stiffer than isotropic MREs with a more pronounced nonlinear behaviour. MREs with large particles are stiffer than the equivalent samples with small particles but the difference is not that great. Isotropic samples with large particles are 19% stiffer than isotropic MREs with small particles, while for anisotropic MREs this number drops to 13%. For design purposes the Young modulus E is more useful. The median value of E at 5% and 15% strain for all four samples are reported in Table 42.

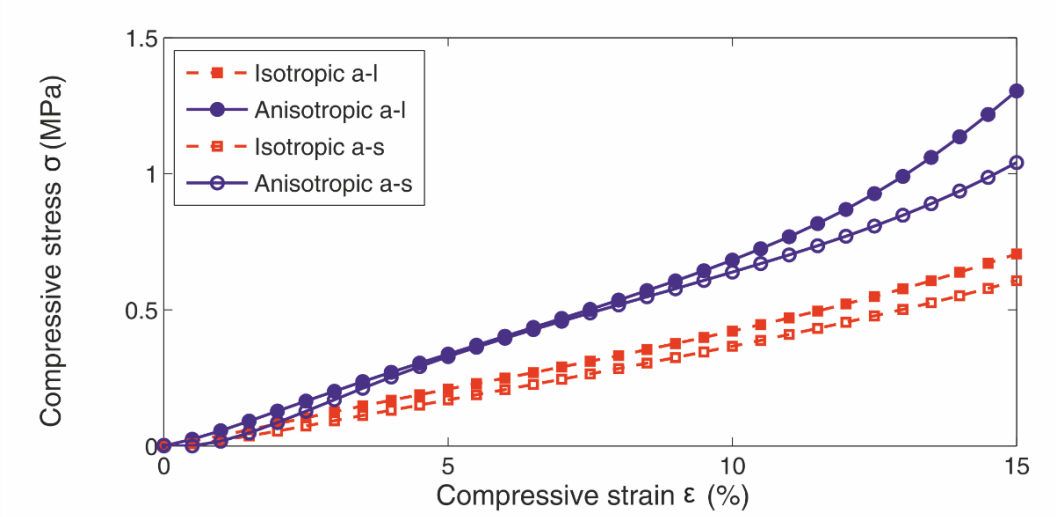

Figure 117: Static strain-stress curves for anisotropic a and isotropic a samples with large (<220μm) and small (4-6μm) particles at zero field.

Table 42: Zero field static compression modulus.

	S_M 5% (MPa)	S_M 15% (MPa)	E (median) (MPa)
Isotropic a_l	4.18	4.70	3.983
Anisotropic a_l	6.75	8.69	6.8995
Isotropic a_s	3.39	4.05	3.3315
Anisotropic a_s	6.57	6.94	6.07

Although, the BS ISO 7743-1:2011 standard requires the samples to be compressed up to 20% strain, this was not possible for anisotropic samples due to the load capacity of INSTRON E1000 machine. For this reason, the samples were compressed up to 15% strain and the compression modulus S_M (Secant modulus) is measured at 5% and 15% strain instead of those at 10% and 20% indicated on the ISO standard. Young modulus E is then calculated $E = S_M(1 - \varepsilon)$ for 5% and 15% strain and the median value is reported. The zero field static strain-stress curves of all disk and rectangular samples are presented in Figure 118 and the values of the compression static modulus E measured at 5% and 15% static strain in Table 43.

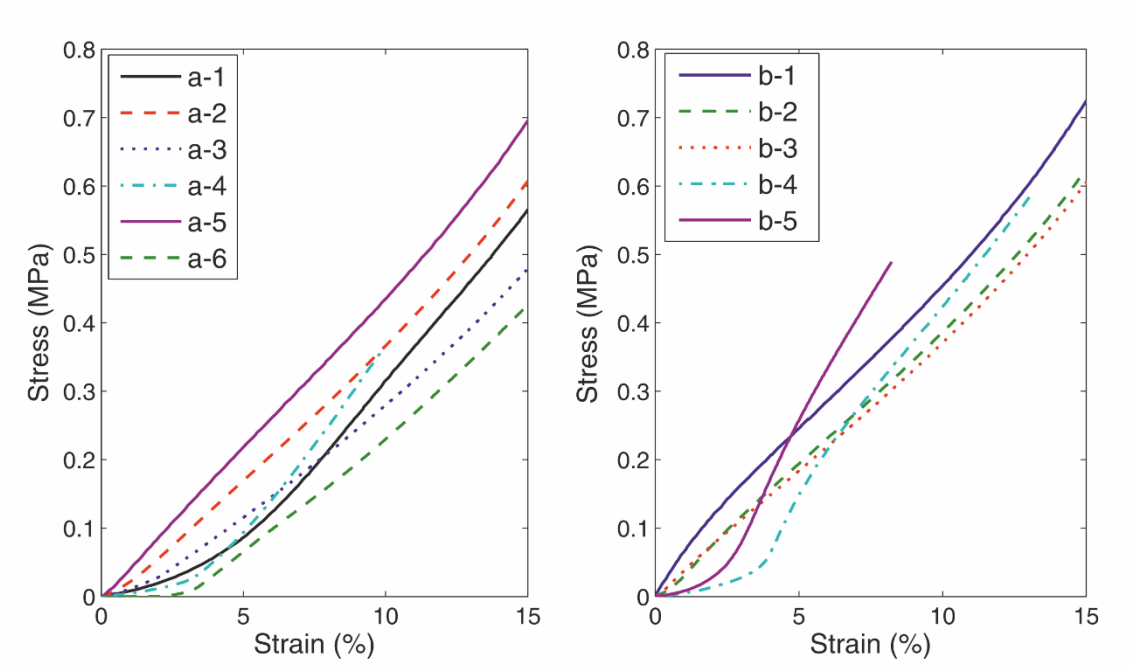

Figure 118: Static stress-strain curves of disk and rectangular shaped isotropic MRE samples.

Table 43: Static compression modulus E of disk and rectangular isotropic MRE samples

sample	**H** (mm)	**D** (mm)	**S**	***E*** (MPa)	**sample**	**H** (mm)	**H1** (mm)	**H2** (mm)	***E*** (MPa)
a_1	6.25	29	1.17	3.5	**b_1**	6.25	22	22	4.4
a_2	12.5	29	0.56	3.6	**b_2**	10.5	22	22	3.6
a_3	21	29	0.34	2.5	**b_3**	22	22	22	3.5
a_4	12.5	56.5	1.14	3.2	**b_4**	5.5	34	34	3.4
a_5	10.5	15.5	0.37	3.5	**c_3**	6.25	30	60.5	5.2
a_6	14.5	41.5	0.7	3					

List of References

Abramchuck S, Kramarenko E, Stepanov G, Nikitin L V, Filipcsei G, Khokhlov A R, and Zrınyi M. 2007. "Novel highly elastic magnetic materials for dampers and seals: Part I. Preparation and characterization of the elastic materials." *Polym. Adv. Technol.* 18 (11): 883–890.

Agirre-Olabide I, Lion A and Elejabarrieta M J. 2017. "A new three-dimensional magnetoviscoelastic model for isotropic magnetorheological elastomers." *Smart Mater. Struct.* 26: 035021 (9pp).

Alberdi-Muniain A, Gil-Negrete N and Kari L. 2012. "Direct energy flow measurement in magneto-sensitive vibration isolator systems." *Journal of Sound and Vibration* 331: 1994-2006.

Allahyarov E, Menzel A M, Zhu L and Lowen H. 2015. "Magnetomechanical response of bilayered magnetic elastomers." *Smart Mater. Struct.* 23: 115004.

Aloui S, Kluppel M. 2015. "Magneto-rheological response of elastomer composites with hybrid-magnetic fillers." *Smart Mater. Struct.* 24: 025016.

Anderson K, Bravoco R, Hargave W, Roche J, Von Lockette P and Lofland S E. 2015. "Dynamic shear response of hard versus soft magnetic magnetoactive elastomers." *Smart Mater. Struct.* 24: 025022.

Baumgaertel M, and Winter H H. 1989. "Determination of discrete relaxation and retardation time spectra from dynamic mechanical data." *Rheologica Acta* 28 (6): 511-519.

Behrooz M, Sutrisno J, Zhang L, Fuchs A and Gordaninejad F. 2015. "Behaviour of magnetorheological elastomers with coated particles." *Smart. Mater. Struct.* 24: 035026.

Behrooz M, Wang X and Gordaninejad F. 2014. "Modeling of a new semi-active/passive magnetorheological elastomer isolator." *Smart Mater. Struct.* 23: 045013.

Blom P, and Kari L. 2011. "A nonlinear constitutive audio frequency magneto-sensitive rubber model including amplitude,frequency and magnetic field dependence." *Journal of Sound and Vibration* 330 (5): 947–954.

Boczkowska A, Awietjan S F, Pietrzko S and Kurzydlowski K J. 2012. "Mechanical properties of magnetorheological elastomers under shear deformation." *Compocites: Part B* 43: 636-640.

Borbath T, Gunther S, Borin D Yu, Gundermann Th and Odenbach S. 2012. “XmCT analysis of magnetic field induced phase transitions in magnetorheological elstomers.” *Smart. Mater. Struct.* (21): 105018.

Bose H, Roder R. 2009. “Magnetorheological elastomer with high variability of their mechanical properties.” *11th Conference on Electrorheological Fluids and Magnetorheological Suspensions.* J. Phys.:Conf. Ser. 012090.

C, Davis L. 1999. “Model of magnetorheological elastomers .” *Journal of Applied Physics* 85: 3348.

C, Snowdon J. 1968. *Vibration and shock in damped mechanical systems.* New York: Wiley.

Cantera M A, Behrooz M, Gibson R F and Gordaninejad F. 2017. “Modeling of magneto-mechanical response of magnetorheological elastomers (MRE) and MRE-based systems: a review.” *Smart Mater. Struct.* 21: 023001 (21pp).

Chen L, and Jerrams S. 2011. “A rheological model of the dynamic behaviour of magnetorheological elastomers.” *J. Appl. Phys.* 110: 013513.

Chen L, Gong X L and Li W H. 2008. “Damping of Magnetorheological Elastomers.” *CHINESE JOURNAL OF CHEMICAL PHYSICS* 21 (6): 581-585.

Chertovich A V, Stepanov G V, Kramarenko E Yu and Khokhlov A R. 2010. “New Composite Elastomers with Giant Magnetic Response.” *Macromolecular Materials and Engineering* 295: 336-341.

Chung K, Jeong U an Oh J E. 2015. “Effects of Magnetic field input cycle and peptizer on the MR effect of Magneto-Rheological Elastomer Based on Natural Rubber.” *POLYMER ENGINEERING AND SCIENCE.*

Collette C, Kroll G, Saive G, Guillemier V and Avraam M. 2010. “On Magnetorheologic Elastomers for Vibration Isolation, Damping, and Stress Reduction in Mass-varying Structures.” *J. Intell. Mater. Syst. Struct.* 21: 1463-1469.

Danas K, Kankanala S V and Triantafyllidis N. 2012. “Experiments and Modeling of Iron-Particle-Filled Magnetorheological Elastomers.” *Journal of the Mechanics and Physics of Solids* (60): 120-138.

Davey A B, and Payne A R. 1965. *Rubber in Engineering Practice.* London: Maclaren & Sons LTD.

Deng H X, and Gong X L. 2007. “Adaptive Tuned Vibration Absorber based on Magnetorheological Elastomer.” *J. Intell. Mater. Syst. Struct.* 18: 1205-1210.

Deng H X, and Gong X L. 2008. “Application of magnetorheological elastomer to vibration absorber.” *Commun. Nonlinear Sci. Numer. Simul.* 13: 1938-1947.

Du H, Li W and Zhang N. 2011. “Semi-active variable stiffness vibration control of vehicle seat suspention using an MR elastomer isolator.” *Smart Mater. Struct.* 20: 105003.

E, Ponte Castañeda P and Galipeau. 2011. “Homogenization-based constitutive models for magnetorheological elastomers at finite strain.” *Journal of the Mechanics and Physics of Solids* 59 (2): 194-215.

Eem S H, Jung H J and Koo J H. 2011. “Application of MR Elastomers for Improving Seismic Protection of Base-Isolated Structures.” *IEE TRANSACTIONS ON MAGNETICS* 47 (10): 2901-2904.

Eem S H, Jung H J and Koo J H. 2012. “Modeling of Magneto-Rheological Elastomers for Harmonic shear Deformation.” *IEEE TRANSACTIONS ON MAGNETICS* 48 (11).

Evans B A, Fiser B L, Prins W J, Rapp D J, Shields A R, Glass D R and Superfine R. 2012. “A highly tunable silicon-based magnetic elastomer with nanoscale homogeneity.” *Journal of Magnetism and Magnetic Materials* 324: 501-507.

Fan Y C, Gong X L , Jiang W Q, Zhang W, Wei B and Li W H. 2010. “Effect of maleic anhydride on the damping property of magnetorheological elastomers.” *Smart Mater. Struct.* 19 (5): 055015.

Feng J, Xuan S, Liu T, Ge L, Yan L, Zhou H and Gong X. 2015. “The prestress-dependent mechanical response of magnetorheological elastomers.” *Smart. Mater. Struct.* 24: 085032.

Forster E, Mayer M, Rabindranath R, Bose H, Schlunck G, Monkman G and Shamonin M. 2012. “Patterning of Ultrasoft, Agglutinative Magnetorheological Elastomers.” *J. APPL. POLYM. SCI.*

Gong X L, Zhang X Z and Zhang P Q. 2005. “Fabrication and characterization of isotropic magnetorheological elastomers.” *Polymer Testing* 24 (5): 669–676.

Gong X, Fan Y, Xuan S, Xu Y and Peng C. 2012. “Component, Control of the Damping Properties of Magnetorheological Elastomers by Using Polycaprolactone as a Temperature-Controlling.” *Ind. Eng. Chem. Res.* 51 (18): 6395–6403.

Gordaninejad F, Wang X and Mysore P. 2012. “Behavior of thick magnetorheological elastomers.” *Intelligent Material Systems and Structures* 23 (9): 1033-1039.

Gu X, Li J, Li Y and Askari M. 2015. “Frequency Control of Smart Base Isolation System Employing A Novel Adaptive Magneto-rheological Elastomer Base Isolator.” *Journal of Intelligent Material Systems and Structures* 1-10.

Gunther D, Borin D Yu , Gunther S and Odenbach S. 2012. “X-ray micro-tomographic characterization of field-structured magnetorheological elastomers.” *Smart Mater. Struct.* (21): 015005.

Guo P F, Lang Z Q and Peng Z K. 2012. “Analysis and design of the force and displacement transmissibility of nonlinear viscous damper based vibration isolation systems.” *Nonlinear Dyn* 67: 2671–2687.

Harris C M, and Piersol. 2002. *HARRIS’ SHOCK AND VIBRATION HANDBOOK fifth edition.* McGRAW-HILL.

Harrison, Gerlind Schubert and Philip. 2016. “Equi-biaxial tension tests on magnetorheological elastomers.” *Smart. Mater. Struct.* 25 (015015): (13pp).

Hoang N, Zhang N and Du H. 2011. “An adaptive tunable vibration absorber using a new magnetorheological elastomer for vehicular powertrain transient vibration reduction.” *Smart Mater. Struct.* 20: 015019.

Hu Y, Wang YL, Gong X L , Gong X Q, Zhang X Z, Jiang W Q, Zhang P Q and Chen Z Y. 2005. “New magnetorheological elastomers based on polyurethane/Si-rubber hybrid.” *Polymer Testing* 24 (3): 324–329.

J, Li Y and Li. 2017. “On the-dependent mechanical model for adaptive magnetorheological elastomer base isolator.” *Smart Mater. Struct.* 26: 045001 (15p).

Jerome, Crede E. Charles and Ruzicka E. 2002. *Harris' Shock and Vibration Handbook chapter 30: Theory of vibration isolation.* McGRAW-HILL.

Jolly M R, Carlson J D and Munoz B C. 1996. “A model of the behaviour of magnetorheological materials.” *Smart Mater. Struct.* 5: 607-614.

Ju B X, Yu M, Fu J, Yang Q, Liu X Q and Zheng X. 2012. “A novel porous magnetorheological elastomer: Preparation and evaluation.” *Smart Mater. Struct.* 21: 035001.

Kallio M, Lindroos T, Aalto S, Järvinen E, Kärnä T and Meinander T. 2007. “Dynamic compression testing of a tunable spring element consisting of a magnetorheological elastomer.” *Smart Mater. Struc.* 16: 269-278.

Kashima S, Miyasaka F, Hirata K. 2012. “Novel Soft Actuator Using Magnetorheological Elastomer.” *Magnetics, IEEE Transactions on* 48 (4): 1649 - 1652 .

Khimi S R, and Pickering KL. 2015. “Comparison of dynamic properties of magnetorheological elastomers with existing antivibration rubbers.” *Composites Part B* 175-183.

Khimi S R, Pickering K L, Mace B R. 2015. “Dynamic properties of Magnetoreological Elastomers Based on Iron Sand and Natural Rubber.” *J. APPL. POLYM. SCI* 41506.

Kim M S, Yang K M, Lee S H, Yoon J H, Jeong U C, Yang I H and Oh J E. 2014. Variable differential mount apparatus using magnetorheological elastomers. United States Patent Patent US 8,844,914 B2. 30 Sep.

Kim Y K, Koo J H, Kim K S and Kim S H. 2011. “Suppressing harmonic vibrations of a miniature cryogenic cooler using an adaptive tunable vibration absorber based on magnetorheological elastomers.” *Rev. Sci. Instrum.* 82: 035103.

L, Khimi S R and Pickering K. 2015. “Comparison of dynamic properties of magnetorheological elastomers with existing antivibration rubbers.” *Composites Part B* 83: 175-183.

Lejon Jonas. 2012. “On the frequency, dynamic strain amplitude, prestrain, temperature and magnetic field strenght dependance of magnetosensitive elastomers.” Doctoral Thesis, Stockholm, Sweden.

Lerner A A, and Cunefare K A. 2008. “Performance of MRE-based Vibration Absorbers.” *J. Intell. Mater. Sys. Struct.* 19: 551-563.

Li R, and Sun L Z. 2013. “Viscoelastic responses of Silicone-Rubber-Based Magnetorheological Elastomers Under Compressive and Shear Loadings.” *Journal of engineering Materials and Technology* 135: 021008-1 -7.

Li W H, Zhang X Z. 2010. “A study of the magnetorheological effect of bimodal particle based magnetorheological elastomers.” *Snart Mater. Struct.* 19: 035002.

Li W, and Nakano M. 2013. “Fabrication and characterization of PDMS based magnetorheological elastomers.” *Smart Materials and Structures* 22 (5): 055035-1-055035-7.

Li Y, Li J and Li W. 2013. “Design and experimental testing of an adaptive magneto-rheological elastomer base isolator.” United States: IEEE. 381-386.

Lian C, Lee K H and Lee C X. 2015. “Friction and Wear Characteristics of Magneto-Rheological Elastomers Based on Silicone/Polyurethane Hybrid.” *Journal of tribology* 137: 031607.

Lin He, Wei Xu, Wenjun Bu and Liang Shi 2014.''Dynamic analysis and design of air spring mounting system for marine propulsion system.'' *Journal of Sound and Vibration 333 4912-4929.*

Lokander M, and Stenberg B. 2003. “Improving the magnetorheological effect in isotropic magnetorheological rubber materials.” *Polymer Testing* 22 (6): 677–680.

Mitsumata T, and Ohori S. 2011. “Magnetic polyurethane elastomers with wide range modulation of elasticity.” *Polym.Chem.* 2: 1063.

Nayak B, Dwivedy S K and Murthy K. 2004. “Fabrication and characterization of magnetorheological elastomer with carbon black.” *Journal of Intelligent Material Systems* 1-10.

Norouzi M, Alehashem S M S, Vatandoost H, Ni Y Q and Shahmardan M M. 2015. “A new approach for modeling of magnetorheological elastomers.” *Journal of Intellignet Material Systems and Structures* 1-15.

Oguro T, Sasaki S, Tsujiei Y, Kawai M, Mitsumata T, Kaneko T and Zrinyi M. 2017. “Sample Size Effect of Magnetomechanical Response for Magnetic Elastomers by Using Permanent Magnets.” *Journal of Nanomaterials* Article ID 8605413.

Opie S, and Yim W. 2011. “Design and Control of a Real-Time Variable Modulus Vibration Isolator.” *Journal of Intelligent Material Systems and Structures* 22: 113-125.

P, Galipeaua E and Ponte Castañeda. 2012. “The effect of particle shape and distribution on the macroscopic behavior of magnetoelastic composites.” *International Journal of Solids and Structures* 49 (1): 1–17.

Padalka O, Song H J, Wereley N M , Filer J A, Bell R C. 2010. “Stiffness and Damping in Fe, Co, and Ni Nanowire-Based Magnetorheological Elastomeric Composites.” *Magnetics, IEEE Transactions* 46 (6): 2275 - 2277.

Popp KM, Kroger M, Li WH, Zhang XZ and Kosasih PB. 2010. “MRE Properties under shear and squeeze modes and applications.” *J Intell Mater Syst Struct.* 21: 1471-1477.

Schubert G, Harrison P. 2015. “Large-strain behaviour of Magneto-rheological Elastomers tested under uniaxial compression and tension, and pure shear deformations.” *Polymer Testing* 42: 122-134.

Sorokin V V, Ecker E, Stepanov G V, Shamonin M, Monkman G, Kramarenko E Yu and Khokhlov A R. 2014. “Experimental study of the magnetic field enhanced Payne effect in magnetorheological elastomers.” *Soft Matter* 10: 8765-8776.

Sun S S, Chen Y, Yang J, Tian T F,Deng H X, Li W H, Du H and Alici G. 2014. “The development of an adaptive tuned magnetorheological elastomer absorber working in squeeze mode.” *Smart Materials and Sturcutres* 23 (7): 1-8.

Sun S, Deing H, Yang J, Li W, Du H and Alici G. 2015. “Performance evaluation and comparison of magnetorheological elastomer absorbers working in shear and squeeze modes.” *J. Intel. Mater. Syst. Struct.* 1-7.

Sun S, Deng H, Yang J, Li W, Du H, Alici G and Nakano M. 2015. “An adaptive tuned vibration absorber based on multilayered MR elastomers.” *Smart Mater. Struct.* 24: 045045.

Thorin A, Azoug A and Constantinescu A. 2012. “Influence of prestrain on mechanical properties of highly-filled elastomers: Measurements and modeling.” *Polymer Testing* 31: 978-986.

V, Ramamurti. n.d. In *Mechanical Vibration Practice With Basic Theory*, 68-76. CRC Press, Narosa Publishing House.

Vokoun D, Beleggia M, Heller L and Sittner P. 2009. “Magnetostatic interactions and forces between cylindrical permanent magnets.” *Journal of Magnetism and Magnetic Materials* 321: 3758-3763.

Wang Q, Yang F, Guan H, Chen J and Zhao B. 2011. “Study on Magnetic and Physical Mechanical Properties of NBR Composites Filled with Nano-Sro.6Fe2O3.” *Journal of Elastomers and Plastics* 43 (3): 275-284.

Wang Y, Hu Y, Gong X, Jiang W, Zhang P and Chen Z. 2007. “Preparation and Properties of Magnetorheological Elastomers Based on Silicon Rubber/Polystyrene Blend Matrix.” *Journal of Applied Polymer Science* 103: 3143-3149.

Wei B, Gong X and Jiang W. 2010. “Influence of polyurethane properties on mechanical performances of magnetorheological elastomers.” *Journal of Applied Polymer Science* 116 (2): 771-778.

Xin F L, Bai X X and Qian L J. 2016. “Modeling and experimental verification of frequency-, amplitude-, and magnetodependent viscoelasticity of magnetorheological elastomers.” *Smart Mater. Struct.* 25: 105002.

Xu Y, Gong X, Xuan S, Zhang W and Fan Y. 2011. “A high-performance magnetorheological material:preparation,characterizaton and amgnetic-mechanic coupling properties.” *Soft Matter* 7: 5246-5254.

Xu Z, Gong X, Liao G and Chen X. 2010. “An active-damping-compensated magnetorheological elastomer adaptive tined vibration absorber.” *J. Intell. Mater. Syst. Struct.* 21: 1039-1047.

Yang CY, Fu J, Yu M, Zheng X and Ju BX. 2015. “A new magnetorheological elastomer isolator in shear–compression mixed mode.” *Journal of Intelligent Material Systems and Structures* 26 (10): 1290-1300.

Yang J, Du H, Li W , Li Y and Li J. 2013. “Experimental study and modeling of a novel magnetorheological elastomer isolator.” *Smart Materials and Structures* 22 (11): 117001.

Yang J, Gong X G, Deng H, Qin L and Xuan S. 2012. “Investigation on the mechanism of damping behavior of magnetorheological elastomers.” *Smart Mater. Struct.* 21 (12): 125015.

Yang J, Gong X, Deng H, Qin L and Xuan S. 2012. “Investigation on the mechanism of damping behavior of magnetorheological elastomers.” *Smart Mater. Struct.* 21: 125015.

Yang J, Gong X, Zong L, Peng C and Xuan S. 2013. “Silicon Carbide-Strenghened Magnetorheological Elastomer: Preparation and Mechanical Property.” *POLYMER ENGINEERING AND SCIENCE* 2615-21.

Yang J, Sun S S, Du H, Li W H, Alici G and Deng H X. 2014. “A novel magnetorheological elastomer isolator with negative changing stiffness for vibration reduction.” *Smart Mater. Struct.* 23: 105023.

Yu M, Ju B, Fu J and Yang Q. 2012. “Influence of composition of carbonyl iron particles on dynamic mechanical properties of magnetorheological elastomers.” *Journal of Magnetism and Magnetic Materials* 324: 2147-2152.

Yu M, Qi S, Fu J and Zhu M. 2015. “A high-damping magnetorheological elastomer with bi-directional magnetic-control modulus for potential application in seismology.” *APPLIED PHYSICS LETTERS* 107: 111901.

Yu M, Xing Z, Zheng X, Fu J and Choi S B. 2015. “Experimental investigation on the field-dspendent properties of magnetorheological elastomer with circular honeycomb holes.” *Frontiers in Materials* 1 (34).

Yu Y, Li Y and Li J. 2015. “Nonparametric modeling of magnetorheological elastomer base isolator based on artificial neural network optimized by ant colony algorithm.” *Journal of Intelligent Material Systems and Structures.*

Zhang W, Gong X L and Chen L. 2010. “A Gaussian distribution model of anisotropic magnetorheological elastomers.” *Journal of Magnetism and Magnetic Materials* 322: 3797–3801.

Zhang W, Gong X L, Xuan S H and Xu Y G. 2010. “High performance hybrid magnetorheological material: Preparation and mechanical properties.” *Ind. Eng. Chem. Res* 49: 12471-12476.

Zhang W, Gong X, Shouhu X and Jiang W. 2011. “Temperature-Dependent Mechanical Properties and Model of Magnetorheological Elastomers.” *Ind. Eng. Chem. Res.* 50 (11): 6704–6712.

Zhang W, Gong XL, BJiang YC and Fan WQ. 2010. “Investigation of the durability of anisotropic magnetorheological elastomers based on mixed rubber.” *Smart Mater. Struct.* 19: 085008.

Zhang X, Peng S, Wen W and Li W. 2008. “Analysis and fabrication of patterned magnetorheological elastomers.” *Smart. Mater. Struct.* 17: 045001.

Zhou Y, Jerrams S, Betts S and Chen L. 2015. “Fatigue life prediction of magnetorheological elastomers subjected to dynamic equi-biaxial cyclic loading.” *Materials Chemistry and Physics* 146: 487492.

Zhu J T, Xu Z D and Guo Y Q. 2013. “Experimental and Modeling Study on Magnetorheological Elastomers with Different Matrices.” *J. Matter. Civ. Eng.* 25: 1762-1771.

Zhu J T, Xu Z D and Guo Y Q. 2012. “Magnetoviscoelasticity parametric model of an MR elastomer vibration mitigation device.” *Smart Mater. Struct.* 21: 075034.